

Department of Physics and Astronomy

University of Heidelberg

**Dissertation**

submitted to the

Combined Faculty of

Mathematics, Engineering and Natural Sciences

of the Ruperto-Carola-University of Heidelberg. Germany

for the degree of

Doctor of Natural Sciences

Put forward by

Philipp Weidenkaff

born in Heidelberg, Germany

Oral examination: 6th of February 2025

**The eTOF Project at STAR:**

**Characterization, Calibration and Data Validation of a**

**Large-Scale Multi-Gap Resistive Plate Chamber**

**System**

This dissertation has been carried out by

Philipp Weidenkaff

at the

Physikalisches Institut

under the supervision of

Prof. Norbert Herrmann

second referee:

Prof. Ulrich Uwer

**Das eTOF Projekt in STAR:**  
**Charakterisierung, Kalibrierung and Daten-Validierung eines großangelegten Systems aus Mehrfachspalt-Widerstandsplattenkammern**

eTOF ist ein vorwärts-gerichtetes Time-of-Flight (TOF)-Detektor-Upgrade für das STAR-Experiment am relativistischen Schwerionen-Collider (RHIC). Das eTOF-Programm ist eine Zusammenarbeit zwischen STAR und dem Compressed Baryonic Matter (CBM)-Experiment an FAIR. Das eTOF-Rad besteht aus 108 CBM-TOF-Mehrfachschlitz-Widerstandsplattenkammer (MRPC)-Prototypen. Für CBM ist eTOF der erste groß angelegte Test seiner MRPC-Prototypen und seines frei laufend Datenaufnahmesystems (DAQ). Für STAR erweitert eTOF die Vorwärtsakzeptanz seines Time-of-Flight-Systems zur Teilchenidentifikation (PID). Diese erweiterten PID-Fähigkeiten sind wichtig für die Analyse der Beam Energy Scan II-Kampagne von STAR, insbesondere im Fixed-Target-Programm. Die MRPC-Prototypen haben über eine Betriebszeit von mehr als zwei Jahren keine signifikante Alterung gezeigt. Es wird eine durchschnittliche System-Zeitauflösung von  $70,7\text{ ps}$  mit einer Streuung von  $< 4,3\text{ ps}$  RMS zwischen den einzelnen MRPC-Zeitauflösungen erreicht. Die Track-Matching-Effizienz von eTOF liegt bei fast 70 %. Die PID-Fähigkeiten von eTOF werden am Beispiel der Kaon-Identifikation und der Rekonstruktion von  $\Phi$ -Mesonen demonstriert. Es wird gezeigt, dass eTOF eine Kaon-Identifikationsreinheit von fast 85 % erreicht. Durch die Einbeziehung von eTOF erhöht sich die Anzahl der rekonstruierbaren  $\Phi$ -Mesonen um 301 % bei der höchsten Kollisionsenergie des Fixed-Target-Modus ( $\sqrt{s_{NN}} = 7,7\text{ GeV}$ ). Die Vorwärtsakzeptanz für diese Energie wird von  $y - y_{cms} > 0,8$  auf  $y - y_{cms} > 0,3$  erweitert.

**The eTOF project at STAR:**  
**Characterization, Calibration and Data Validation of a Large-Scale Multi-Gap Resistive Plate Chamber System**

eTOF is a forward time of flight (TOF) detector upgrade to the STAR experiment at the rRelativistic Heavy Ion collider (RHIC). The eTOF program is a collaboration between STAR and the Compressed Baryonic Matter (CBM) experiment at FAIR. The eTOF wheel consists of 108 CBM-TOF multi-gap resistive plate chamber (MRPC) prototypes. For CBM, eTOF is the first large-scale test of its MRPC prototypes and its free-streaming data acquisition system (DAQ). For STAR, eTOF extends the forward acceptance of its time of flight system for particle identification (PID). These extended PID capabilities are important for the analysis of STAR's Beam Energy Scan II campaign, especially the in the fixed target program. The MRPC prototypes have shown no significant aging over an operation time of more than two years. An average system time resolution of  $70.7\text{ ps}$  with a spread of  $< 4.3\text{ ps}$  RMS between the individual MRPC time resolutions is achieved. The track matching efficiency of eTOF is close to 70 %. eTOFs PID capabilities are demonstrated on the example of kaon identification and the reconstruction of  $\Phi$ -mesons. eTOF is shown to achieve a kaon identification purity close to 85 %. The inclusion of eTOF increases the number of reconstructable  $\Phi$ -mesons by 301 % at the highest fixed target collision energy ( $\sqrt{s_{NN}} = 7.7\text{ GeV}$ ). The forward acceptance is extended for this energy from  $y - y_{cms} > 0.8$  to  $y - y_{cms} > 0.3$ .

# Contents

<b>1</b>	<b>Introduction and Motivation</b>	<b>7</b>
1.1	Acknowledgements . . . . .	8
1.2	Own Contributions . . . . .	9
<b>2</b>	<b>Physics Context</b>	<b>11</b>
2.1	Phases of Matter . . . . .	11
2.2	Quantum Chromodynamics and the Standard Model of Particle Physics . . . . .	12
2.3	Physics at Highest Baryon Densities . . . . .	14
2.4	Probing Compressed Baryonic Matter in Heavy Ion Collisions . . .	16
2.5	Observables of Hadronic Phases . . . . .	18
2.5.1	Proton Kurtosis . . . . .	19
2.5.2	Hadronic NCQ-Scaling of the Elliptical Flow . . . . .	19
2.5.3	$\Lambda$ -Baryon Measurements . . . . .	21
<b>3</b>	<b>Experiments</b>	<b>22</b>
3.1	FAIR . . . . .	22
3.2	CBM . . . . .	24
3.2.1	The CBM Detector . . . . .	25
3.2.2	CBM-TOF . . . . .	26
3.3	FAIR-Phase 0 . . . . .	28
3.3.1	mCBM . . . . .	28
3.3.2	eTOF at STAR . . . . .	30
3.4	STAR . . . . .	30
3.4.1	The STAR Detector . . . . .	31
3.4.2	Beam Energy Scan II . . . . .	33
<b>4</b>	<b>STAR-eTOF</b>	<b>35</b>
4.1	Detector Geometry . . . . .	35
4.2	The Physics Case of the eTOF Upgrade . . . . .	37
4.3	Multi-Gap Resistive Plate Chambers . . . . .	39
4.3.1	Particle Identification with TOF . . . . .	39
4.3.2	MRPC Working Principle . . . . .	41
4.3.3	Prototype MRPC2 THU . . . . .	46
4.3.4	Prototype MRPC3 USTC . . . . .	48
4.4	Front-End Electronics . . . . .	48
4.4.1	PADI . . . . .	48
4.4.2	GET4 . . . . .	50



4.5	Data Path . . . . .	52
4.5.1	Timing Synchronization System . . . . .	55
<b>5</b>	<b>Software Development and Calibrations</b>	<b>57</b>
5.1	StRoot and StMakers . . . . .	57
5.2	eTOF Data Structures . . . . .	59
5.3	eTOF Data Production Chain . . . . .	62
5.3.1	StETofDigiMaker . . . . .	62
5.3.2	StETofCalibMaker . . . . .	62
5.3.3	StETofHitMaker . . . . .	64
5.3.4	StETofMatchMaker . . . . .	68
5.4	Calibration Algorithms . . . . .	71
5.4.1	StETofQAMaker . . . . .	71
5.4.2	calibrate_etof.C . . . . .	72
5.4.3	Position Corrections . . . . .	73
5.4.4	Timing Corrections . . . . .	74
5.4.5	Walk Corrections . . . . .	77
5.4.6	Alignment Corrections . . . . .	78
5.4.7	Run-by-Run Offset Calibrations . . . . .	79
<b>6</b>	<b>eTOF during Beam Energy Scan II</b>	<b>81</b>
6.1	Datasets . . . . .	81
6.2	Changes in Operation Conditions . . . . .	82
6.3	Pre-Amplifier Damages . . . . .	82
6.3.1	2019 PADI Damage Events . . . . .	83
6.3.2	2020 PADI Damage Events . . . . .	86
6.4	DAQ Stability . . . . .	93
6.4.1	GET4 Inactivity . . . . .	93
6.4.2	Clock Jumps . . . . .	97
<b>7</b>	<b>Detector Performance</b>	<b>101</b>
7.1	Signal Observations . . . . .	101
7.1.1	Aim of this Study . . . . .	101
7.1.2	ToT Uniformity . . . . .	102
7.1.3	Signal Velocities . . . . .	104
7.1.4	Signal Reflections . . . . .	107
7.1.5	Dark Rate . . . . .	110
7.1.6	Conclusions of this Study . . . . .	115
7.2	Efficiency . . . . .	116
7.2.1	Aim of this Study . . . . .	116
7.2.2	Detector Efficiency - Overlap Analysis . . . . .	117
7.2.3	Matching Efficiency . . . . .	124
7.2.4	Conclusions - Efficiency . . . . .	137

7.3	Time Resolution . . . . .	138
7.3.1	Aim of this Study . . . . .	138
7.3.2	System Time Resolution . . . . .	139
7.3.3	Detector Resolution . . . . .	142
7.3.4	Time Resolution Dependencies . . . . .	145
7.3.5	Conclusions: Time Resolution . . . . .	152
<b>8</b>	<b>Physics Performance</b>	<b>154</b>
8.1	The KFParticle Reconstruction Package . . . . .	154
8.2	$\Lambda^0$ Reconstruction . . . . .	156
8.2.1	Analysis . . . . .	156
8.2.2	Proton PID Purity Estimate from Lambda Decays . . . . .	159
8.3	$\phi$ -Meson Reconstruction . . . . .	162
8.3.1	Kaon Identification and Purity . . . . .	162
8.3.2	$\phi$ Reconstruction with Combined TOF . . . . .	168
<b>9</b>	<b>Conclusions</b>	<b>173</b>
9.1	Learnings for CBM . . . . .	173
9.2	BES-II Data for STAR . . . . .	174
<b>10</b>	<b>Danksagungen</b>	<b>177</b>
<b>11</b>	<b>References</b>	<b>178</b>
<b>12</b>	<b>List of Publications</b>	<b>184</b>

# 1 Introduction and Motivation

To enlighten me more,  
What holds the world together at its innermost core  
-J.W. v. Goethe, Faust I

Doctor Faust's old saying describe one of the main motivations that have been driving scientific research in physics since its inception. Over the course of the 20th century, humanity has learned that matter consists of atoms, that atoms themselves consist of their electron shell and a nucleus, that the nuclei are made up of nucleons, and finally, that nucleons are made up of quarks and gluons. Now, nearly three decades after the discovery of the gluon, their behavior is still not fully understood. This is especially true in large systems at high net-baryon densities. The latest and next generation of heavy ion collision experiments aim to shed light at this complex world.

Compressed Baryonic Matter (CBM) is one of these next generation heavy ion experiments, situated at the Gesellschaft für Schwerionenforschung (GSI) in Darmstadt. It aims to achieve the highest possible net baryon densities and interaction rates. During the time of this thesis, its detector development is well advanced. Large-scale detector prototype tests and system integration tests are ongoing in mini-CBM@SIS-18 and STAR-eTOF@RHIC.

STAR is a last generation heavy ion at the relativistic heavy ion collider (RHIC) in Brookhaven. Its Beam Energy Scan II (BES-II) program explores the collision energy range of  $\sqrt{s_{NN}} = 27 \text{ GeV}$  down to  $\sqrt{s_{NN}} = 3 \text{ GeV}$ . In this energy range, the interactions in the collision change from being dominated by hadronic degrees of freedom to a state in which quarks and gluons are the dominant degrees of freedom. STAR has been designed as a collider experiment. To access the lower energies of the BES-II program with the high energy RHIC accelerator, STAR is operated as a fixed target (FXT) experiment. This operation mode requires an upgrade to extend its acceptance into the FXT forward region.

eTOF is a collaboration project between CBM and STAR. 108 multi-gap resistive plate chamber (MRPC) prototypes for CBMs time of flight system (CBM-TOF) have are installed in the forward region of STAR to provide the necessary particle identification capabilities for the FXT operation. For CBM-TOF, this is the largest system test for its MRPC prototypes and their free-streaming data acquisition system.

This thesis documents the learnings gained over the course of the eTOF project. A calibration scheme for eTOF data has been developed and the performance of the MRPC prototypes after calibration has been quantified. This thesis also serves as a documentation of the software developed for eTOF and the peculiarities in

eTOF's data which have to be taken into account in further analysis. Finally, the value of eTOF data for the physics analysis of BES-II data is demonstrated.

**Chapter 2** will introduce the relevant concepts of physics and provide the grander context for the research in this work.

**Chapter 3** will introduce the two heavy ion experiments connected to this work - CBM and STAR - as well as the STAR BES-II program.

**Chapter 4** will provide a more in-depth introduction to the eTOF project, its MRPC detectors and its hardware.

**Chapter 5** describes the software chain of eTOF and the data calibration algorithms which were developed over the course of this work. This chapter is also meant as a software documentation reference for future works on eTOF data.

**Chapter 6** documents the different datasets taken with eTOF during BES-II and conditions of the system during the corresponding run periods. It also contains an analysis of the hardware issues with the read-out chain which were observed during these run periods.

**Chapter 7** shows a systematic analysis of eTOF's detector performance. The main performance metrics are the efficiency and time resolution of the detectors. A study of the MRPC dark rate during BES-II operations is also shown to provide insight into MRPC aging.

**Chapter 8** then takes a look at particle identification and the reconstruction of short-lived particles with eTOF and demonstrates the advantages eTOF provides for BES-II physics analysis.

Finally, **Chapter 9** summarizes the learnings from this work, both from the perspective of CBM and its TOF system tests and for STAR and the BES-II data analysis.

## 1.1 Acknowledgements

The eTOF project depends on the work of many people. Their contributions shall be acknowledged here:

Prof. Norbert Herrmann, Dr. Ingo Deppner and Dr. Geary Eppley for the initial design of eTOF, its installation and runtime operation.

Prof. Yi Wang, Dr. Pengfei Lyu and Dr. Qiunan Zhang for the development and test of the Tsinghua type MRPC prototypes.

Prof. Yongjie Sun for the development and test of the USTC-type MRPC prototypes.

Dr. Dongdong Hu and Dennis Sauter for the assembly of the eTOF modules.

Jochen Frühauf for the design and installation of eTOF's clocking and read-out scheme.

Dr. Wengxiong Zhou for the development of the eTOF gDBP firmware.

Dr. Pierre-Alain Loizeau for the development of the software interface between the eTOF detector and STAR DAQ.

Dr. Gene van Buren and Dr. Daniel Brandenburg for their help to integrate eTOF software into the STARROOT framework.

Florian Seck and Yannik Söhnngen for their contributions to the eTOF data reconstruction software.

Without their efforts, this work would not have been possible.

## 1.2 Own Contributions

The authors own contributions to the eTOF program are as following:

**The development of eTOF data reconstruction software.** The author is the main developer of the classes StEtofCalibMaker, StEtofHitMaker and StEtofCalibMaker and added to the development of StEtofDigiMaker and StEtofMatchMaker<sup>1</sup>. The reconstruction chain is described in Chapter 5.3.

**The development of the eTOF calibration scheme in STAR.** The author adapted the MRPC calibration algorithms from previous cosmic tests<sup>2</sup> to the STAR environment and implemented the calibration procedure in the STAR software framework. The calibration procedure is described in Chapter 5.4.

**The first-pass calibration eTOF BES-II data.** The author created a first-pass calibration for eTOF's 2019 AuAu collider run, the 2020 AuAu fixed target and collider runs and 2021 collider runs (see Chapter 6.1)<sup>3</sup>. The analyses presented in this thesis are based on those calibrations unless explicitly mentioned otherwise.

**The investigation of pre-amplifier damage events.** The author lead the investigation of the 2020 pre-amplifier damage events on the data side<sup>4</sup>. The results of this investigation are shown in Chapter 6.3.

**The investigation of TDC instabilities.** An analysis of the systematics of TDC outages in eTOF is shown in Chapter 6.4.1. A strategy to mitigate the impact of those outages is shown in Chapter 7.2.

**The characterization of MRPC prototypes with respect to signal behavior and long-term stability.** Chapter 7.1 shows an analysis of the 108 eTOF MRPC prototypes with respect to their signal uniformity, their signal reflection behavior<sup>5</sup> and their dark rate.

**The analysis and monitoring of eTOF's detector performance with respect to time resolution and efficiency.** This includes regular calibration and analysis of fast offline data during BES-II to monitor the stability of eTOF's detector performance as well as the systematic evaluation presented in Chapter 7.3 and 7.2.

**Demonstration of the Usage of eTOF data in physics analysis and their value to STAR's physics capabilities.** The author implemented the usage of eTOF

---

<sup>1</sup>Main developer of both: F. Seck

<sup>2</sup>Initial development by N. Herrmann

<sup>3</sup>Further calibration refinements, especially with respect to run-by-run offsets are done by Y. Söhnngen

<sup>4</sup>An investigation on the hardware side has been done by I. Deppner and J. Frühauf.

<sup>5</sup>Signal reflection have been analyzed together with Y. Söhnngen

data into the KFParticle analysis framework. Chapter 8 demonstrates the physics improvements provided by eTOF on the example of  $\Lambda^0$ -baryon and  $\Phi$ -meson reconstruction and quantifies eTOF's PID performance.

Furthermore, the author served as software coordinator and representative in the QA team for eTOF in 2021 and early 2022.

## 2 Physics Context

The ultimate goal of the project presented in this thesis is to understand how matter behaves at the highest densities humanity can achieve with current technologies. In nature, matter of a similar density can only be found within the intense gravitational field of a neutron star. Under such conditions, atoms cease to exist. The de-localized electron shells, which primarily determine their physical properties, are compressed into the nuclear core. Similar conditions in lab can only be achieved by colliding heavy ions at relativistic velocities in particle accelerators. This nuclear matter exists at the distant frontier of two fields of physics. On the one hand, the relevant degrees of freedom are sub-atomic particles which are described by quantum fields in the standard model of particle physics. On the other hand, the sheer amount of involved particles requires many-body approaches from statistical physics. The following sections introduce the relevant concepts from both fields of physics.

### 2.1 Phases of Matter

Matter around us exists in different phases, depending on its pressure and temperature. As a starting point for this topic serves the example of one of the most common substances around us: water. At atmospheric pressure, water is a solid (ice) up to a temperature of  $0^{\circ}\text{C}$ . It then melts into the life-sustaining liquid we have at room temperature. When further heated to  $100^{\circ}\text{C}$ , it vaporizes.

Those three phases distinguish themselves by the degrees of freedom and forces which govern their behavior:

Lattice excitations in crystalline ice, long-range van-der-waals forces in water and short-range collision interactions in water vapor. The state of a thermodynamic system within a given phase is described by an equation of state which

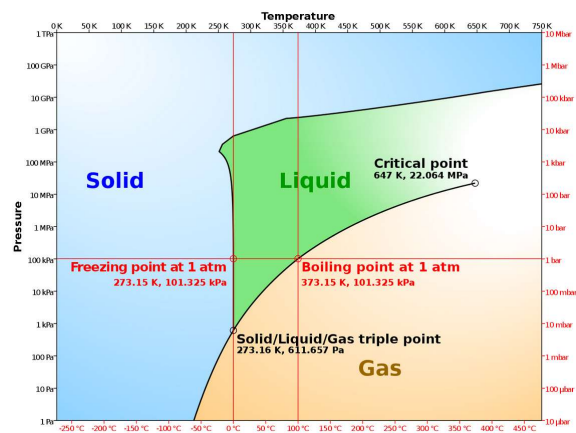


**Figure 2.1:** Example of a phase diagram of water. Solid lines show first-order phase transitions. Source: [1]

links the state variables, temperature, pressure and volume, together.

If one looks at the changes in a system not only as a function of temperature, but also of pressure (or, equivalently density), one can now draw a two-dimensional phase diagram like the one shown in Figure 2.1.

When changing from one phase into another, the system undergoes a phase transition. Phase transitions are mathematically characterized by an unsteadiness in one or more state variables or their derivatives. One distinguishes between two types of phase transitions. In first-order phase transitions, state variables become directly unsteady and latent heat is released or absorbed. In second-order phase transitions only a derivative of a state variable becomes unsteady. In this case, the transition occurs as a smooth cross-over between the phases and no latent heat is present. In water, a first-order phase transition occurs between liquid water and vapor at low temperatures. Liquid water has a significantly smaller volume at the phase boundary than vapor. As the temperature of the system increases, this volume difference becomes smaller. At temperatures above  $647\text{ K}$ , this difference vanishes and the phases become indistinguishable. The point at which this change occurs, is a phase transition of second order, a so-called a critical point. Close to the critical point, small localized density fluctuations can cause the transition of small bubbles of the system from one phase into the other. The size of these bubbles increases as correlation length in the system diverges in the vicinity of the critical point. In water (and other liquids), this leads to the phenomenon of critical opalescence: When the correlation length in the system reaches the wavelength of visible light, the liquid becomes opaque. Once the critical point is passed, the system clears up again.

One can also understand phase transitions in terms of the breaking down of symmetries, which a system exhibits. The breaking of such symmetry is linked through the Goldstone-theorem [2] to the emergence of the new degrees of freedom which govern the physics in the new phase of matter. Ice obeys a discrete translational symmetry along its crystalline lattice. This symmetry is no longer present in liquid water. Water waves can be interpreted as quasi-particles that now describe motion in liquid water systems.

Chapter 2.3 will expand on these concepts and translate them to the physics of nuclear matter.

## **2.2 Quantum Chromodynamics and the Standard Model of Particle Physics**

The interactions of fundamental particles are described by the standard model of particle physics [3]. The standard model is formulated as a set of perturbative quantum field theories. It consists of six quarks (called up, down, charm, strange, top, bottom) and six leptons (the electron, muon and tau-lepton and their corresponding neutrinos) as well as the respective anti-particles. There are three



fundamental forces included in the standard model: The electromagnetic force, the weak force and the strong force. The fourth known fundamental force, gravity, is not included in the standard model. Particles interact with each other through the exchange of gauge bosons: The photon for the electromagnetic force, the charged W-bosons and the neutral Z-boson for weak force and the eight gluons for the strong force. Additionally there is the Higgs boson, which couples to all the other elementary particles and is responsible for their rest mass. An overview of all these particles is shown in Figure 2.2.

The electric charge, net-lepton number and net-quark numbers ( $N_{particles} - N_{antiparticles}$ ) are among the conserved quantities in the standard model. Since only net-particle number is conserved, the generation of additional particle-antiparticle pairs from the vacuum or any of the interaction bosons is possible. The part that is most important to this work is quantum chromodynamics (QCD), the theory of strong interaction. In QCD, quarks (and their anti-particles) carry one of three possible conserved color charges (or anti-color charges respectively) which couple to eight interaction bosons, the gluons. Gluons themselves, also carry color charges and

can thus change the quark color charge during the interaction. Another feature of QCD is the so-called "running of the coupling". The QCD coupling exhibits a strong dependence on the transferred momentum  $Q$  in the interaction. At  $Q \approx M_Z = 91.2 \text{ GeV}/c^2$ , the strong coupling  $\alpha_s$  is approximately 0.12 and thus well in the perturbative regime [5]. However, at lower transfer energies (or conversely larger length scales), the coupling rises and increases beyond the perturbative regime around  $\Lambda_{QCD} \approx 340 \text{ MeV}$  [6]<sup>1</sup>. In the non-perturbative regime of QCD, only numerical methods based on a discrete spacetime (lattice-QCD) can be used to calculate QCD processes from first principles. A consequence of this running coupling is that, at close distances, quarks are quasi-free, while at larger distances,

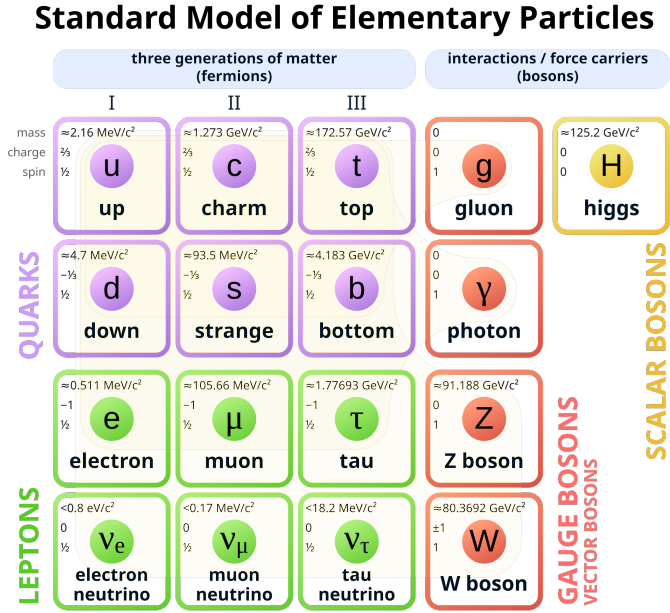


**Figure 2.2:** The elementary particles in the standard model of particle physics [4].

<sup>1</sup>The precise value of  $\Lambda_{QCD}$  depends on the parametrization of the  $\beta(a_s)$ -function and the choice of the renormalization scheme. The given value is calculated in the modified minimal subtraction scheme ( $\overline{MS}$ ), assuming three active quark flavors.

they are confined in a potential  $V(q\bar{q}) \propto r$ . Therefore, at a certain distance, it is energetically favorable to generate a quark-anti-quark pair and form color-neutral bound states (hadrons) then keeping quarks separated. This is why we can not observe free quarks in nature. There are two main types of color-neutral quark bound states: Baryons and Mesons. Baryons are made up of three quarks, one with each color. Mesons consist of a quark and an anti-quark with opposite colors. The most relevant hadrons for this thesis are the states made up of the lightest three quarks (up (u), down (d) and the slightly heavier strange (s) quark): The lightest mesons, pions (combinations of up and down quarks) and kaons (containing a strange quark) and the lightest baryons, protons (uud) and neutrons (udd). These particles are sufficiently long-lived to be detected directly in particle detectors. Additionally, also the lightest strange baryon, the  $\Lambda$ , and the  $\phi$  meson (ss) will be reconstructed from their decay products.

In the limit of massless quarks, QCD is invariant under separate unitary transformations for quarks of left-handed and right-handed chirality. The chiral components of the quark doublet are defined by applying the projection operator to the quark doublet:

$$Q_L = \left(\frac{1 - \gamma^5}{2}\right) \begin{pmatrix} u \\ d \end{pmatrix}, \quad Q_R = \left(\frac{1 + \gamma^5}{2}\right) \begin{pmatrix} u \\ d \end{pmatrix} \quad (2.1)$$

The unitary chiral transformation is written as:

$$Q_L \rightarrow U_L Q_L, \quad Q_R \rightarrow U_R Q_R \quad (2.2)$$

This (approximate) chiral symmetry is spontaneously broken in the ground state by the interaction of quarks with the non-zero vacuum quark condensate. The light mesons can be interpreted as the Nambu-Goldstone bosons of this broken symmetry, which explains why their masses are significantly higher than the pure quark masses, but small compared to the baryonic scales. At low energies, QCD interactions can be described using the new degrees of freedom from this broken symmetry in meson-exchange models.

At typical distances inside a nucleus, the interactions between the quarks inside manifest as a short-range force between the hadrons known as the residual strong force. For the most stable baryons around us, the neutrons and protons, this force is attractive and holds the nuclei together in the matter around us.

## 2.3 Physics at Highest Baryon Densities

We can now attempt to describe phases of nuclear matter. Inside a nucleus at ground state, nuclear matter has long been described by the liquid drop model [7] held together by the residual strong force. At higher temperatures, hadrons are no longer bound together inside this drop resulting in a free gas of hadrons. As thermal collision energies approach  $\Lambda_{QCD}$  a transition to a phase with quasi-free

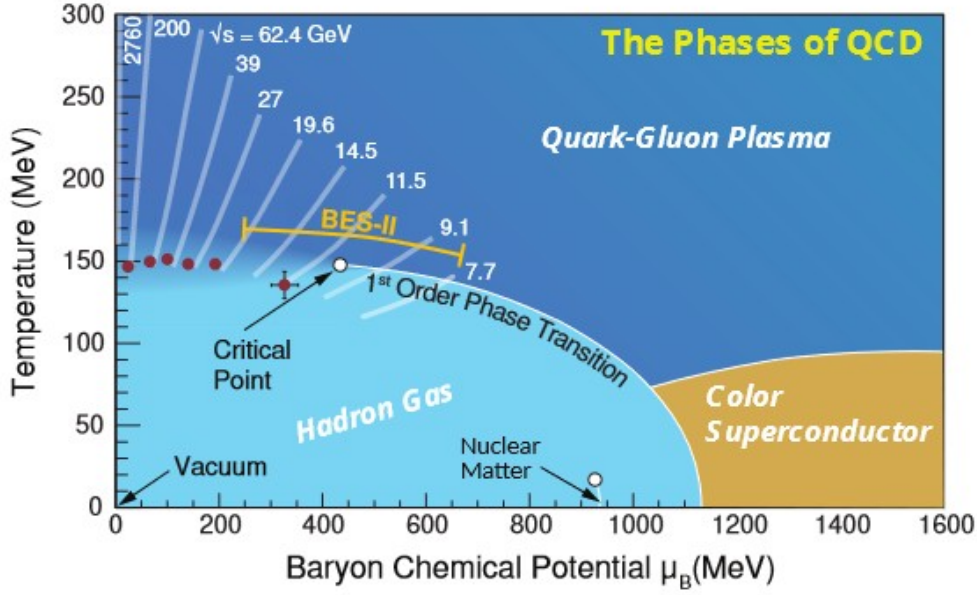


**Figure 2.3:** A sketch of the phase diagram of baryonic matter as function of temperature  $T$  and baryon-chemical potential  $\mu_B$ . White lines indicate the system evolution in heavy ion collisions at different energies during the STAR Beam Energy Scan I and LHC. Red dots indicate measure chemical freeze-out points. Indicated phase transitions and position of the critical point are schematic only. Source: [10]

quark interactions is expected: the quark-gluon plasma (QGP). The existence of such a phase was observed by the experiments at CERN[8] and RHIC[9] in the early 2000s. However, the precise structure of a phase diagram for these phases is still largely unknown. An example of a schematic phase diagram is shown in Figure 2.3.

This phase diagram is usually formulated as a function of temperature and baryon-chemical potential, the amount of energy needed to add one baryon to the system. This representation accounts for the differences between pure baryon pressure and mixed pressure from baryons and anti-baryons. At low baryon-chemical potential i.e. low net-baryon densities, lattice QCD predicts a smooth cross-over between hadron gas and QGP [11]. This prediction is consistent with observations at RHIC and LHC [12]. The transition temperature is approximately  $155 \text{ MeV}$  according to recent measurements [13]. At low temperatures, and densities close to the matter density in nuclei, the phase transition from nuclear liquid to hadron gas occurs. This transition also vanishes at lower baryon-chemical potential. At medium temperature and chemical potential, numerical lattice QCD calculations do not converge sufficiently fast due to the fermionic sign problem [14]. Calculations within this regime are done in the framework of low-energy effective field theories (LEFTs). LEFTs typically involve a reformulation of QCD interactions as four-quark interactions mediated by mesonic propagators. Recent calculations

suggest the existence of a critical end-point to the cross-over region at a temperature of  $T \approx 105 \text{ MeV}$  and a baryon-chemical potential of  $\mu_B \approx 635 \text{ MeV}$  [15]. Consequentially, a first-order phase transition at even higher chemical potential is expected. The experimental confirmation of this and similar predictions is one of the main goals of ongoing research in this field. Observables that indicate the position of the critical point or a first-order phase transition are given in Chapter 2.5.

At very high baryon densities, similar calculations indicate the existence of another new phase called color superconductivity. This regime is not experimentally accessible with existing technologies.

Further input to this phase diagram with new measurements and new questions is provided by astronomical observations [16]. In the interior of neutron stars, net-baryon densities up to 5 times nuclear matter density are expected at very low temperatures. Neutron stars are stabilized by the balance between their own gravitation and the pressure from the compressed nuclei inside. For a given density, this pressure depends on the equation of state of the QCD-matter inside. However, at a certain mass, the pressure is not able to stabilize neutron star anymore and it collapses into a black hole. The recent observation of neutron stars with masses close to two solar masses[17] poses a new puzzle: to stabilize such a massive neutron star, the equation of state has to be "hard". A major contribution to the incompressibility of the EoS is the Pauli pressure of the fermionic quarks. However, the presence of strange quarks in this matter, as suggested by heavy ion collision experiments, lowers the Pauli pressure as more possible quantum states are available. One possible solution to this puzzle would be a repulsive potential between strange baryons and the surrounding nuclear matter [18]. This motivates further studies of in-medium effects especially on the  $\Lambda$  baryon, as the lightest strange baryon.

## 2.4 Probing Compressed Baryonic Matter in Heavy Ion Collisions

Matter cannot be compressed to densities close to or above nuclear matter with current technologies over longer times. Temporarily, high baryon densities can be achieved during particle collisions. For the study of bulk properties of dense baryonic matter, heavy ion collisions are the best available tool due to the larger system size.

Figure 2.4 shows schematically the time evolution of a relativistic heavy ion collision of two Lorentz-contracted heavy ions. Heavy particles are generated in initial hard scattering. Later, soft multiple scattering creates large amounts of quarks and gluons in thermal equilibrium, forming an expanding fireball. The initially very hot and dense quark-gluon plasma cools down as it expands until the phase transition towards a hadron gas occurs. Quarks recombine into various

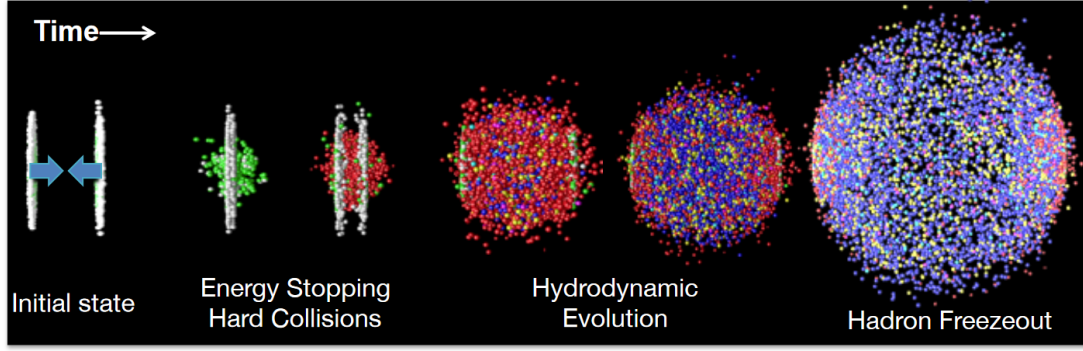


**Figure 2.4:** Schematic evolution of a relativistic heavy ion collision [19].

mesons and baryons which scatter according to the declining temperature. Soon after the phase transition, the chemical freeze-out occurs after which no new particles are created from scattering. The collision ends with the kinetic freeze-out when scattering stops and particles propagate largely undisturbed until they reach particle detectors where they are observed.

The most common ions for heavy ion studies are gold and lead due to their relatively high mass and easy handling compared to heavier radioactive ions. Uranium can also be used to study the heaviest systems. The dependence of the maximum reachable baryon density on the collision energy is non-trivial. The lower the collision energy, the less of this kinetic energy can be put into the compression of the medium during the collision. On the other hand, at high energies, the medium is dominated by newly produced quark-antiquark pairs, with a net-baryon density of zero. Figure 2.5 shows an estimate of the net-baryon densities at the freeze-out for various collision energies at the Relativistic Heavy Ion Collider (RHIC) in Brookhaven, USA and the Facility for Anti-Proton and Heavy Ion Re-

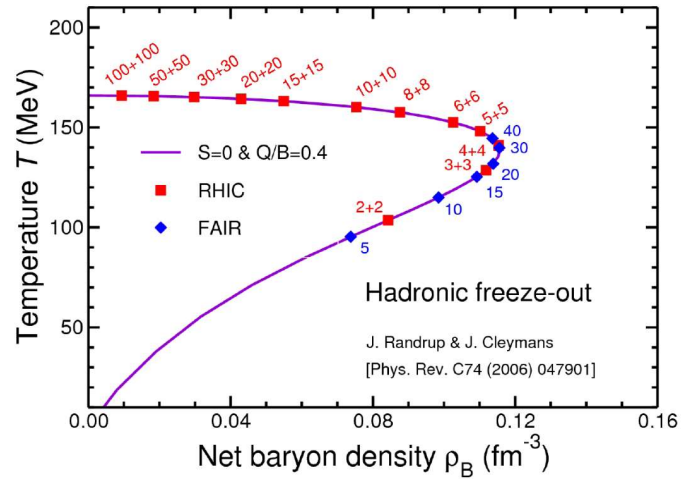


**Figure 2.5:** Temperature and net-baryon density at the hadronic freeze-out for various collision energies (in GeV) at the RHIC (collider) and FAIR (fixed target) facilities calculated based on statistical models[20].

search (FAIR) in Darmstadt, Germany. These estimates for the density at freeze-out are based on statistical models of the collisions. The maximally achieved densities during the evolution of the collisions are not directly measurable in the experiment. The maximum density is reached in collision at center of mass energies  $\sqrt{s} \approx 8 \text{ GeV}$  and is easily reached by modern accelerator facilities. Since reaching high energies is not a concern, experiments researching high baryon density matter are often build as fixed target (FXT) experiments. Here, only a one accelerated projectile beam is shot at a thin target foil. The rate of interactions can be calculated as

$$N_{interaction} = N_{projectiles} \cdot \sigma_{NN} \cdot d_{column,target} \quad (2.3)$$

where  $N_{projectiles}$  is the rate of projectile ions from the accelerator,  $\sigma_{NN}$  the nucleon-nucleon interaction cross-section and  $d_{column,target}$  is the column density of target atoms. Thus, high interaction rates are reached in FXT experiments by simply increasing the target thickness. This makes FXT experiments primed to study rare probes or measure precise shapes of distributions for specific observables.

## 2.5 Observables of Hadronic Phases

The exploration of the QCD phase diagram is a multi-messenger science. Signals sensitive to the vicinity of a critical point or a phase transition are smeared out since the final state carries the complete convoluted thermodynamical history of the collision. Thus, a combination of many different observables is required before final conclusions about landmarks in the QCD landscape can be made. This section does not aim to give a complete overview over all the measurements of current interest in this field, but to motivate the physics requirements and preliminary analysis presented in Chapter 8.

The most recent extensive dataset to map out the QCD phase diagram with heavy ion collisions has been the Beam Energy Scan (BES) of the STAR (see Chapter 3.4) collaboration at RHIC. In the years 2010 and 2011 data at nine different center of mass energies,  $\sqrt{s_{NN}} = 200, 62.4, 54, 39, 27, 19.6, 14.5, 11.5$  and  $7.7 \text{ GeV}$  have been taken. One general result was that the phase transition likely happens in the energy range of  $\sqrt{s_{NN}} < 20 \text{ GeV}$ .

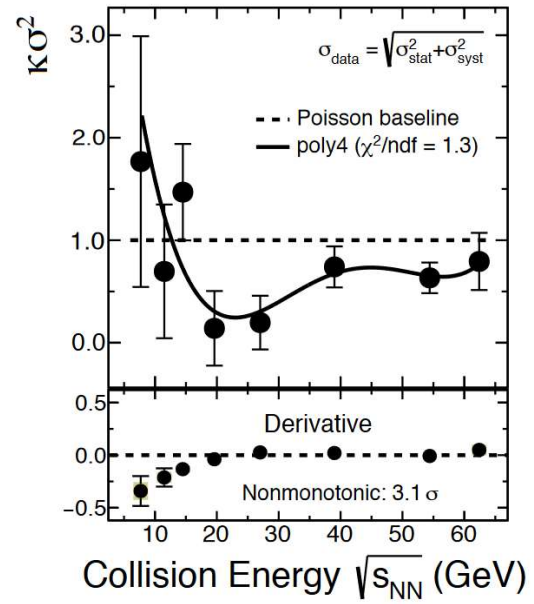
In this region, BES-I did not provide sufficient statistics as the collider geometry of STAR does not allow for high event rates. This triggered the development of the Beam Energy Scan phase II (BES-II, more in Chapter 3.4.2) for which the work presented in this thesis was performed. A comprehensive overview of the measurements in the BES I can be found in reference [21].



### 2.5.1 Proton Kurtosis

Baryon number, strangeness and electric charge are globally conserved quantities in a QCD system. Subsets of these quantities, like the net-proton number for the baryon number, can thus fluctuate by exchange with other subsets of the same conserved quantity. The fluctuations are then limited by the correlation length in the system, which diverges in the vicinity of a critical point. Event-by-event fluctuations of particle yields in heavy ion collisions can thus be used as a probe for the QCD critical point. Higher order moments of event-by-event multiplicity distributions are more sensitive observables to such fluctuations, but are also increasingly sensitive to systematic errors.

The kurtosis of net-proton multiplicities is a commonly used observable for such a measurement as protons are the cleanest identifiable particle. As one lowers the beam energy over the region of the critical point, one expects to observe a minimum in the kurtosis, followed by a change of sign relative to the Poissonian default and then a maximum [23]. Indeed, the STAR BES has observed hints of such a structure [22], which can be seen in Figure 2.6. A non-monotonic behavior was observed with a significance of  $\approx 3.1 \sigma$ . However, this measurement is still hindered by large statistical uncertainties, which should be improved with BES-II data.



### 2.5.2 Hadronic NCQ-Scaling of the Elliptical Flow

The motion of particles in an expanding hydrodynamic system can be separated into (random) thermal motion and collective motion, the so-called flow. The azimuthal distribution of particles from a collision can be described by a Fourier-expansion into flow harmonics. The  $n$ -th flow coefficient is defined as  $v_n = \langle \cos(n(\phi_i - \Psi)) \rangle$ , where  $\phi_i$  is the polar angle of the  $i$ -th particle in a sample (for example, one specific particle species at a given interval in

**Figure 2.6:** Proton kurtosis results from the STAR Beam Energy Scan phase I. Top panel shows the measurements compared with the Poissonian default. Data points are fitted with a forth order polynomial. Bottom panel shows the derivative of the fit function at the data points. A hint of non-monotonic behavior is observed with a significance of  $3.1 \sigma$ . Source: [22]

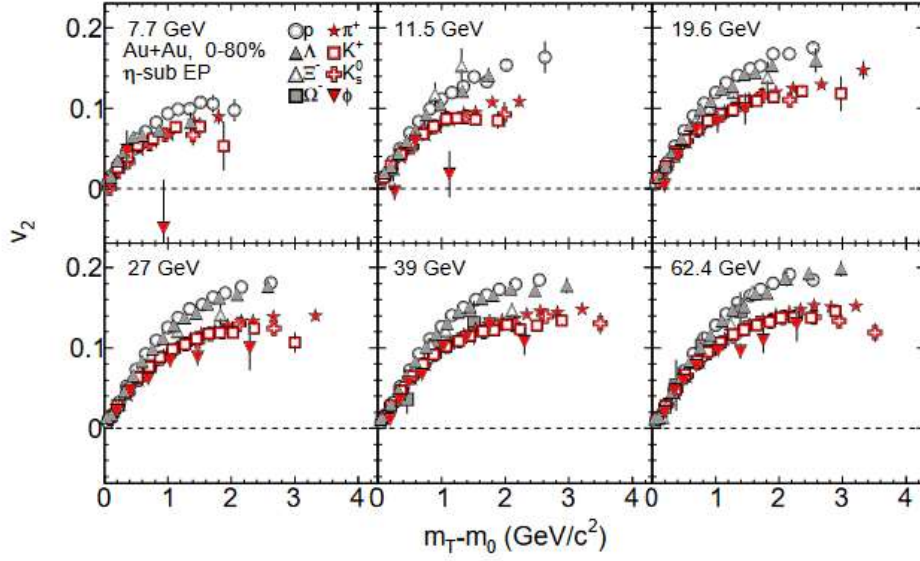


**Figure 2.7:** BES-I results for the elliptic flow of identified hadrons as function of reduced transverse mass in 0 – 80% most central AuAu-collisions at various beam energies. Baryons are shown as gray symbols, mesons in red. Error bars denote combined statistical and systematical errors. At higher energies, clear baryon-meson splitting is observed. At 11.5 GeV and below, the  $\phi$  meson shows a strong deviation from the general meson behavior, albeit with large errors. Source: [25]

transverse momentum in a dataset) and  $\Psi_i$  is the polar angle of the symmetry plane of the reaction, the so-called event plane. The average is taken over all particles and all events in a given sample. For hadrons forming by quark recombination out of a quark-gluon plasma fireball, one expects an almost universal behavior when comparing particle species as quarks and gluons inside the plasma are thermally equilibrated and strongly coupled. More than that, one expects the flow of quarks to add up during hadronization and thus, the elliptic flow  $v_2$  of hadrons to scale with the number of constituent quarks (NCQ) [24].

At higher energies, this so-called NCQ-scaling behavior is indeed observed and interpreted as a strong signature of quarks and gluons as the dominant degrees of freedom during collisions. In the BES-I, a clear splitting between baryons and mesons was observed for energies of 19.6 GeV and above. At 11.5 GeV, the  $\phi$  meson starts to show large deviations from the mesonic band. This could be interpreted as a hint that the quark-dominated regime is coming to an end around these energies, but the statistical and systematic uncertainties still prevent a definitive answer. Studies with more statistics and at more energies from the BES-II should help to



answer this question.

### 2.5.3 $\Lambda$ -Baryon Measurements

As the lightest baryon containing strangeness, the  $\Lambda$ -baryon has multiple points of interest. Strangeness enhancement has long been seen as a major indicator of a quark-dominated regime. In a hot and dense quark-gluon plasma,  $s\bar{s}$  pairs created from the vacuum can recombine with other quarks from the medium into strange hadrons instead of annihilating. This effect leads to an enhancement of strangeness production in large collision systems (with consequentially an extended quark-gluon plasma medium) compared to the scaled expectation from small systems (pp collisions or peripheral AA collisions). The BES-I has found a significant enhancement in the  $\Lambda/\pi$  ratio at the lowest measured energies, consistent with previous measurements by the NA49 collaboration [26], but the expected peak this distribution is below the energy range of BES-I. Since the  $\Lambda$  is the lightest baryon not present in the initial colliding nuclei, it is also an important probe to test the baryon production in a collision. The ratio of baryons to mesons as function of  $p_t$  in different centrality intervals is sensitive to the collision dynamics. The BES-I found a change in the qualitative behavior of the  $\bar{\Lambda}/k_s^0$  between 19.6 GeV and 11.5 GeV. At low energies, this ratio is monotonically rising with  $p_t$ , while at higher energies, the ratio begins to drop after a peak around  $p_t = 2 \text{ GeV}/c$  [26]. However, the statistics at 11.5 GeV are still too limited for a final conclusion.

Semi-peripheral heavy ion collisions introduce very large total angular momenta into the fireball. This vorticity of a medium with non-zero charge induces a strong magnetic field which in turn can lead to a spin polarization of the produced particles.  $\Lambda$ -baryons provide a good probe to measure this polarization as in the decay to  $p-\pi$ , the proton is preferentially emitted into the direction of the  $\Lambda$ -spin.

In BES-I a non-zero global polarization of  $\Lambda$  and  $\bar{\Lambda}$  was observed, which rises with lower beam energies [27]. Again, so far, the errors are quite significant, but more systematic measurements with improved statistics would provide insights into the collision dynamics, inner structure and hydrodynamical properties of the QGP.

Additionally, the  $\Lambda$ -baryon is an intermediate state in the decay of multi-strange baryons ( $\Omega$  and  $\Xi$ ). The formation of these rare probes contains rich information about the strangeness interactions in the fireball phase. Their reconstruction via  $\Lambda$  reconstructions thus plays an important role in understanding this not directly observable phase.

Combined with the astrophysical question about the in-medium potential (see 2.3), these observations make a good case for further  $\Lambda$  studies in the BES-II.

## 3 Experiments

This chapter aims to introduce the two experiments for which this work was performed: "Compressed Baryonic Matter" (CBM) at the "Facility for Antiproton and Ion Research" (FAIR) in Darmstadt, Germany and the "Solenoid Tracker At RHIC" (STAR) at the "Relativistic Heavy Ion Collider" (RHIC) in Brookhaven, USA.

### 3.1 FAIR

The "Facility for Antiproton and Ion Research" (FAIR) is a new high luminosity accelerator facility. It was designed as an upgrade of the existing "Gesellschaft für Schwerionenforschung" (GSI) facility in Darmstadt, Germany. The heart of the new complex is the future "Schwerionen-Synchrotron-100" (SIS-100) accelerator. Using the existing SIS-18 accelerator installation as a pre-accelerator, SIS-100 is planned to deliver high quality beams of ions from protons up to the size of uranium. The ions will be accelerated to maximal kinetic energies ranging from  $29\text{ GeV}$  (protons) to  $10.7\text{ GeV}$  (uranium) [20]. The Main feature of  $1100\text{ m}$  long accelerator ring, however, is the highest currently planned luminosity in this energy range of up to  $10^{12}$  ions per second.

The FAIR project was started in 2007 as a multinational project with Germany, France, Poland, Finland, India, Slovenia, Sweden, the United Kingdom and Russia as shareholders. The most recent date of completion for the FAIR complex was 2025, but recent political events have led to an ongoing re-evaluation of this goal.

Scientifically, research at FAIR is divided into the four main pillars:

- Atomic, Plasma Physics and Applications (APPA [29]) is an umbrella for the four different collaborations BIOMAT, FLAIR, HED and SPARC. Making use of the extended particle storage capacities in FAIR, it focuses on low energy research in diverse fields of physics.
- PANDA (antiProton ANihilation at DArmstadt [30]) focuses on antiproton annihilation physics, seeking to answer questions about the generation of hadronic mass, nucleon structure and exotic particles.
- NuStar (Nuclear Structure, Astrophysics and Reactions [31]) focuses on the structure of heavy nuclei, their stability and generation in the universe. It consists of multiple separate experiments all making use of radioactive beams and the Super-FRS (Superconducting Fragment-Separator).
- and finally CBM.

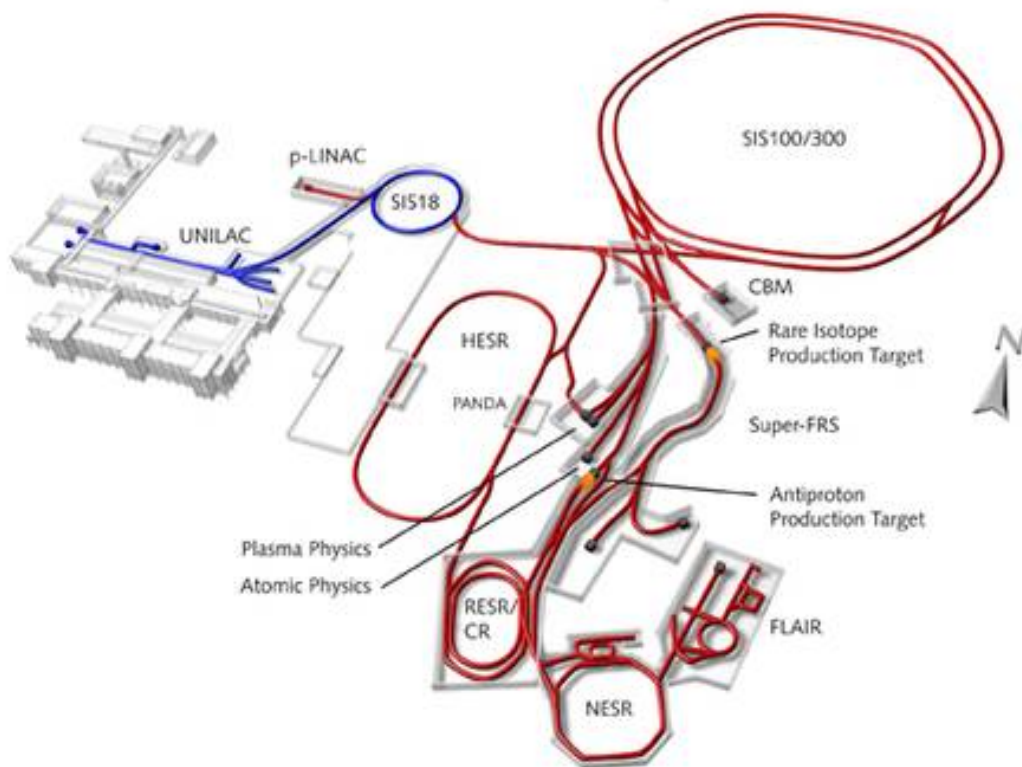


*Figure 3.1: The FAIR accelerator complex. Source: [28]*

## 3.2 CBM

Compressed Baryonic Matter (CBM) is one of the four pillars of FAIR. As one of the two experiments to which this thesis is connected, it warrants a more elaborate description.

CBM's focus is the exploration of the phase diagram of dense baryonic matter through heavy ion collisions at intermediate energies (up to 12 AGeV kinetic energy). This energy range is exactly the energy range in which the highest baryon densities are expected and where theoretical calculations allow for the existence of the QCD critical point (see Chapter 2.3 and Figure 2.5). This energy region has been previously explored at various experiments at the Alternating Gradient Synchrotron and the RHIC in Brookhaven, USA, but so far, statistical limitations have prevented conclusive answers about the existence of the QCD critical point or a first-order phase transition. Using the high luminosity of SIS-100, a continuous, de-bunched extraction scheme and the advantages of the fixed target configuration, CBM aims at an interaction rate of up to 10 MHz to quickly produce to date statistically unrivaled datasets (see Figure 3.2 for a comparison of previous and planned experiments in this energy range). With an interaction rate four orders of magnitude higher than during the Beam Energy Scan II at STAR, CBM aims to answer the open questions that are left in this field after the Beam Energy Scan. Namely those are likely to be: the nature of the QCD phase transition at high baryon densities, existence and position of the critical point and the shape of the QCD equation of state. The large available statistics allow to utilize rare probes like multi-strange hadrons and hadrons below their production threshold, or measurements which are very susceptible to statistical errors like higher moment particle multiplicity distribution measurements. A comprehensive overview of the physics of CBM can be found in the CBM physics book [33].

The high interaction rate at CBM forces another peculiarity in the experimental design. The data rate produced from all events is too large for complete archiving. Thus a significant reduction in data volume is needed beforehand. However, to select rare "interesting" events among all taken data is a task too complex to be implemented in conventional hardware triggers. CBM's solution is the so-called first level event selector (FLES [34]). The data acquisition systems of all CBM

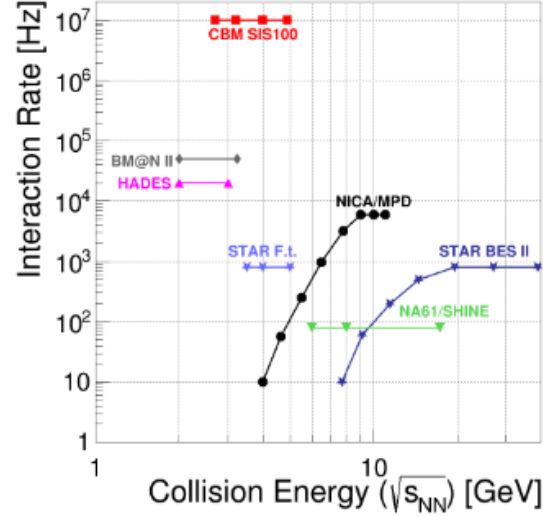


*Figure 3.2: Comparison of achievable interaction rates in current and planned heavy ion experiment. Source: [32]*

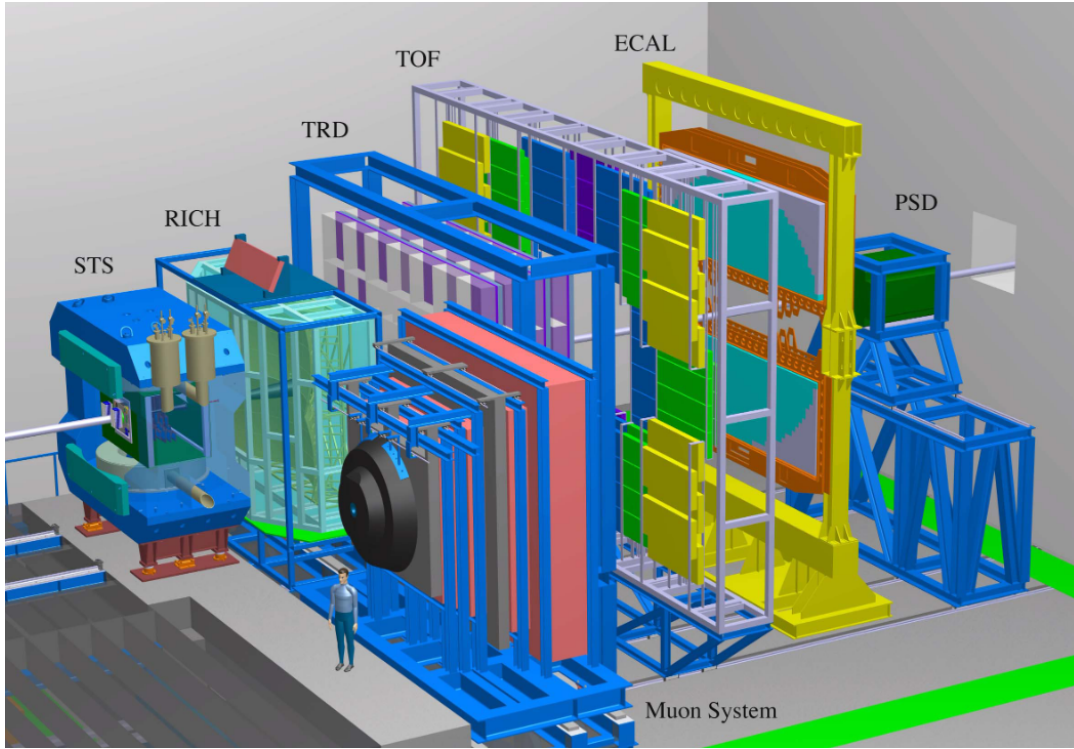


**Figure 3.3:** Planned lay-out of the CBM detector and its subsystems. Along the beam-line, those are: The silicon tracking system, exchangeable ring-imaging Cerenkov detector and muon systems, the transition radiation detector, the time of flight wall, an electromagnetic calorimeter and finally, the projectile-spectator detector. Source: [32]

subsystems will be free-streaming, resulting in approximately a  $10\text{ Tb/s}$  continuous data stream at the highest interaction rate. This data will be analyzed online in the FLES computing cluster to reconstruct tracks, form events, apply calibrations, and look for interesting low level physics observables (like the presence of specific particles or high track multiplicities). Based on this analysis, events will be selected to be written to disk.

### 3.2.1 The CBM Detector

The planned lay-out of the detector can be seen in Figure 3.3. It consists (ordered in the direction of the beam) of a beam monitor and start time detector, an exchangeable target box with a micro-vertex detector (MVD) and afterwards, a high precision silicon tracking system (STS) inside a dipole magnet. The STS is CBMs main tracking and momentum measurement detector. Outside the magnetic field follows then an exchangeable system of either a ring-imaging Cerenkov detector for electron identification or a muon identification system based on gas-electron multiplier chambers (GEMs) and iron absorbers. The exchange between those two systems will be based on the physics goals of a given run as the high material

budget of the muon setup disturbs the identification of other particles. Behind those two systems, a transition radiation detector is placed for further electron discrimination and as an intermediate tracking point between STS and the time of flight system (TOF) behind it. The CBM-TOF system is planned as a  $120\text{ m}^2$  wall of multi-gap resistive plate chambers and will act as CBM's main particle identification detector and will be described in more detail in the next section. Furthest away from the target, two calorimeters were initially planned: An electromagnetic calorimeter (ECAL) for electron and photon measurements and the projectile spectator detector (PSD), a hadronic calorimeter in the far forward region to determine centrality and event plane from spectator particles. In recent plans, the PSD has been replaced by a forward wall based on plastic scintillators fulfilling similar functions. The ECAL has been removed.

### 3.2.2 CBM-TOF

The CBM time of flight wall (for more details, see the technical design report: [35]) is planned to cover an area of  $12 \times 9\text{ m}$  at a variable distance to the target from  $6\text{ m}$  to  $12\text{ m}$ . The physics program of CBM sets harsh demands on its time of flight system:

- To identify particles correctly, or more specifically, provide a sufficient  $K/\pi$  separation of at least 3 standard deviations even at the minimal distance of  $6\text{ m}$ , a system time resolution of better than  $80\text{ ps}$  is required. With an assumed start time resolution of  $\leq 50\text{ ps}$ , the intrinsic detector resolution of the TOF detectors has to be better than  $60\text{ ps}$ , including electronics.
- To understand particle yields in multi-differential analyses sufficiently well, a detector efficiency of more than 95 % is necessary.
- To ensure that track matching is unambiguous, an occupancy of less than 5% for central events is required. Occupancy is the average fraction of electronic channels which show signals in a given event. Occupancy can also be understood as the probability to have a second hit on the same channel and event as any given first hit, which would lead to ambiguities in the track matching.
- To deal with the high interaction rate of CBM, the counters in the most forward region have to be able to deliver this performance at an incoming particle flux of up to  $25\text{ kHz/cm}^2$ . In the outermost regions, the flux drops below  $1\text{ kHz/cm}^2$ .
- The detector and read-out system need to be able to withstand the radiation environment while delivering free-streaming data at the maximal interaction rate.

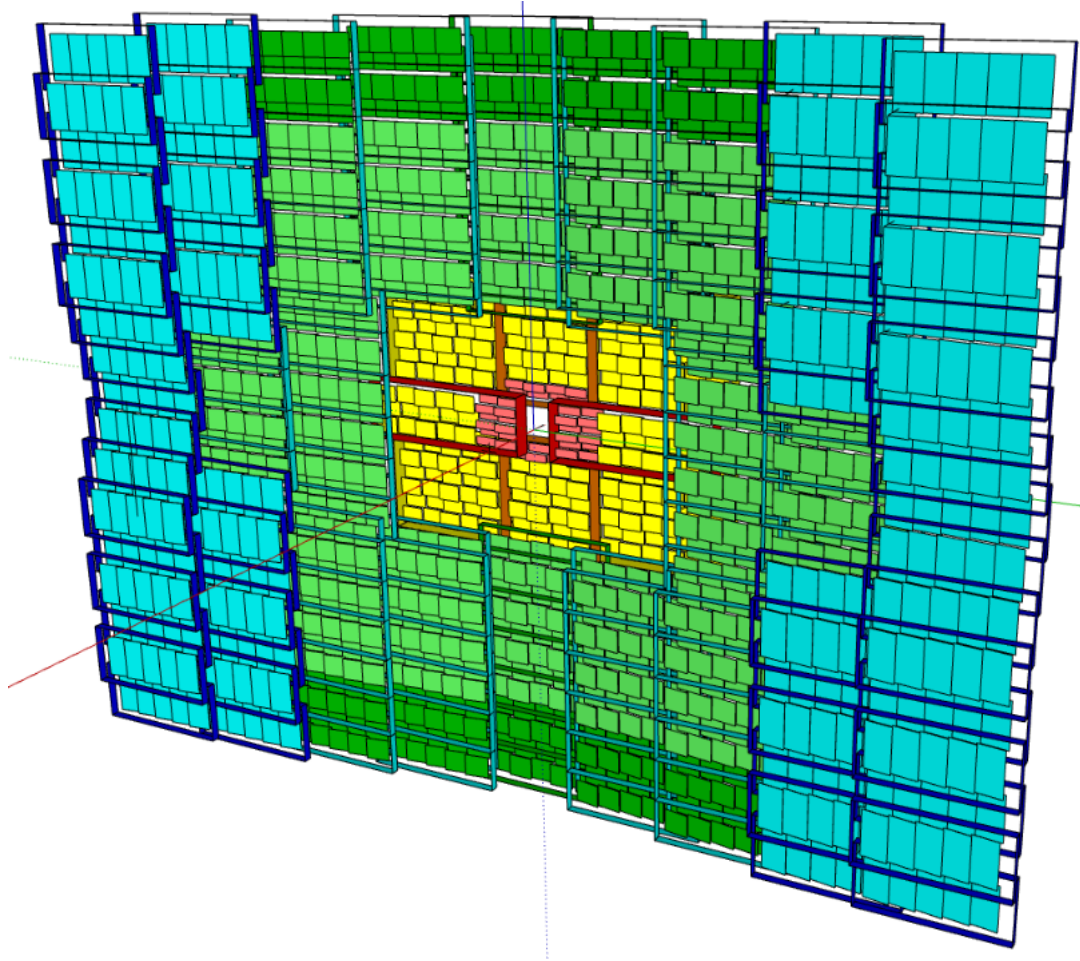


**Figure 3.4:** Geometry of the CBM-TOF wall as described in the technical design report. Shown in cyan and dark green are float glass MRPCs with 50 cm and 27 cm strip width respectively, designed at USTC, Hefei, China. In light green, resistive glass MRPCs designed at the Tsinghua University, Beijing, China are shown. In yellow and red, high rate resistive glass counters with 20 cm and 10 cm strip length respectively, designed at the IFIN-HH, Bucharest, Romania, are shown. Source: [35]



The detector technology of choice to achieve those requirements is multi-gap resistive plate chambers (MRPC) with strip read-out electrodes. This working principle of these detectors will be described in detail in Chapter 4.3.2. Initial plans for the TOF system contain 1376 counters with around 100.000 electronic read-out channels. In order to adjust to the different particle flux environments, the inner counters are built with special low-resistive glass instead of normal float glass, which increases the rate capability of the counters. Closer to the center of the wall, the read-out strips are also shortened from 27 *cm* down to 10 *cm* to reduce the particle rate per strip and thus data rate on a single electronics channel.

The front-end read-out of CBM-TOF MRPCs consists of the "pre-amplifier and discriminator" (PADI) and the "GSI event-driven time to digital converter with 4 channels" (GET4). Both components were developed specifically for CBM-TOF and will be described in more detail in Chapter 4.4. Both are radiation hard application-specific integrated circuits (ASIC) to survive in the environment close to the counters. From there, the output data stream of the GET4s will be routed through multiple concentrator stages to the FLES interface board (FLIB) and then combined with the data from other subsystems used in the online event selection in the FLES computing cluster.

At the time of the beginning of this project, CBM-TOF had already advanced MRPC prototypes. In beam-times at CERN in 2015 and 2016 ([36] and [37]) it has been shown that efficiency and time resolutions close to the CBM-TOF design values could be reached with preliminary versions of the read-out electronics. What was missing at that point were dedicated tests under similar particle fluxes as in CBM and long-term stability tests with the final electronics.

## 3.3 FAIR-Phase 0

Due to delays in the construction and planning pushing the availability of SIS-100 to 2025 and beyond, in early 2018, FAIR saw the need for an intermediate research program. This so-called FAIR-Phase 0 program aims to make use of already existing facilities at GSI, mainly the SIS-18 accelerator, and accelerator facilities at other locations for prototype testing, system development and first physics studies with FAIR equipment. The FAIR-Phase 0 program of CBM-TOF consists of two projects with complementary goals: mCBM at SIS-18 and eTOF at STAR.

### 3.3.1 mCBM

mini-CBM is supposed to be a demonstrator version of the full CBM experiment which all sub-systems contributing their prototypes in a common installation at the SIS-18 accelerator. It has two main goals: high rate detector and read-out tests and the system integration development of the CBM subsystems. Additionally, the aim is to perform physics benchmark tests, especially the measurement of the



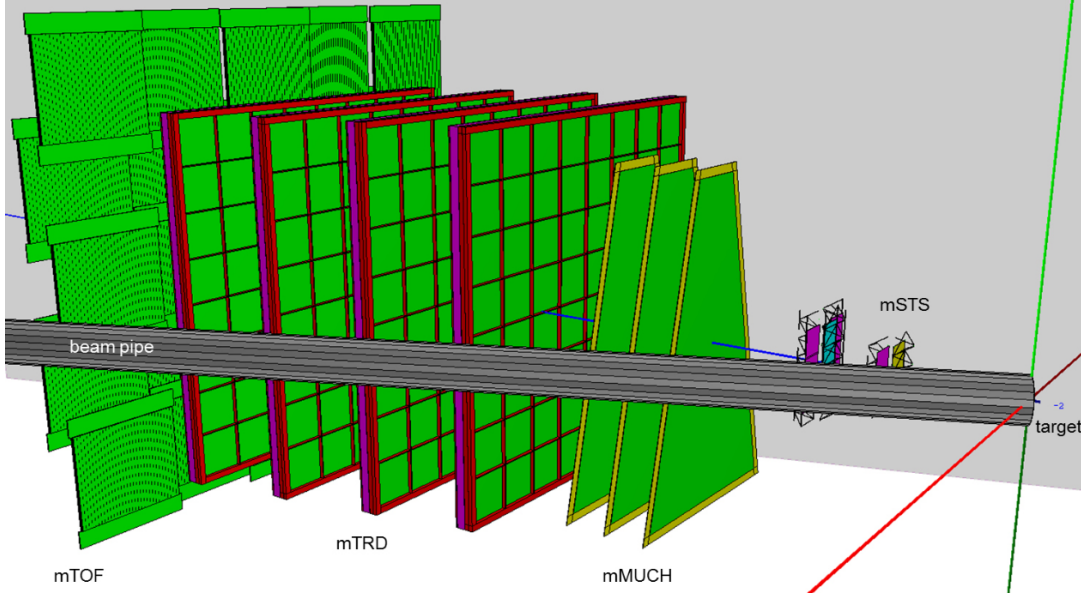


*Figure 3.5: Schematic view of the mCBM design setup Source: [38]*

excitation function of the  $\Lambda^0$ -baryon at high statistics. SIS-18 is the only accelerator facility available to perform high rate tests at a close to final CBM load, albeit at lower energies. mCBM is designed as a fixed target experiment using this beam and operating close to the target to get the highest possible particle flux. The mCBM setup sits at  $25^\circ$  off the beam-line. In its design setup for the physics benchmark runs, it consists of 2 STS stations with 13 silicon strip sensors, 3 MUCH-GEM prototypes, 4 TRD stations, 5 TOF Modules with in total 25 MRPCs with high-resistive glass (Tsinghua design), 4 RICH modules, 8 PSD modules along the beam-line, up to 49 "shashlik"-modules for the ECAL and one or two MVD stations close to the target [38]<sup>1</sup>. Figure 3.5 shows a view of this setup.

Since the first beam-times in late 2018, mCBM has succeeded to show correlations in time and space between sub-system data as well as reached interaction rates of up to  $10^7$  ions/s. With the most recent data, first reconstructions of  $\Lambda$ -baryons are attempted to prepare for the planned measurement of the  $\Lambda$  excitation function in the 2024 benchmark run.

For CBM-TOF, mCBM detector test in 2019 showed an upper limit for the system time resolution of mTOF at  $< 90$  ps and an efficiency above 90 % at an interaction rate of  $\approx 2$  kHz for the Tsinghua type counters [39]. High rate tests in 2021 show a system time resolution  $< 70$  ps and an efficiency above 90 % for the Bucharest type counters of the innermost wall at a particle flux of up to  $25$  kHz/cm<sup>2</sup> [40]. mCBM operations have also shown the need for further development of the intermediate read-out chain between FEEs, detector control and computing clusters as operations at high interaction rates caused frequent FEE stability issues.

<sup>1</sup>This description is based on the initial technical design report. The actual implementation of mCBM has been done slightly different and varied between data taking periods.

### 3.3.2 eTOF at STAR

Complementary to the high rate and integration tests at mCBM, the CBM-TOF group is also working on the end-cap time of flight (eTOF) project at STAR. Here, 108 CBM-TOF MRPCs (72 USTC-type float glass counters and 36 THU-type resistive glass counters) which were installed as an additional time of flight system to provide PID in the very forward region to STAR. As the CBM-TOF development is concerned, eTOF focuses on long-term stability tests of the data acquisition, large system integration and synchronization, testing of the low rate float glass counters and high statistics estimates of production variances between counters. An elaborate description of this project will be given in Chapter 4.

## 3.4 STAR

The Solenoid Tracker at RHIC (STAR) was initially designed to search for signatures of the quark-gluon plasma. The relativistic heavy ion collider (RHIC) is able to accelerate ions up to gold to energies of up to 100  $AGeV$ . As previous research showed that individual signals of the QGP are washed out in heavy ion collisions, STAR was built as a flexible multi-purpose detector able to measure many observables simultaneously. The plan was also from the beginning to make use of the unprecedented high particle multiplicities at RHIC to aim for event-

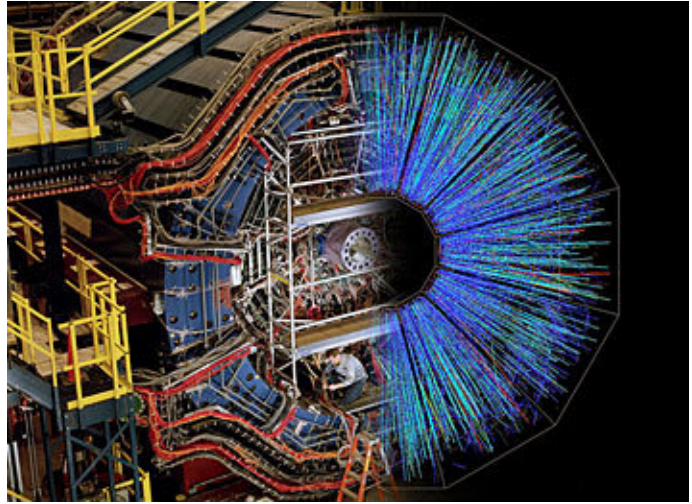


*Figure 3.6: The Star detector, overlaid with a view of particles tracks reconstructed in the TPC. Source: [41]*

by-event level correlations of global observables like temperature, flavor ratios, reaction geometries and density fluctuations [42]. During the 2000s, STAR, together with the other RHIC experiments, ran an extensive program on QGP research at the highest RHIC energies ( $\sqrt{s_{NN}} = 130 GeV$  and  $\sqrt{s_{NN}} = 200 GeV$ ) which culminated in the confirmation of the existence of the QGP in 2005 [9].

Other highlights of STAR's early research include the first observation of elliptic flow at RHIC [43], Evidence of delayed hadronization due to a previous quark-gluon plasma phase in central heavy ion collisions [44], observed evidence of high  $p_t$  jet suppression [45] and measurements of close to equal baryon to anti-baryon ratios [46]. With the design and construction of LHC at CERN, STAR lost its edge in

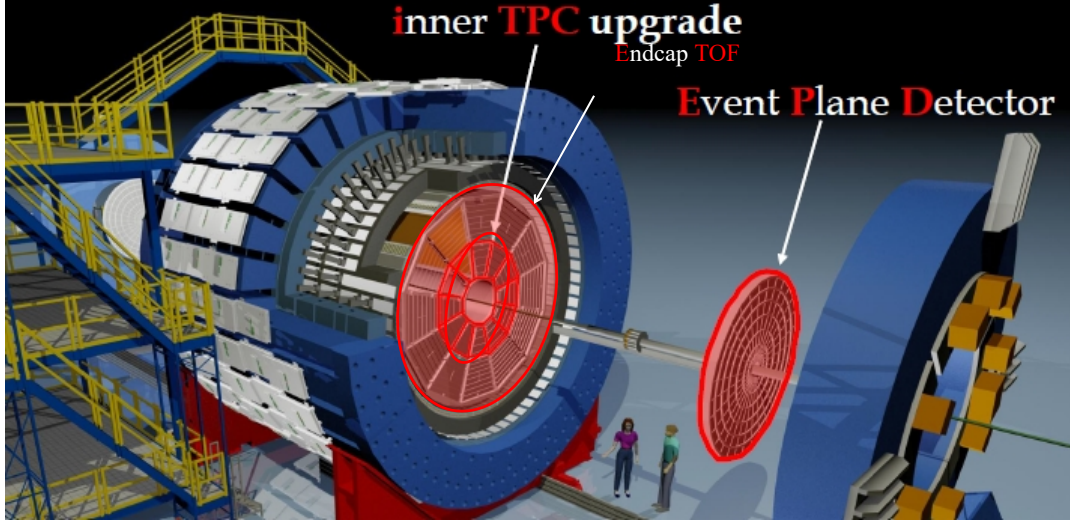


*Figure 3.7: Schematic view of the STAR detector with its upgrades for BES-II. Taken from: [41]*

the high-energy range and partially refocused on the on-set of the QGP in its 2010 decadal plan. This new focus point resulted in the Beam Energy Scan program (BES-I), mainly in 2010 and 2011. Some of the results of this program have already been presented in Chapter 2.5. BES-I had three primary goals: Pin-pointing the onset of QGP signatures observed in the high energy runs, establishing the order of the phase transition between hadron gas and QGP and the search for a QGP critical point [47]. It managed to establish the weakening of QGP signatures in the region below  $\sqrt{s_{NN}} = 19.6 \text{ GeV}$  due to an observed behavior change in the anisotropic flow  $v_2$  and a hint to critical behavior below  $\sqrt{s_{NN}} = 7.7 \text{ GeV}$  in the net proton number fluctuations. However, the conclusiveness of the results of BES-I is limited by uncertainties in the measurements. Especially at the lowest energies, the high energy collider design of RHIC limits interaction rates. To alleviate these limitations, the Beam Energy Scan phase-II program was initiated which will be described in Chapter 3.4.2.

### 3.4.1 The STAR Detector

The heart of the STAR detector is the time projection chamber (TPC) [48] [49]. At the time of its construction, it was the largest of its kind, only to be surpassed by the ALICE TPC at LHC. It has a length of  $4.2 \text{ m}$  and a radius ranging from  $0.5 \text{ m}$  to  $4 \text{ m}$  from the beam-line and is separated into two halves along beam direction, east and west of the interaction point. Along polar direction, the TPC is divided into 12 trapezoidal sectors. Along radial direction, those are separated into an inner TPC (iTPC) and an outer TPC.

The name-giving solenoid magnet of STAR creates a constant magnetic field of up to  $0.5\text{ T}$  inside the TPC. The TPC is filled with a drift gas consisting of 90% argon and 10% methane and has a constant electric drift field of  $133\text{ V/cm}$ . On the outer sides of both halves, the TPC is read out by multi-wire proportional chambers. Drifting electrons from primary ionization along the tracks of particles hit a grid of anode wires with a  $20\text{ }\mu\text{m}$  diameter. The avalanches created in the high field close to the wires induce an image on a set of read-out pads from which particle tracks are reconstructed. With the upgrade of the iTPC in 2019, which increased the pad density in the inner part, there are in total 175,440 read out pads.

The angular coverage of a detector in the longitudinal direction is typically given in terms of the pseudo-rapidity  $\eta = -\ln[\tan(\frac{\theta}{2})]$ . The outer TPC covers a pseudo-rapidity range of  $-1 < \eta < 1$  and the inner TPC extends the coverage to  $|\eta| < 1.5$ . The track reconstruction efficiency is around  $\approx 90\%$  for protons and pions and  $\approx 70\%$  for kaons.

The STAR TPC delivers both momentum and  $dE/dX$  information, allowing for full PID in the low momentum region. According to simulations [49], the TPC can achieve a transverse momentum resolution around  $\frac{\sigma_{p_t}}{p_t} \approx 0.5\%$  in the outer TPC pseudo-rapidity range and  $\frac{\sigma_{p_t}}{p_t} \approx 1.0\%$  of the pseudo-rapidity range which is only covered by the iTPC. The  $dE/dX$  resolutions are of order  $\sigma_{dE/dX} \approx 7\%$  and  $\sigma_{dE/dX} \approx 10\%$  in those  $\eta$  ranges respectively. Together, this allows for a kaon/pion separation up to  $\approx 700\text{ MeV}/c$ . For higher momenta, STAR relies on time of flight systems for particle identification.

STAR, in the BES-II setup, has two TOF systems. The barrel-TOF (bTOF) system [50], installed in 2008, surrounds the TPC with a layer of pad read-out MRPCs. The MRPCs have an intrinsic time resolution of  $\approx 65\text{ ps}$  and, in start-less operation mode, a system resolution around  $\approx 80\text{ ps}$ . For most of the BES-II energies, bTOF operates in the so-called start-less mode, which means that the event start time is not provided by an additional detector, but instead calculated from the arrival time of  $dE/dX$  identified particles and their respective track lengths. At higher collider energies, the start time can also be provided by the vertex position detector (VPD), an array of plastic scintillators close to zero degrees from the beam axis and  $4.5\text{ m}$  distance from the center of the TPC. The second TOF system is the endcap-TOF on the eastern side of the TPC, which will be described in detail in Chapter 4.

Outside the TOF barrel, there is a barrel electromagnetic calorimeter (BEMC) [51] for energy measurements. The STAR BEMC consists of 120 modules, each segmented into 40 towers. Each tower is a sampling calorimeter consisting of 20 layers of  $5\text{ mm}$  lead and 21 layers of  $5\text{ mm}$  plastic scintillators. A typical energy resolution of  $16\%/\sqrt{E/\text{GeV}}$  is achieved. A similarly constructed endcap electromagnetic calorimeter (EEMC) covers the west side of the TPC.

On each side of the TPC, outside the magnet, is the Event Plane Detector (EPD) [52]. It consists of two wheels, one on each side, each with 372 plastic scintillator tiles. The EPD is segmented into the same 12 azimuthal sectors as the TPC. It covers the very forward rapidity range from  $2.14 < |\eta| < 5.19$ . The EPD is primarily

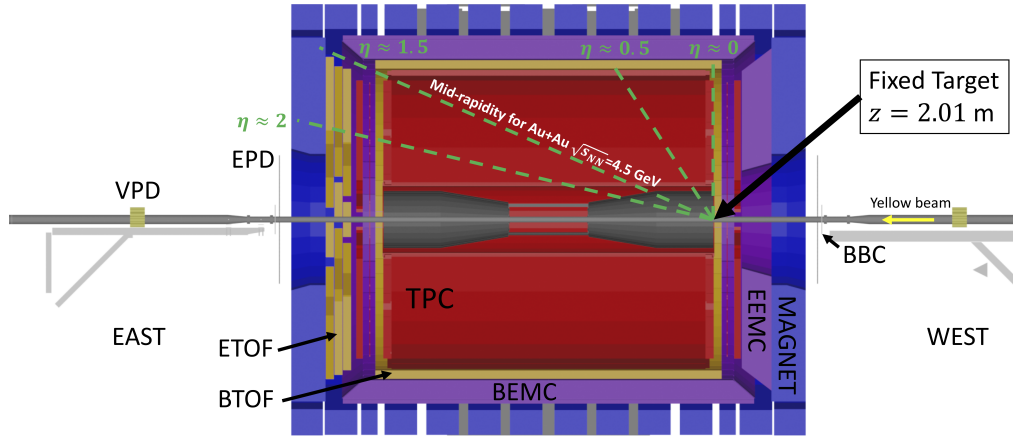


**Figure 3.8:** Orthogonal view of the STAR detector in the FXT setup for BES-II. With Courtesy: J. D. Brandenburg [53]

used to determine the symmetry plane of a collision (event plane) based on the azimuthal distribution of forward particles and is part of the STAR trigger system.

### 3.4.2 Beam Energy Scan II

The BES-II program [54][55] focusses on the center of mass energies below  $\sqrt{s_{NN}} = 20 \text{ GeV}$ . RHIC provided 5 different low beam energy settings:  $9.8 \text{ GeV}$ ,  $7.3 \text{ GeV}$ ,  $5.75 \text{ GeV}$ ,  $4.59 \text{ GeV}$  and  $3.85 \text{ GeV}$ . Compared to the BES-I data taking, an improvement of luminosity by a factor 4-11 has been achieved [56]. These beam energy settings correspond to the collider center of mass energies per nucleon of  $19.6 \text{ GeV}$ ,  $14.6 \text{ GeV}$ ,  $11.5 \text{ GeV}$ ,  $9.2 \text{ GeV}$  and  $7.7 \text{ GeV}$  and the FXT center of mass energies per nucleon of  $4.5 \text{ GeV}$ ,  $3.9 \text{ GeV}$ ,  $3.5 \text{ GeV}$ ,  $3.2 \text{ GeV}$  and  $3.0 \text{ GeV}$ . Additionally, three higher energy settings have been used in FXT for the runs at center of mass energies of  $7.7 \text{ GeV}$ ,  $6.2 \text{ GeV}$  and  $5.2 \text{ GeV}$ . The highest FXT energy at  $\sqrt{s_{NN}} = 7.7 \text{ GeV}$  provides the overlap with the collider program to improve the understanding of acceptance effects and systematics for the FXT program. On the detector side, STAR received three new components with the upgrade of the inner TPC (iTPC), the endcap time of flight system (eTOF) and the event plane detector (EPD). The full BES-II detector setup can be seen in Figure 3.8.

As with BES-I the main physics goals are to study: The turn-off of QGP signatures, the QCD critical point and the nature of the QCD phase transition. The BES-II covers a baryon-chemical potential range from  $\mu_B \approx 720 \text{ MeV}$  at the lowest FXT energy to  $\mu_B \approx 200 \text{ MeV}$  at the highest collider energy, which covers the range where newer theoretical calculations[15] expect the QCD critical point. Among



the priorities for analysis [57] are:

- Excitation function, Elliptic flow and rapidity dependence of the  $\phi$ -Meson (see 2.7).
- Net-proton kurtosis (see 2.6).
- Directed flow of identified particles near mid-rapidity. BES-I observed a minimum of the net-proton directed flow around  $\sqrt{s_{NN}} = 20 \text{ GeV}$ , which, in some hydrodynamic models, is interpreted as a sign for a first-order phase transition [54]. The eTOF and EPD upgrade will allow to extend mid-rapidity measurements to the higher momentum FXT energies.
- Di-lepton yields in the mass range of the  $\rho$ -meson. The "melting" of the  $\rho$ -meson is seen as a signature of chiral symmetry restoration. BES-I has seen an excess yield below the  $\rho$ -peak, albeit with large error bars [55].
- The lifetime of the hyper-triton. Here, BES-I results suggested a lifetime shorter than the free  $\Lambda$  lifetime, which would require additional decay channels. The BES-I result is also in disagreement with measurements at LHC, which suggest a lifetime closer to that of the free  $\Lambda$ .

All BES-II datasets have been successfully collected in the years 2019-2021. At the time of this writing, data calibration and production efforts are still ongoing. This thesis focuses on the performance and calibration of the eTOF systems during BES-II and aims to show its physics performance.

## 4 STAR-eTOF

### 4.1 Detector Geometry

The eTOF@STAR project was started in 2017 as a joint effort between the CBM and STAR collaborations. With the start of the FAIR-PHASE 0 project, the CBM-TOF group was looking for mature heavy ion experiments to test their MRPC prototypes in and contribute to physics research. STAR at the same time was planning the BES-II program with focus on lower energies. As RHIC has not been able to stabilize gold beams at energies below  $\sqrt{s_{NN}} = 7.7 \text{ GeV}$ , lower center of mass energies than that can only be realized in FXT mode. For the FXT mode however, the STAR detector needed improved PID in the forward region.

At the heart of the eTOF system are 108 multi-gap resistive plate chamber (MRPC) time of flight counter. eTOF is arranged as a wheel of 36 modules with 3 MRPCs each. They are clustered into 12 sectors to match the sectors 13-24 of the STAR east side TPC. The sectors 15, 16, 21 and 22 (36 MRPCs in total) are made from low-resistive glass counters produced by the Tsinghua University (THU) CBM-TOF group in Beijing, China (see 4.3.3). The remaining sectors are equipped with float glass counters produced by CBM-TOF group of the University of Science and Technology of China (USTC) in Hefei, China (see 4.3.4). Each MRPC has 32 read-out strips. For the center module of each sector, the strips are oriented orthogonal to the radial direction (or parallel to global  $\phi$  direction) from the beam axis. For the side modules in each sector, the strips are parallel to the strips of the center module and thus slightly offset from the orthogonal of the radius. In each module, the counter closest to the beam-line is labeled as counter 1, the one furthest away from the beam-line labeled as counter 3. The MRPCs inside each module are tilted at an angle of  $10^\circ$  to face better at the FXT interaction spot. They overlap for 2 strips with the next counter.

Inside each sector, the three modules are placed in three planes orthogonal to the beam axis. The center module (module or z-plane 1) is closest to the interaction point. Z-plane/module 2 is the module clockwise from the center module and z-plane/module 3 is the module counter-clockwise from sector center. The distance between the z-planes is  $15 \text{ cm}$ . Due to this arrangement, there is a significant overlap between the side modules of adjacent sectors. Counter 1 of module 2 of each sector is partially in front of counter 1 of module 3 of the previous sector. A conceptual image of the eTOF wheel can be seen in Figure 4.1.

The active area of the eTOF wheel has an inner diameter of  $\approx 105 \text{ cm}$  and an outer diameter of  $\approx 205 \text{ cm}$ . The center of the wheel is positioned at a distance of  $280 \text{ cm}$  along the east side beam-line from the center of the TPC [59]. This covers

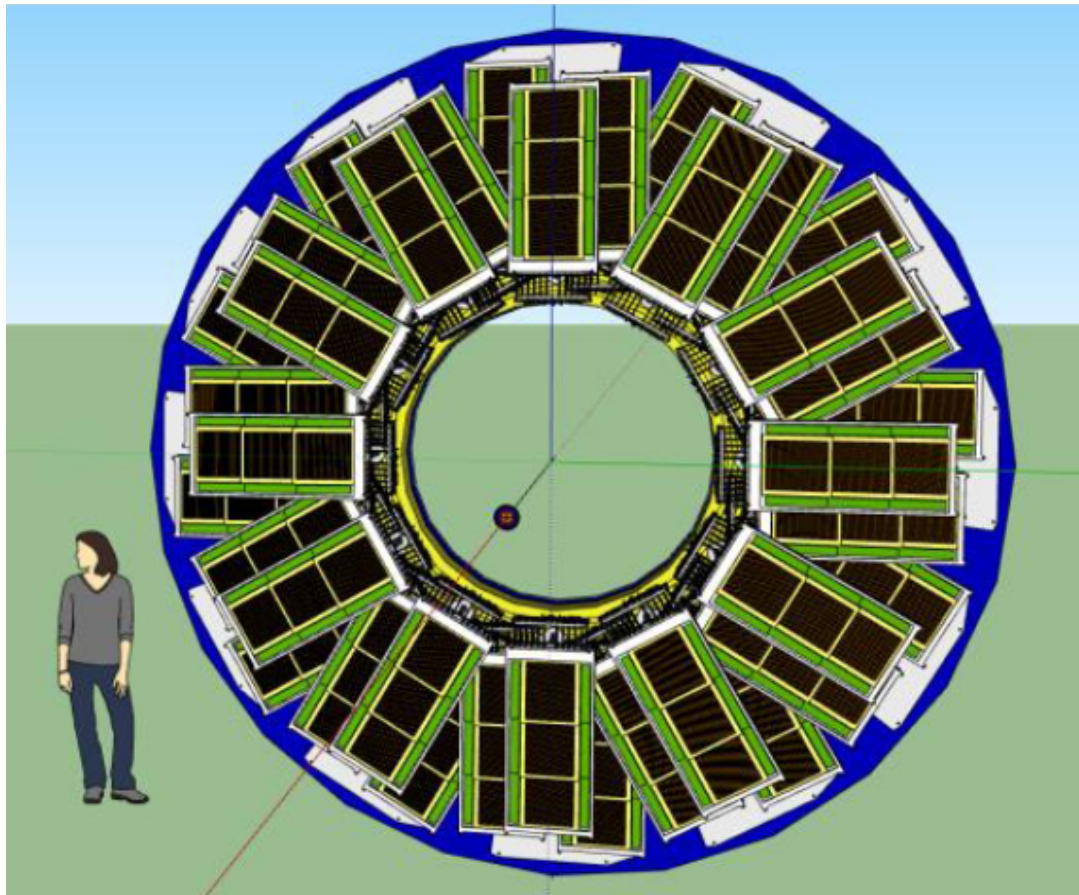


*Figure 4.1: Conceptual design view of the eTOF wheel. Source:[58]*



the pseudo-rapidity range from  $1.05 < \eta < 1.70$  in the collider mode and from  $-1.50 < \eta < -2.20$  relative to the FXT target position. This leaves only a small acceptance gap to the bTOF system which covers  $|\eta| < 0.9$  in collider mode.

## 4.2 The Physics Case of the eTOF Upgrade

The following section summarizes the physics case for eTOF outlined in the initial design paper. Further information can be found in [59].

Figures 4.2 to 4.5 show the expected extension of the phase space coverage with the eTOF upgrade for the most abundant species of identified particles, electrons, pions, kaons and protons. The acceptance for different particle species is limited by the geometrical acceptance in pseudo-rapidity and the detector's ability to identify those particles. The mass resolution of a TOF system depends on the time resolution of the system as well as the momentum and path length resolution of the tracking detector. In the low- $p_t$  region, the acceptance is limited by multiple scattering, which limits the correct track reconstruction. In the high- $p_t$  region, the time resolution of the TOF system is the limiting factor. eTOF is designed to achieve a system time resolution of  $\sigma_{tof} < 80 \text{ ps}$  including the start time system.

The extension of rapidity coverage through eTOF allows STAR to see mid-rapidity for most identified particle species and FXT energies. This provides important advantages for the measurements of various physics observables:

One of the most important indicators of the baryon-chemical potential is the anti-baryon to baryon ratio, which is mostly dominated by the anti-proton to proton ratio. Due to the stopping of produced particles inside the nucleus matter at BES-II energies, anti-protons are emitted more towards mid rapidity. The proton density-rapidity function on the other hand is largely flat. Consequently, the anti-proton to proton ratio peaks at mid-rapidity and the extracted (uncorrected) baryon-chemical potential would be about  $50 \text{ MeV}$  lower at  $y_{cm} = 0$  compared to  $y_{cm} = 1.2$  [59]. This is a similar magnitude as the change in  $\mu_b$  expected between consecutive BES-II energies. A precise estimate of the true baryon-chemical potential inside the fireball thus requires a large angular coverage.

Pions are the most abundant produced particles. Studying the width of their rapidity distributions can provide insight into the equation of state of the nuclear matter. A change in the speed of sound, which would be a strong indication of a first-order phase transition would widen the rapidity distribution compared to the expectation from Landau hydrodynamics.

Dileptons are a probe of the early stages of the collision. The reconstruction of those offers an insight into chiral symmetry restoration via the "melting" of the  $\rho(770)$  meson. In the chirally restored case, the  $\rho$  meson is supposed to have the same spectral function as its chiral partner, the  $a_1(1260)$  meson. This happens slowly via a broadening of the  $\rho$  peak into a broad excess of dileptons in the low mass region from  $200 \text{ MeV}/c^2$  to  $700 \text{ MeV}/c^2$  [59]. Measuring the rapidity dependence of the  $\rho$  broadening will help to separate the collision energy de-

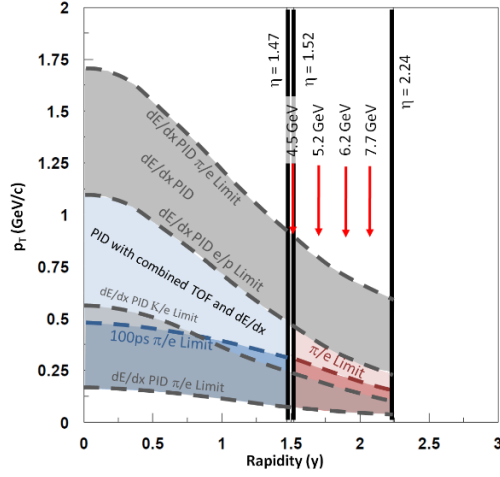


**Figure 4.2:** STAR FXT acceptance in  $p_t$  vs.  $y_{lab}$  phase space for electrons. Acceptance limits for TOF PID with bTOF (blue) and eTOF (red) are given for time resolutions of 80 ps and 100 ps. Grey line indicates PID limits by  $dE/dX$  with the STAR TPC only. Red arrows indicate mid-rapidity at various  $\sqrt{s_{NN}}$ . Source: [59].

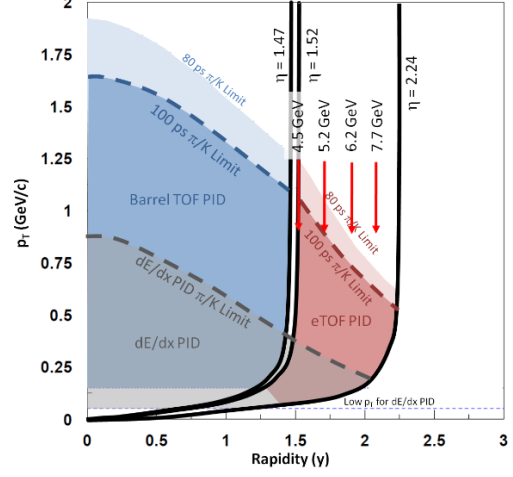


**Figure 4.3:** STAR FXT acceptance in  $p_t$  vs.  $y_{lab}$  phase space for pions. Acceptance limits for TOF PID with bTOF (blue) and eTOF (red) are given for time resolutions of 80 ps and 100 ps. Grey line indicates PID limits by  $dE/dX$  with the STAR TPC only. Red arrows indicate mid-rapidity at various  $\sqrt{s_{NN}}$ . Source: [59].

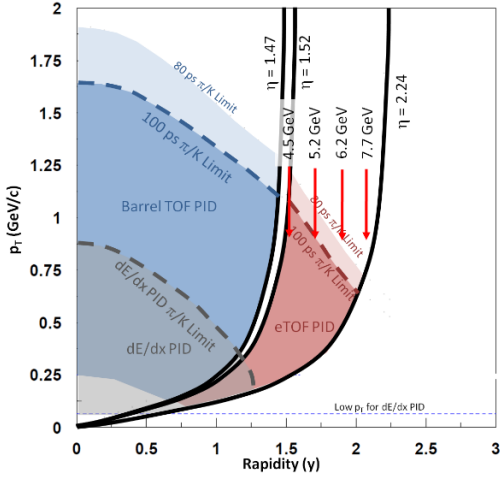


**Figure 4.4:** STAR FXT acceptance in  $p_t$  vs.  $y_{lab}$  phase space for kaons. Acceptance limits for TOF PID with bTOF (blue) and eTOF (red) are given for time resolutions of 80 ps and 100 ps. Grey line indicates PID limits by  $dE/dX$  with the STAR TPC only. Red arrows indicate mid-rapidity at various  $\sqrt{s_{NN}}$ . Source: [59].

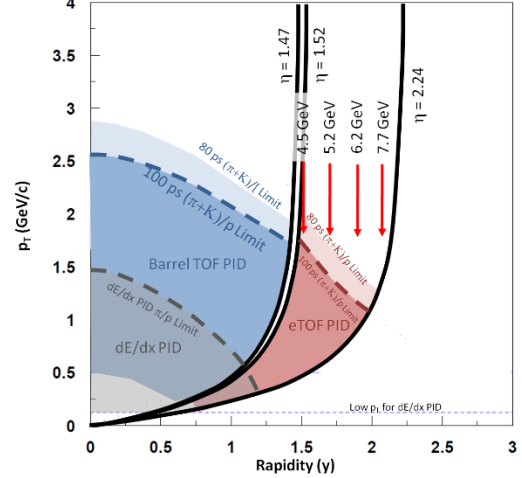


**Figure 4.5:** STAR FXT acceptance in  $p_t$  vs.  $y_{lab}$  phase space for protons. Acceptance limits for TOF PID with bTOF (blue) and eTOF (red) are given for time resolutions of 80 ps and 100 ps. Grey line indicates PID limits by  $dE/dX$  with the STAR TPC only. Red arrows indicate mid-rapidity at various  $\sqrt{s_{NN}}$ . Source: [59].

pendence from the baryon density dependence of this effect. Understanding the mechanism of the  $\rho$  broadening is central to understand chiral symmetry in QCD matter. Dilepton reconstruction is typically PID-limited as the  $dE/dX$  of electrons overlaps with pions in the relativistic rise in gas ionization detectors. Thus eTOF identification is needed to extend STAR's rapidity coverage for dileptons.

The directed and elliptic flow of particles shows interesting behavior in the region of the BES-II. On top of the behavior change of the elliptic flow NCQ scaling (see 2.5.2), the directed flow  $v_1$  of protons at mid-rapidity has shown a change of sign between  $\sqrt{s_{NN}} = 7.7 \text{ GeV}$  and  $\sqrt{s_{NN}} = 11.5 \text{ GeV}$  in BES-1 measurements. This behavior is not fully understood on the theory side, and various interpretations include both a cross-over transition or a first-order phase transition. To improve such measurements in BES-II, eTOF allows mid-rapidity coverage in the FXT mode and an extension of the fit range in COL mode, which decreases the sensitivity to statistical fluctuations.

Finally, the extended pseudo-rapidity coverage increases of course the fraction of the total particle yield which is measured in the detector. This naturally increases the sensitivity for highly statistics-limited measurements of those yields, namely the measurements of higher moments of event multiplicity distributions. As described in Chapter 2.5, measurements of higher moment event-by-event multiplicities are one way to access experimentally critical fluctuations in the vicinity of the QCD critical point. The addition of eTOF will however require adjustments to the analysis strategies as an extension of the rapidity window will introduce a rapidity-dependent low- $p_t$  cut due to the geometric acceptance (see: [59]).

## 4.3 Multi-Gap Resistive Plate Chambers

### 4.3.1 Particle Identification with TOF

Sub-atomic particles are uniquely described by their mass and their charge. For charged particles, a tracking detector is able to determine their momentum-to-charge ratio from the curvature of their track in a given magnetic field:

$$\frac{p_t[\text{GeV}/c]}{q[e]} = 0.3 \cdot r[m] \cdot B[T] \quad (4.1)$$

Here,  $p_t$  is the component of the momentum transverse to the magnetic field,  $q$  charge of the particle (in units of the elementary charge  $e$ ),  $r$  the radius of the track bending, and  $B$  is the magnetic field strength. The total momentum  $p$  of the track can then be directly calculated as the direction of the track relative to the magnetic field is known. To correctly identify a particle, one additionally needs to know either the energy or velocity of the particle to calculate the mass and one needs to be able to differentiate between single-charge and higher-charge particles.

Two general methods to measure a particle's energy exist: Calorimetric measurements determine the total energy of the particle. They are destructive measurements, in the sense that they stop the particle and make it unusable for further measurements. Thus, calorimeters are typically placed on the outermost side of composite detector experiments. The biggest strength of calorimeters is their ability to measure neutral particles, making them an important part of modern particle physics experiments. For identification of individual tracks, their accuracy is however limited.

dE/dX measurement on the other hand rely on the local energy deposition of a traversing particle. Many detector types, like wire chambers, silicon detectors or gas electron multiplication chambers, have decent dE/dX capabilities. The local energy loss of a particle depends on its momentum, charge and its interaction mechanisms with the detector material. For hadrons, the local energy loss due to inelastic scattering with the electron shell of atoms in the surrounding material is described by the Bethe-Bloch formula:

$$\left\langle -\frac{dE}{dx} \right\rangle = K z^2 \frac{Z}{A} \cdot \frac{1}{\beta^2} \cdot \left[ \frac{1}{2} \ln \frac{2m_e c^2 \beta^2 \gamma^2 W_{max}}{I} - \beta^2 - \frac{\delta(\beta\gamma)}{2} \right] \quad (4.2)$$

Here,  $\left\langle -\frac{dE}{dx} \right\rangle$  is the average local energy loss of the traversing particle,  $K = 0.307075 \text{ MeV mol}^{-1} \text{ cm}^2$  a constant coefficient,  $z$  the charge number of the traversing particle (in units of the elementary charge),  $Z$  the charge number of the target particles and  $A$  their atomic mass number.  $m_e$  is the electron mass,  $W_{max}$  is the maximal energy transfer in one collision and  $I$  the mean excitation energy of the electrons.  $\beta$  is the relativistic velocity of the traversing particle (as fraction of the speed of light  $c$ ) and  $\gamma$  its relativistic Lorentz factor.  $\delta(\beta\gamma)$  is a density correction at very high energies [60].

The quadratic charge dependence of the energy loss makes dE/dX measurements an excellent tool to distinguish high charge particles. However, at high momenta, the logarithmic dependence on  $\beta$  limits the separation of protons, pions and kaons (compare Figures 4.2 to 4.5 for the case of the STAR TPC).

The most flexible method to distinguish hadrons at higher momentum is the time of flight (TOF) method. Time of flight is at its core a simple speed measurement. A track from a tracking detector is extrapolated to a timing detector. The arrival time on the timing detector  $t$  is measured precisely and compared to an event start time  $t_0$ , which is interpreted as the time of the collision. The difference between arrival time on the timing detector and start time is called the "time of flight"  $\Delta t_{tof}$ . From time of flight  $\Delta t_{tof}$ , track length  $L$ , track momentum  $p$  the mass of the particle can be calculated [20]:

$$m_0 = \frac{p}{c} \cdot \sqrt{\frac{c^2 \Delta t_{tof}^2}{L^2} - 1} \quad (4.3)$$

The error in this mass calculation can be derived as:

$$\sigma_{m_0} = \sqrt{m_0^2 \cdot \left(\frac{\sigma_p}{p}\right)^2 + \left(\frac{E^2}{m_0 \cdot c^4}\right)^2 \cdot \left(\frac{\sigma_L}{L}\right)^2 + \left(\frac{E^2}{m_0 \cdot c^4}\right)^2 \cdot \left(\frac{\sigma_{tof}}{\Delta t_{tof}}\right)^2} \quad (4.4)$$

using  $E^2 = p^2 c^2 + m^2 c^4 = \left(\frac{pc^2 \cdot \Delta t_{tof}}{L}\right)^2$ . With  $\gamma = \frac{1}{\sqrt{1 - \frac{v^2}{c^2}}} = \frac{E}{mc^2}$  the relative error simplifies to:

$$\frac{\sigma_{m_0}}{m_0} = \sqrt{\left(\frac{\sigma_p}{p}\right)^2 + \gamma^2 \cdot \left(\frac{\sigma_L}{L}\right)^2 + \gamma^2 \cdot \left(\frac{\sigma_{tof}}{\Delta t_{tof}}\right)^2} \quad (4.5)$$

For eTOF, time of flight for high relativistic particles is typically  $> 16 \text{ ns}$ , which, with a system time resolution of  $\sigma_{tof,sys} = 80 \text{ ps}$ , leads to  $\frac{\sigma_{tof}}{\Delta t_{tof}} < 0.5\%$ . This is small compared to the expected momentum uncertainties for eTOF tracks, which vary between  $1.5\% < \frac{\sigma_p}{p} < 4.0\%$  depending on particles species and the number of TPC points on the track (For extended estimates of the momentum resolution for eTOF see: [59]). As the influence of the timing error scales with  $\gamma$ , it is still the dominant error for high relativistic particles (mainly pions and electrons). However, for protons and kaons in the momentum range of the eTOF acceptance (approximately  $p_P < 4 \text{ GeV}/c$  and  $p_K < 1.7 \text{ GeV}/c$ ), the influence of the momentum uncertainty is similar to the influence of the timing uncertainty and must not be neglected. The uncertainty of the path length depends on the resolution of the vertex position and the position resolution of the MRPC. The vertex position resolution in STAR depends on the particle multiplicity of the event, but is typically in the order of a few hundred microns in COL mode [59]. In FXT mode, the position of the target provides even more precise information on the vertex position. The position resolution of MRPCs is typically  $\sigma_x < 0.5 \text{ cm}$ . As the tracks intersect with the MRPC plane almost orthogonally, this resolution however only translates into a negligible uncertainty in the total track length. Thus, the path length uncertainty should be well below  $\sigma_L < 0.1 \text{ cm}$ . Given a typical track length of  $2.5 \text{ m} - 5.0 \text{ m}$  the path length uncertainty is significantly less impactful than the other uncertainties.

### 4.3.2 MRPC Working Principle

A resistive plate chamber (RPC) in its simplest configuration consists of two parallel high-voltage plates, two additional parallel plates made of a high-resistive material (typically glass, Bakelite or ceramics) and a gas gap in between. A net of spacers, typically made from fishing lines, keeps the gas gap open and the resistive plates at a uniform distance. One distinguishes between two general types of RPCs: Trigger-RPCs with a single large gap and timing or multi-gap RPCs (MRPCs), with multiple smaller gaps, divided by additional resistive plates. This work concerns timing MRPCs. The high-voltage electrodes produce a strong

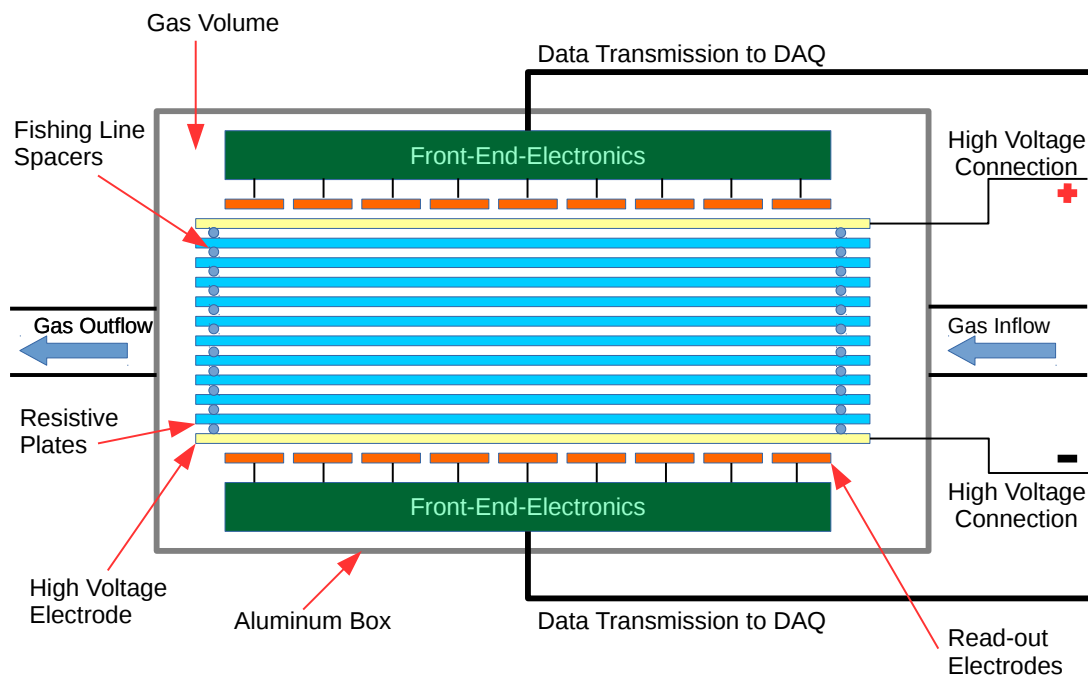


**Figure 4.6:** Schematic view of an MRPC in single stack configuration. Source: [61]

constant electric field inside the gas gap. On the outside of the high-voltage plates, read-out electrodes pick up the induced image of moving electrical charges inside the gas gap to generate a signal which is read-out by the front-end electronics (FEE). The entire detector is contained in a gas volume surrounded by a housing box.

Signal generation in an (m)RPC starts when an incoming particle ionizes the gas in the gas gap. A minimum ionizing particle loses on average  $2 \frac{\text{MeV cm}^2}{g}$ , normalized to the density of the gas. This corresponds to about 8 primary ionizations per traversed centimeter of typical RPC gas [63]. In the constant electric field generated by the high-voltage electrodes, the electrons knocked out during the initial scattering are accelerated towards the anode plate. The electrons will soon themselves gather enough momentum that they can ionize gas atoms with which they scatter. The electrons freed from these

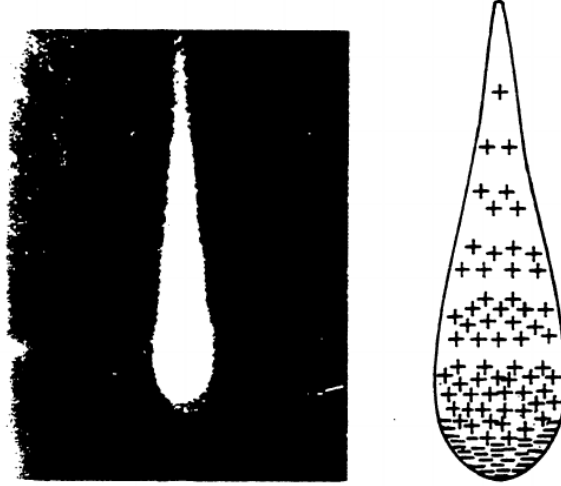


*Figure 4.7: Left: Photograph of an electron avalanche in a cloud chamber. Right: Schematic distribution of charges inside the avalanche. Negative electrons are concentrated at the tip of the avalanche, while positive ions slowly drift in the opposite direction. Source: [62]*

secondary collisions are of course also accelerated and ionize further gas atoms. An exponentially growing gas avalanche forms which is moving towards the anode. The positively charged ions drift, slowly, due to their much higher mass, towards the cathode.

As the electrons of the avalanche are constantly accelerated by the field and decelerated in the collisions with gas atoms, the avalanche moves at a constant drift velocity. The drift velocity depends on the mass of the charge carriers (electrons in this case), the electric field strength, and the density of the gas. A typical drift velocity for the electron avalanche in an MRPC is  $v_{drift} \approx 200 \frac{\mu\text{m}}{\text{ns}}$  [61]. The total number of electrons in an avalanche as function of the drift distance  $x$  can be described by an exponential function of the form:

$$n(x) = n_{prim} \cdot e^{\int \alpha(x) dx} \quad (4.6)$$

The exponential coefficient is called the first Townsend-coefficient  $\alpha(x)$ . It depends the local electric field and the gas mixture in the gap. In the constant field of an MRPC, the Townsend-coefficient in generally does not depend on  $x$  unless

the field is significantly distorted by the presence of other avalanches at very high rates. Once an avalanche reaches a certain size, the so-called Raether-limit (around  $10^9$  electrons) [62], the space charge of the avalanche starts to distort the electric field significantly. This field distortion can lead an increased emission of long-range real photons which can be ionizing by themselves. These photons can be reabsorbed far away from the avalanche and start new avalanches uncorrelated to the primary particle. When reabsorbed close to the development axis of the avalanche, they may ionize electrons behind the avalanche, in the most extreme case on the surface of the cathode glass plate. These electrons create significant secondary avalanches whose signal is merged with the primary avalanche into a so-called streamer signal. Due to the significantly higher charge per incoming primary particle, streamer signals reduce the electric field significantly at their location. Thus, the streamer probability should be low for a high rate MRPC. Here, the name-giving resistive plates come into play. Once the avalanche reaches the resistive plate, it discharges. The electric charge of the avalanche slowly diffuses through the resistive plate and neutralizes with positive charges from the other side of the next gap or the HV electrode. The resistivity of the plate determines how quickly this process happens and thus how quickly the electric field in the MRPC is restored. MRPCs with a lower resistivity of the resistive plates have therefore a higher rate capability. The resistivity of the plates depends on the bulk resistivity of the plate material and the thickness of the plates.

As the high-resistive plates are permeable to high frequency signals, the moving avalanche inside an RPC gap can induce a signal directly in the read-out electronics on the outer sides of the RPC. There are two different types of geometry for the read-out electrodes, on which the spatial resolution of the MRPC depends. One consists of rectangular shaped metallic read-out pads that are connected to an individual FEE channel at one point on the pad. This geometry has the advantage of a high granularity, which makes it easier to distinguish nearby hits in the same event. The disadvantage is a higher required number of read-out channels and an unknown delay due to the signal travel time from the projection of the avalanche to the read-out point on the pad. This delay requires additional corrections to avoid spoiling the time resolution of the MRPC. The position resolution of the pad geometry depends the width  $d$  of the pads in  $x$  and  $y$  direction:

$$\sigma_{pad,x} = \frac{d_x}{\sqrt{12}}, \quad \sigma_{pad,y} = \frac{d_y}{\sqrt{12}} \quad (4.7)$$

Typical pad sizes vary from 2 *cm* to 6 *cm*.

Alternatively, the read-out electrodes can consist of parallel metallic strips which are read out by individual read-out channels on both sides. The strips have a typical pitch (distance between strip centers) of 1 *cm* – 2 *cm* and a length equal to the length of the MRPC. The induced signal travels to both sides of the strip and is read out there. The position of the avalanche along the strip (conventionally called the local  $y$  position of the hit) and the arrival time of the hit can then be calculated



from the arrival times on the two sides of the strip:

$$y = \frac{t_1 - t_0}{2} \cdot v_{signal}, \quad t_{hit} = \frac{t_1 + t_0}{2} + c \quad (4.8)$$

here,  $t_1$  and  $t_2$  are the arrival times on the signals on the two sides of the strips,  $v_{signal}$  is the signal velocity along the strip and  $c$  is a constant delay depending on signal velocity and strip length which will be absorbed into calibration offsets. Furthermore, the convention that side 0 is the right side of the strip and side 1 is the left side of the strip<sup>1</sup> will be used. For a strip MRPC, the resolution in  $x$  direction (across the strips) depends also on the width of the strip. The resolution in  $y$  direction depends, as the signals on both sides originate from the same avalanche, only on the resolution of the read-out electronics:

$$\sigma_{strip,x} = \frac{d_x}{\sqrt{12}}, \quad \sigma_{strip,y} = \frac{\sigma_{FEE} \cdot v_{signal}}{\sqrt{2}} \quad (4.9)$$

As modern read-out electronics have time resolutions below  $50\text{ ps}$  and signal velocities on the strip are typically  $v_{signal} \approx 2/3 \cdot c$ , strip MRPCs usually have better spatial resolutions than pad MRPCs.

The time resolution of an MRPC (per gap) can be estimated as [64]:

$$\sigma_t = \frac{1.28}{(\alpha - \eta) \cdot v_{drift}} \quad (4.10)$$

Here,  $\alpha$  is the first Townsend-coefficient,  $v_{drift}$  is the drift velocity of the avalanche and  $\eta$  is the attachment coefficient, which describes the loss of avalanche electrons to the reabsorption by gas atoms. One defines the effective Townsend coefficient  $\alpha_{eff} = \alpha - \eta$  to describe the avalanche growth analogue to Eq. 4.6 including the electron reattachment effect. As both the (effective) Townsend-coefficient and the drift velocity increase with a higher electric field, the field strength in the gap is the most important parameter for a good MRPC time resolution.

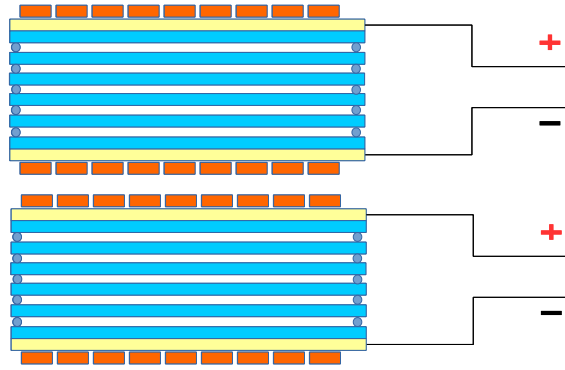


**Figure 4.8:** Schematic view of an MRPC in double stack architecture. Adapted from: [61]

<sup>1</sup>when looking at the MRPC with positive  $x$  axis phasing upwards and the  $z$  axis pointing towards the observer (right-handed coordinates)

For MRPCs, the main component gas in the gas gap is usually a gas with high electronegativity. Typical choices are freon or tetrafluoroethane. Compared to the gases used in other detector types, such gases have a small effective Townsend-coefficient due to the re-absorption of free electrons by fluorine atoms. On the one hand, this gas choice delays the signal generation, but on the other hand provides a high dielectric strength which allows to apply high electric fields without spark formation. These gases are often mixed with a photon quencher (isobutane) and a delta electron absorber (sulfur hexafluoride). Sulfur hexafluoride, as the gas with the highest dielectric strength also helps to increase the applied electric field and thus improves the time resolution. The photon quencher is typically a more complex molecule with a large number of transition frequencies for a broad photon absorption cross-section. In eTOF, the used gas mixture is 94.5 %  $C_2H_2F_4$ , 5 %  $C_4H_{10}$  and 0.5 %  $SF_6$ .

The efficiency of an RPC on the number of primary ionizations in a small region of the gap closest to the positive electrode. Only in this efficient region, a primary ionization has enough time to grow into a signal above discrimination threshold before neutralizing on the resistive plate. The size of the efficient region depends on the effective Townsend coefficient. If the gap size is increased at a given field strength, the efficient region is also enlarged accordingly. However, the charge per avalanche increases exponentially with the gap size. This charge has to be replenished through the HV electrodes to conserve the electric field in the gap. This process is limited by the power of the HV supply and the resistivity of the HV electrode. A large gap size thus limits the rate capability of an RPC. By using RPCs with multiple narrow gaps (MRPCs), the signal from the individual gaps add up, creating a larger total efficient region. The total charge of an average avalanche in this case increases linearly with number of gaps, circumventing the exponential increase with the size of a single gap. The signal from each gap can also be seen as an independent measurement of the arrival time of the primary particle. Thus, by using multiple gaps the total time resolution of the MRPC improves.

Another option to increase the number of gaps for a given available total high-voltage is a so-called double stack architecture. Here, two MRPCs are stacked inverted towards each other, such that they have a common HV polarity in the center and the opposite polarity on the outside. This way, half of the total high-voltage can be applied to each side of the double stack. The signals from the read-out electrodes are then merged in a three-way junction before the read-out electronics.

### 4.3.3 Prototype MRPC2 THU

The Tsinghua-type MRPCs used in eTOF are prototypes for the MRPC2 of CBM, which will be used in the intermediate rate region, with a rate requirement of  $10\text{kHz}/\text{cm}^2$ . Such a high rate capability is not achievable with normal soda lime float glass resistive plates at room temperature. Instead, a specialized low-resistive

glass has been developed at Tsinghua University, Beijing [65]. This black, opaque glass has a bulk resistivity of  $\approx 10^{10} \Omega/cm$  compared to a typical bulk resistivity of  $\approx 10^{12} \Omega/cm$  for conventional float glass.

The THU-type MRPCs have a double stack architecture with  $2 \times 4$  gas gaps with a gap size of  $250 \mu m$ . The  $2 \times 5$  glass plates are polished down to  $0.7 mm$ . Nylon fishing line is wrapped around 5 pins on each side in a Z-like shape between each of the plates to ensure a uniform gap size. The fishing line layout can be seen in Figure 4.9. The outside of the outermost plates of each stack are covered by a colloidal graphite spray HV electrode. The read-out electrodes consist of 32 copper strips on PCBs on each side of a stack. The central PCB has read-out strips on both sides. The strips have a length of  $27 cm$ , width of  $7 mm$  and a gap of  $3 mm$  between them. This gives the MRPC a nominal active area of  $32 cm \times 27 cm$ . The read-out strips are designed with a simulated wave impedance of  $50 \Omega$ . For stabilization of the outer PCBs, a  $6 mm$  thick honeycomb structure is added on the outer side. On the side of the first read-out strip, glass, PCB and honeycomb extend slightly beyond the active area. A hole is drilled through the PCB and honeycomb to allow to glue the high-voltage connection to the HV electrode with carbon tape. A detailed description of the detector design can be found in the production readiness review [66].

At an operating high-voltage of  $\pm 5.2 kV$  (applied to positive and negative HV electrode of each stack), which was used for most of eTOF operation, the resulting electric field is  $104 kV/cm$ . At this high-voltage, the MRPC prototype has shown to have a time resolution of  $\sigma_{tof} < 62 ps$  and an efficiency  $\epsilon \approx 93 \%$  [67] (Note: The cited cosmic test was performed with the CBM gas mixture of 90 %  $C_2H_2F_4$ , 5 %  $C_4H_{10}$  and 5 %  $SF_6$ ).

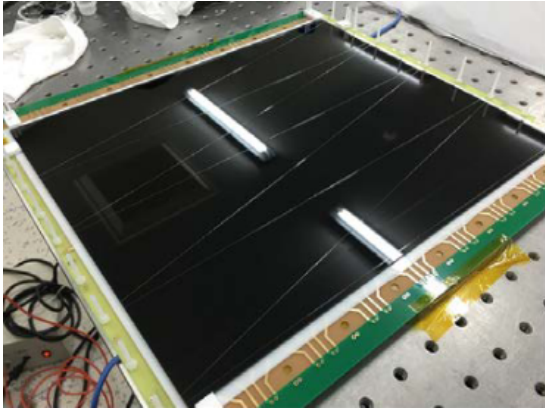


**Figure 4.9:** A THU-type MRPC3a during assembly with the fishing line layout visible. Source: [68]

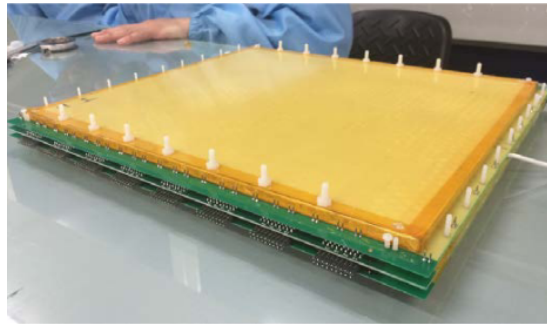


**Figure 4.10:** A THU-type MRPC3a fully assembled. Source: [68]

### 4.3.4 Prototype MRPC3 USTC

The USTC-type MRPCs in eTOF are prototypes for the CBM MRPC3bs. They cover a region with a rate requirement below  $2.5 \text{ kHz/cm}^2$ . This requirement can be fulfilled by the significantly cheaper float glass, given that it is thin enough.

The USTC-type MRPCs are build in a  $2 \times 5$  gap double stack architecture with a gap size of  $230 \mu\text{m}$ . In the float glass process, the glass plates can be created with a thickness of only  $280 \mu\text{m}$ . The thin glass plates however need more support structure in the form of a denser fishing line layout. The fishing lines are arranged in parallel line with a distance of  $2 \text{ cm}$  (see 4.11). Analogous to the THU-type counters, the read-out electrodes consist of  $7 \text{ mm}$  wide read-out strips with a  $3 \text{ mm}$  gap in between them and a length of  $27 \text{ cm}$  on three PCBs. Consequential, the active area is also  $32 \text{ cm} \times 27 \text{ cm}$  and the design impedance is  $50 \Omega$ . The high-voltage electrodes consists of a graphite layer on the outer side of the outer two glass plates of each stack. This graphite layer is insulated against the PCB by a Kapton foil. A  $30 \text{ mm} \times 4 \text{ mm}$  copper pad in a cut-out in the Kapton foil on the side of the first read-out strip serves as high-voltage connection on which the wiring is soldered. A detailed description of the detector design can be found in the production readiness review [66].

Due to the smaller gap size, the USTC-type counters require a higher electric field than the THU-type counters to reach plateau efficiency. At an operating high-voltage of  $\pm 6.4 \text{ kV}$  (applied to positive and negative HV electrode of each stack), which was used for most of eTOF operation, the resulting electric field is  $111.3 \text{ kV/cm}$ . At this high-voltage, the MRPC prototype has shown to have a time resolution of  $\sigma_{tof} < 56 \text{ ps}$  and an efficiency  $\epsilon \approx 99 \%$  [67] (Note: The cited cosmic test was performed with the CBM gas mixture of  $90 \%$   $\text{C}_2\text{H}_2\text{F}_4$ ,  $5 \%$   $\text{C}_4\text{H}_{10}$  and  $5 \%$   $\text{SF}_6$ ).

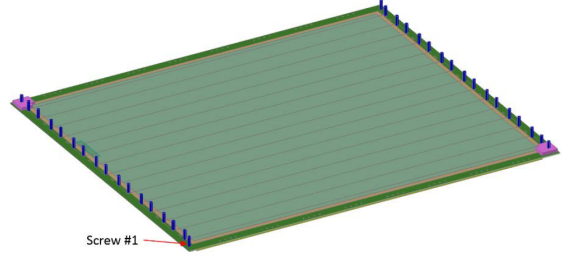


**Figure 4.11:** Image of a USTC-type MRPC during assembly with the fishing line structure visible. Source: [66]

## 4.4 Front-End Electronics

### 4.4.1 PADI

The first step of MRPC read-out in eTOF is the pre-amplifier and discriminator (PADI) chip. PADI is a custom development project started for the CBM-TOF MRPCs. eTOF uses the version PADI-X. A block diagram of the chip can be seen in Figure 4.12. The chip has 8 channel and consists of two main stages. The first

stage is the pre-amplifier stage with an amplification factor of 251, a bandwidth of  $411\text{ MHz}$  and a noise level around  $5\text{ mV}_{rms}$  [69].

Afterwards, a constant threshold discriminator converts the amplified analog signal into a digital low voltage differential signal (LVDS) with a width equal to the time over threshold of the analog signal. An applied threshold voltage lowers the baseline voltage at the discriminator by the same amount. A pulse is discriminated until it crosses the zero-line. The threshold voltage can be adjusted over a range of  $\pm 750\text{ mV}$  through an SPI control interface. This allows also to discriminate input with inverse polarity. For a typical MRPC input signal of  $\approx 30\text{ mV}_{peak}$ , PADI has a leading edge time resolution of  $\approx 20\text{ ps}$  ([70], see Figure 4.13).

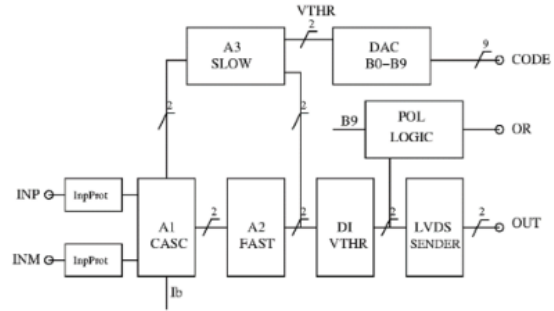


**Figure 4.12:** Simplified block diagram of PADI X. Source: [69]

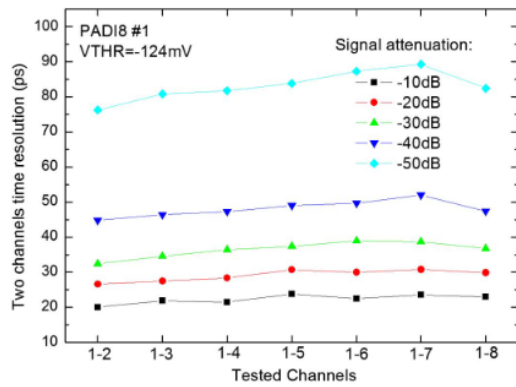


**Figure 4.13:** Time resolution of PADI 8/X for different attenuation settings of a  $250\text{ mV}$  input pulse. The black line most closely resembles a typical MRPC signal of  $\approx 30\text{ mV}$ . Source: [69]

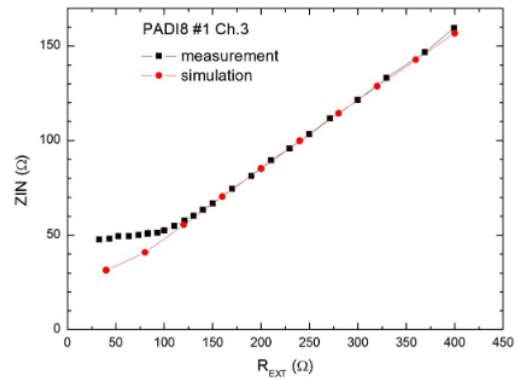


**Figure 4.14:** Single-ended input resistance of PADI 8/X as function of the external resistor setting. The differential input resistance corresponds to twice this value. A clear saturation at  $R_{in} = 50\text{ }\Omega$  single-ended or  $R_{in} = 100\text{ }\Omega$  differential is observed Source: [70]

PADI has fully differential input channels with an adjustable input impedance by an external resistor. With PADI-X, measurements show that the input resistance can not be adjusted to a differential impedance below  $100\text{ }\Omega$ . Impedance matching with the  $50\text{ }\Omega$  differential impedance of the eTOF MRPCs is instead achieved with a parallel resistor to ground (Compare Figure 4.14).





(integral) non-linearity between the measured fine time and the actual arrival time of a signal. The measured integral non-linearities in GET4 of the fine time bins are below 0.6 bins (compare Figure 4.16). Without correcting the non-linearities, a time resolution of  $\sigma_t < 27 \text{ ps}$  is measured (see Figure 4.17). The delay chain provides a history of  $6.25 \text{ ns}$  into a 2-part hit register, each covering a  $3.25 \text{ ns}$  half clock cycle for each channel. As the two parts can store one independent hit, the dead time of a GET4 channel is at worst  $3.25 \text{ ns}$ .

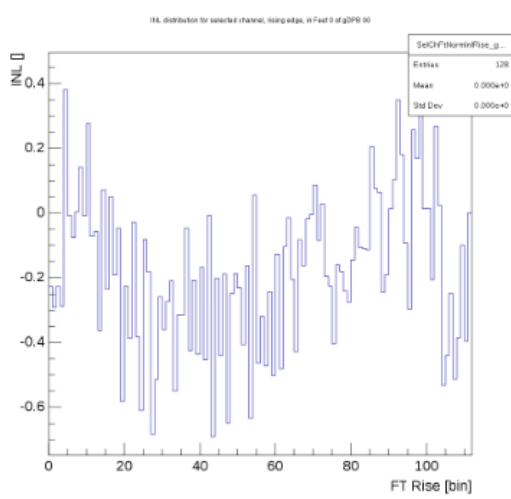


**Figure 4.16:** Measured integral non-linearities of GET4 fine time bins. On the X-axis, the 112 fine time bins are shown. The Y-axis shows the integral non-linearities of a given bin, i.e. the displacement of the bin center time compared to the linear expectation in units of fine time bins ( $55.8 \text{ ps}$ ). The integral non-linearities are determined by adding up the differential non-linearities of all previous bins. Differential non-linearities are determined by the number of entries in a given time bin compared to the average when a large number of time-uniform input signals (e.g. white noise) are applied. The integral non-linearities in GET4 are small compared to FPGA TDCs. Source: [71]

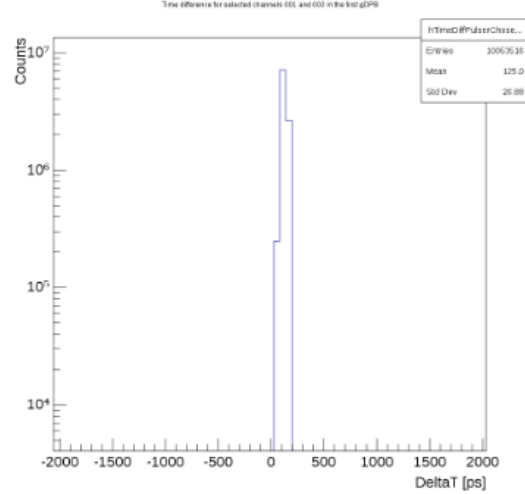


**Figure 4.17:** Measured distribution of the time difference between the arrival of a common LVDS signal on two GET4 chips. A time resolution of  $27 \text{ ps}$  is achieved under lab conditions. Source: [71]

From the hit registers, leading and falling edges of the hits are determined and the time over threshold (ToT) is calculated on the chip. The 8 bit ToT value can be adjusted to reflect different ToT ranges. In eTOF, each of the 256 ToT bins

represents  $0.2\text{ ns}$ . The hits are then converted into a 30 bit internal data word and stored in eight separate read-out FIFOs, one for each hit register of the four channel. Each FIFO can store up to 7 hits plus one epoch message and are read out by an eight piece token ring read-out. GET4 communicates with the back-end data acquisition system via a serial link. A 32 bit GET4 hit message contains (counting from the least significant bit):

- 8 bit ToT value
- 7 bit fine time value
- 12 bit coarse time value
- 2 bit GET4 channel address
- 1 bit delay-lock-loop lock flag
- 2 bit hit message header

If a FIFO becomes full, hit messages are dropped, and a FIFO full error message is sent instead. This way, data loss is guaranteed to be known. All GET4 error messages are inserted into the data stream and, in the case of bandwidth limitations, take priority over hit messages.

eTOF contains 1728 GET4 chips, placed into PCB boards with 8 chips each, for one side of each counter. To keep the timing information of all chips synchronous, a sync signal from a common clock source is inserted into the GET4s. Upon receiving the sync signal, the internal coarse time counter is reset to zero on the next clock edge. The sync signal can be sent at any multiple of 4096 clock cycles ( $25.6\text{ }\mu\text{s}$ ), thus, once a counter is in sync, the coarse time counter will be at 4095 when receiving the sync signal. Otherwise, an "out of sync" error message is sent. If GET4 receives a command to restart itself, it will re-synchronize to the system on the next sync signal, resetting the coarse time counter to zero. During the coarse time counter re-synchronization, the epoch counter is also updated to any previously received epoch sync initialization value. If the current epoch value differs by more than one from the initialization value, an epoch sync error message is issued.

The configuration of GET4 is done via a separate slow control interface. It allows, among other options, to adjust time over threshold settings, reinitialize the GET4, reset the epoch counter to a given value and bit rate of the serial link. GET4 contains also an SPI master that controls the SPI interfaces of PADI and allows setting of thresholds through GET4s slow control interface.

## 4.5 Data Path

After the GET4, the eTOF data from one side of a module are routed into a first concentrator stage on the module's backplane, the GBTX (= Gigabit transmitter



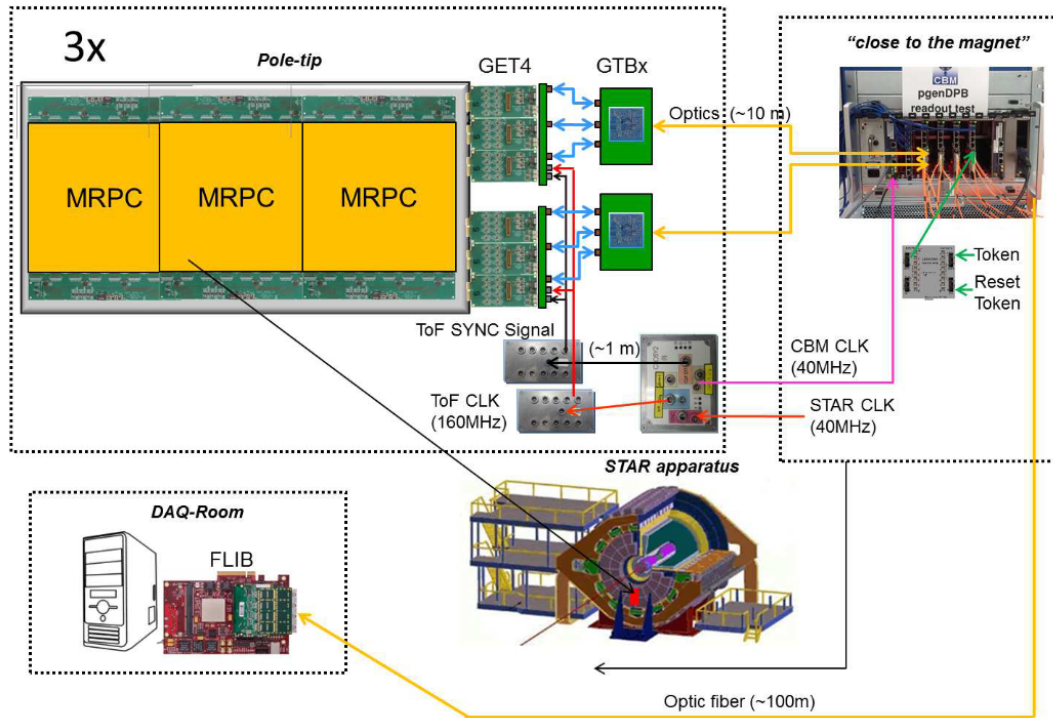


**Figure 4.18:** The eTOF DAQ and clocking system. With courtesy: J. Frühauf

[72]). The GTBx is a CERN-developed radiation-hard, high-bandwidth ASIC chip to interface optical and analogue links. It implements a bi-directional link with an FPGA board (the gDPB) located outside the radiation environment. Both the data stream from the FEE and the slow control stream to the GET4s are routed over these optical links. The GTBx is data-agnostic to both of these streams.

The 6 GTBx of one sector are connected to one gDPB (= GET4 data processing board). The gDPB is a firmware-based system implemented on the AFCK board (= Advanced FMC carrier board Kintex [73]). The AFCK is an open source carrier board for a Xilinx Kintex 7 FPGA, available over the Open Hardware Repository (OHW). Field programmable gate arrays (FPGA) are collections of small adjustable individual logic blocks which can be combined into complex logic circuits according to a hardware description file (firmware). The circuitry can be adjusted by simply loading a new firmware onto the FPGA. This technology keeps the component development time and cost low, but at the trade-off of higher price per chip and lower radiation hardness than ASICs with the same functionality. These features make FPGAs good choices for high complexity, low quantity applications like the gDPB. The Kintex 7 [74] is an FPGA with 478,000 logic blocks and a 34 MB Block Ram. The AFCK adds two standard SATA connectors as I/O interfaces to the FPGA, two high-pin count mezzanine card connectors, a Mini-USB UART JTag connector to update the FPGA firmware and a PCI-express connector to integrate the AFCK into an  $\mu$ TCA-crate. In eTOF, all 12 AFCKs are housed in a  $\mu$ TCA-crate

close to the STAR magnet, outside the magnetic field region. This crate takes care of power management, clock and trigger distribution between the AFCKs as well as providing an optical link to the FLIB (first level event selector interface board). The gDPB firmware implements the following functionalities:

- A coarse time counter for the  $160\text{ MHz}$  CBM clock.
- An extended epoch counter of 32 bits for a dynamic range of  $\approx 30.5\text{ h}$ .
- Extension of GET4Messages to from 32 bit to 64 bit words. The added information contains the address of the gDPB to allow unambiguous identification of the channel of origin.
- For epoch messages, the extended epoch of the gDPB is included and a flag if the epoch number in the message diverges by more than 1 from the epoch counter of the gDPB.
- Integration of STAR trigger messages into the data stream. The STAR trigger tokens are sent by the STAR trigger system to each gDPB. The arrival time of the token at the gDPB is registered on the coarse time clock. A special trigger message, including trigger ID, STAR trigger time and CBM trigger coarse time is added to the data stream.
- Micro-slice building. A  $\mu\text{slice}$  is a self-contained data structure including hit, error and epoch messages from all FEES connected to the gDPB, as well as potential STAR trigger message from a given time interval. In eTOF, each  $\mu\text{Slice}$  corresponds to a time interval of  $1.024\text{ ms}$  [75].
- Transmission of  $\mu\text{Slice}$  via  $10\text{ Gbit}$  optical fiber to the back-end DAQ.
- Distribution of slow control commands to the corresponding FEES.
- Automatic reconfiguration and synchronization of FEES with epoch mismatches. This is triggered if an epoch message is received from a GET4 which differs in its epoch counter by more than 1 from the internal epoch counter of the gDPB. Reconfiguration takes a few seconds during which the GET4 is considered inactive.
- Activation status of each connected GET4 is logged in each epoch and added as a system message into the data stream ("pattern message").

The final hardware stage of the eTOF data acquisition chain is the FLIB (FLES interface board [76]), a custom FPGA PCI-Express card developed for the first-level event selector (FLES) of CBM. The FLIB receives  $\mu\text{Slices}$  and is directly able to transfer them to the PC memory, circumventing the bottleneck of the PC's CPU. In eTOF, two FLIB cards collect the data from six gDPBs (and six sectors respectively) in one DAQ PC (called etofin001). On this PC, the  $\mu\text{Slices}$  are merged into time

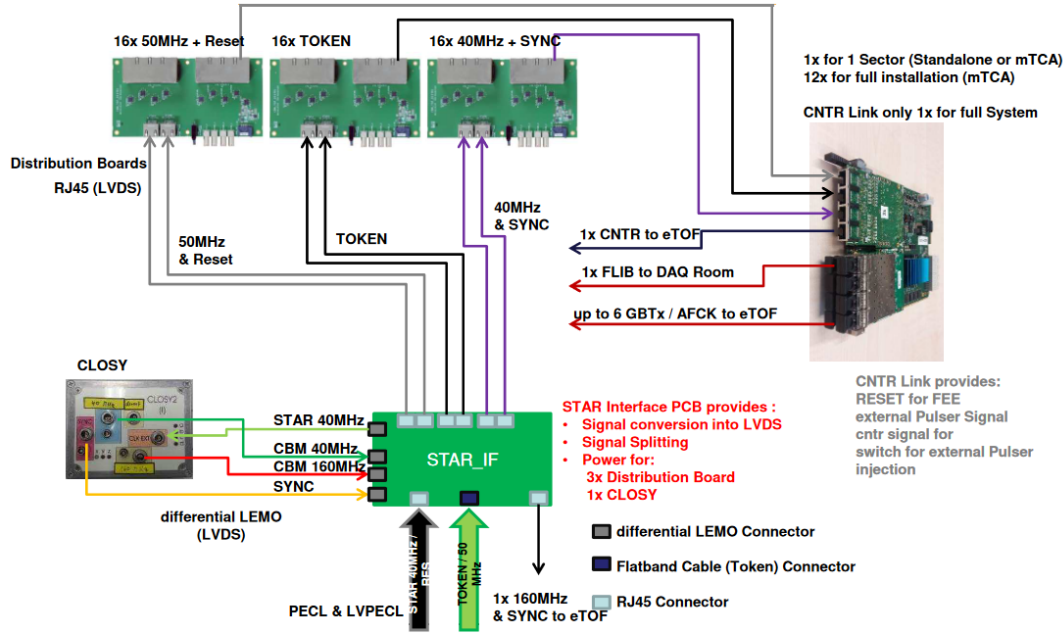


**Figure 4.19:** Scheme of the interconnections between STAR and eTOF clocking systems. With courtesy: J. Frühauf [77]

slices (TS). Time slices contain multiple consecutive  $\mu$ Slices from all gDPBs (In case of eTOF: Ten  $\mu$ slices per TS). To ensure that all events are completely contained within one TS, one  $\mu$ Slices overlaps between consecutive TS. eTOF events are build in parallel event building processes from the time slices. The algorithm for event building in eTOF is simple: When a STAR trigger token is found in a time slice, the time period of  $t_{trigger} - 2.5 \mu s < t_{message} < t_{trigger} + 0.5 \mu s$  is considered an event. All data messages, system messages and error messages from this time period as well as the trigger message are then sent to the unified STAR DAQ and included in a STAR raw event.

### 4.5.1 Timing Synchronization System

The eTOF clock system runs as a slave to the STAR main clock. A custom interface PCB provides the 40 MHz STAR clock, the STAR reset signal and the trigger token input to the eTOF system. The eTOF main clock is a CLOSY (= Clock Synthesizer) developed at GSI for CBM. It receives the STAR 40 MHz clock signal as external input. CLOSY generates a 40 MHz "CBM" clock signal, which is fed back into the interface PCB and the sync signal which is distributed directly to the FEEs on the MRPC modules. In addition to the sync, a 160 MHz external clock signal can be provided directly to the FEEs. However, this option has not been used during BES-II operation. From the interface PCB the trigger token, sync and reset signals are distributed to all the gDPBs through a set of separate distribution boards. The CBM clock is provided to a SiLabs clock generator add-on PCB on the gDPBs. This

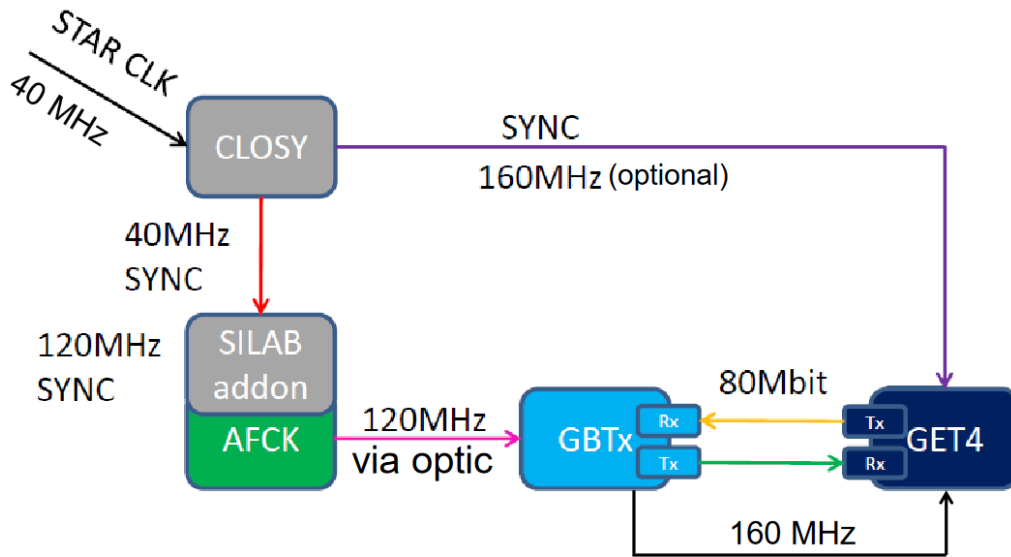


**Figure 4.20:** Schematic view of the eTOF clock distribution system. With courtesy: I. Deppner [78]

additional clock generator creates the required clock domains for the gDPB, as well as a  $120\text{ MHz}$  clock for the GBTX boards. The GBTX boards receive this  $120\text{ MHz}$  through their optical connections from the gDPB and generate a  $160\text{ MHz}$  internal clock, which is distributed to the FEEs. This clock replaces the optional external clock directly from the CLOSY. Figures 4.19 and 4.20 illustrate this system.

To further control the synchronization of the system, a pulse signal is generated from the STAR trigger token in the gDPB. This pulser signal is routed through the GBTX to the first channel of the first GET4 on each FEE card (Left side of strip 1 and right side of strip 32 on each MRPC). The signal is registered and digitized in the GET4 channel. The resulting pulser digi (see Chapter 5.2) in the data stream can be recognized due to its characteristic ToT and delayed arrival after the trigger time (see Chapter 5.3.2). Comparing the time difference between pulser digis from different parts of the system allows to analyze the electronic resolution and to detect timing shifts in between components, provided that these shifts occur on the level of at least and entire MRPC side.

## 5 Software Development and Calibrations

This chapter contains a detailed function description of the eTOF software for calibration and data reconstruction. It is also intended as a reference for future maintainers and developers. As such, it delves to a level of detail that is not required for the further understanding of this thesis. Chapter 5.1 and 5.2 will provide an overview over the STARROOT framework and the data structures for eTOF. Chapter 5.3 will provide an in-depth description of the eTOF reconstruction software, which consists of the following classes:

- StETofDigiMaker, which converts DAQ messages from individual electronic channels into StETofDigi data objects.
- StETofCalibMaker, which applies various timing and ToT calibrations to the data.
- StETofHitMaker, which merges StETofDigi objects into position-resolved hit-clusters.
- and StETofMatchMaker, which matches eTOF hits to TPC tracks.

Chapter 5.4 will finally provide an in-depth algorithmic description of the data calibration procedure for eTOF.

A simplified overview over the eTOF software is shown in Figure 5.1.

### 5.1 StRoot and StMakers

The analysis and reconstruction software of STAR is mainly based on the StRoot library, an extension of the CERN ROOT library.

StRoot has two main event structures: The "StEvent" class and the "StMuDst" class (= micro data structure). StEvent contains the full information collected by the STAR data acquisition system (as available in the raw DAQ files). It is needed for the production and calibration of STAR's raw tracking data. It contains an event header and "St[subsystem-name]Collection" objects for each subsystem. Each Collection contains again a subsystem event header and vectors of pointers to the subsystem specific detector data objects. "StMuDst" is a slimmed down version of the "StEvent" for quicker processing. The total memory size is reduced approximately by a factor of six compared to "StEvent" data. It varies from subsystem to subsystem which information is propagated into the MuDsts. The main data reduction comes from the omission of individual track points and short tracks (below 11 track points) in the TPC. For eTOF, the full event information is contained

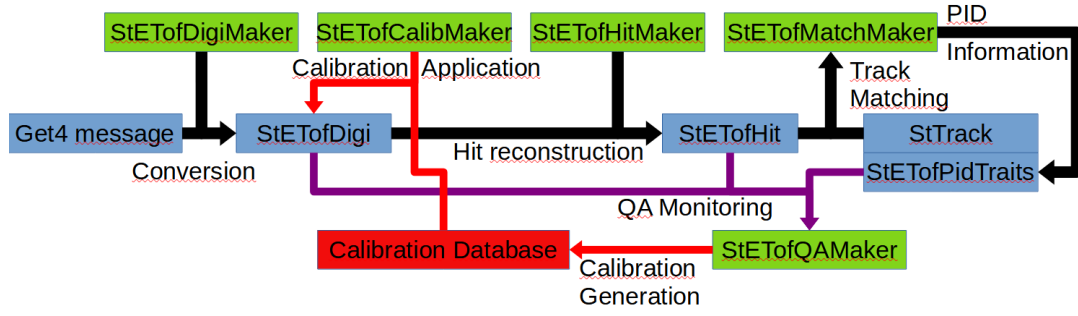


**Figure 5.1:** Simplified diagram of the reconstruction and calibration software for eTOF. Blue squares represent data containers, while Green squares represent StMaker-derived classes. Black arrows show the main data reconstruction path: GET4 data messages are converted into StEtofDigis, calibrated in the StEtofHitMaker and merged into StEtofHits in the StEtofHitMaker. The StEtofHits are then matched to StTracks from the TPC in the StEtofMatchMaker. The PID information from those matches is saved into the StEtofPidTraits attached to the tracks. Red arrows show the calibration path: StEtofQAMaker generates an extensive set of QA histograms, from which a calibration is created and stored in an SQL database. StEtofCalibMaker then reads calibration values from this database or a local file and applies it to Digis in the next iteration.

in the MuDsts, such that calibration and reproduction can always be done from the MuDst level. Additionally, the "StPicoDst" data structure exists, which is a further reduction compared to MuDsts. StPicoDsts are derived from the ROOT TTree class and do not rely on the full StRoot library, but on the independent "StPico" library. StPicoDsts are the data structure which is most commonly used in STAR physics analysis. As such, they contain primarily information useful in final analysis and neglect calibration and hardware information. This provides a significant improvement in processing time, however, re-calibrations from StPicoDst-level are usually no longer possible.

The core of the reconstruction software is the so-called "big full chain" (bfc), initialized by the macro "bfc.C". It is derived from the "TChain" class of ROOT and operates as a chain of StMaker objects on a collection of events. A "StMaker" is an object which processes "StEvent", "StMuDst" or "StPicoDst" files. It contains methods to initialize itself ("init()"), initialize specific runs("initRun(runnumber)"), process events ("make()"), finalize specific runs ("finishRun(runnumber)") and finish itself ("finish()"). The "bfc", once provided with a list of input files and a list of makers, calls the "init()" method of each maker, then opens input files and calls the "initRun(runnumber)" method for the runnumber of the current run in the current input file. Then, it loops over each event in the current input file and calls the "make()" function of each maker on the current event. Once all events in the current input file are processed, the next input file is opened. If the new input file belongs to a different run than the previous file, "finishRun(runnumber)" for the old run and again "initRun(new\_runnumber)" is called for each StMaker before

the events in the new input file are processed. Once all input files are processed, "finishRun()" for the final run followed by "finish()" is called for all makers. Then, the chain is over.

## 5.2 eTOF Data Structures

eTOF data reconstruction is processed in three steps: First, the conversion, mapping and calibration of the primary GET4 messages. Second, the merging of individual channel signals into 2-d localized hits on the detector surface. And third, the matching of hits to TPC tracks and calculation of PID traits like mass and velocity. Each of these steps corresponds to a separate data structures. "StETofDigi" for single channel signals, "StETofHit" for reconstructed detector hit and "StETofPidTraits" for the track matches. Analogue, a MuDst version exists for each of these classes, "StMuETofDigi", "StMuETofHit" and "StMuETofPidTraits" and a picoDst version for hits and pid traits, "StPicoETofHit" "StPicoETofPidTraits". The MuDst and picoDst versions only differ in some internal storage formats from the StEvent version and are functionally identical.

The StETofDigi class contains the following information (here given through the corresponding getter methods):

- rawTime(): Full GET4 time stamp including epoch time.
- calibTime(): calibrated time with offset and walk calibrations applied.
- rawTot(): GET4 ToT value in bins.
- calibTot(): gain calibrated ToT, converted to nanoseconds.
- sector(): sector of the MRPC of origin, corresponding the STAR TPC sectors. Starting with sector 13 at the top and counting up counter-clockwise.
- zPlane(): Z-Plane of the MRPC of origin, corresponding to the module inside the sector. Module 1 is the center module of the sector, closest to the interaction point. Module 2 is counter-clockwise, Module 3 is clock-wise of the sector center.
- counter(): MRPC of origin inside the module. Counter 1 is closest to the beam-line, counting outwards.
- strip(): MRPC read-out strip of origin. Strip 1 is closest to the beam-line, counting outwards.
- side(): side of the MRPC strip of the GET4 channel of origin. Side 0 is clockwise of the detector center when looking from the interaction point, side 1 is counter-clockwise.

- `elChan()`: electronic channel of the GET4 chip. Ranges from 0-3.
- `GET4Id()`: GET4 number inside the current gDPB. Ranges from 0-143.
- `rocId()`: hexadecimal address of the gDPB of origin. Maps directly to `sector()`.
- `associatedHit()`: After hit reconstruction, used as forward link (pointer) to the reconstructed hit in which this digi was used.

The `StETofHit` class contains the following information (here given through the corresponding getter methods):

- `sector()`: Analogue to `StETofDigi`.
- `zPlane()`: Analogue to `StETofDigi`.
- `counter()`: Analogue to `StETofDigi`.
- `time()`: Best estimate of the arrival time of the hit, calculated from all contributing digi times and truncated to the  $51.2 \mu s$  STAR bTOF clock range.
- `totalTot`: Total ToT of all contributing digis.
- `cluster size()`: Number of single strip hits merged into this hit. Corresponds to half the number of contributing digis.
- `localX()`: reconstructed X-position of the hit in the local reference frame of the counter. (0,0) corresponds to the center of the detector, negative X-values are closer towards the beam axis, positive X-values are further outwards.
- `localY()`: reconstructed Y-position of the hit in the local reference frame of the counter. (0,0) corresponds to the center of the detector, negative Y-values are clockwise of the center, positive X-values are counter-clockwise of the center.
- `associatedTrack()`: After track matching, used as forward link (pointer) to the `StTrack` object (TPC track) to which this hit was matched.
- `idTruth()`: For monte-carlo simulations only: track id of the true MC-track of origin.
- `qaTruth()`: For monte-carlo simulations only: fraction of ToT coming from the true MC-track, in case hits have been wrongly reconstructed from more than one MC interaction.

The `StETofPidTraits` class contains the following information (here given through the corresponding getter methods):

- `etofHit()`: Backwards link (pointer) to the matched eTOF hit.



- `thetaLocal()`: Angle of incident of the track projection onto the detector surface, relative to the detector normal. An angle of zero degree corresponds to perpendicular hit.
- `deltaX()`: Distance between projected track intersection and local hit in the local X-direction of the MRPC.
- `deltaY()`: Distance between projected track intersection and local hit in the local Y-direction of the MRPC.
- `position()`: Three-vector with the position of the hit in the global STAR reference frame.
- `timeOfFlight()`: time difference between the event start time and the time of the hit.
- `pathLength()`: Distance between the origin of the track and the tracks intersection with the MRPC surface along the helical track trajectory.
- `beta()`: relativistic calculated velocity of the particle, as fraction of the speed of light.

Additionally, each event also contains an `StETofHeader` with event-wide information. Those are (again, given through the corresponding getter methods):

- `trgGdpbFullTime()`: Time of the trigger token measured by the gDPBs (epoch and clock-cycle time, without fine time), decided by majority of gDPBs.
- `trgSTARFullTime()`: STAR clock time of the trigger token provided by the trigger token, decided by majority of gDPBs.
- `rocGdpbTs()`: maps gDPB hex addresses to the individual times of the trigger token as measured by those gDPBs.
- `rocStarTs()`: maps gDPB hex addresses to the STAR clock time of the trigger token as received by those gDPBs.
- `starToken()`: Trigger identifier of the STAR trigger token.
- `starDaqCmdIn()`: STAR DAQ command in this event<sup>1</sup>. Not used in eTOF software.
- `starTrgCmdIn()`: STAR trigger command in this event<sup>1</sup>. Not used in eTOF software.
- `eventStatusFlag()`: Indicates truncated event when maximal size is exceeded or events when parts of eTOF missed the trigger signal.

---

<sup>1</sup>compare: <https://www.star.bnl.gov/public/daq/RunControlDocs2011.pdf>

- `mismatchFlagVec()`: Vector with a flag for each GET4. If the flag is set, the corresponding GET4 was inactive during this event, either due to an epoch mismatch or an ongoing GET4 restart procedure.
- `goodEventFlagVec ()`: Vector with a flag for each Counter. If the flag is set, this counter had no inactive GET4s in this event and received valid pulser signal on both sides.

## 5.3 eTOF Data Production Chain

### 5.3.1 StETofDigiMaker

The first step of eTOF data production is the `StETofDigiMaker`. It is the only part of the chain which directly reads in raw DAQ files. DAQ files are a stream of gDPB messages already separated into events by the event builders on the eTOF DAQ PC. An event in DAQ file contains all messages in the time span of  $-2.5\ \mu s$  to  $+0.5\ \mu s$  around a received STAR trigger token. Its purpose is to convert this stream of messages into StROOT compatible data objects and generate the `StETofCollection` structure for later makers to act on. It is able to write both `StEvent` and `MuDst` files as output. Its `Init()`, `FinishRun()` and `Finish()` methods only return the success flag. `InitRun()` only initializes a hardware map to convert GET4 identifiers into sectors, modules, counters and channel. The `Make()` method generates a new `StETofCollection` object of the event and then loops over all messages in the event in the following logic:

- If the message is a hit message, convert it into an `StETofDigi` and store it into the collection
- If the message is a trigger message, store it in a temporary vector
- If the message is a system message corresponding to a GET4 status flag pattern message, convert the bit indices of the message to geometrical addresses using the hardware map and fill the corresponding entries of `mismatchFlagVec`.
- ignore all other system messages

Once all individual messages have been treated, the `StETofHeader` is filled from the temporary trigger message vector and the `mismatchFlagVec`. Afterwards, the created event is checked for memory issues.

### 5.3.2 StETofCalibMaker

Unfortunately named, the main purpose of `StETofCalibMaker` is not to make a calibration, but to apply it to eTOF data. It is the first step of eTOF data processing.

The Init() method initializes control histograms. InitRun() initializes access to calibration and geometry information from either a database or local parameter file. This information contains:

- A map from electronic channels to hardware addresses.
- A timing window setting relative to the trigger time to cut down more precisely on the interaction time then the initial  $3\mu s$  window in the DAQ files.
- Signal velocity parameters for each counters to convert time differences between both ends of a strip into a local Y-position.
- Digi time offset calibration values for each channel.
- Run-specific shifts in digi times for on counter-level.
- Digi time walk calibration values for each channel.

The make() method then applies the calibration in the following logic:

- Access StETofDigi collection and StETofHeader from file.
- Reset Digis to contain only raw information if they have been previously calibrated (The calibration usually requires multiple iterations).
- Decide on a common trigger time and run reset time based on the most common occurrences between all gDPBs. The run reset time is the measured time on each gDPB the arrival of the reset signal from the STAR bTOF clock. A reset is send at the beginning of each STAR run. Trigger time is the measured time on each gDPB the arrival event trigger token.
- Apply electronics to hardware mapping to all digis.
- Flag potential candidates for pulser digis based on their ToT value and timing relative to the trigger.
- Calculate the pulser offsets for all counters based on the pulser digi candidates ( corresponding to the method calculatePulserOffsets() ).
  - Loop over pulser candidates and find best fitting pulser digi for each counter based on the deviation in time and ToT from the nominal values for the pulser digis. Exclude the picked digis from hit building.
  - Compare time of the three pulsers inside each GBTX. Time differences between those three pulsers are saved between events. If one of them jumped by a  $6.25 ns$  coarse time clock cycle, this can be detected and corrected. If pulsers jump by different time intervals or jump frequently, they are marked as instable and ignored for further corrections. The proper time for an instable pulser is then reconstructed from the saved time differences and the other two pulsers.

- Calculate time difference between the corrected pulsers on each counter and a chosen reference pulser and compared to average values from ten previous event. 6.25 ns clock jumps of full GBTX boards are corrected this way.
- Save fully corrected pulser times for each counter.
- Fill the `StETofHeader::goodEventFlagVec()` based on the presence of both pulser digis and the absence of any mismatch flags from `StETofHeader::mismatchFlagVec()` on each counter.
- Check for potentially duplicated digis due to gDPB firmware issues and reset then to raw information. They are thus ignored by the further chain.
- For all digis inside the reduced timing window, the `calibToT` member is filled with a gain-corrected ToT.
- For all digis inside the reduced timing window, the `calibTime` member is filled with the calibrated time.
- Calibrated time contains the following corrections (each subtracted):
  - Common reset time of the run.
  - Corrected Pulser offset to reference time.
  - Calibration time offsets for each specific channel.
  - Walk calibration time offsets depending on digi ToT.

The `finishRun()` method clears the intermediate storages for the calibration and geometry information. The `finish()` method only writes the collected QA histograms to a separate histogram output file.

### 5.3.3 StETofHitMaker

The third step of the reconstruction chain is the `StETofHitMaker`. Its purpose is to relate the FEE signals in form of digis to geometrical particle crossing positions and times. The algorithm for the reconstruction of `StETofHits` has been adapted from the procedure developed by Norbert Herrmann for CBM over the recent years. It consists of two major steps: Matching of digi pairs on both sides into single strip hits and combining hits close in time and position into clusters. Additionally, an algorithm to detect and correct clock jumps of individual GET4s has been implemented.

In detail, the makers core methods operate as following: `init()` only again initializes a set of QA histograms, which are written into a separate histogram output file at the end of the processing in the `finish()` method. `initRun()` initializes parameter access from database or local files. The relevant parameters to this maker are a cluster building radius, a software dead time, a maximum Y-position (up

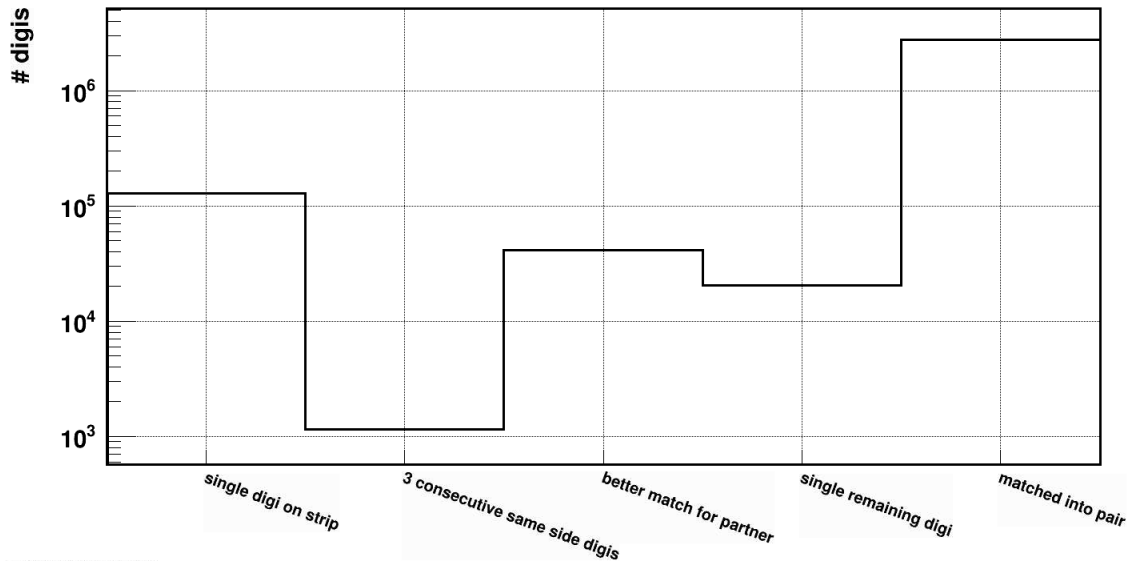


**Figure 5.2:** Distribution of Digi usage in hit reconstruction. Example of a THU counter in the  $\sqrt{s} = 7.7$  GeV FXT run in 2019.

until which a hit is considered to be correctly on the detector surface) and signal velocities for each counter. Additionally, this method also initializes a map with a preferred direction of clock-jumps for each counter.

The main hit reconstruction algorithm in the `make()` method and its sub-routines operates as following:

- Access eTOF data containers from the collection.
- Clear all existing hits from potential previous hit-building iterations.
- Fill an intermediate container mapping each strip to a vector with all digis from both electronic channels on the sides of this strip.
- `matchSides()`:
  - Loop over all strips and access the vector with digis on this strip.
  - Sort the digis in this vectors in ing order of their calibrated time.
  - While the intermediate storage vector is not empty, repeat the following steps:
    - \* If there is only a single digi on a strip or two digis from the same side for the strip , erase them, as there is no possible matching partner.
    - \* If the first two digis on the strip are from the same side, check the third digi.
    - \* If the third digi is again on the same side, erase the first digi start again with the remaining vector.

- \* If the third digi is on the opposite side, check if it is closer in time to the first or the second digi. Erase the worse fitting digi of the first two.
- \* If the first two digis are from different sides, calculate the Y-position of the resulting hit from the time difference of the two digis and the signal velocity of the counter. Is the (absolute) Y-position smaller than the allowed maximum (typically  $\pm 15\text{ cm}$  for the  $27\text{ cm}$  long strips), construct an StETofHit object with the calculated Y-position, an X-position corresponding to the center of the current strip, a cluster size on 1, the average time of both digis (modulo  $51.2\text{ }\mu\text{s}$  to match the bTOF clock range), and the total ToT of both digis. Then, save this object into an intermediate storage for the current counter, save indices of the contained digis in the original eTOF collection in a vector mapped to this hit index and erase the match digis from their temporary storage vector for the strip.
- \* If the calculated Y-position is outside the allowed maximal range, check if the third digi is a better fit of either of the first two digis. If that is the case, one digi of the first physical hit was lost. As geometrically very close physical hits with a larger time difference than the lower limit given by the digi ToT are unlikely, it is assumed that the second hit is an afterpulse of the first. Afterpulses typically occur at the same position as the primary hit. Thus, the timing of the first hit can be reconstructed from the position of the second hit and the remaining digi from the first hit. The reconstructed first hit is saved as above and all three digis are erased all three from the intermediate storage vector.
- \* If the third digi is not a better fit for either of the first two, check if the first two digis could form a hit on the detector surface under the assumption that one of the GET4s on either side incurred a clock jump by  $6.25\text{ ns}$ . If that is the case, merge them into a hit as above, correct the clock-jump based on the clock jump direction map, flag the hit as clock-jump candidate by adding 100 to the cluster size, and erase the two digis afterwards. The clock jump direction map is by default set to assume backwards clock jumps (corresponding to missed clock edges) for each GET4. It is updated at run-time by StETofMatchMaker based on the observed timing of eTOF hits which are flagged as clock jumps and matched to TPC tracks (see Chapter 5.3.4).
- \* If neither of those two checks allow to create a valid hit, still merge them into a hit (as they will not have better alternatives) under the implicit assumption that further calibration steps will shift the hit to the correct position.

Figure 5.2 shows an example distribution how digis fall into the categories mentioned above.

- `fillUnclusteredHitQA()`: If the QA flag for StETofHitmaker is set, fill QA histograms based on the side-matched unclustered hits produced so far.
- `mergeClusters()`:
  - Access the intermediate storage vectors with single strip hits for each counter. As the previous loop over strips in match sides processed the strips in ascending order, the hits in those storage vector are also ordered in ascending order of strips (or X-position respectively).
  - While there are hits in the intermediate storage vector of a counter, repeat the following steps:
    - \* Start with the first hit and take it as basis of a cluster.
    - \* If the next hit is on an adjacent strip, compare the time difference and position difference between the two hits to the maximum cluster building radius. If  $\sqrt{(\delta Y/v_{sig})^2 + \delta t_{hit}^2} < r_{max,cluster}$ , merge them into one hit. The cluster size is incremented, the total ToT of both hits added and time X-position and Y-position are averaged, weighted with the ToT contribution of both hits. Then, merge the vectors of contained digi indices erase the second hit from the intermediate storage.
    - \* Continue with the next hit. Check again if it this hit fits into the cluster as above, until a hit is found that does not fit to the cluster.
    - \* Once a next hit does no longer fit into the current cluster, write the completed cluster hit into the final StETofHit collection and erase it from the temporary storage vector.
    - \* Then, continue with the next hit to form a new cluster.
- `assignAssociatedHits()`: After reconstructing the hits, loop over all hits, access the vectors with associated digi indices, access each digi and set the pointer to the associated hit.
- `fillHitQA()`: If the QA flag for StETofHitmaker is set, fill QA histograms based on the final hits.

The hit building algorithm has to be redone after each calibration step to take the updated digi calibrations into account and potentially adjust the matching of digis into hits as well as the cluster building.

### 5.3.4 StETofMatchMaker

The final step of the eTOF data reconstruction is the matching of eTOF information to TPC tracks. This is handled in the StETofMatchMaker class. The code is adapted from the StBTofMatchMaker class. Internally, StETofMatchMaker uses an additional data structure, StructETofHit, to combine StETofHits information and information about track intersections with the eTOF plane. It contains the following data members:

- sector. Sector of the contained hit or intersection.
- plane. Module/z-plane of the contained hit or intersection.
- counter. Detector number inside the module of the contained hit or intersection.
- strip. Strip of the contained hit or intersection. Used for internal indexing of hits and intersection.
- hit time. Calibrated time of the contained hit.
- localX. Detector-local X-position of the contained hit or intersection. Contains the local position of the hit after matching hit and intersection.
- localY. Detector-local Y-position of the contained hit or intersection. Contains the local position of the hit after matching hit and intersection.
- tot. Time over threshold of the contained hit.
- cluster size. Cluster size of the contained hit.
- index2ETofHit. Index of the contained StETofHit hit in the event/MuDst collection.
- globalPos. Three-vector of the position of the contained intersection in the global STAR reference frame.
- trackId. Id of the intersecting global track.
- theta. Angle between the track extrapolation at the intersection and the normal of the detector.
- matchFlag. Flag to record the ambiguity of matching. 1 - One to one match, no ambiguity. 2 - Multiple hit candidates for a given track. 3 - Hit in overlap region. Multiple hit candidates one different counters for the track.
- deltaX. Distance between hit and intersection in local X direction.
- deltaY. Distance between hit and intersection in local Y direction.



- `isPrimary`. Flag set if the track is a primary track.
- `beta`. Velocity of the particle as fraction of the speed of light.
- `pathlength`. path length along the projected track helix from the primary vertex to the intersection.
- `tof`. Time of flight of the particle between event start time and the time of the hit.

As in the other eTOF makers, `init()` initiates control histograms which are written to a separate output file in `finish()`. `InitRun()` initializes matching parameters (track cuts on low momentum, number of TPC track points, fraction of track points included in the fit and maximal matching distances in X and Y direction, maximum Y-position of hits) and STAR geometry information from database or local files. If `StETofHitMaker` is used in the same chain, it also sets a pointer to the instance of the `HitMaker`. The `make()` method handles the matching of tracks to eTOF hits in eight steps and corresponding sub-methods (the alphabetical enumeration matches the one in the code and control histograms):

- Clean up any previously created `StETofPidTraits` and create a map of primary tracks to their respective global track version.
- A. `readETofDetectorHits()`. Loop over all eTOF hits and check if their Y-position is within the set maximum to be considered physical hits on the detector. Then, copy the information of the valid hits into a `StructETofHit` and push those into an intermediate hit storage vector.
- B. `findTrackIntersections()`.
  - Loop over all tracks and apply track cuts (in the `validTrack( StTrack )` method) based on pseudo-rapidity, momentum, TPC hits per track and TPC hits used in the track fit.
  - Extrapolate the remaining tracks to the eTOF plain (`extrapolateTrack-ToETof()`). The track extrapolation along its helical trajectory is handled in the `StHelix` class. The `StETofGeometry` class handles intersecting the helix with the eTOF counter planes and conversion for the global intersection point into the counter local coordinate frame. The `StETofGeometry::helixCrossCounter()` method fills vectors crossed geometry node ids, local and global crossing points, incident angles and path lengths for each track.
  - Fill an intermediate intersection storage vectors with intersections in form of `StructETofHit` objects.
- C. `matchETofHits()`. Loop over the storage vector of hits. For each entry, loop over the storage vector for intersections. If a hit and an intersection are

on the same counter and the local distances in X and Y are smaller than the set maximum match distances, declare this pair matched. Generate a new StructEtofHit object with the information of both (as described above) and store it in intermediate match candidate storage vector.

- D. sortSingleMultipleHits(). This step resolves the cases of one hit being matched to multiple tracks. First, copy the match candidate storage vector. Then, loop over the match candidates and copy all matches to the same track as the first one into an temporary storage vector. Then, erase them from the copied match candidate storage vector. Then, loop over the temporary storage vector and find the match candidate with the smallest deviation  $d = \sqrt{\delta X^2 + \delta Y^2}$  between hit and intersection. Push this best match into a storage vector for single track matches and erase all other candidates. Repeat this process until no matches are left in the copied storage vector.
- E. finalizeMatching(). This step resolves the remaining disambiguities in the matching, when more than one possible match candidate exists for a single track. First, copy the single track match storage vector. Then, again, copy those matches that match to the same track as the first one to another intermediate storage vector and erase them from the copied vector. Then find the match with the smallest deviation  $d$  between hit and intersection. Push this best match into a storage vector for final track matches and erase all other candidates. If there is exactly one candidate for a track, assign matchflag 1 to the match. If there are multiple possible matches to a track, assign matchflag 2 and if there are matches on different counters, assign matchflag 3 (overlap hit). Repeat this process again until no matches are left in the copied storage vector. The possibility to use TPC dEdX information to determine the best match in this step has been explored. In this case, the tof and specific energy loss of match candidates would be compared to eight particle hypotheses (electron, pion, kaon, proton, deuteron, triton, Helium-3 and Helium-4). If for at least one hypothesis, dEdX and TOF information matches, this match would be preferred over matches with closer distance but no matching particle information. This option has shown negligible effect on the purity of the matching in Monte-Carlo simulations and was thus omitted in the production version.
- F. fillPidTraits(). This step fills the StEtofPidTraits object which will be stored in the output file. The StGlobalTrack is accessed, the information of the StructEtofHit is copied into the StEtofPidTraits object attached to the track and a link to the matched StEtofHit is set.
- G. calculatePidVariables(). The time of flight of the match is calculated from the time of the hit and the event start time. From the TOF and the path length between primary vertex and intersection, the relativistic velocity  $\beta$  is calculated. The StEtofPidTraits are updated with this information.

- `H. fillQaHistograms()`. In this step, QA histograms on the final PID traits are filled (in addition to intermediate process QA histograms which have already been filled in the previous steps). Additionally, the timing of hits with a cluster size over 100 (flagged as clock-jump candidates in the `StETofHitMaker`) is also monitored. For these hits on each counter, a distribution of the difference between the measured time of flight and the expectation from the track momentum and a pion mass hypothesis ( $tof - tof_\pi$ ) is monitored.
- `checkClockJumps()`. Once sufficient statistics has been accumulated in the clock jump monitoring histogram, this method checks the  $tof - tof_\pi$  distributions. Depending on whether there are more counts in the time region corresponding to a clock-jump forward or backwards in time, the clock-jump direction map is updated and propagated to the `StETofHitMaker` (see Chapter 5.3.3).

## 5.4 Calibration Algorithms

eTOF data require extensive calibration before they are ready to use in physics analysis. This section will describe the calibration chain and the various effects which are corrected in the calibration process. These effects are partially interconnected or can only be seen clearly once more dominant effects are corrected. For this reason, the calibration procedure has to be iterative. For each iteration, the chain consists of four steps:

- Running of the data reconstruction chain as described in the previous section.
- Creation of a QA file in `StETofQAMaker`.
- Creation of a calibration file out of the QA file with the ROOT script `calibrate_etof.C`.
- Application of this calibration file in `StETofCalibMaker` during next iteration of the calibration.

### 5.4.1 StETofQAMaker

`StETofQAMaker` is another `StMaker` class. However, it is not part of the reconstruction chain. Instead, its purpose is to be a central collection of calibration and control histograms. In its `init()` method, in the order of 10,000 control histograms are created. The `initRun()` method, geometry, signal velocities and alignment information is accessed from the data base. Additionally, containers for run-specific observables are reset. Subsequently, the histograms are filled in the `make()` method with information from the previously calibrated digis, reconstructed hits and matched PID traits. The range and binning of the calibration histogram changes in between

the calibration steps. In early calibration steps, control histograms are typically very wide to capture outliers. In later calibration steps the histograms (and the corresponding fits) narrow down for more fine-grained corrections. The `finishRun()` method of `StETofQAMaker` fills histograms with run-specific information. The `finish()` method finally write an output file containing all the QA histograms.

### 5.4.2 `calibrate_etof.C`

`calibrate_etof.C` is the ROOT macro in which the QA histograms from `StETofQAMaker` are fitted to extract calibration values. This macro also creates the calibration files which are read by `StETofQAMaker`. It takes a QA file from `StETofQAMaker` and a previously created calibration file as input . If no calibration file is provided, a new one is created. The previously created calibration file has to contain the calibration which was already applied to the data from which the QA histograms were created. Furthermore, it also creates a output calibration file. It reads the current calibration step from the input calibration file (or starts at the first one if no input calibration file exists) and then performs the next calibration step in one of six calibration modes. A user-adjustable array defines which calibration mode is used in which step. The six calibration modes are:

- Mode 1: Average based position and ToT gain calibration.
- Mode 2: Single channel walk calibration.
- Mode 3: Counter-averaged timing calibration.
- Mode 4: Counter-averaged walk calibration.
- Mode 5: Single strip timing calibration.
- Mode 6: Box-fit based position and ToT gain calibration.

The different calibration modes will be explained in more detail in the following sections. In each of this modes, a specific type of QA histogram is inspected. Depending on mode, these histograms are available for each counter, strip or channel. The corresponding calibration offsets are extracted from those histograms and added to the previously determined calibration offsets from the input calibration file. The resulting total value is then stored in a calibration histogram and saved in the output calibration file.

Typically, calibration starts with two iterations of mode 1 with decreasing histogram scale to get the hit positions well enough under control to allow for track matching. Then, mode 3 is used to remove the coarse timing offsets between eTOF and the STAR clock. Afterwards, mode 5 and 6 are alternated until the timing and position are well enough under control that a counter-average walk calibration can be applied with mode 4. If sufficient statistics is available, the calibration can be improved by alternating modes 2, 5 and 6. The sequence will fine-tune the walk

correction for each strip (mode 2), ensure that ToT-averaged timing of each strip is unchanged (mode 5) and correct the small position shifts introduced by the walk calibration (mode 6). Separating timing offsets from walk corrections in this way allows to apply high statistics walk calibrations to data samples with insufficient statistics.

### 5.4.3 Position Corrections

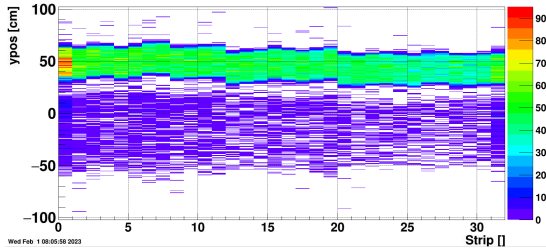


**Figure 5.3:** Position calibration histogram of an example counter before position correction. The Y-position of hits on the detector is shifted from their nominal position ( $-13.5 \text{ cm} < y < 13.5 \text{ cm}$ ) due to cable length differences and clock phase differences. A number of hits are incorrectly reconstructed closer to  $y = 0$  as the reconstruction algorithm favors such positions in case of ambiguities.

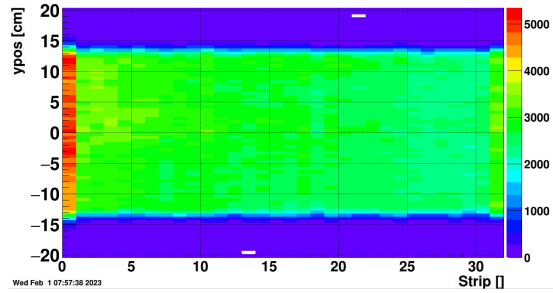


**Figure 5.4:** Hit position distribution of an example counter after calibration. Hit positions are mostly confined to the nominal counter width of  $-13.5 \text{ cm} < y < 13.5 \text{ cm}$ . The first strip has an increased counting rate as it picks up avalanches where the glass plates are extended to the left for the high-voltage connection.

The first step towards calibrating eTOF data is always correcting the reconstructed hit positions. This is necessary early on to allow for a successful track matching. Only with matched tracks, absolute time calibrations can be done. The reconstructed position of hits on a example counter before calibration can be seen in Figure 5.3. In this histogram, the range from  $-13.5 \text{ cm} < y < 13.5 \text{ cm}$  is where the physical surface of the detector is placed in the geometry. One can see that the main distribution of the detector hits are shifted from the center by about  $50 \text{ cm}$ . The shift also varies slightly between the strips of the counter. Two major effects shift cause this shifting of the hit: The major shift of all detector hits is caused by a clock phase between the two gDPBs to which the two sides of the detector are connected. The shifts between individual strips are due to slight differences in the signal path length due to cabling and signal routing on the FEE PCB. One can also observe a low background between  $-50 \text{ cm} < y < 30 \text{ cm}$ , which occurs due to the hit reconstruction algorithm preferring digi pairs with a smaller time difference to construct hits. In calibration mode 1, the calibration offset value is simply the mean of each bin (= strip) of this histogram. This shifts the main hit distribution

close to zero, so that the histogram range can be reduced without the danger of outliers falling through the scheme. The disadvantage of this simple approach is that, if the distribution of hits along the strip is inhomogeneous, the average is not precise enough to align the strips with a resolution below 1 cm. Thus, for the fine calibration in calibration mode 6, a modified box function is fitted to the projection of the hit distribution along each strip:

$$f(y) = N \cdot (\text{erf}(y+y_0-d/2) \cdot \text{erf}(y+y_0+d/2)) \cdot \text{pol2}(y, a, b, c) + \text{pol2}(y, d, e, f) \quad (5.1)$$

Here,  $y$  is the Y-position along the strip,  $\text{erf}$  is the error function,  $y_0$  is the center of the box and  $d$  is the width of the box and  $N$  is the average height of the box. The first, multiplied, second-order polynomial  $\text{pol2}(y, a, b, c)$  modifies the top of the box to allow for some inhomogeneities in the hit distribution on the counter. The second, added, second-order polynomial  $\text{pol2}(y, d, e, f)$ , allows to describe some background from wrongly reconstructed hits outside of the edge of the counter. The box center parameter  $y_0$  is used as the calibration offset value. Yet, even with this complex fitting function, the fit only converges reliably if proper starting parameters are set. This is the reason, a coarse calibration in mode 1 has to be done first to get the offset close to its final value. Figure 5.4 shows the result of the position calibration. The strip centers are aligned within approximately 1 mm (see Figure 5.5).

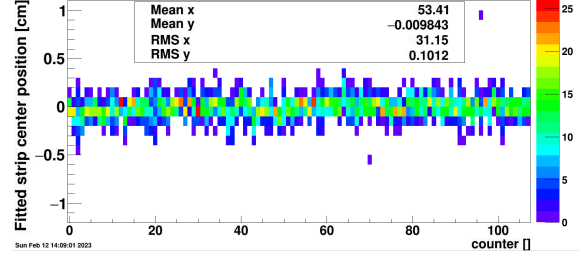


**Figure 5.5:** Fitted strip centers for each counter after position correction. Each entry for one counter bin corresponds to a single strip on that counter. The RMS for the alignment between strips is around 1 mm

#### 5.4.4 Timing Corrections

Time measurements have no inherent meaning without a point of reference. In STAR, the reference point for timing measurements is the start time  $t_{start}$ . It represents the time of the collision in each event. The start time is constructed either by the VPD or the bTOF (startless mode). The VPD uses the time difference between very forward and very backward particles. These particles can be assumed to be spectators of the collision and thus having a velocity close to the beam velocity. At high energies for STAR (above  $\sqrt{s_{NN}} \approx 50$  GeV), this system can provide a start time resolution of  $\approx 50$  ps. At the lower energies in BES-II, STAR is operated in the so-called startless mode. In this case, matched tracks which can be identified by the  $dE/dX$  and momentum measurements of the TPC (and thus have a known velocity) are used to extrapolate back to the time of the collision at the vertex.

eTOF is operated on a separate clock system and thus, time differences to the start time are not meaningful without calibration. The largest effect which has to

be corrected is the time delay between the reset of the two clocking systems. As the eTOF clock system runs as a slave of the bTOF clock system, the reset signal at the beginning of the run arrives with a significant delay. This shift can be as large as several hundred nanoseconds (See Figure 5.6). While the delay is similar across most of the eTOF system, it is prudent to correct it on a counter level to also correct the smaller time shifts between individual eTOF counters.

Previous calibration schemes for CBM-TOF detector tests relied on three or more layers of MRPCs to solve the equation system for time shifts of all involved counters and track velocity. This approach is impossible in STAR as eTOF consists for most part only of a single layer of detectors. The alternative approach used for eTOF uses the momentum information of the TPC and assumes a pion mass hypothesis for all tracks to calculate an expected velocity. From this expected velocity, an expected time of arrival at the eTOF plane can be calculated:

$$tof_{\pi} = \frac{L}{c} \cdot \sqrt{1 + \frac{m_{\pi}^2}{p^2}}, \quad (5.2)$$

where  $L$  is the path length from the vertex along the extrapolated track until the intersection with the eTOF detector plane,  $c$  is the speed of light,  $m_{\pi}$  is the pion mass and  $p$  is the momentum measurement from the TPC. Figure 5.7 shows difference between this expected pion time of flight and the measured time of flight for all tracks on an example counter as function of the track momentum.

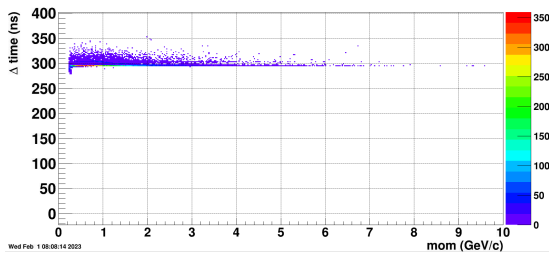


**Figure 5.6:** Difference between measured time of flight and expected time of flight with a pion mass hypothesis for matched tracks on an example counter as function of momentum. This figure shows the raw time differences before calibration. A major offset due to the reset delay can be observed.

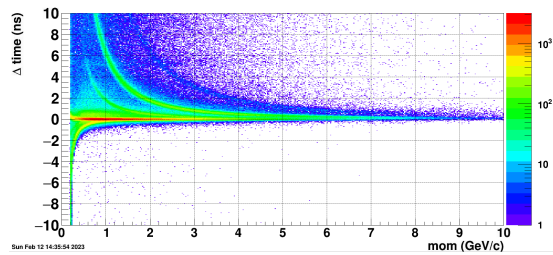


**Figure 5.7:** Difference between measured time of flight and expected time of flight with a pion mass hypothesis for matched tracks on an example counter as function of momentum. This figure shows the time differences after coarse calibration. The actual pions are seen as a horizontal line at zero time difference. Electrons, kaons, protons and deuterons are visible as curved lines, merging with the pion line for higher momenta.

Since actual pions make up by far the largest fraction of the particle cocktail in a collision at BES-II energies, the pion peak in this distribution can be used to

determine the calibration offsets. For a coarse calibration (calibration mode 3), simply the position of the maximum bin of this distribution (projected onto the Y-axis) is used as calibration offset.

For the finer calibration (calibration mode 5), simply picking the maximum bin of the distribution is no longer sufficient as the targeted alignment is better than peak width. The peak has to be fitted with a Gaussian distribution. In order to obtain an approximately Gaussian peak shape that can be reliably fitted, only tracks in the momentum range of  $0.5 \text{ GeV}/c < p < 3 \text{ GeV}/c$  are considered. This cut ensures that the low-energy region with multiple scattering and high energy loss is excluded and that protons are still well separated from the pion peak. Kaons merge into the pion peak for momenta above  $1 \text{ GeV}/c$ , but their lower production yield ensures that the resulting distortion of the peak shape is small. At this level, it is also no longer sufficient to apply this calibration at the counter level. Time offsets between individual strips have to be corrected as well. Figure 5.8 shows the offsets for the strips of an example counter after coarse calibration, but before fine calibration. Time shifts of up to  $200 \text{ ps}$ , mainly due to signal path length differences between FEE channels, can be observed.

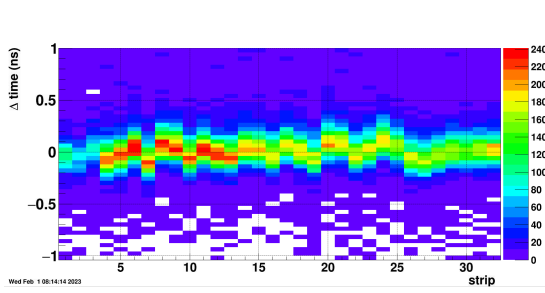


**Figure 5.8:** Difference between measured time of flight and expected time of flight with a pion mass hypothesis for matched tracks on each strip of an example counter. Track momentum is restricted to the range of  $0.5 \text{ GeV}/c < p < 3 \text{ GeV}/c$ . This figure shows the time differences after coarse calibration. Significant offsets between the different strips can be observed.

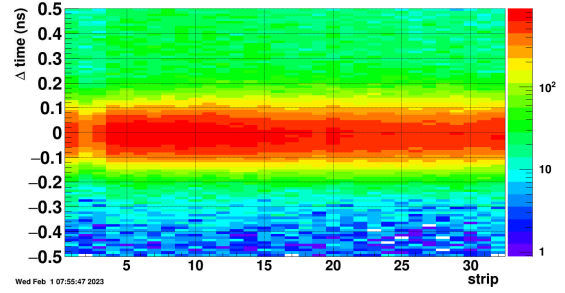


**Figure 5.9:** Difference between measured time of flight and expected time of flight with a pion mass hypothesis for matched tracks on each strip of an example counter after calibration. Track momentum is restricted to the range of  $0.5 \text{ GeV}/c < p < 3 \text{ GeV}/c$ . The alignment of the peaks is better than  $10 \text{ ps}$  RMS.

The calibration offset for the fine calibration is determined as the center of a Gaussian fit around the pion peak. To ensure that the fit is not disturbed by the kaonic tail towards higher time differences, the fit range is restricted to a small region around the maximum. Figure 5.9 shows  $\text{tof} - \text{tof}_\pi$  of each strip of the same example counter after fine calibration. The alignment of the timing peaks is better than  $10 \text{ ps}$ .



### 5.4.5 Walk Corrections

The time walk (or slewing) effect is a feature of any constant threshold discriminator such as PADI. Smaller signals are registered with a larger delay compared to larger signals due to their slower signal growth before reaching the threshold (compare Figure 5.10). Walk correction is the final, most delicate step of the eTOF calibration. Without it, eTOF can reach a system time resolution below  $120\text{ ps}$ , but it is needed to push the system toward the target resolution of  $80\text{ ps}$ .

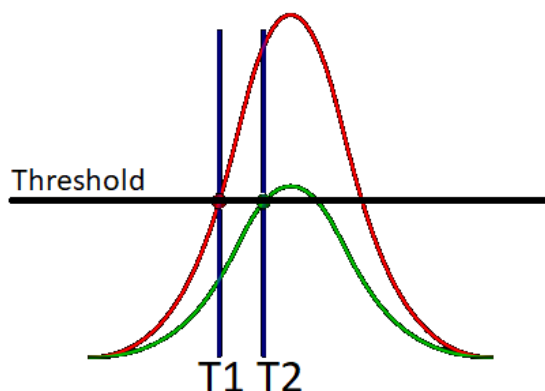


**Figure 5.10:** Visualization of the time walk effect. When discriminated at a constant threshold, larger signals are detected earlier (T1) than smaller signals (T2), even if the signal development started at the same time. Adapted from: [79]

For the calibration, the walk effect translates to a dependence of the measured digi time on the time over threshold of the digi. The time of a digi also depends on the Y-position of the initial hit (i.e. the signal travel time along the strip). When correcting for this effect, one relies on the reconstructed Y-position of the hit, which depends on the time of the digis of both sides. Thus the walk delay is also influenced by the walk delay of the opposite digi. If both digis on the two sides of a strip have similar ToT, this is not an issue. However, for hits with largely different digi ToT, this leads to a smearing of the observed dependency. In practical terms, the walk correction histogram shows the difference between reconstructed time of the hit and the pion expectation ( $tof - tof_\pi$ ) depending on the ToT of the digi on one side of the detector. An example can be seen in Figure 5.11.

The same track selection criteria apply as for the timing in calibration mode 5. The determination of the calibration offsets in the walk calibration is done in a similar way to the strip-wise time calibration: The time offset distribution is for each bin in ToT is fitted with a constrained Gaussian function around the maximum. The center parameter of this Gaussian function is used as calibration offset. A walk offset is stored for 25 ToT bins for each channel. As the time walk effect depends on the analog pulse shape and pre-amplifier gains vary slightly from channel to channel, the walk correction in principle has to be done for each channel separately. However, determining the offsets for each channel requires high statistics, more than typically available in a calibration pre-production. Thus, the determination of the walk offset is done in two granularities: In calibration mode 4, all matched tracks from one counter are included in the calibration histogram and the same offsets are applied to all channels. In calibration mode

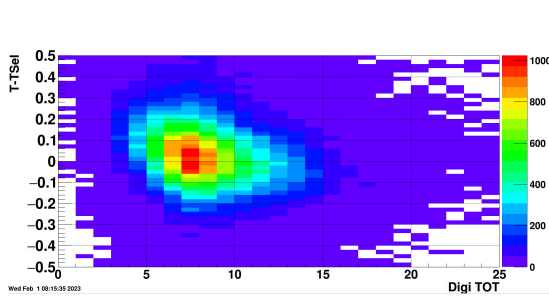


**Figure 5.11:** Counter-averaged walk effect before calibration for an example counter. On the X-Axis, the raw ToT of single digis in GET4-bins (corresponding to 200 ps/bin) is plotted. The Y-Axis shows  $tof - tof_\pi$  for the associated hits. An histogram entry is filled for each digi in a hit.

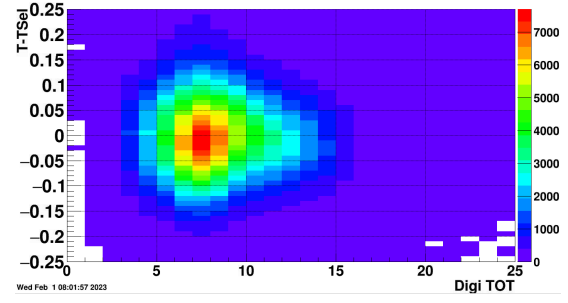


**Figure 5.12:** Counter-averaged walk effect after calibration for an example counter. On the X-Axis, the raw ToT of single digis in GET4-bins (corresponding to 200 ps/bin) is plotted. The Y-Axis shows  $tof - tof_\pi$  for the associated hits. An histogram entry is filled for each digi in a hit. Post-calibration RMS of the Gaussian fit center parameters is  $\approx 10$  ps

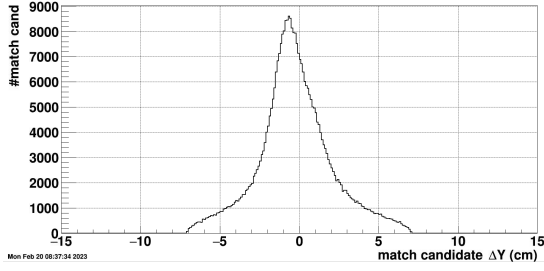
2, a calibration histogram is filled for each channel separately. A full channel-by-channel walk calibration can be done with the full production of one dataset and then applied in a later reproduction or future datasets. As the walk effect is a pure hardware feature it is not assumed to change between datasets, assuming the timing correction is well separated. For datasets where this is not possible, the counter-averaged walk calibration provides a serviceable alternative with only a minor trade-off in performance.

### 5.4.6 Alignment Corrections

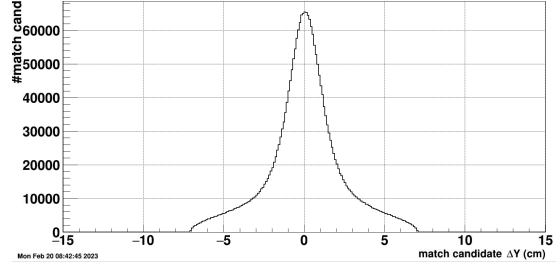
The position correction adjusts the hit positions with respect to the geometry. However, the eTOF geometry itself may still be misaligned with respect to the TPC. Such a misalignment is visible as a systematic displacement of the extrapolated track intersections from their respective hits. The extrapolation of the track towards eTOF requires momentum and magnetic field information, the alignment also depends on the calibration of the TPC and may change accordingly.

Figure 5.13 shows an example of a misaligned counter along its local Y-coordinate. The peak of the  $\Delta Y$  distribution between hit and intersection is shifted by  $\approx 1$  cm towards negative values. The track matching uses a large maximum matching distance of  $|\Delta Y| < 7$  cm to allow to match hits and intersections even on severely misaligned counters. In a separate macro, `pl_geometry.C`, the peak of this distribution is fitted with a Gaussian function and the center of this fit is used as calibration offset.

This procedure is done for each counter in X- and Y-direction. The calibration offsets are saved into a geometry database and applied to the position of the



**Figure 5.13:** Difference in local Y-position between matched hits and projected track intersections on an example counter, before alignment correction. Maximum allowed matching distance is  $|\Delta Y| < 7$  cm.



**Figure 5.14:** Difference in local Y-position between matched hits and projected track intersections on an example counter, after alignment correction. The changes in peak shape between before and after the alignment are due to the repeated matching process and other calibration (position, walk) which have been done in between.

counter upon initialization of the geometry. A constant offset in Z direction is applied for THU-type counters to adjust for a slight difference in module design that is otherwise taken into account in the geometry.

### 5.4.7 Run-by-Run Offset Calibrations

One unfortunate feature of eTOF's DAQ system is that clock phase shifts between the different DAQ electronic elements and the bTOF clock are not recovered exactly after a DAQ restart. This limits longevity of a produced calibration. In periods with frequent DAQ restarts, the available statistics between restarts may also be insufficient to produce a calibration with good quality. eTOF DAQ restarts are not visible from the data stream, but it is ensured during the beam-time that DAQ restarts can only happen in between runs. Thus, the clock phase shifts translate into timing and position shifts between individual runs, which must be corrected before statistics-intensive fine calibrations are done. It has been observed that most shifts occur between the bTOF start time and the complete eTOF system. The second most common class of clock phase shifts occurs on the level of GBTX boards, corresponding to one side of a full module. This class of shifts also leads to shifts in the Y-position of hits on those counters. Shifts on individual counters are less common, but have been observed, nevertheless. To avoid manually disentangling those cases, the resulting correction has to be done on single counter and single run level. Figure 5.15 and 5.16 show the position and time shifts of an example counter during the 2019 FXT campaign.

The calibration offsets are determined from such histograms in a separate macro, `calibrate_RbR_offsets.C`. The correction of the hit position shifts closely follows procedure in the position fine calibration (calibration mode 6). The projection of the hit position for a single run is fitted with a box function and the center of the box

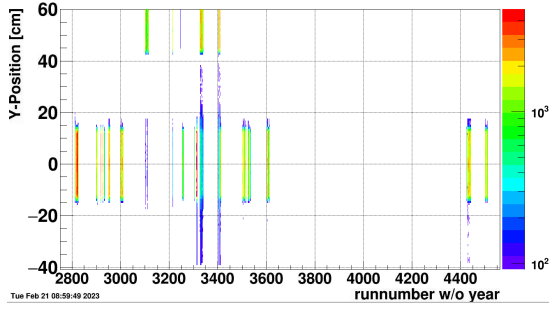


**Figure 5.15:** Hit position shifts between runs for an example counter over the course of the 2019 FXT campaign. The X-axis denotes the individual runs. The first two digits correspond to the day in the year and the later two digits to the run on that day. Empty bins on the X axis are non-existing runs. The Y-axis shows the Y-position of all hits on the counter. Bins with less than 100 entries are not shown for better readability.

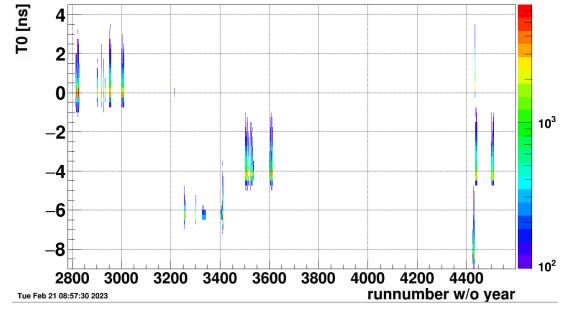


**Figure 5.16:** Timing shifts between runs for an example counter over the course of the 2019 FXT campaign. The X-axis denotes the individual runs. The first two digits correspond to the day in the year and the later two digits to the run on that day. Empty bins on the X axis are non-existing runs. The Y-axis shows  $tof - tof_\pi$  for all track matches on the counter. The Y-axis has been re-binned and bins with fewer than 100 entries are not shown for better readability.

is used as calibration offset. The time correction in turn follows the procedure for the fine time calibration (calibration mode 5). The peak of the projected  $tof - tof_\pi$  distribution for each run is fitted with a constrained Gaussian function and the center parameter from the fit is taken as calibration offset. However, due to the limited statistics available in a production sample of a single run, all tracks have to be taken into account. The run-by-run calibration offsets for both time and position are written into a calibration histogram for each run and stored in a common calibration file separate from the other calibration parameters. When committing the local files to the STAR database, a separate database entry is generated for each run and the run-specific time and position offsets are added to the global time and position offsets.

## 6 eTOF during Beam Energy Scan II

### 6.1 Datasets

This chapter aims to provide a brief chronological overview of the eTOF data-taking during BES-II. It will also document the special conditions on the detector in each run period as a reference for later analysis works.

A single sector of eTOF (sector 18) was installed during the 2018 STAR isobar run for DAQ integration tests. The full installation of eTOF was completed before the start of the BES-II campaign in November 2018. The final BES-II data taking with eTOF ended in July 2021. During this time, eTOF was included in the following STAR physics runs:

Start date	End date	Production tag	Setup	$\sqrt{s}$ [GeV]	Number of events
25.03.19	03.04.19	production_19GeV_2019	COL	19	580 <i>M</i>
04.04.19	03.06.19	production_14p5GeV_2019	COL	14.5	320 <i>M</i>
10.12.19	24.02.20	production_11p5GeV_2020	COL	11.5	230 <i>M</i>
28.01.20	29.01.20	production_31p2GeV_fixedTarget_2020	FXT	7.7	100 <i>M</i>
01.02.20	02.02.20	production_19p5GeV_fixedTarget_2020	FXT	6.2	100 <i>M</i>
02.02.20	03.02.20	production_13p5GeV_fixedTarget_2020	FXT	5.2	100 <i>M</i>
04.02.20	05.02.20	production_7p3GeV_fixedTarget_2020	FXT	4.5	100 <i>M</i>
13.02.20	14.02.20	production_5p75GeV_fixedTarget_2020	FXT	3.5	100 <i>M</i>
30.01.20	01.09.20	production_9p2GeV_2020	COL	9.2	160 <i>M</i>
29.07.20	14.09.20	production_26p5GeV_fixedTarget_2020	FXT	7.2	320 <i>M</i>
31.01.21	01.05.21	production_7p7GeV_2021	COL	7.7	100 <i>M</i>
01.04.21	28.06.21	production_3p85GeV_fixedTarget_2021	FXT	3.0	2 <i>B</i>
06.05.21	06.05.21	production_44p5GeV_fixedTarget_2021	FXT	9.2	50 <i>M</i>
06.05.21	07.05.21	production_70GeV_fixedTarget_2021	FXT	11.5	50 <i>M</i>
08.05.21	08.05.21	production_100GeV_fixedTarget_2021	FXT	13.7	50 <i>M</i>

During the STAR high-energy proton-proton campaign in 2022, eTOF participated in multiple additional runs for detector quality assurance, but it was not consistently part of the physics data taking.

## 6.2 Changes in Operation Conditions

After the full installation in 2019, eTOF was first operated at a cautious high-voltage setting of  $\pm 5400\text{ V}$  and  $\pm 4900\text{ V}$  for USTC and THU-type counters, respectively. The first data taking period of the  $19.6\text{ GeV}$  run showed a reduced efficiency due to this. On 27.03.19, the high-voltages of the USTC-type counters were raised to  $\pm 6000\text{ V}$ , and on the 04.04.19 to  $\pm 6200\text{ V}$ . This setting was kept until the end of the 2019 beam-time period. During all of the beam time in 2019, a gas mixture of 90% R134a and 10% iso-buthane was used.

On 09.04.19 (day 99) a beam loss event at RHIC during a maintenance period hit eTOF. 47 pre-amplifier channels of eTOF were permanently destroyed afterwards. Further pre-amplifier damage events on 12.04.19 and 20.04.19 destroyed approximately one-third of all pre-amplifier channels in eTOF. The MRPCs closest to the beam-line were most affected. Afterwards, eTOF was declared inoperable for the remainder of the 2019 beam-time.

In early November 2019, eTOF underwent extensive repairs. All PADI pre-amplifier boards were replaced. The new boards contain an additional ESD protection diode in parallel to the PADI input to avoid damage similar to the events in early 2019. To reduce the likelihood of electronics damage from discharges in the MRPC further, the gas mixture was also adjusted to include 0.5% sulfur-hexafluoride as additional avalanche quencher. The high-voltages of eTOF detectors were consequently adjusted to  $\pm 6300\text{ V}$  for USTC-type MRPCs and  $\pm 5200\text{ V}$  for THU-type MRPCs. This high-voltage setting was maintained for the remainder of BES-II.

eTOF performed stably during the  $11.5\text{ GeV}$  collider run in 2020 and the FXT program in spring. However, on 19.02.20, another beam event occurred. Unlike 2019, pre-amplifier channels were not completely destroyed, but continued to function at a reduced efficiency. A more extensive look at these beam events will be taken in Chapter 6.3. eTOF's effective efficiency remained constant during the  $9.2\text{ GeV}$  collider run. A final pre-amplifier damage event occurred on 09.09.20. Approximately 15% of all eTOF pre-amplifier channels showed various degrees of reduced efficiency afterwards.

During the 2021 beam time, eTOF was operated under the same conditions as in 2020 and performed consistently. No further damage events occurred during this beam time. However, control runs in 2022 show significant further deterioration of the pre-amplifiers during STAR's  $200\text{ GeV}$  collider beam time.

## 6.3 Pre-Amplifier Damages

As mentioned in Chapter 6.2, eTOF's PADI pre-amplifiers suffered multiple damage events.

### 6.3.1 2019 PADI Damage Events

During April 2019, multiple successive beam-related events fully destroyed approximately one-third of all pre-amplifier channels. Figures 6.1 to 6.4 show the state of the eTOF system as seen from the online run monitoring plots. The STAR online run monitor automatically samples between 1000 and 2000 events from each run and processes them during runtime to generate overview histograms to assess the state of all sub-detectors.

The shown histograms depict the number of digis in each channel of eTOF in the run sample, so-called digi density plots. Unrelated to the pre-amplifier damage, certain GBTX (empty columns in the digi density plots) and FEE cards (1/3 empty columns in the digi density plots) had to be disabled due to synchronization problems.

The damage event on 09.04.2019 can be clearly correlated with an "unexpected beam abort" in RHIC as noted by the shift crew in the STAR electronic shift log:

"- At 7:10am, while ramping up voltages in our detector for the current fill(RHIC Fill # 22970), "unexpected beam abort" happened. We then brought down the detectors. "[80]

The shift crew further noted:

[...] "we noticed some single channels on the digi density plot that had either 0 counts or far too many." [80]

These single empty, almost empty or hot channels can be clearly seen in the digi density plots over the following days (see Figure 6.2). The majority of those damaged channels are on the counters closest to the beam-line (channels 1-32 on each GBTX). The hot channels were disabled in the following days to avoid DAQ issues due to the high channel rate.

Also the second damage event, on 12.04.2019, is related to a beam abort. The shift crew noted:

"MCR<sup>1</sup> lost the beam before a planned dump. They need access for repairs of the problematic injector. [...] During the unexpected beam dump a few minutes ago all HV regions in the ETOF tripped off except region 4 negative." [80]

Figure 6.3 shows the state of the system after this second damage event. The MRPCs closest to the beam (lower third of the histogram) are severely damaged. In addition to a large number of empty channels, the density of digis on the remaining channels in this region is varying by one order of magnitude. As the incoming particle rate should be constant across regions of equal pseudo-rapidity (which closely translates to the channel number in GBTX), such a fine-grained

---

<sup>1</sup>MCR = machine control room

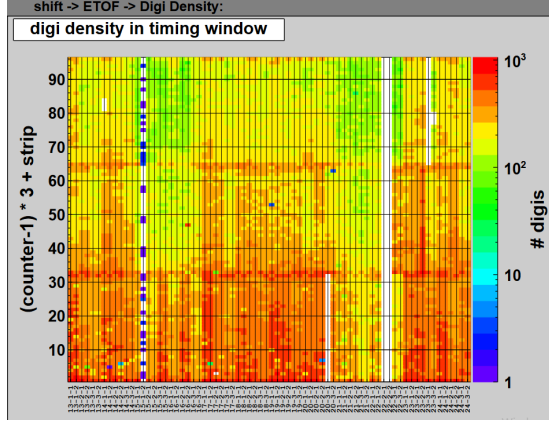


Figure 6.1

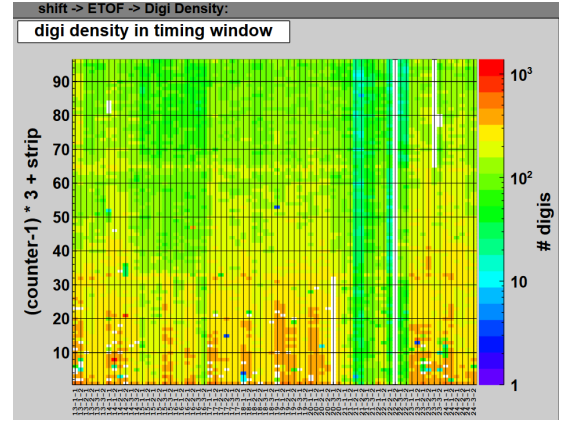


Figure 6.2

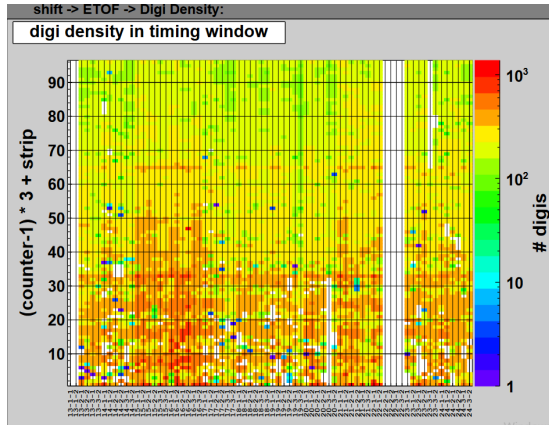


Figure 6.3

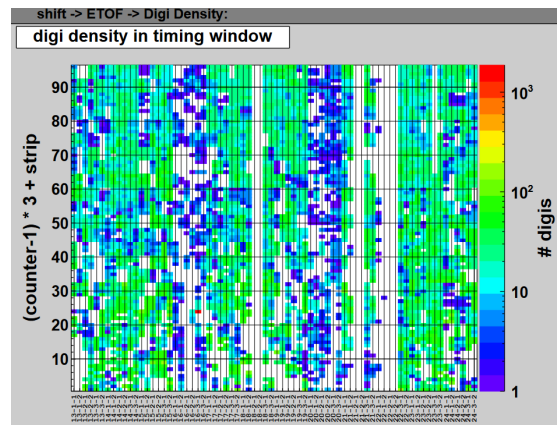
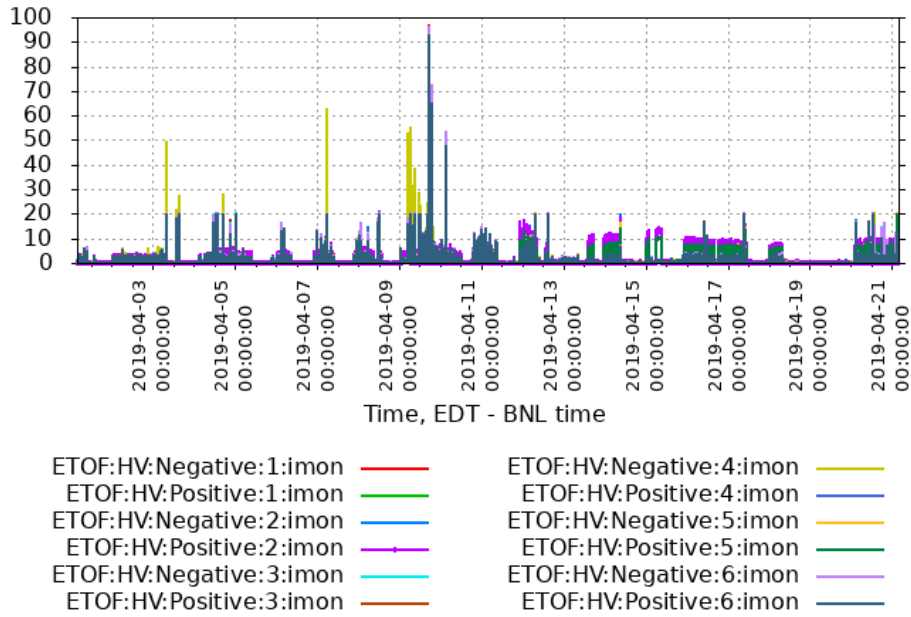


Figure 6.4

"Digi density" plots from eTOF online monitoring, showing the number of digis on each channel of eTOF in a sample of 1000-2000 events for each run. X-Axis: GBTX address, given as sector-module-side. Y-Axis: Channel number inside GBTX. **Figure 6.1:** Example run from 05.04.19, before damage events. **Figure 6.2:** Example run from 10.04.19, after first damage events. **Figure 6.3:** Example run from 14.04.19, after second damage event. **Figure 6.4:** Example run from 20.04.19, when eTOF was declared non-operational.





**Figure 6.5:** Current at each eTOF HV supply unit during the time period of the 2019 PADI damage events in mA.

high variance cannot reflect actual particle flux. It suggests a similar variance in single channel efficiency. Indeed, the most affected counters have also shown a significantly reduced track matching efficiency. The counters furthest from the beam are much less affected, but a significant variance in digi density can also be seen here.

In the early morning of 20.04.2019, the shift crew noted another beam dump event:

"Cathode and Anode on TPC tripped due to an unexpected beam dump. For cathode: ramped the voltage down to 0, reset the interlocks, ramped the voltage back up. Fo anode: cleared all trips, ramped voltage to 0.

eTOF tripped due to unexpected beam dump. Voltage to dropped to 0. We turn the high-voltage off and turn it on back to standby."[80]

Figure 6.4 shows the state of eTOF after this event. Approximately one in three channels are empty and a large fraction of the remainder is damaged to varying degrees. eTOF was declared inoperable for physics data taking shortly after this event.

Figure 6.5 shows the current drawn from the eTOF HV supply over the full time period of the damage events. The damage event on 09.04.2019 can be seen clearly as a series of significant power spikes. Slightly smaller spikes in the days before, however, did not lead to similar damage. The later damage events on 12.04.2019

and 20.04.2019 can be seen as series of small spikes. A large spike above  $20\text{ mA}$ , as seen in the previous event, is not observed. This is likely due to the discharge happening so quickly that internal safety fuse of the HV supply tripped, as noted by the shift crew.

After the end of the 2019 beam period, in November 2019, all PADI pre-amplifier cards have been replaced. The damaged pre-amplifiers were studied at GSI by J. Frühauf and I. Deppner. According to this analysis, the damaged channels fall into the following categories:

- Threshold control damaged and baseline voltage stuck at zero. The chip registers signals at the noise level, leading to excessive data rates.
- Threshold control damaged and baseline voltage stuck at the maximal negative setting ( $-650\text{ mV}$ ). This setting corresponds to the maximal threshold setting of PADI. Small input signals are discriminated and the efficiency of the channel is thus reduced.
- Baseline voltage stuck below the maximal negative settings. This corresponds to an even further reduced efficiency and requires more extensive damage to the chip.
- Pre-amplifier input stage destroyed. The channel shows no reaction to input pulses anymore, resulting in an empty channel.

The observed damages could be reproduced with generated pulses of  $\approx 40\text{ V}$  at the input stages. This scenario is compatible with a nearly instantaneous discharge of the electric field of the MRPC through the pre-amplifier input. This could be caused by direct exposure of the MRPC to the spray from the beam hitting nearby material.

To avoid a repetition of such damage, the replacement FEE cards installed in November 2019 were equipped with an overcharge protection diode parallel to the pre-amplifier input. Additionally, the gas mixture was adjusted to contain 0.5 % sulphur-hexafluoride, a strong electron quencher, to reduce the induced charge on the pre-amplifier per incoming particle.

### 6.3.2 2020 PADI Damage Events

The repairs after the 2019 beam period were successful in preventing the full destruction of the pre-amplifiers channels as they had been observed in the 2019 run. No empty channels have been observed during the 2020 beam operation. Offline analysis shows eTOF performed without issues from December 2019 to mid February 2020. However, offline analysis showed that after 19.02.20, the distribution of hits on eTOF counters less homogeneous between strips. A large number of channels show a significantly lower number of digis than their immediate neighbors. As opposed to the damage in 2019, this issue is less severe on the

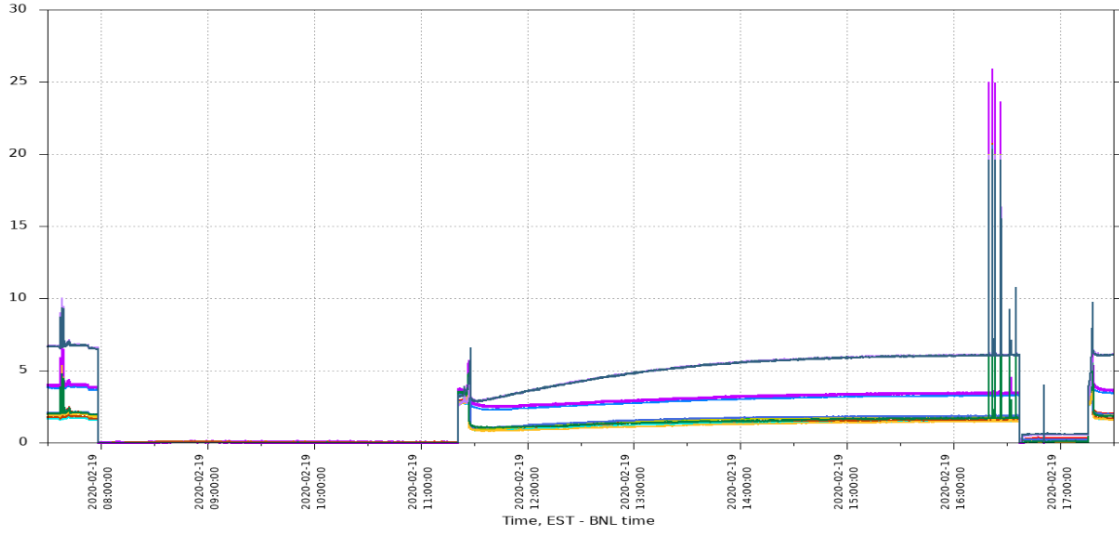


**Figure 6.6:** Current draw (in mA) for each eTOF HV supply unit during the time period of February 2020 damage events.

affected channels and not immediately recognizable from the (logarithmic) digi density plots.

The change in performance can be traced to an event between 16:00 and 16:30 on 19.02.20. Figure 6.6 shows the currents drawn by all eTOF HV supply units during this time frame. Multiple current spikes can be seen in this period. Curiously, this event happened during a detector maintenance period. No ions in the beam-line are recorded by the RHIC beam monitoring. bTOF and most other STAR sub-detectors see no corresponding current spikes. Only on the TPC field cage, similar current spikes can be seen during this time. eTOF was set to stand-by high-voltages for the remainder of the maintenance period by the detector operators after this event.

Figure 6.7 shows the difference before and after the event on an example counter. Afterwards (red line), at least 19 channels on this counter show significantly fewer entries relative to their neighbors than before. It is clearly recognizable that this is a single channel effect, no pattern of four or eight neighboring channels (corresponding to full GET4 or full PADI chips respectively) are visible. The pattern of low hit channels remains visible with small fluctuations until the end of the 9.2 GeV COL run period. It can thus be assumed to be a permanent damage.

To quantify this change on the full system, the number of channels with unusually low digi is compared. A low digi channel is defined for this purpose to have fewer than 80 % of digis in a given time frame (one run or one data file in a run) compared to the plateau value of the counter. This counter plateau value is calculated as the average of the channels with the third to sixth highest entries on the counter. The two channels with the highest entries are omitted as the channels connected to the first strip on a counter typically show approximately twice as

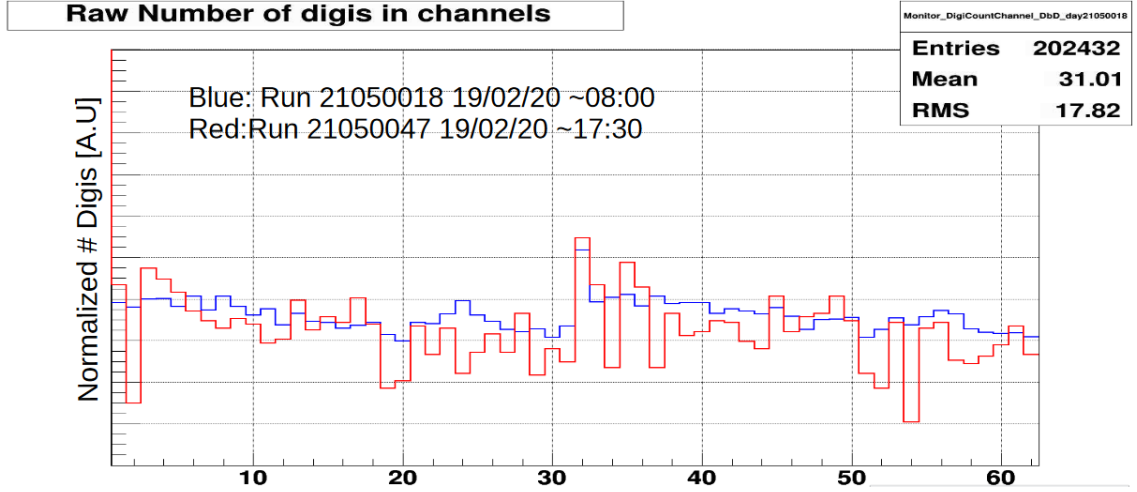


**Figure 6.7:** Performance difference before and after the damage event on 19.02.20 for an example counter. On the X-axis, the channel on the RPC is shown. Channel 1-32 correspond to the left side of the counter, Channel 33-46 to the right side of the counter. On the Y-axis, the relative number of digis in each channel is shown. The Y-axis has been normalized to the same number of total digis for both runs. The blue line shows the last run before the maintenance period, the red line the first run after the damage.

many hits as other channels and would thus distort the average. The threshold of 80 % of this plateau value is chosen to account for the normal differences between channels on a counter, mostly due to the pseudo-rapidity dependence of the incoming particle flux.

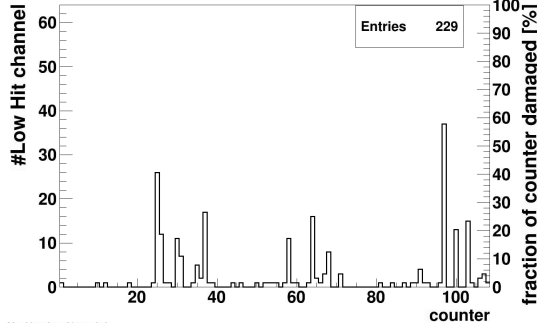
The following analysis has been done using data from the fast offline production of the respective runs. Fast offline data is a subset of  $\approx 8000$  events for each run which have been produced within two days after the data taking for early quality assurance. For most of BES-II the status bit, which documents the activity of a GET4 TDC in a given even (see Chapter 6.4.1), has not been included in the fast offline data. It is therefore not directly possible to distinguish between a low digi channel due to GET4 inactivity and other causes.

Figures 6.8 and 6.9 show the number of those low digi channels before and after the damage event on 19.02.20.

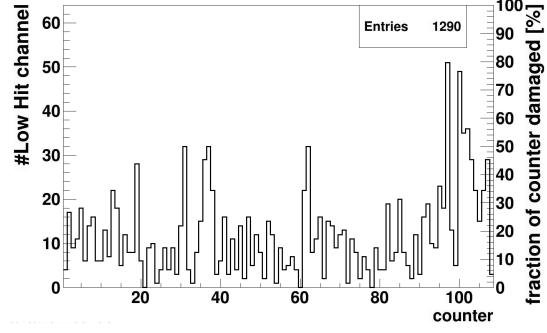
During the FXT running, fewer than 250 channels are typically counted as low digi channels due to GET4 inactivity. The distribution of low digi channels on the counters loosely follows the average GET4 inactivity fraction on the counters (compare figures 6.8 and 6.13). In March 2020 and following, more than 1000 additional low hit channels are found. Sector 23 and 24 (counter 90 - 108) are especially affected. On average, low digi channels have 58.6 % of the digis compared to the counters plateau value on USTC-type counters and 67.7 % on THU-type counters.

Figure 6.10 shows further insight into the distribution of low hit channels:

- The top left panel shows that THU counters are less affected than USTC



**Figure 6.8:** Number of low digi channels for each eTOF counter during 2020 31.2 GeV FXT data (averaged over two days of running), before the damage event. This serves as baseline for GET4 inactivity related low hit channels. Other fixed target runs show similar numbers of low hit channel.



**Figure 6.9:** Number of low digi channel for each eTOF counter in March 2020 during 9.2 GeV collider data taking (day 66, March 6th), after the damage event. Approximately 1000 more low hit channels are visible compared to fixed target data.

counters. 25 % of all low hit channels are on THU counter, which make up one third of all channels of eTOF. Since THU counters are operated at a lower high-voltage and thus less energy is stored in the MRPCs' electric field, this observation is consistent with a hypothesis that the damage is caused by a discharge of the electric field partially through the pre-amplifier.

- The top right panel shows that counters closer to the beam took more than twice as much damage compared to counters furthest away from the beam. This is consistent with the observations from 2019, when the damage was caused by a field discharge due to high beam-induced particle flux. However, this assumption is inconsistent with the absence of beam in RHIC during the 19.02.2020 event as reported by the RHIC beam monitor.
- Bottom left panel shows the pseudo-rapidity dependence of the digi density. This is represented by the normalized amount of digis in each channel of a module, averaged over all modules. The error bars indicate the variance between the modules for a given channel. The counter closest to the beam (channels 1-32) show a much larger error bars due to the high amount of low digi channels. The channels furthest away from the beam show very small error bars, indicating a uniform behavior between the different channels. A wave-like pattern can be seen, especially on the second and third counter in each module, with a period of 8 channels. This indicates that the observed low digi channels are related to the internal structure of the PADI chip. The outer channels (1 and 8) of each PADI chip are less affected by the damage than the center channels. Unrelated to the low digi issue, the first two channels of each counter in a module shows approximately twice as many digis as the other channels, likely due to the differing detector geometry on

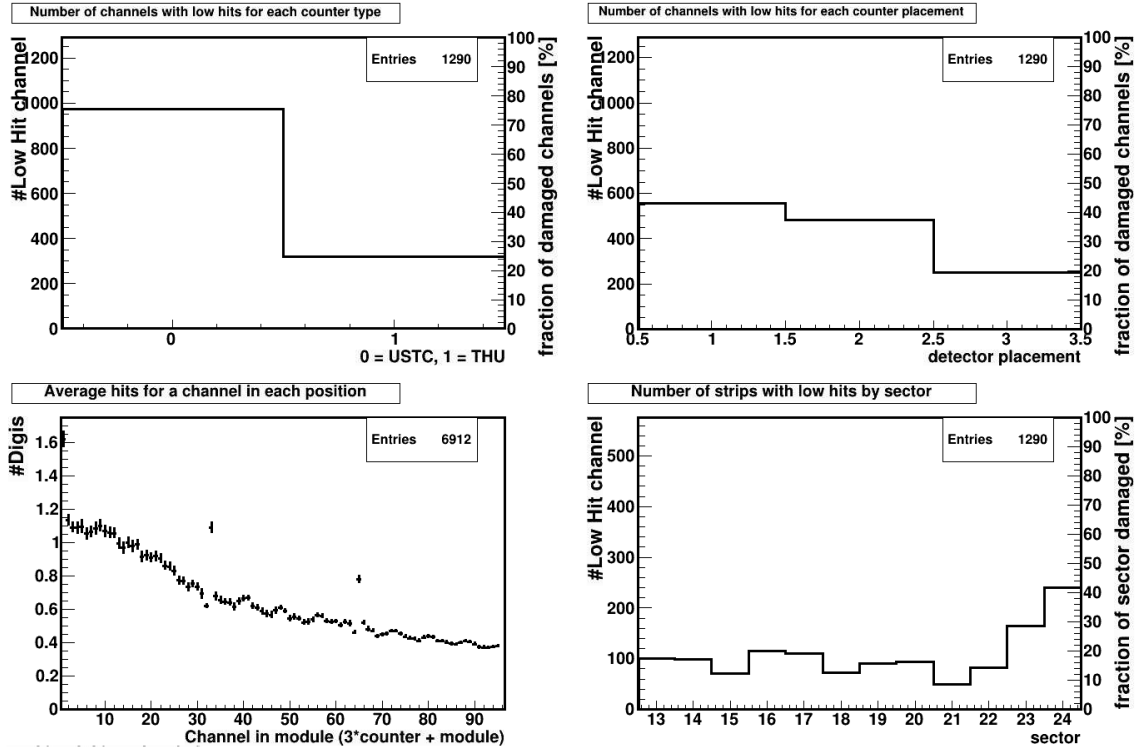


**Figure 6.10:** *Top left:* Fraction and total number of low hit channels between USTC and THU counters after the damage event on 19.02.20. *Top right:* Fraction and Total number of low hit channels separated by the detector number in the modules. Detector placement 1 refers to the counter closest to the beam, 3 is furthest away from the beam. *Bottom left:* Normalized number of digis in each channel in the modules, averaged across all modules and both sides. Channel 1 at most forward pseudo-rapidity, channel 96 is closest to mid-rapidity. *Bottom right:* Total number of low hit channels in each sector and fraction of each sector with low hit channels.

this edge.

- Bottom right panel shows that not all sectors are affected equally. Sector 23 and 24 are damaged more severely. Shortly after this event, module 23-1 also had to be taken out of the run due to extreme dark currents.

After the end of the 2020 beam period, on 09.09.20, a second damage event has been observed. During this time, STAR was taking cosmic data while RHIC was developing machine settings for coherent electron cooling (CEC). Multiple current spikes can be seen on eTOF and also on bTOF. Feedback from the accelerator operators indicate that heavy ion bunches were accidentally injected into RHIC and lost. In the aftermath of this second event, 2207 low digi channels have been found, 1507 channels on USTC-type counters and 620 on THU-type counters. This condition remained constant throughout the entire duration of the 2021 beam-time. The damage is more uniformly distributed than in the event of 19.02.20. On average, low digi channels have in 2021 60.1 % of the digis compared to the counters plateau value on USTC-type counters and 64.6 % on THU-type counters. This is similar to the channels damaged in February 2020. The relative efficiency reduction  $\delta\epsilon$  of USTC and THU-type counters compared to the start of 2019 can be estimated as:

$$\delta\epsilon = \frac{1}{N_{total}} \cdot N_{low\ digi} \cdot (1 - \epsilon_{low\ digi}) \quad (6.1)$$

where  $N_{total}$  is the total number of channels of each type (4608 for USTC-type counters and 2304 for THU-type counters),  $N_{low\ digi}$  is the number of low digi channels of this type and  $\epsilon_{low\ digi}$  their average fraction of digis relative to the plateau. Using this, a relative efficiency reduction of 12.9 % for the USTC-type part and 9.5 % for the THU part of the system is estimated. The matching efficiency (see Chapter 7.2 for a complete definition) reduced from 68.5 % to 59.7 % for USTC counters and from 69.4 % to 64.3 % for THU counters. This corresponds to a relative efficiency reduction of 13.3 % and 8.2 %, respectively. These numbers align closely with the above estimate from the raw number of digis per channel. This shows that the low digi channels are indeed affected by a reduction in signal detection efficiency and not just a reduction in noise counts.

During the 2021 beam period, no further damage events have been observed. The BES-II program has been completed in 2021. eTOF was not part of the high energy collision at  $\sqrt{s} = 200\ GeV$  program in 2022. The damage taken in 2020 has been simulated by PADI developer M. Ciobanu and more destructive tests have been performed by J. Frühauf. It was found that even with the added protection diode, PADI could be damaged by repeated extremely large pulses ( $U = 400\ V, ToT = 100\ ns, f = 10\ Hz$  compared to typical MRPC pulses of  $U \approx 30\ mV, ToT \approx 1.5\ ns, f \approx 100\ Hz$ ) [81]. The such induced damage causes an low resistance connection between the positive PADI input and ground. The negative part of PADI's differential input is largely unaffected. This leads to smaller signals at the discrimination stage, resulting in a lower efficiency, as observed in the data.

The CBM-TOF group has attempted to reproduce the PADI damage at mCBM. An MRPC was tested both in direct exposure to the beam and directly behind a thick target to induce beam fragmentation. Even at the highest mCBM interaction rates, no PADIs have been damaged in a similar way as at RHIC [82].

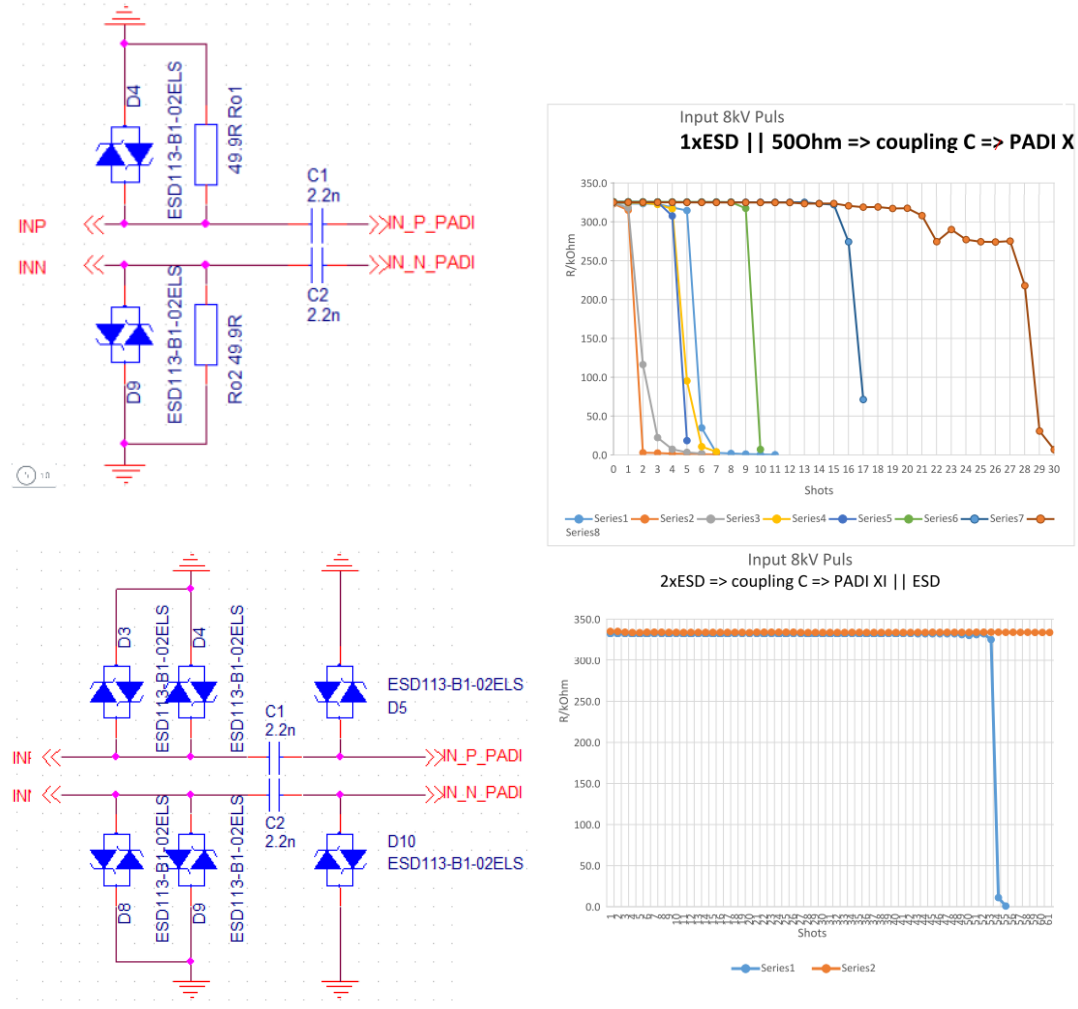


**Figure 6.11: Top:** PADI input protection scheme for 2020-2022 runs. **Bottom:** im-PADI test channels after injection of a se-proved PADI input protection scheme for ries of 8kV input pulses. Resistance drop 2023 run. With Courtesy: J. Frühauf. **Figure 6.12:** Input resistance of multiple indicated lasting damage to the PADI channel. **Top:** PADIs with 2020 protection scheme. **Bottom:** PADIs with 2023 protection scheme. With Courtesy: J. Frühauf.

In order to ensure the stability of CBM's future DAQ system, an improved protection scheme has been developed and tested at GSI. The schematics of this scheme and the one used in 2020-2022 can be seen Figure 6.11. Two additional ESD protection diodes have been added, one parallel to the existing one and one after



the coupling capacitor in front of the input of PADI. Figure 6.12 shows the results of destructive tests on both versions with an  $8\text{ kV}$  input pulse. In the old scheme, most channels are suffering damage (as seen from the loss of input resistance to ground) after approximately ten shots from the charge gun. A high variability can be seen in the susceptibility for different channels. With the new scheme, the first damage occurs after 50 shots.

## 6.4 DAQ Stability

### 6.4.1 GET4 Inactivity

One of the main goals of the eTOF project from the perspective of CBM-TOF was to test the stability and synchronization of its DAQ chain in a large system. eTOF with its 1728 individual GET4 chips and multiple month continuous runtime in each year of BES-II provides ample opportunity for this. As such a large system is difficult to maintain synchronized, eTOF features an automatic detection of epoch mismatches in GET4s and re-synchronization of those. An epoch mismatch is issued in the gDPB if it receives an epoch message from any GET4 which differs from its own internal epoch counter by more than one count. The gDPB will then send a GET4 restart command via slow control to this GET4. Upon receiving its next sync signal, this GET4 will reset its coarse time counter and set its epoch counter to the proper value (see chapters 4.4.2 and 4.5). From 2020 on-wards, eTOF logs for each GET4, if it has an epoch mismatch or is in an ongoing recovery process in a given event ("status bit", see Chapter 5.2).

This section will present an analysis of distribution and correlations of these status bits on the example of the 2020 FXT data. The dataset covers a sample of 3.7M events from 170 runs taken over a period of 9 days (with a 7 day interruption in between). In this sample, 163M out of a total of 6443M status bits are set, a fraction of  $\approx 2.5\%$ . 12M calibrated digis (excluding pulser digis) are found on GET4s in events with the status bit set, compared to a total of 2494M (non-pulser) digis found in the sample, a fraction of only  $\approx 0.5\%$ . A set status bit thus correlates with an average reduction of  $\approx 80\%$  in digi data volume from the corresponding GET4. One can thus assume a GET4 with a set status bit to be inactive in a given event. Consequently, the inactivity fraction of a GET4 will be considered to equal to the percentage of its status bits set.

Figure 6.13 shows the distribution of set status bits (as fraction of possibly set status bits) on all eTOF counters. The majority of counters shows little impact from epoch mismatches and reconfiguration with inactivity fraction  $< 2\%$ . In contrast, counter 96 (corresponding to detector 1 in module 3 of sector 23) is inactive for more than  $60\%$ . In this case, the high GET4 inactivity is correlated with an abnormally high dark current on this counter which led to an electric short shortly after this data was taken. The MRPC was subsequently deactivated for the remainder of the 2020 beam-time and replaced for the 2021 data taking

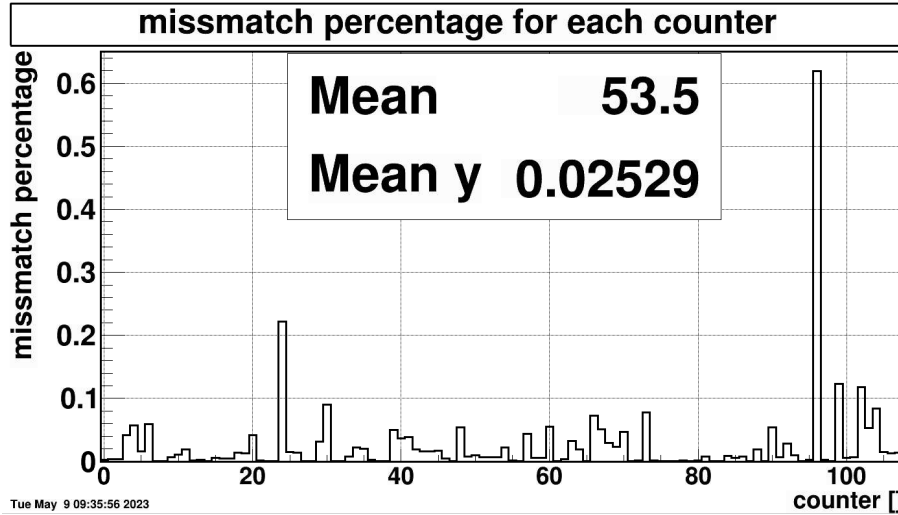


**Figure 6.13:** Average percentage of status bits (epoch mismatch or reconfiguration) set on each eTOF counter in the 2020 FXT data sample. The counter number on the X-axis can be converted to geometrical addresses as:  $counter = 9 \cdot (sector - 13) + 3 \cdot (module - 1) + (detector - 1)$ . On average, 2.5 % of all status bits are set in a given event.

period. Counter 23 (corresponding to detector 2 in module 2 of sector 15) is another significant outlier with an inactivity of more than 20 %. However, here no such physical explanation could be found. Instead, multiple corresponding GET4s exhibited instable behavior over the full duration of the data sample.

Figure 6.14 shows the multiplicity distribution of set status bits on the same counter and the in same event. It can be seen that counters with a high average number fall into two categories: Counters have between 1 and 4 frequently inactive GET4s (32 counters with 1 to 4 GET4s missing in at least  $10^5$  events) or 8 inactive GET4s (27 counters with 8 GET4s missing in at least  $10^5$  events). These two behaviors correspond to two different instabilities. In the first case, single GET4s lock onto external clock generated in the GBTX with a phase close to a full clock cycle. Due to their internal clock jitter, their clock edge may then randomly come either before or after the sync signal. Those GET4s thus appear to jump by one clock cycle are forced into reconfiguration on receiving a sync signal. Adjusting the clock phase in firmware (during DAQ restart procedure) has shown to change which GET4s are affected. However, as the clock phase cannot be adjusted for individual GET4s the issue could not be consistently cured. The second category, 8 GET4s are inactive at the same time, corresponds to a full side of the counter getting out of sync. This could be caused by an instability in the sync signal, which is distributed commonly for a full FEE board of 8 GET4s. If the sync signal arrives too close to a clock edge, clock jitter may cause the fine time to vary by one clock cycle, which would trigger frequent re-synchronizations of all GET4s on this FEE board. Also in this case, DAQ restarts (and corresponding changes in clock phases)

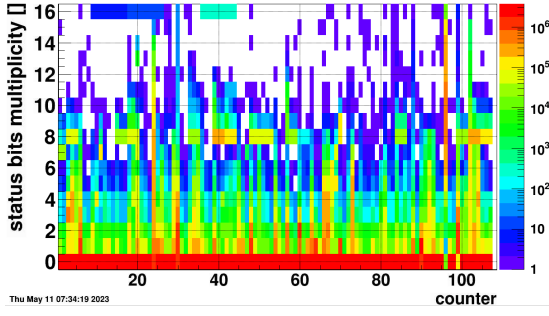


**Figure 6.14:** Status bit multiplicity per event for each counter. A clear excess at 8 GET4s with set status bit in the same event on one counter can be seen. This corresponds to a full side of the counter being inactive in the same event.

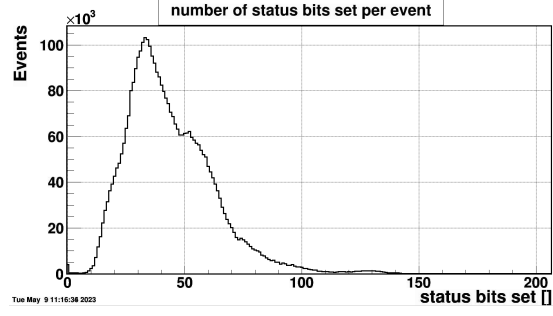


**Figure 6.15:** Status bit multiplicity per event on all of eTOF. Only  $< 5000$  events out of 3.7M total events in the sample show no GET4 outages at all. On average 43.7 GET4s have an active status bit in each event.

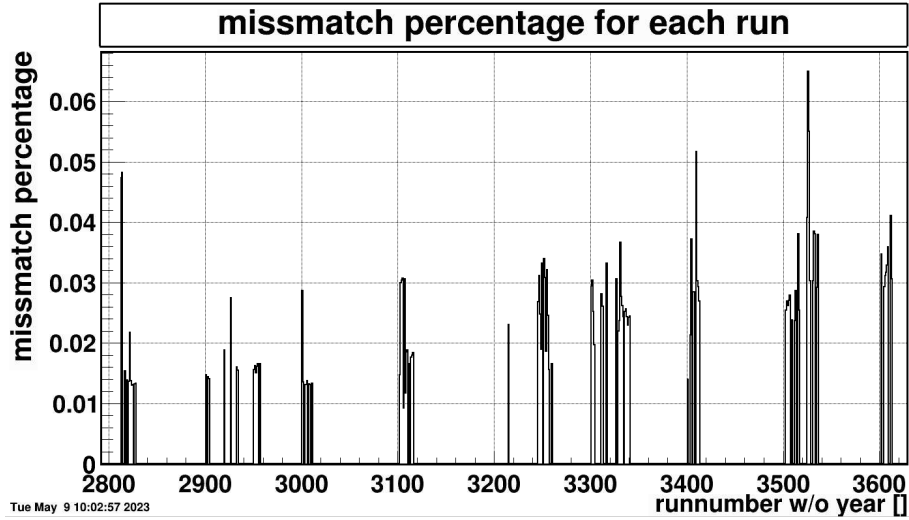
have shown to change which counters are affected, but the issue could not be consistently cured.

Figure 6.16 shows the temporal variation of the GET4 inactivity. The fraction of set status bits varies between  $< 1.5\%$  and  $> 6\%$ . Days 28 to 31 have a significantly lower inactivity fraction than the time period after. Runs with a high inactivity fraction often follow runs in which eTOF was not included due to a restart of eTOF's DAQ system or STAR pedestal runs. It has also been observed that modules with a very high rate of errors or re-synchronizations destabilize the full system and thus had to be taken out of the DAQ stream.

In effect, the observed GET4 outages mean that eTOF's efficiency is varying event by event on the order of a few percent. This effect is larger than the tolerances in the system efficiency determination for high precision physics analysis like an event-by-event fluctuation analysis. Figure 6.15 shows the distribution of the total number of set status bits per event. While on average 43.7 status bits are set in each event, less than 5000 events out of this sample of 3.7M events show no status bits at all. This means, that it is not possible to avoid the efficiency variance by simply focusing on events with full efficiency. This detector feature has to be taken into account when calculating the reconstruction efficiency in physics analysis. A common way to handle efficiency determination in STAR is a so-called embedding analysis. In this procedure, simulated Monte-Carlo (MC) tracks and MC eTOF hits are added to experiment data events and reconstructed alongside the physics data. The reconstruction efficiency is then calculated as the fraction of MC tracks which are correctly reconstructed and matched to their eTOF points.

Doing so poses several challenges:

- Handling 1728 individual flags per event is not practical for analyzers.
- Status bits are only sent if a GET4 is turned on. If a chip or a large part of the system has been turned off, the status bit does not account for this.



**Figure 6.16:** Average percentage of GET4s with set status bits in each run in the surveyed data sample. The first two digits in the run number denote the day in the year (2021) and the last two digits denote the run number during the day. Empty bins correspond to non-existing run, bad runs or runs without eTOF included.

- Due to the limited precision of track extrapolation, a track may be reconstructed to point to strips connected to a different GET4 than the one the particle actually crossed. This may give a wrong expectation of the local efficiency of the system.

To alleviate these issues, a new flag has been introduced. The goodEvent flag is available in the event header of reconstructed muDST and picoDST data for use by non-eTOF expert analyzers (see Chapter 5.2). It is set for each counter and each event if the counter in question has zero GET4 status flags set and the pulser digis (see Chapter 4.5.1) on both sides of the counter are found. This reduces the number of flags to account for to 108 flags per event. As both pulser digis are required to be present in an event, the goodEvent flag also guarantees that the counter was included in the DAQ stream during this event. The algorithm to match TPC track extrapolations to eTOF hit operates on counter level as no two MRPCs are oriented in the same geometric plane with respect to the interaction vertex. As the goodEvent flag corresponds to full counters, there is no ambiguity if an intersection area was active during an event.

The downside of this approach is that a significant fraction of data are not flagged as goodEvent. Figure 6.17 shows the average fraction of counters per event with goodEvent flag for each run in the data sample. On average this good data fraction is 80 %. Consequently,  $\approx 20\%$  of all data is not flagged as goodEvent, even though only  $\approx 2.5\%$  of GET4s are inactive on average. The good data fraction varies between 63 % and 88 %, depending on the run in the sample.

Solely focusing on events and counters with goodEvent flag set is thus only

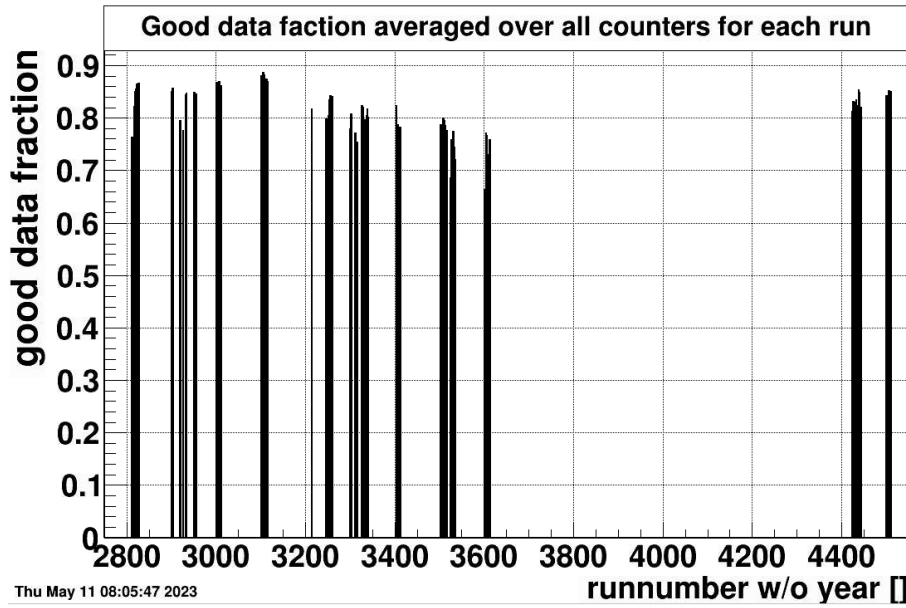


**Figure 6.17:** Average fraction of counters with goodEvent flag set per event in all runs of the data sample. The average good data fraction is 80.4 %. The first two digits in the run number denote the day in the year (2021) and the last two digits denote the run number during the day. Empty runs bins correspond to non-existing run, bad runs or runs without eTOF included.

recommended for analyses which require a precise understanding of the detectors acceptance and efficiency.

## 6.4.2 Clock Jumps

Two kinds of timing shifts have been observed in eTOF:

- Clock phase shifts can occur when the DAQ system is reinitialized during a restart. The 160 MHz clocks generated in the GBTX may lock with a different phase to the 120 MHz clock the GBTX receives from the gDPB or the gDPB clock may lock with a different phase to its input clock from CLOSY. These phase shifts lead to run-by-run offset in time and position on full counters. Examples of such shifts and the algorithm to deal with them in calibration have been shown in Chapter 5.4.7.
- Clock jumps refer to shifts in the timing of GET4s by full coarse time clock cycles of 6.25 ns. This section will take a closer look at those.

When a GET4 is restarted, its coarse time counter can shift. When a GET4 receives a reset slow control signal, it will resynchronize on the next sync signal. The delay between the sync signal and the coarse time clock edge depends on

cable length and clock phase shifts, which are different for each GET4 and after each full DAQ restart. If the sync signal arrives close to a clock edge, the signal jitter between both signals may cause it to arrive randomly before or after the clock edge and thus either of the two clock cycles can be set as the new starting point of the coarse time counter. This can cause a clock jump of GET4 by  $6.25\text{ ns}$  in either direction relative to previously taken data. Alternatively, any noise signals on the clock could in principle cause GET4 to miss clock edges or count extra.

In data, such jumps can be detected clearly once digis have been merged into hits. Since re-synchronization typically happens on either individual GET4 or FEE-card/counter side level only digis on one side of a strip will be affected. The y-position along the strip is calculated from the time of digis on both sides and the signal velocity on the strip by  $y = \frac{t_2 - t_1}{2} \cdot v_{\text{signal}}$ . If the GET4 on one side clock-jumped, the position of a hit is shifted by  $56.9\text{ cm}$  for USTC and  $51.5\text{ cm}$  for THU-type counters due to their different signal velocities. Figures 6.18 and 6.19 show examples of hit position distributions with clock jumps.

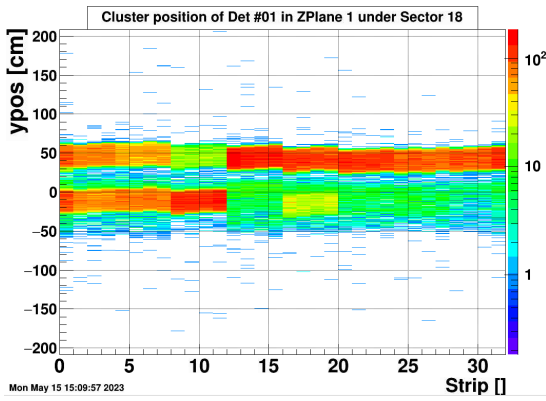


**Figure 6.18:** Example of the hit position of a USTC counter with large clock jump fraction before correction and calibration.

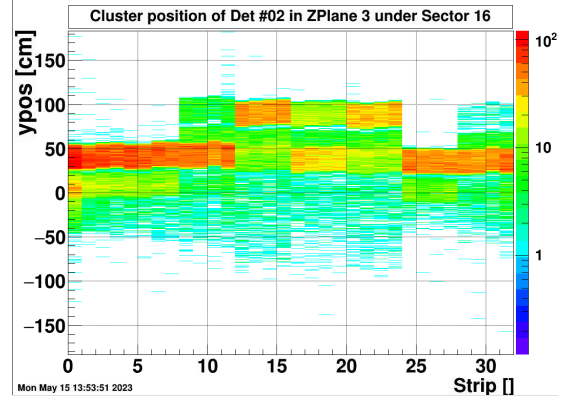


**Figure 6.19:** Example of the hit position of a THU counter with large clock jump fraction before correction and calibration.

Clock-jumped hits are displaced both in time and position. To mitigate the impact of clock-jumps in software, two correction algorithms have been implemented:

- Clock jumps which appear on full counter side simultaneously can be caught by looking at the time difference of pulser digis. The pulser signals are generated when the STAR trigger signal arrives and should thus have a fixed delay between each other. These signals are inserted into the first channel of each FEE card and digitized. If one FEE card clock-jumps relative to a chosen reference FEE card, its pulser offset will be shifted by  $6.25\text{ ns}$  compared to the value in previous events. If this new offset persists over at least 10 events, all digis from this FEE card will have their calibrated time corrected by this new offset. This algorithm is designed to catch rare time shifts. Frequent

shifts could be caused by an instability in the pulser system and thus not correspond to a clock jump in the data. Thus, pulser offset shifts which do not correspond to full clock jumps or do not persist over multiple events are not applied as calibration offsets to the data. The complete algorithm of the pulser correction is described in Chapter 5.3.2.

- Clock jumps of individual GET4s cannot be seen from the pulsers. The recognition of such clock jumps thus relies on the displacement of hits reconstructed from clock jumped digis along the y-axis of the detector. During hit reconstruction (see Chapter 5.3.3), all hits with a y-position within the expected distance for a clock jump from both counter edges are flagged as clock jump candidates. This flagging is done by adding 100 to the cluster size of the hit. Their position is then shifted by one clock cycle (multiplied by the counter's signal velocity), such that the hits end up on the nominal counter surface. As clock jumps have been observed to occur both forward and backward in time, it is a priori not clear how the time of clock jumped hits has to be corrected. The time of the hits is first corrected according to a preset default (backward in time). During track matching, clock jumped hits can be matched to TPC tracks. The measured time of flight for such a matched hit can then be compared to the expectation which can be calculated from the path length and momentum of the track as well as a pion mass hypothesis ( $ToF - ToF_{exp}$ ). The difference between measurement and expectation will be close to one clock-cycle if the assumed default time correction was wrong. Once sufficient statistics are accumulated for each GET4, the correction hypothesis used in the hit reconstruction (backward or forward in time) is updated for any following reconstructed events (see Chapter 5.3.4).

Figure 6.20 shows the  $ToF - ToF_{exp}$  of matched hits with clock-jump flag after correction and calibration. The three visible peaks correspond to the main pion peak (at  $\Delta t = 0$ ) and two shifted pion peaks at  $\pm 6.25 ns$ . Slower particles form the tails of those peaks towards larger  $ToF - ToF_{exp}$  values. The two shifted peaks correspond to pion matches which have not been successfully corrected and are thus shifted by one clock cycle in time. The main contribution to these peaks are hits from GET4s with a wrong default shift direction. These hits occurred before sufficient statistics in one run have been accumulated to adjust the direction of the clock-jump correction on one GET4. The performance of the clock-jump correction algorithm can be judged by comparing the entries in the side peaks to the main peak. The peak at  $\Delta t = +6.25 ns$  has a significant background from slow particles. To reduce the influence of this contribution, a tight cut integral of  $\pm 0.2 ns$  around each peak is compared. The main peak contains 2406k hits, the positive and negative shifted peaks contain 94k and 15k hits, respectively. Based on these numbers, it is calculated that at least 95 % of all clock-jumped are successfully corrected by this algorithm. Clock-jump flagged hits account for 1.6 % of all matched hits in the 31.2 GeV FXT data. The residual uncorrected clock-jumped hits thus account for only  $< 1\%$  of all eTOF hits.

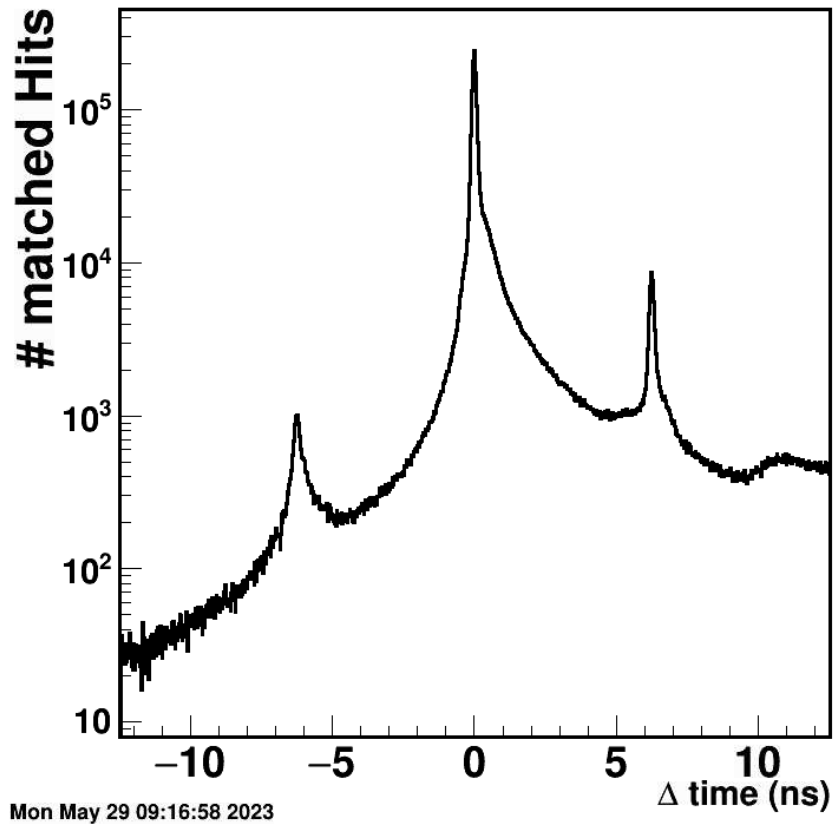


**Figure 6.20:** Difference between measured ToF and expectation ( $\text{ToF} - \text{ToF}_{\text{exp}}$ ) for matched hits flagged as clock-jumped. This dataset has been taken during the 31.2 GeV FXT run in 2020 from all eTOF MRPCs.



# 7 Detector Performance

## 7.1 Signal Observations

### 7.1.1 Aim of this Study

The eTOF program with its 108 counters is the first large-scale evaluation of CBM-TOF MRPC prototypes and their DAQ system. Therefore, it provides the first opportunity to study counter differences and construction variations with significant statistics. The basic observables presented in this section are largely independent of experimental circumstances and thus directly transferable from STAR to CBM. They should provide insight into how granular calibrations and experiment controls need to be for CBM operations. These observables are:

- Uniformity of the time over threshold (ToT) spectrum is the best measure of signal uniformity that is accessible from the data stream. Mean ToT and ToT RMS for each channel will be the direct observables. The variance between different counters and strips is studied to ensure that the MRPCs are comparable with each other.
- Signal velocities depend on the impedance of the read-out strip. In the hit reconstruction, they are used as a simple calibration parameter to convert the time difference between digis on both sides into a Y-position of the hit. In principle, a uniform behavior is expected for all channels of a counter type, as strip width and electrode distance are identical. Here, the aim is to test this hypothesis.
- Signal reflections can occur if there is an impedance mismatch between the pick-up electrode strip and the input of the pre-amplifier. By quantifying the issue of signal reflections, one can determine quality of impedance matching between the pick-up electrode and the pre-amplifier.
- The dark rate of the detector is a critical issue for an experiment with a free-streaming data acquisition like CBM. Extra dark rate always means extra data rate for the DAQ systems to handle. For a triggered experiment like STAR, a moderate dark rate is unlikely to have an impact on data quality. The majority of noise hits will be filtered out by the trigger system. eTOF@STAR has the longest running time of all CBM-TOF test experiments, so it is a good place to ensure that the MRPC prototypes dark rate stays low over a long period of operation. In that way, it is complementary to high rate aging tests at mCBM and ultra-high  $\gamma$ -irradiation tests performed in Bucharest.

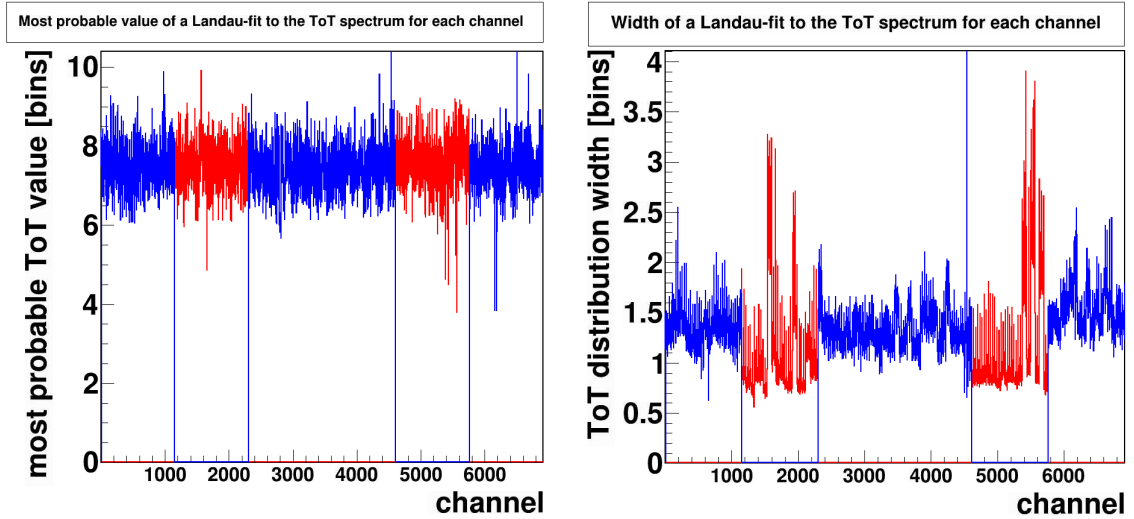


**Figure 7.1:** Most probable value (left) and width (right) of a Landau fit to the raw ToT distribution of each channel in eTOF. USTC-type counters are shown in blue, THU-type counters in red. One bin corresponds to a ToT of  $0.2\text{ ns}$  with the GET4 setting used. These data were collected during February 2020.

Unless explicitly mentioned otherwise, the data presented in this section have been taken during the fixed target program in 2020 at  $\sqrt{s} = 7.7\text{ GeV}$ .

### 7.1.2 ToT Uniformity

In order to parametrize the ToT distributions of all 6912 electronic channels of eTOF, a Landau fit was applied. The description of the ToT distribution by a Landau function is purely phenomenological<sup>1</sup> and is only supposed to allow a quantitative comparison of the peak positions and widths of the Landau distribution between the different channels. Figure 7.2 shows examples of such a ToT distribution and the corresponding Landau fit.

Figure 7.1 shows the raw ToT peak positions and fitted widths for each channel in eTOF. The peak positions are fairly uniform around a mean of  $1.5\text{ ns}$ , with a spread of about 20% around this value. This homogeneity is removed by the re-scaling of the mean ToT in the gain calibration (see Chapter 5.3.2). Larger differences are observed in the width of the distributions. Three major effects are visible:

- USTC-type counters show a larger width in the ToT distribution compared

<sup>1</sup>The energy distribution of the primary ionization in the RPC gas process follows a Landau distribution. The ToT of an RPC signal further depends on distance between the primary ionization and the glass plates, the dynamics of the avalanche development, the signal propagation along the read-out strip and finally the discrimination and ToT calculation. These effects influence the ToT more than the primary ionization and there is thus no principle reason why the ToT distribution should be Landau-shaped.

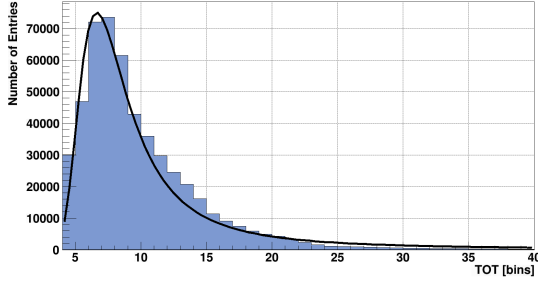


**Figure 7.2:** Example of a ToT distribution for one channel of a USTC-type counter and the corresponding Landau fit. One bin corresponds to  $0.2 \text{ ns}$ .

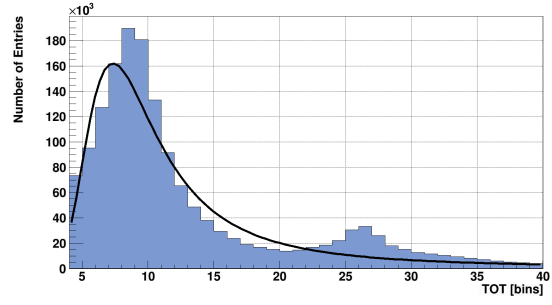


**Figure 7.3:** Example of a ToT distribution for one channel of a THU-type counter with a pronounced secondary peak due to merged reflections. This secondary peak distorts the fitted mean and width of the distribution. One bin corresponds to  $0.2 \text{ ns}$ .

to THU-type counters. This can be explained by the different high-voltage settings, gap size and the fact that the USTC has two additional gaps.

- A regular pattern can be seen where the ToT distribution of the first channel on each side of each counter is wider than that of other channels. This pattern is especially visible on the THU-type counters. The glass plates extend further than the first strip at the edge of the counter due to the high-voltage connector. This extra area is within the electric field and avalanches can form there. Those avalanches can also induce a signal on the first strip, leading to about twice as many total hits on the first strip compared to the other strips. Since there is no strip directly above this area, larger avalanches that would typically create multi-strip clusters instead induce a significant portion of their total charge into the first strip. This enhances the fraction of large ToT values in the distribution and results in the observed larger width.
- A number of channels have a significantly enlarged width compared to the majority of channels. This includes 14 full counter sides as well as some individual channels. The effect is especially visible among THU-type counters (For example, see channel 5400-5800 in Figure 7.1, right side). Closer inspection shows that this enlargement is due to the presence of a pronounced secondary peak in the ToT distribution, which distorts the fitted width. An example of such a distribution can be seen in Figure 7.3. This secondary peak is formed by primary signals merging with a reflection. The enlarged width of the Landau fit in Figure 7.1 can thus be understood as a proxy measure of the probability of such signal mergers occurring on a given channel. We will take a closer look at this issue in Chapter 7.1.4

### 7.1.3 Signal Velocities

There are multiple ways to extract signal velocities from data. The simplest method is by analyzing the distribution of hits along a strip. Under homogeneous illumination, the hits should form a box distribution with a width equal to the physical width of the strip. As the Y-position of a hit is proportional to the signal velocity assumed in the initial calculation, the real signal velocity can be calculated as:

$$v_{sig,real} = v_{sig,assumed} \cdot \frac{d_{box,fitted}}{d_{strip,physical}} \quad (7.1)$$

The hit distribution is fitted with a combination of a box function and two polynomials which describe the inhomogeneities of the hit distribution.<sup>1</sup> An example of such a distribution with the corresponding fit can be seen in Figure 7.4. One major advantage of this method is that plenty of statistics is available since every reconstructed hit can be used. This allows for a highly granular study of signal velocities, down to single-channel level.

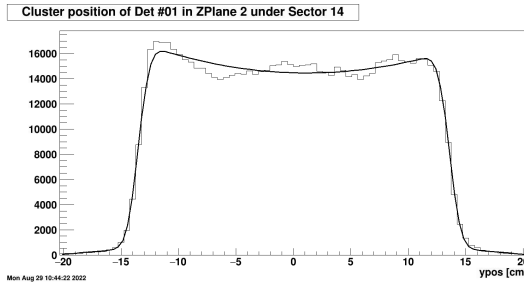


**Figure 7.4:** The Y-position distribution of reconstructed hits for an example counter with the corresponding box fit.

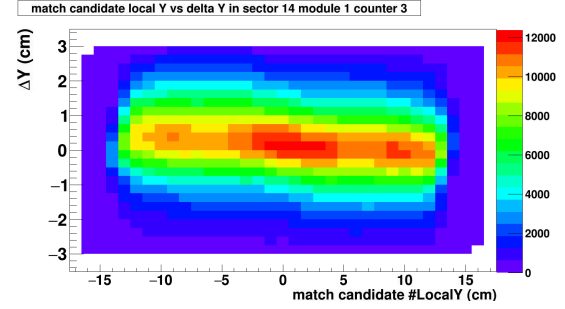


**Figure 7.5:** Y-position versus  $\Delta Y$  for an example counter. A slight slope can be observed due to an incorrectly assumed signal velocity.

An alternative way to extract the signal velocities is by analyzing the deviation in the Y-position between hits and their matched of TPC tracks with the counter surface,  $\Delta Y$ , as function of the hit's local Y-position.  $\Delta Y$  should be influenced only by the pointing accuracy of the track intersection and the Y-position resolution of the RPC. Geometric alignment is corrected during calibration and the influence of the inhomogeneities in the magnetic field is taken into account during the track

<sup>1</sup>The fitted box function used here is:  $f(y) = N \cdot (erf(y + y_0 - \frac{d}{2}) \cdot erf(y + y_0 + \frac{d}{2})) \cdot pol2(y, a, b, c) + pol2(y, d, e, f)$ ,

where  $y$  is the Y-position of the hits,  $y_0$  is the center of the strip and  $d$  is the width of the box.  $erf(y + y_0 \pm \frac{d}{2})$  are two error functions describing edges of the box and  $pol2(y, a, b, c)$  is a second-order polynomial with parameters  $a, b, c$ , which is used to model inhomogeneities on top of the counter. Another second order polynomial is added to describe the background from wrongly reconstructed hits, which may end up outside the physical surface of the counter.

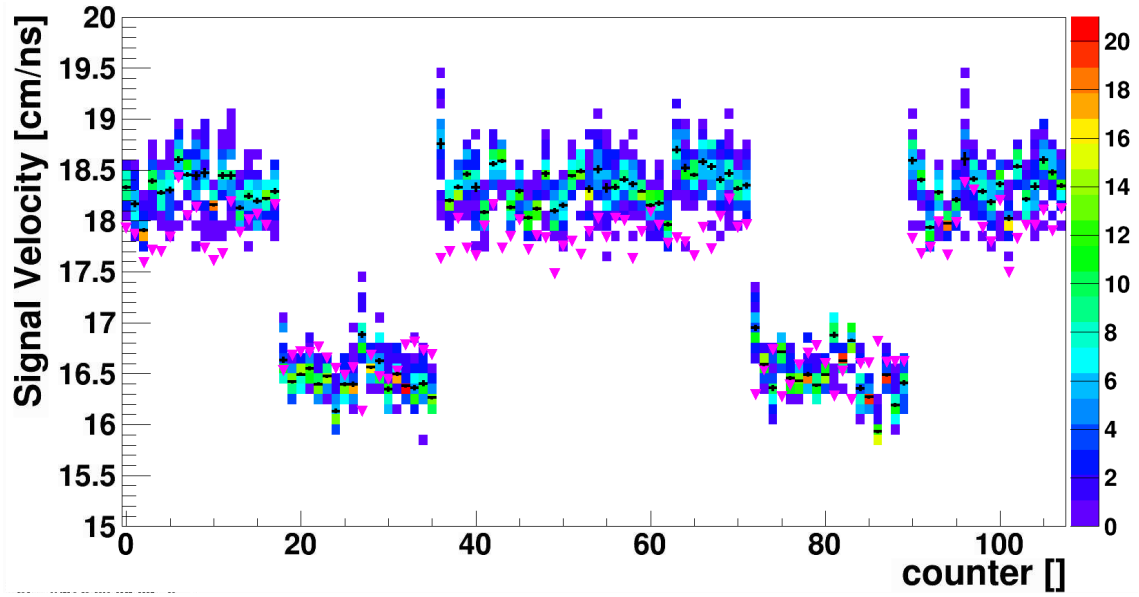


**Figure 7.6:** Measured signal velocities for all eTOF counters. Counters 0-17, 36-71 and 90-107 are USTC-type, counters 18-35 and 72-89 are THU-type. Color scale entries represent the signal velocity from the box fit method for a single strip on a given counter. Black crosses represent the mean signal velocity on the counter, derived from averaging over the individual strip box fits. Pink triangles represent the results from the track match deviation method for a full counter. A significant difference between USTC-type and THU-type counters can be observed. The differences between individual strips are comparable to the differences between counter averages.

extrapolation. A roughly Gaussian distribution for this distribution centered at zero is expected in this case. If there is a discrepancy between the assumed signal velocity and the real signal velocity of the RPC, the Y-position of the hit will be systematically shifted. This shift will be proportional to the Y-position of the hit <sup>2</sup>. To determine the signal velocity this way, the  $\Delta Y$  distribution is divided into slices of 1cm in  $Y$  and then each slice is separately fitted with a Gaussian distribution. The fitted centers positions of all slices are then fitted again with a linear function. From the slope  $m$  of this function and the assumed signal velocity, one can then calculate the true signal velocity as  $v_{sig,real} = v_{sig,assumed} * (1 + m)$ . An example of a  $\Delta Y$ -vs- $Y$ -plot with a slight deviation between real and assumed signal velocities can be seen in Figure 7.5.

The results of these two methods are summarized in Figure 7.6. For USTC-type counters, the signal velocities typically fall between 18.0 and 18.5  $cm/ns$ . For THU-type counters, the typical signal velocities are around 16.5  $cm/ns$ . The comparison between the two methods serves as a check for systematic uncertainties. For the USTC-type counters, the track match deviation method shows systematically lower signal velocities than the box fit method. For THU-type counters, the results do not show a significant systematic deviation. Both methods show similar variations between counters, but those variations are not well correlated between the two methods. Neither method can be assumed to be more precise. Additionally, an unexpected large deviation in the signal velocities between strips on the same counters is observed in the box fit approach. It is expected that the physical differences in signal velocities due to manufacturing variations between individual strips are very small. Yet, the observed variance measured between individual strips is similar to that between full counter averages. The two methods also provide inconsistent results. It thus has to be assumed that the main source of variances between all those results stems from systematic uncertainties in the determination of the signal velocities. These uncertainties in both methods arise from inhomogeneities in the Y-position distribution on the counter. In the box fit method, the pure box function (in this case, the two error functions) does not reliably converge to an inhomogeneous hit distribution on the counter. However, adding additional functions to describe the distributions on top of the box, like the second-order polynomial used here, can interfere with the width parameter. In the track match deviation method, a local increase of hits (which may be shifted from their correct position due to other effects) in the center of the counter will also cause a shift in the deviations towards the tracks. This could be misinterpreted as a signal velocity mismatch.

Thus, only a single averaged signal velocity will be used for all USTC-type and THU-type counters, respectively. The variance in signal velocities around those means is interpreted as additional uncertainty in the Y-position of reconstructed hits. The values of  $v_{sig,USTC} = 18.21 \text{ cm/ns}$  and  $v_{sig,THU} = 16.49 \text{ cm/ns}$  were chosen for the two types. The observed variance in the fitted signal velocities

---

<sup>2</sup> $Y = 0$  is the center of the strip

corresponds to an additional uncertainty in the Y-position of  $\sigma_{y,Signal} \approx 4\text{ mm}$ .

### 7.1.4 Signal Reflections

The read-out of an MRPC can be seen as a plate capacitor. In this view, the read-out electrodes function as the capacitor plates, with the glass and gas between them acting as the dielectric. The wave impedance for signals traveling along the read-out strips thus depends on the total thickness of the glass plates, the glass material, the total gas gap width, the gas composition, and the width of the read-out strip. Of these parameters, the width of the read-out strip is the most easily adjustable. If the impedance of the strip does not closely match the impedance of the read-out electronics, part of the signal will be reflected at the impedance gap. This can lead to multiple effects:

- Reduced signal amplitude: Part of the signal is reflected, which reduces the overall signal strength. This can cause small signals to be suppressed by the discriminator, leading to a reduction in the counter's efficiency.
- Signal merging: A reflected signal can arrive within the time over threshold of the primary signal on the other side of the strip. The TDC may fail to recognize the falling edge of the primary signal, causing the reflected signal to merge into the same digitization. The measured ToT is then prolonged until the reflected signal's falling edge arrives. This phenomenon will be referred to as the absorption of a reflected signal into a digi in the following.
- Mis-reconstructed hits: A reflected signal can arrive after the ToT and be registered as a separate signal. This can result in mis-reconstructed hits. When a digi is merged with its own reflection, the reconstructed hit will be positioned at the outer edge of the counter. These mis-reconstructed hits can be incorrectly matched to tracks, potentially contributing to background in particle identification.

The differential input impedance of PADI-X was designed to be adjustable down to  $25\ \Omega$  through the use of an external resistor. However, measurements show that the chip cannot be adjusted to a differential input impedance below  $50\ \Omega$  [70]. This differential input impedance corresponds to a single-ended input impedance of  $100\ \Omega$ . THU-type MRPCs were designed to have a read-out electrode impedance of  $50\ \Omega$  (single-ended). To match the  $100\ \Omega$  input impedance of the PADI-X, a  $100\ \Omega$  resistor has been added between the read-out electrodes and ground in the eTOF prototypes. In practice, reflectometry measurements by P. Lyu have shown an electrode impedance of  $59\ \Omega$  [83] for THU-type counters. For USTC-type counter, a single stack prototype was measured to have an impedance of  $92\ \Omega$  [84]. This would correspond to an impedance of approximately  $46\ \Omega$  for an

equivalent double-stack configuration with the additional electrodes in the center. The reflection coefficient for an impedance-mismatched transition is calculated as

$$\Gamma = \frac{Z_{strip} - Z_{FEE}}{Z_{strip} + Z_{FEE}} \quad (7.2)$$

Since the mismatch between MRPC strip impedance and the PADI-X input impedance is small, less than 12 % of the signal will be reflected for both counter types. Such small reflected signals are very unlikely to pass the pre-amplifier's discrimination threshold. Therefore, few reflection-related features were expected to be observed at STAR-eTOF.

However, as already seen in Figure 7.3, a secondary peak in the ToT spectrum was observed. This peak appears at exactly the distance from the main peak that a signal needs to travel back and forth along the read-out strip ( $\approx 3 ns$ ). The second peak is interpreted as normal digis, which are stretched due to the arrival of a reflected signal from the other side of the counter. This feature is strongly visible in 5 out of 18 THU counters (the enlarged ToT distribution widths seen in Figure 7.1) but is absent in USTC counters.

It is also observed that a fraction of hits exhibit strong ToT asymmetry ( $\alpha_{ToT} = \frac{ToT_{right} - ToT_{left}}{ToT_{left} + ToT_{right}}$ ) between the ToT of the digis on the left (positive Y-Position) and the right (negative Y-Position) side of a counter. Figures 7.7 and 7.8 show these asymmetry distributions for USTC and THU-type counters. This observation is counterintuitive since the digis on both sides are induced by the same avalanche. For this feature as well, there is a significant difference between USTC and THU-type counters. The USTC-type counters show a distinct pattern: The hits are concentrated in one of three regions in the ToT asymmetry vs. Y-position plane. At  $y = \pm 10 cm$  and directly in the middle of the counter, hits are concentrated around a ToT asymmetry close to zero. Each of these concentration regions then extends along a line approximately linearly anti-correlated with the Y-position (see red-colored areas in Figure 7.7). This pattern is also weakly recognizable on the THU-type counters, but the observed asymmetries are smaller and the concentration of hits in this pattern is less pronounced. One feature expected from abundant signal reflections is an enhancement of hits near the counter edge due to additional hits reconstructed from a near-side digi and its own reflection on the far-side. However, this feature is not observed in either THU-type or USTC-type counters.

The observed pattern can be better understood in a different representation. Figures 7.9 and 7.10 show the ToT of the digi on the left side<sup>3</sup> of the counter as function of the hit's Y-position for USTC and THU-type counters, respectively. The corresponding plots for right-side<sup>4</sup> digis look mirrored at  $Y = 0$ . Two classes of digis can be seen: One where the ToT is independent of the Y-position of the hit and another where the ToT linearly depends on the Y-position of the hit.

<sup>3</sup>the side corresponding to positive Y-positions

<sup>4</sup>the side corresponding to negative Y-positions



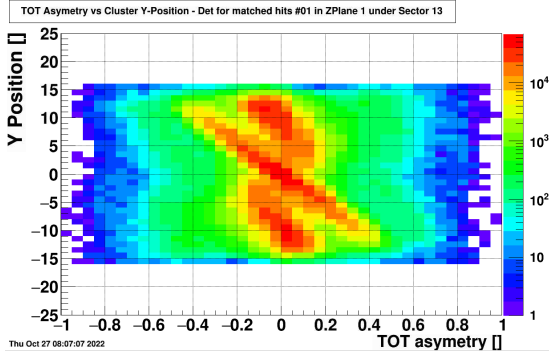


**Figure 7.7:** ToT asymmetry  $\alpha_{ToT} = \frac{ToT_{right} - ToT_{left}}{ToT_{left} + ToT_{right}}$  in hits of an example USTC counter as function of the hit's Y-position.

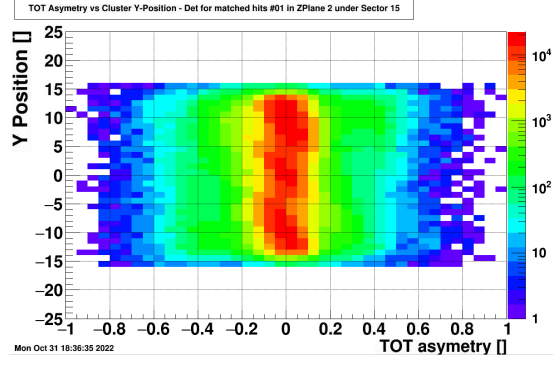


**Figure 7.8:** ToT asymmetry  $\alpha_{ToT} = \frac{ToT_{right} - ToT_{left}}{ToT_{left} + ToT_{right}}$  in hits of an example THU counter as function of the hit's Y-position.

Again, this pattern is much more pronounced on the THU-type counters. Analysis by Yannick Söhngen shows the slope of the diagonal branch in the USTC-type counters is approximately  $19.0 \text{ cm/ns}$  [85]. This value is close to the signal velocity on the USTC-type counters (compare Figure 7.6). This result is incompatible with a hypothesis that the observed signal are prolonged due to signal diffusion on the electrodes. However, one would expect exactly this dependence if the signals were prolonged due to the absorption of reflections. From this plot, it can also be estimated, that approximately 40 % of digis in USTC-type counters have their ToT significantly distorted due to the absorption of a reflection.

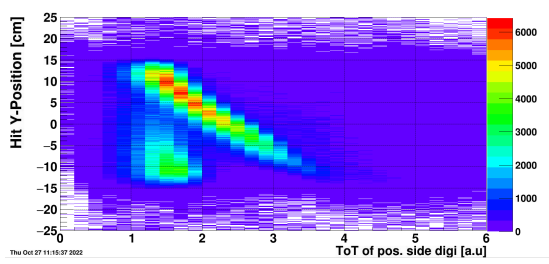


**Figure 7.9:** ToT of left side digi as function of their reconstructed hit's Y-position on USTC counters. With Courtesy: Yannick Söhngen.

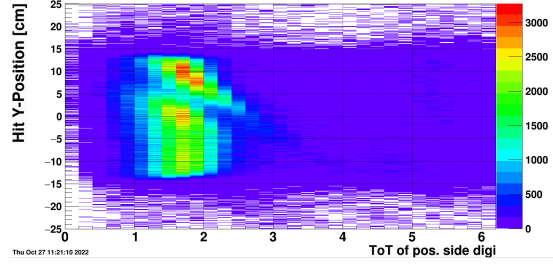


**Figure 7.10:** ToT of left side digi as function of their reconstructed hit's Y-position on THU counters. With Courtesy: Yannick Söhngen.

The pattern in Figures 7.7 and 7.8 can now be understood as follows: Avalanches with low ToT do not produce reflections above the discrimination threshold and show mostly small asymmetries. Large avalanches close to either edge of a USTC-type counter are reflected on both sides. On the near-side, the reflection of the far-side digi arrives long enough after the near-side primary digi that it is registered as an independent digi. The signal travel time back and forth along the strip is approximately  $3 \text{ ns}$ , which is long compared to a peak ToT of about  $1.5 \text{ ns}$  for

USTC-type counters. Thus, the primary digi is registered with its correct ToT. The secondary digi can be suppressed with a software dead time. On the far side, however, the reflection of the near-side digi arrives on the far side very close in time to the primary far-side digi and thus stretches the ToT of the primary far-side digi by a short time. The further away from the counter edge this happens, the more the far-side digi is stretched and the asymmetry increases.

For the THU counters, due to both a lower signal velocity and shorter peak ToT, the absorption of a reflection happens only for avalanches on the high end of the ToT spectrum. The observed ToT asymmetries are smaller and a smaller fraction of hits fall into the three pattern branches.

A significant presence of reflections in both USTC and THU-type counters explains many of the observed correlations in the time over threshold measurements. However, the previous reflectometer measurements indicate that only a small portion ( $< 15\%$ ) of the initial signal should be reflected at the connection between the read-out electrode and PADI. Further studies of the raw electric signals are needed to resolve this apparent discrepancy between expectation and observation. The distortion of the ToT due to the absorption of reflections may impact the time resolution of the MRPC as a correction of the time walk will not be entirely possible. Chapter 7.3.4 will attempt to quantify this effect.

### 7.1.5 Dark Rate

For MRPCs, one needs to separate between noise and dark rate: Noise signals are electrical distortions in the read-out that are interpreted as signals. Dark rate corresponds to signals from real avalanches inside the MRPC, which are however not initiated by a trackable particle. Dark rate signals are visible on both sides of a strip and can be reconstructed into hits. Dark rate can be induced by multiple processes. Thermal motion of electrons in the glass plates causes electric charges to concentrate in pointed irregularities on the surface of the glass plates. This can lead to sufficient distortions of the electric field to allow local ionization of the gas, which develop into visible signal avalanches. This process is enhanced in the presence of dust pollution in the gas

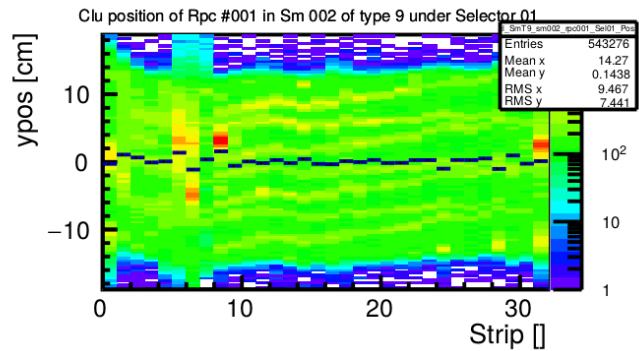


**Figure 7.11:** Dark rate hit position distribution on a THU-type prototype counter in cosmic test from 2017. Visible enhancement of dark rate along fishing lines (diagonal and horizontal yellow lines) and one hot spot likely due to dust pollution. Source: [61]

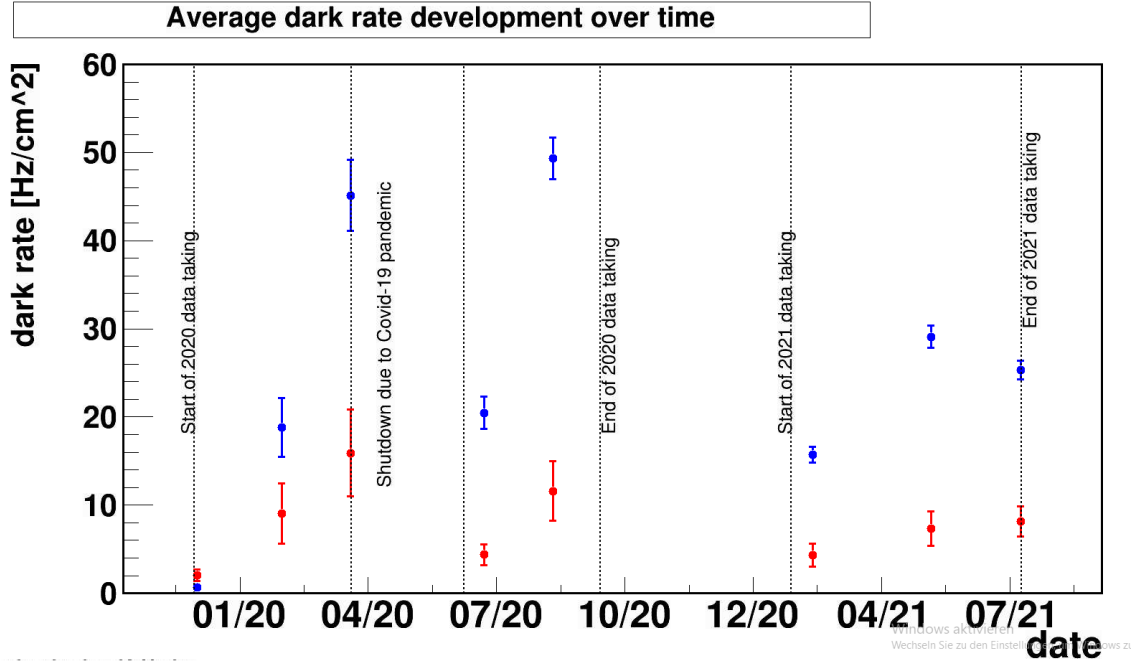


**Figure 7.12:** Evolution of the average dark rate for USTC (blue) and THU (red) type counters over the years 2020 and 2021, normalized to detector surface. Data are taken from STAR pedestal runs. Error bars show variance between counters (RMS). Statistical errors are smaller than the marker size. Data points from left to right: 1. Start of 2020 data taking. 2. 2020 FXT data taking, after two month data taking at 11.5 GeV Au-Au COL. 3. Interruption of data taking due to Covid-19. 4. Dark rate after two month recovery during Covid shut-down. 5. End of 2020 data taking after 9.2 GeV Au-Au COL data taking 6. Start of 2021 data taking, 7. End of 7.7 GeV Au-Au COL data taking (longest continuous data run). 8. End of 2021 data taking after 200 GeV O-O COL data taking.

which distorts the field lines. Local ionizations from low energy ionizing radiation, environmental radioactivity or cosmic rays also contribute to the dark rate.

In CBM-TOF MRPC prototypes, dark rate hits show a similar cluster size and ToT distribution as hits from primary collision particles. In previous cosmic measurement the main source of dark rate for similar prototypes has been identified: The fishing line spacers between glass plates have a circular cross-section. The electric field lines of the MRPC's high-voltage bend around those fishing line spacers and are compressed in their vicinity. Field distortions (from dust or point charges) in this region are much more likely to lead to avalanches above threshold. Looking at the distribution of hit positions over the counter surface, the position of the fishing line spacers is clearly visible. An example of a THU-type counter can be seen in Figure 7.11

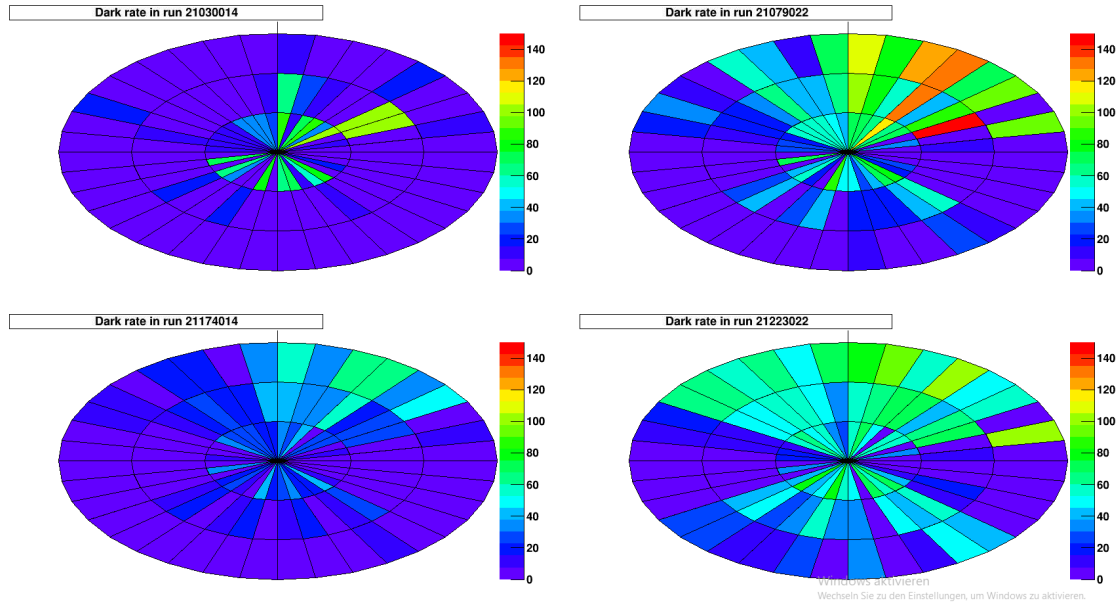
Figure 7.12 shows the evolution of the average dark rate for USTC-type and THU-type counters mainly over the years 2020 to 2022. The data have been taken from STAR pedestal runs, which are triggered by a periodical pulser. A

time-window of  $2.5 \mu s$  before each trigger has been read out. The event-averaged number of digis in this time window has been used to calculate the rate for every counter. This rate has been normalized to the active detector area of  $27 \text{ cm} \times 32 \text{ cm}$  and divided by the average rate of  $\text{digis}/\text{hits} = 2.5$  to allow easier comparison to particle fluxes. Counters with zero dark rate have been removed from the calculation of the average for each type as it is assumed that their FEE was not active during a specific run. Typically, about 1000 Digis have been used for a single counter measurement. This brings the relative statistical error to  $\sigma_{\text{stat,relative}} = \frac{\sqrt{N}}{N} < 3.5\%$ . In the average over the counters of each type, this error becomes negligible compared to the systematic differences between individual counters.

New MRPCs typically have a dark rate around  $1 \text{ Hz}/\text{cm}^2$ . Directly at the start of 2020 data taking, after being in continuous operation from January 2019 to July 2019, after USTC-type counters show dark rate very similar to this, while THU-type counters have a dark rate of about  $2 \text{ Hz}/\text{cm}^2$ . Over the course of the 2020 beam-time, the dark rate rises to  $\approx 12 \text{ Hz}/\text{cm}^2$  for THU counters and over  $\approx 50 \text{ Hz}/\text{cm}^2$  for USTC-type counters. At the start of 2021 data taking, after one week of operation, the dark rates are down to  $\approx 5 \text{ Hz}/\text{cm}^2$  and  $\approx 17 \text{ Hz}/\text{cm}^2$  respectively. During the 2021 data taking the dark rates are rising again, but to lower levels as seen in 2020. It should also be noted that the variance between counters are significantly smaller in 2021 compared to similar rates in 2020. A measurement in early 2022 (not shown in Figure 7.12) without high-voltage on the MRPCs shows a dark rate purely due to electronics noise on the order of  $\approx 0.1 \text{ Hz}/\text{cm}^2$ .

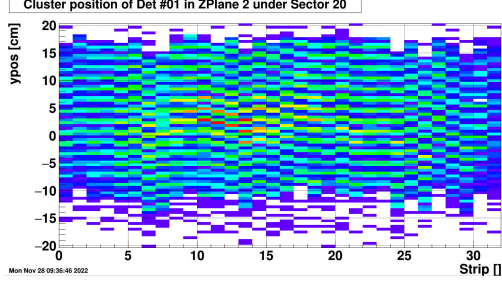
Especially at the end of Run 2020, the dark rate is not negligible compared to typical particle fluxes at STAR of  $\approx 300 \text{ Hz}/\text{cm}^2$ . However, using a tight trigger window of  $100 \text{ ns}$  reduces the chance to mistake a noise hit for a track match to below  $0.5 \%$ . At CBM rates, even this dark rate can be neglected, but studies will be needed to assess how high the dark rate can rise under exposure to the high interaction rates at CBM. The observations here show no indication of an irreversible increase in the dark rate.

Figure 7.13 shows the individual counter dark rates for four different runs during the 2020 data taking period. A clear difference between USTC-type and THU-type counters can be observed, as expected from the average. The four THU sectors are located in the 8 o'clock to 10 o'clock position and the 2 o'clock to 4 o'clock position. It is also visible, that not all counters react equally to the conditions during the beam operation. The dark rate on the top side of the eTOF wheel increased massively during February 2020. During this time period, a suspected beam loss event occurred, during which pre-amplifiers were damaged (see Chapter 6.3). The high particle flux during such an event could be correlated with this observed dark rate increase. The lack of similar events in 2021 could then also explain the observed lower dark rate variance between counters in this period. The bottom side of the wheel is less affected. Neighboring counters do not necessarily show similar dark rate increases. During the Covid-19 shutdown,



**Figure 7.13:** Dark rate (in  $\text{Hz}/\text{cm}^2$ ) for individual counters in four pedestal runs during 2020 data taking with approximate positions on the eTOF wheel. Azimuthal bins represent a module each, starting with sector 13, module 1 counter-clockwise of the 12 o'clock position. Radial bins represent one counter inside a module starting with counter 1 (closest to the beam-line) in the bin closest to the center. Top left: Dark rates in early February 2020, during FXT campaign. Corresponds to data point 2 in Figure 7.12. Top right: Dark rate before the Covid-19 shutdown. Corresponds to data point 3 in Figure 7.12. Bottom left: Dark rate after 2 months of shutdown due to Covid-19. Corresponds to data point 4 in Figure 7.12. Bottom right: Dark rate at the end of 2020 operations. Corresponds to data point 5 in Figure 7.12.

the dark rate of the whole wheel decreased again, but did not yet reach the same levels as at the start of the data taking period in 2020. Especially the counters with high dark rate before the shutdown still show an elevated dark rate. Until the end of the 2020 data taking, the dark rate increased again, but more uniformly than before.



**Figure 7.14:** Position of dark rate hits on an example USTC-type counter. Parallel patterns at 2 cm spacing can be observed, corresponding to the parallel fishing line spacing in the USTC counters. Distortions in y-direction are calibration artifacts.

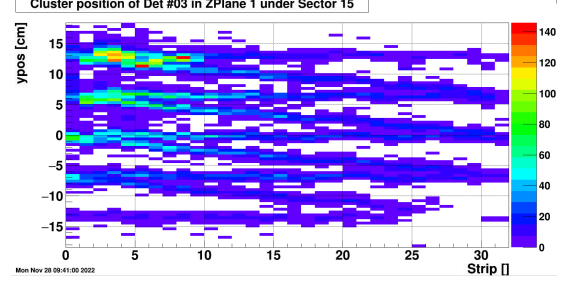


**Figure 7.15:** Position of dark rate hits on an (higher dark rate) example THU-type counter. Z-shaped patterns corresponding to the fishing lines on THU-type counters can be observed. Distortions in y-direction are calibration artifacts.

Figures 7.14 and 7.15 show the hit positions of dark rate hits in run 20030014 (Corresponding to data point 2. in Figure 7.12) for an example counter of USTC and THU-type, respectively. One can clearly observe the tight parallel line structures at a 2 cm distance on the USTC-type counter and the Z-shaped patterns on the THU-type counter. Both correspond to the layout of the fishing lines in those counter types. This confirms that the main source of noise is located closely to the fishing lines, matching observations from cosmic tests and mCBM. The higher amount of fishing lines in the USTC-type counters could be one reason for their higher average dark rate.

One hypothesis for the observed rise and fall of dark rates is activation of the MRPC material by interaction with particle flux. The subsequent decay of these activated states can ionize the MRPC gas and introduce avalanches which are seen by the detector. This hypothesis explains the increasing dark rate over the course the beam-times and the reduction after the winter breaks. Since the collision energies and interaction rates were higher in 2020, the resulting particle flux on the MRPCs was higher than in 2021. This explains why the dark rates at the end of the 2020 run were higher than after the 2021 run. In mCBM operations, similar increases in dark rate up to  $\approx 30 \text{ Hz/cm}^2$  directly after beam-times and an exponential decline over multiple weeks have been observed [82].

Alternatively, the origin of the change in dark rate could be polluted (ionized) gas accumulating close to the fishing lines. The gas exchange inside the gap normally happens on faster timescales than the observed decrease of the dark rate after the end of irradiation. However, close to the cylindrical fishing lines the gas

exchange is slower. The CBM-TOF Bucharest group has studied MRPC prototypes after high intensity photon irradiation at the multi-purpose irradiation facility of IFIN-HH in Bucharest [40]. After irradiation with a total dose of  $13\text{ kGy}$  within 40 hours using a high intensity  $Co^{60}$ -source, the MRPCs were shown to return to pre-irradiation dark rates within two weeks. However, when disassembling the counter after the irradiation, a multi-colored layer of deposits was observed on the glass with the structure of the fishing lines clearly visible. Extensive chemical analysis of the deposit showed a high fluorine content, presumably from the fall-out of  $C_2F_4$  from the working gas. Those studies also show a large flux dependence of the dark rate.

### 7.1.6 Conclusions of this Study

The most important result of this study is that at the most basic level, not all MRPCs are created equal. Especially the THU counters show significant variance in the ToT spectra. Signal velocities show significant variances on all counters. Dark rates also increase differently between counters. For CBM, this reinforces the need for precise quality control as well as the need to produce a number of additional counters to replace under-performing counters. The effects of the observed variances on the counter performance in STAR will be studied in the next sections using the example of the 2019 FXT data.

The signal velocity behavior is largely consistent between counters, but the observed variances between counters and the differences between the two tested methods suggest a limited accuracy of the methods. Both methods rely implicitly on the assumption of a homogeneous hit distribution on the counter surface. In eTOF, this homogeneity is not given to the extent it was observed in cosmic measurements. While various potential causes (walk calibration, hit reconstruction, reflections) have been and are being studied by the eTOF group, this issue is not fully understood. Ultimately, the uncertainty in the signal velocity translates into an uncertainty in the y-Position of the reconstructed hits. The influence of this worsened resolution on the track matching in eTOF will be studied in Chapter 7.2.

Reflections are much more prevalent than expected. Going forward, the impedance of the next generation of CBM-TOF MRPC prototypes will be studied once the design is finalized. The next generation of the PADI pre-amplifier allows to tune its input resistance exactly to the detector.

However, a discrepancy remains between the small measured impedance mismatch and the observed high probability of reflections. One hypothesis to explain this discrepancy is that the observed distortions are not due to reflections at the input of the pre-amplifier, but a feature of the double stack architecture. As the signals from both stacks of the MRPCs are merged through a three-way junction, signals from each stack could travel backward along the read-out strip of the other stack. This hypothesis will have to be checked in direct signal observations which are not possible at STAR and will have to be continued in cosmic measurements.

The dark rate, and more generally aging, remains a field of active research in the CBM-TOF group. The results presented here show that the observed dark rate increase is largely reversible. This is in agreement with the observations at mCBM and in Bucharest at higher particle flux and shorter timescales. What is clear from all studies in this regard is that the main source of dark rate is closely related to the fishing lines. To counteract any issues stemming from this for longer term CBM operation, a next generation of CBM-TOF prototypes is developed. Tests to replace the cylindrical fishing lines with rectangular spacers are ongoing. In addition, the new counters will be sealed around the gas volumes to force the gas flow directly through the gas gap and thus increase the exchange of polluted gas. As high rate environments have always been the primary concern with aging, further studies of the new prototypes will be conducted at mCBM and Bucharest.

## 7.2 Efficiency

### 7.2.1 Aim of this Study

Efficiency for a system like eTOF has three different aspects:

- The detector efficiency, defined as the probability for the detector (MRPC) to detect an incoming particle.
- The matching efficiency, defined as the probability to match a reconstructed particle track pointing to the detector with a hit on the detector.
- The reconstruction efficiency, defined as the fraction of particles which are correctly detected and identified by the full detector system over the total number of all particles produced in the collisions.

This chapter will focus on the first two points, detector efficiency and matching efficiency. Out of those, detector efficiency is more important for CBM-TOF as it is expected to be transferable between the experiments. This comes with the caveat that due to safety concerns for the TPC operation at STAR, the planned CBM-TOF gas mixture (including 5 %  $SF_6$ ) cannot be used. The detector working point and absolute efficiency are thus not directly transferable to CBM. The long-term stability of the detector efficiency, however, remains a point of interest for CBM-TOF in the eTOF program.

For STAR on the other hand, matching efficiency is the more important quantity, as it directly enters into the reconstruction efficiency which is used to correct measured particle yields. The matching efficiency can be understood as a product of the detector efficiency and a factor describing the likelihood to extrapolate a track correctly towards eTOF. This factor depends on TPC momentum resolution, local material budget, magnetic field, track fit quality, particle species and particle momentum. Due to the previously described instabilities (see Chapter 6.4.1)



with the FEEs, eTOF's matching efficiency will also vary between runs and even individual event.

The final aspect of efficiency, the reconstruction efficiency, depends on particle type and phase space region. It is typically determined during specific physics analyses within the area of interest of those analyses. The established method to estimate the reconstruction efficiency in STAR is a so-called embedding analysis. In this method, simulated tracks are included (embedded) into the real data sample and processed through the normal data reconstruction chain. The reconstruction efficiency is then estimated from the fraction of embedded particles which are correctly reconstructed and identified. At the time of this writing, no large-scale embedding datasets have been generated for datasets including eTOF. Thus, an extended analysis of the reconstruction efficiency is not part of this work.

### 7.2.2 Detector Efficiency - Overlap Analysis

In CBM-TOF's detector development, the established method to determine the efficiency of an MRPC prototype has been to stack multiple MRPCs behind each other (see for example [66]). A track can then be constructed from hits on the reference MRPCs (REF). This track is intersected with a detector under test (DUT). The detector efficiency of the DUT is calculated as the fraction of tracks for which a hit on DUT can be found within a certain radius in space and time around the calculated intersection point. This method has been most successful if the reference track was constructed from hits of at least three reference detectors between which the DUT is sandwiched. Using such an interpolating reference, compared to an extrapolating reference (where all reference detectors are on the same side of the DUT), removes systematic uncertainties in the detector efficiency due to particle absorption.

In STAR, direct measurements of the detector efficiency rely on regions where two eTOF MRPCs overlap. The MRPCs inside each module overlap for two strips each. This is a narrow region and only allows to determine the efficiency of the detector at its edge. As the electric field of the MRPC is not as homogeneous at the edge as it is in the center, this introduces a bias into the measured efficiency of the detector. There is a second, larger, overlap region between the first MRPC in the second module of each sector and the first MRPC of the third module of the next sector. This region is sketched in Figure 7.16. It extends up to the middle of the front counter and covers approximately one third of a counter's area. This analysis will thus focus on this sector overlap. Using the

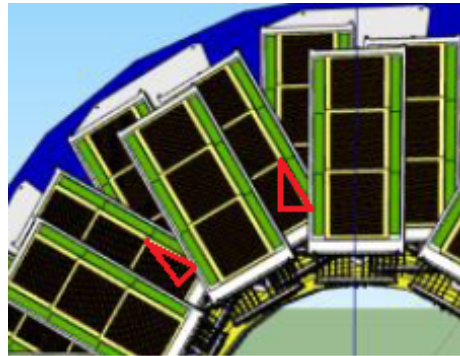


*Figure 7.16: Sketch of the overlap region between sectors on the eTOF wheel.*

$p_{track}$	$> 1 \text{ GeV}/c$
$\beta$	$> 0.98$
$\beta$	$< 1.02$
nSigmaPion	$< 3$
RefHitDeviation	$< 3 \text{ cm}$
Primary Track	true

**Table 7.1:** Cuts applied on reference tracks and their respective matched reference hits for the overlap analysis.

first MRPC in module 3 of each sector and the STAR TPC allows to create an interpolating reference for the first MRPC of module 2 of the next sector. This setup allows to test 12 of the MRPCs in eTOF for their efficiency.

The FXT data are most suited for such an analysis, as the primary tracks originate from a constant vertex position and cross the eTOF planes at steep angle. This analysis will focus on the FXT run at  $\sqrt{s_{NN}} = 7.7 \text{ GeV}$  taken in 2020. In this dataset, the efficiency is not impacted by the pre-amplifier damages described in Chapter 6.3.

To provide a high quality reference, strict cuts are placed on the track variables and the matching criteria between track and reference hit. The exact cuts can be seen in table 7.1.

Here,  $p_{track}$  is the momentum of the track and  $\beta$  is the relativistic velocity.  $\beta$  is calculated from the track path length, the STAR start time and the eTOF reference hit time. nSigmaPion is the deviation of the track dEdX from a pion dEdX, normalized to the TPC resolution. RefHitDeviation is the distance between the extrapolated intersection of the track with the reference detector plane. These criteria are intended to select straight, primary tracks while preserving sufficient statistics in the overlap region. The pion dE/dX cut has little particle discrimination power at this particle momentum, but it is still useful to remove a few mismatched reference hits from the sample.

For each selected pair of reference track and reference hit on the MRPC in the back, an intersection point with the DUT plane is calculated. There are two approaches to do this: In the helix approach, the tracks helix is calculated from the track momentum, the primary vertex and the magnetic field using the StHelix class. This helix is then intersected with the DUT plane. This procedure is identical to the normal track matching procedure described in Chapter 5.3.4. The predicted intersection in

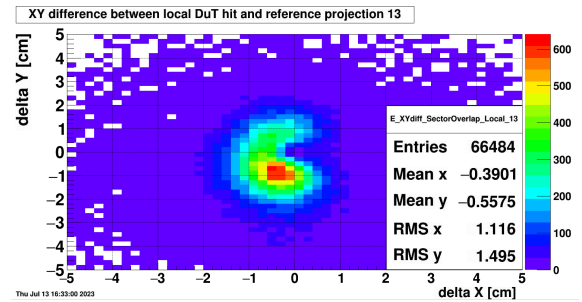


**Figure 7.17:** Position differences in DUT-local  $x$  and  $y$  coordinates between hits on DUT and interpolation in the helix approach.

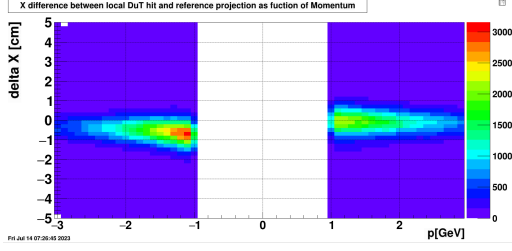


**Figure 7.18:** Difference in DUT-local X-position between the straight line extrapolation to the DUT and hits on DUT as function of reference track charge · momentum, before correction.

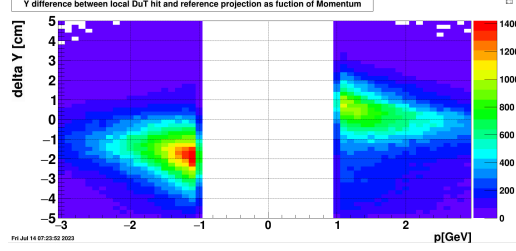


**Figure 7.19:** Difference in DUT-local Y-position between the straight line extrapolation to the DUT and hits on DUT as function of reference track charge · momentum, before correction.

this approach does not match well with the position of the closest eTOF hit (see Figure 7.17). The observable spiral pattern in the position difference between hit and intersection indicates a non-trivial bias in the prediction of the track intersection. This approach is therefore rejected for the further analysis.

To eliminate any uncertainties due to TPC alignment and track extrapolation, a straight line approach is taken instead. In this approach a straight line from the reference hit to the FXT vertex is intersected with the plane of the DUT counter. Since the counters are tilted towards the beam axis and rotated with respect to each other, this calculation has to be done in three dimensions. The DUT plane is described in global coordinates and normal form as follows:

$$\overrightarrow{DUT} : (\vec{x} - LtM(\begin{pmatrix} 0 \\ 0 \\ 0 \end{pmatrix})) \cdot LtM(\begin{pmatrix} 0 \\ 0 \\ 1 \end{pmatrix}) = 0 \quad (7.3)$$

Here, LtM denotes the transformation from the detector-local coordinate frames to the global coordinate frame using the geometry description of eTOF. This plane is then intersected by inserting the straight line:

$$\vec{x} = n \cdot \left( LtM(\begin{pmatrix} x_{ref} \\ y_{ref} \\ 0 \end{pmatrix}) - \vec{V} \right) \quad (7.4)$$

where  $x_{ref}$  and  $y_{ref}$  are the local coordinates of the reference hit and  $\vec{V}$  is the reconstructed global position of the event vertex. The distribution of the position difference between hit and intersection in this approach can be seen in Figure 7.20. The distribution is wide, but spiral pattern in the helix approach has vanished (compare with Figure 7.17)

In this simple approach, the calculated intersection point with the DUT plane deviates significantly from the true crossing point, as the tracks are curved in

STAR's magnetic field. This curvature can be ignored on the short distance between DUT and REF (approximately  $15\text{ cm}$ ), however, on the full distance between vertex and REF (approximately  $5\text{ m}$ ) it leads to a significant (momentum- and charge-dependent) angle of incident on the REF. The true intersection point of the track with the DUT plane is thus displaced from the straight line assumption.

To correct this issue, a simple data-driven correction is applied. The position difference in DUT-local X and Y coordinates between all track intrapolations and all DUT hits in a large radius around the intrapolation point are plotted as function of the track momentum and charge. An example for these plots (before correction) can be seen in Figure 7.19. These distributions are fitted with a Gaussian function, separately in bins of  $100\text{ MeV}$ . The calculated intersections are then shifted by the Gaussian means of the corresponding bin fit in both directions.

Figures 7.20 and 7.21 show the momentum-integrated differences in the X-Y plane between the intrapolation point and DUT hits before and after momentum correction for an example counter.

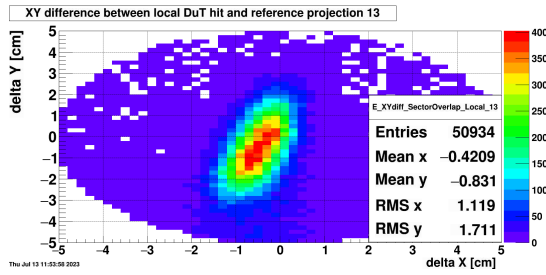


**Figure 7.20:** Position differences in DUT-local  $x$  and  $y$  coordinates between hits on DUT and intrapolation in the straight line approach *without* momentum correction for an example counter.

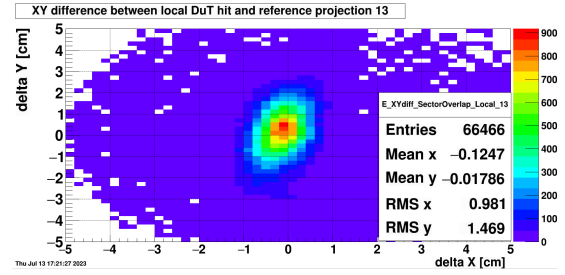


**Figure 7.21:** Position differences in DUT-local  $x$  and  $y$  coordinates between hits on DUT and intrapolation in the straight line approach *with* momentum correction.

After momentum correction, the hits show an approximately Gaussian distribution around the intrapolation point in both  $x$  and  $y$  direction. For almost all counters the RMS values are within  $1.0 \pm 0.1\text{ cm}$  in  $x$  and  $1.5 \pm 0.1\text{ cm}$  in  $y$ . The only exception is detector 19-3-1, due to a larger fraction of non-Gaussian background. A counter is considered efficient if a hit on the DUT is found within  $\Delta y < 4.5\text{ cm}$  and  $\Delta x < 3.0\text{ cm}$ . This cut corresponds approximately to  $3\sigma$  limits of the distribution and is thus expected to contain  $> 99.0\%$  of all correlated hits. To reduce uncorrelated matches a loose time cut of  $\pm 1\text{ ns}$  between the measured time of the DUT hit and the expected time calculated from the time of the reference hit, the measured velocity of the track and the distance between REF hit and DUT hit is applied. Furthermore, only events with `goodEventFlag()` set on both DUT and REF will be taken into account.

Figure 7.22 shows the efficiency of all DUT counters (first counter of the second module of each sector). The average counter efficiency is calculated by dividing

the number of references with a corresponding DUT hit by the total number of references within the sketched area in the center of the overlap. This area cut is used to remove edge effects. The errors provided in the figures are only statistical.

The following observations can be made:

- Counter 24-2-1 is missing from this analysis. This is due to the fact that its reference counter, 23-3-1 does not have a sufficient number of events with `goodEventFlag()` set. In this case, the FEE instability can be correlated to an increased dark current and a developing electric short which forced this counter to be taken out of the data taking a few weeks later.
- Counter 19-2-1 has two GET4s with a large fraction of outages (here visible between  $-8 < x < -4$  and  $4 < x < 8$ ) and consequently a significantly reduced hits compared to their neighbors. One GET4 is more than 65 % inactive. One full half of the detector is 10 % synchronously inactive. Even though only events that do not show any GET4 outages have been taken into account, the detector efficiency is significantly reduced compared to all other counters. This correlation could mean either that the FEE instability corrupts also apparently good data or that an electric issue in the counter causes the FEE instability.
- The average efficiency varies greatly between the tested counters. Omitting the above mentioned two counters, the measured efficiency varies between 75 % and 85 %. No difference between USTC and THU-type counters can be observed within these variations.
- The measured average efficiency of the best case counter is significantly below the expected values which have been achieved in cosmic measurements (99 % and 93 % in USTC and THU-type counters, respectively [67]).
- A gradient along the y-axis of the DUT counter can be observed. The measured efficiency in the center of the DUT is approximately 10 % higher than at the edge of the cut area. Since the lower edge of the cut area is 4.5 cm away from the physical edge of the counter, this cannot be explained by edge effects (field inhomogeneity) of the counter.

To understand the observed low efficiency, the method was cross-checked in simulations. Unfortunately, at the time of this writing, no large-scale simulation data production including eTOF is available. In a private production with limited computing resources, 50000 simulated AuAu collision event at  $\sqrt{s_{NN}} = 7.7 \text{ GeV}$  based on the ultra-relativistic quantum-molecular dynamics (UrQMD) model have been generated. The particle tracks from these events have been propagated through the STAR geometry using the GEANT3 transport model. The eTOF detector response has been modeled using the StEtofSimMaker code developed by Y. Söhnngen and F. Seck. In this simulation data sample, a simulated eTOF

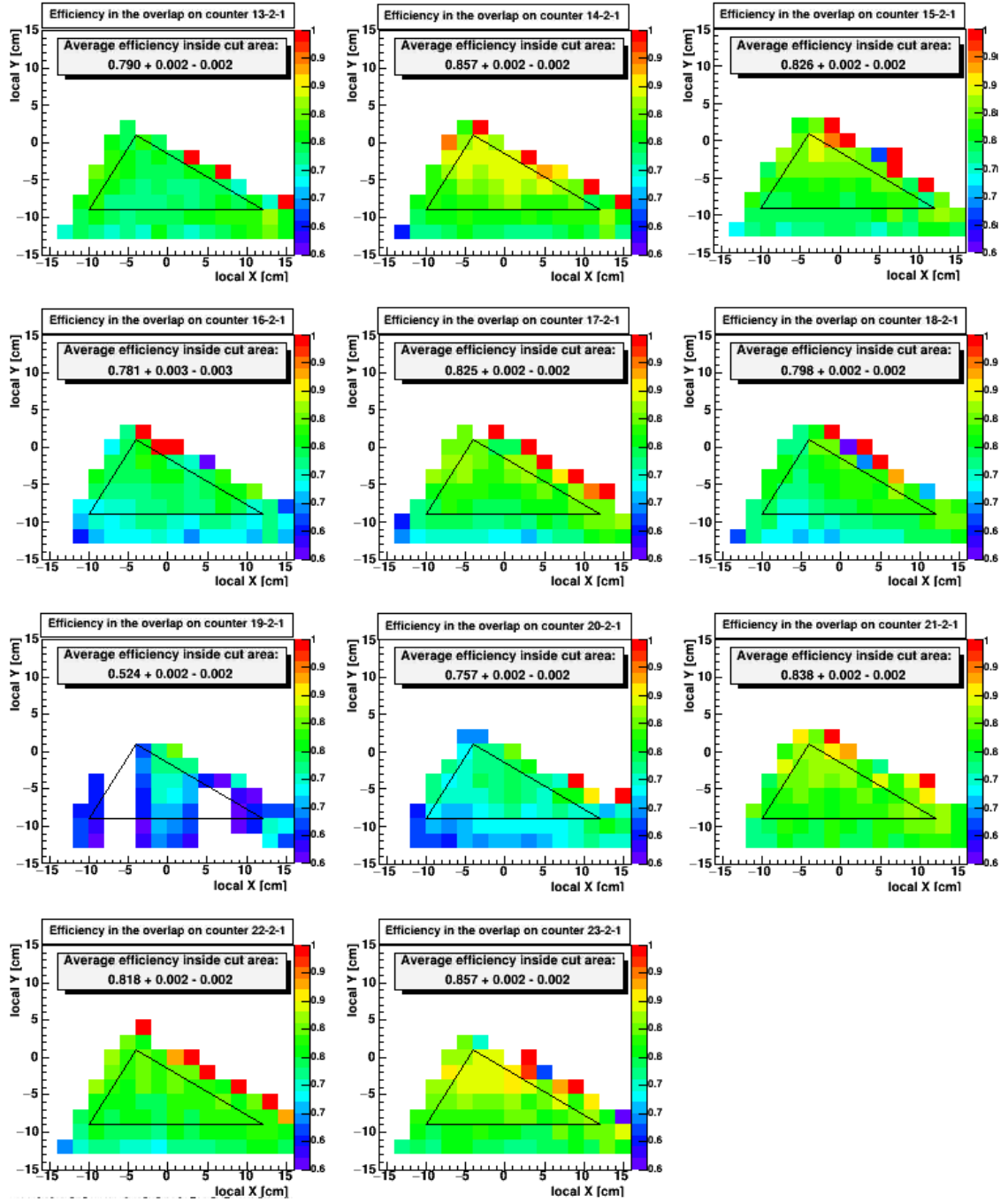


**Figure 7.22:** Efficiency of all DUT counters (first counter of the second module of each sector) as function of the position of the interpolation point on the surface of DUT. Counter 24-2-1 is not included as there are no valid references. Upper and lower limit of the 68.3% statistical confidence interval are given.

hit is generated for each GEANT track crossing point, corresponding to an input detector efficiency of 100 %. cluster size and ToT of this simulated hits are drawn randomly from measured distributions. The position and timing of the simulated hit are smeared with input time and position resolutions. In this case, a time resolution of 60 ps as well as perfect eTOF position resolution have been assumed. From the simulated eTOF hits, StEtofDigis are then generated, taking into account randomized channel ToT gain variances and FEE channel dead times. These StEtofDigis are then processed by the normal data reconstruction chain of StEtofHitMaker and StEtofMatchMaker. The same overlap analysis as above is applied to the simulation data.

The simulated data sample contains a total of 2819 good reference hits in the overlap region. This number of references is statistically insufficient for a conclusive understanding. It can only provide hints to why the measured overlap efficiency in data is as low as observed. On average, in the simulated sample, the overlap efficiency inside the cut region is 86.8 %, compared to 82.2 % in the data sample. Assuming a simple linear scaling:

$$\frac{OvEff_{data}}{DetEff_{data}} = \frac{OvEff_{sim}}{DetEff_{sim}} \quad (7.5)$$

where OvEff and DetEff stand for the measured overlap efficiency and the intrinsic true detector efficiency and using  $DetEff_{sim} = 100 \%$ , one can estimate the true detector efficiency in the data as  $DetEff_{data} \approx 94.7 \%$ . This is in line with the expectations from cosmic data. The simulated data also show a spread in the overlap efficiency between 81 % and 92 %, despite equal input detector performance, but with a large statistical error of 2.5 %. This is a similar spread range as in the data sample. One reason for the low measured overlap efficiency is the matching between TPC track and reference hit.

The loss of DUT hits in the simulation can be broken down as follows:

- A: For only 85 % of all valid references, a GEANT track intersection with the same MC truth ID as the reference hit was found on the DUT counter. Correspondingly, 15 % of cases have no GEANT track intersection matching the reference MC truth ID. The most likely explanation is that the reference hit was produced by a secondary particle created inside the DUT.
- B: For 76 % of all valid references, at least one digi with a MC truth ID matching the reference hit was found on the DUT. The most common explanation for this further reduction is that digis are lost due to FEE dead time in the presence of other tracks.
- C: For 69 % of all valid references, a hit with with a MC truth ID matching the reference hit could be reconstructed on the DUT. This is a consequence of missing digis one side of a strip due to FEE dead time.



- D: For 66 % of all valid references, a fully reconstructed hit with a MC truth ID matching the reference hit found on the DUT within the cut range around the expected position. This further reduction is due to the uncertainties in the expected hit position.
- E: For only 6 % of all valid references more than one DUT hit within the cut range was found.
- F: As the measured overlap efficiency is higher than the probability to find a hit with matching MC truth ID inside the cut radius another hit with different MC truth ID has to be inside the cut radius for 20 % of all valid references. This is a consequence of A and E.

Generally, interference from other tracks appears to be a big problem in this analysis (see points A, B and F). This observation does not match the expectation from the relatively low primary track density. Since the overlap region is located behind the sector boundary of the TPC, the high material content along the trajectory of tracks in the overlap region may create significant interference from secondary tracks. Further simulation investigations with higher statistics will be required to validate this or a similar method once high-statistics simulations are available. As it stands, measurements from cosmic data and mCBM provide more trustworthy insight into the detector efficiency for CBM-TOF prototypes than the scaled estimate from eTOF's overlap analysis.

### 7.2.3 Matching Efficiency

While the detector efficiency is most important for CBM-TOF, matching efficiency is the quantity that is more relevant to STAR physics analysis. It is defined as the fraction of tracks pointing to eTOF active area which can be matched to an eTOF hit successfully. It depends on the extrapolation of the TPC track to eTOF and the detector efficiency. STAR is not designed as a forward detector. Thus the material budget in front of eTOF is not minimized and the magnetic field is no longer homogeneous close to the eTOF wheel. This limits the quality of the track extrapolation.

Matching efficiency also depends on the chosen criteria track matching. The track provides momentum, specific energy loss and the position where it intersects with eTOF. The eTOF hits provide their local position, hit time and time over threshold. There is little correlation between the specific energy loss of a track and the time over threshold of the hit, as the later heavily depends on the location of the primary ionization in the MRPC gap. This information is thus not used in track matching. The timing information is also discarded in the first step, as matching based on timing to measure the time of flight of the reconstructed particle would lead to auto-correlations. Therefore, only the position information from track and hit are used as criteria for the track matching.



To calculate the position difference, the track intersection with any eTOF counters is transformed into the local reference frame of the counter. Here, the resolutions in local  $x$  and  $y$  are not equal. Local  $x$  is strip position of the hit. The resolution in this direction is mostly determined by the strip pitch. Local  $x$  also corresponds largely to the transverse direction of the track<sup>5</sup>. Local  $y$  is the position along an MRPC strip for the detector hit. The resolution in this direction depends on the FEE time resolution. For the track, local  $y$  largely corresponds to the azimuthal direction and thus to the direction of the Lorentz force in the toroidal magnetic field of STAR. The chosen cuts have to take these different resolutions into account.

The choice of a cut distance is a trade-off between efficiency and purity. A wider cut includes a larger fraction of the correct matches, but also an increasing number of wrongly matched hit. The topic of purity will be discussed in Chapter 7.2.4.

Figures 7.23 and 7.24 show the distance between intersections and close-by detector hits for all eTOF counters in a data sample from the  $\sqrt{s_{NN}} = 7.7 \text{ GeV}$  FTX runs in 2020. An elliptic cut with a half axis of  $5 \text{ cm}$  in local  $x$  direction and  $7 \text{ cm}$  in local  $y$  direction has been applied around the intersection point. One can see an approximately Gaussian-shaped central peak in both directions with significant tails towards larger distances. The central peak has been fitted with a Gaussian function. It is slightly displaced from zero due to residual misalignment, which was considered small compared to the width of the peak. The central peak is assumed to correspond to well-matched pairs of track intersections and detector hits, while the tails contain an increasing fraction of combinatorial background.

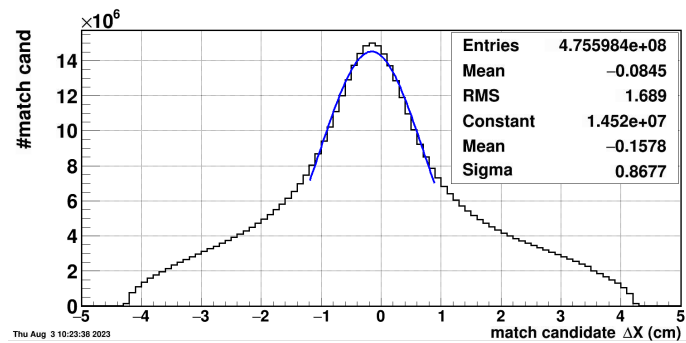


**Figure 7.23:** Difference between projected track intersection point and close-by hits in detector-local  $x$  coordinate.

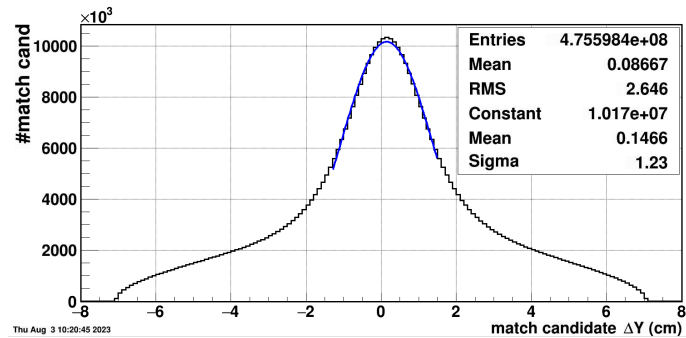


**Figure 7.24:** Difference between projected track intersection point and close-by hits in detector-local  $y$  coordinate.

<sup>5</sup>The two directions are identical in the center of the middle module of each sector and are rotated by  $30^\circ$  for the side modules

The width of the Gaussian fits provides an estimate of the combined position resolution of the MRPC and the TPC track extrapolation. At  $\sigma_x = 0.87 \text{ cm}$  and  $\sigma_y = 1.23 \text{ cm}$  these combined resolutions differ significantly from what would be expected as pure MRPC resolution. The pure MRPC resolutions can be estimated from the strip pitch and the time resolution of the electronics, following the equations 4.9. Using the strip pitch of  $1 \text{ cm}$  for all eTOF counters as well as a typical electronics resolution of  $25 \text{ ps}$  (see Chapter 7.3.3 for further discussion of the electronics resolution in eTOF) and an average signal velocity of  $\approx 18 \text{ cm/ns}$  (see Chapter 7.1.3), one arrives at  $\sigma_{x,MRPC} < 0.29 \text{ cm}$  and  $\sigma_{y,MRPC} < 0.32 \text{ cm}$ . This suggests a major contribution due to the limited pointing accuracy of the TPC.

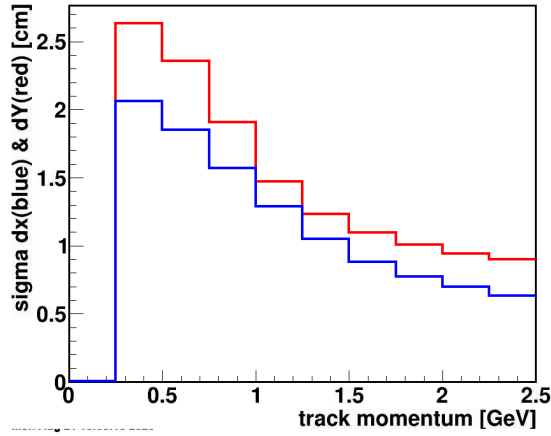


**Figure 7.25:** Width of the distance distribution between hit and projected track intersection (matching width) as function of track momentum. The distributions in  $x$  and  $y$  are fitted in their full range by a Gaussian distribution, as opposed to the center only fit in Figure 7.23 and 7.24.

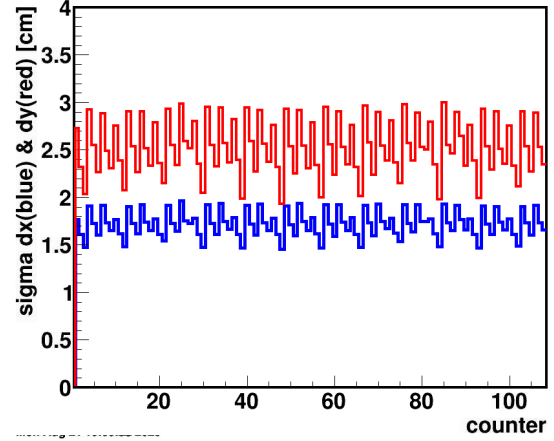


**Figure 7.26:** Width of the distance distribution between hit and projected track intersection (matching width) for each eTOF counter separately. The distributions in  $x$  and  $y$  are fitted in their full range by a Gaussian distribution, as opposed to the center only fit in Figure 7.23 and 7.24. The counter numbering ( $x$ -axis) is calculated as  $(\text{sector} - 13) \cdot 9 + (\text{module} - 1) \cdot (\text{detector} - 1)$ .

For simplicity of the further discussion, the matching width (in  $x$  and  $y$  separately) is defined as the width of a Gaussian fit over the full range of the distribution of the difference in  $x$  and  $y$  between track intersections and close-by eTOF hits. Looking more differential into the matching behavior, it can be observed that the matching width strongly depend on track momentum (see Figure 7.25). The MRPC position resolution is largely independent of the particle momentum<sup>6</sup>. On

<sup>6</sup>Hit clusters over more than one strip allow for an improved position resolution of the MRPC, but as the avalanche charge in the MRPC depends more on the (random) depth of the primary ionizations in the gap than on the total energy deposition. The cluster size is therefore only weakly correlated with track momentum.

the other hand, the pointing accuracy on the TPC is momentum dependent due to the curvature of the track and scattering of the particle along its trajectory. The strong momentum dependence is an indication that the observed large matching width is indeed due to limitations in the track reconstruction and not due to a significant underestimation of the MRPC resolution. For high momentum particles, the matching width is significantly improved, but still large compared to the native MRPC resolution.

The matching width is also not equal for all eTOF counters. In Figure 7.26 a clear pattern can be observed. In each module (every three counters), the first <sup>7</sup> counter has the largest matching width, while the third counter has the smallest. The matching width improves the further away a counter is from the beam axis due to a longer track length in the TPC (and thus more track fit points). Less clearly, but still visible is that the first module<sup>8</sup>, the center module, in each sector (each group of nine counters) has a slightly smaller matching width than the second and third module. This is both due to the shorter extrapolation distance from the last TPC track point and due to the influence of the material budget of the TPC sector boundaries on the outer modules.

For the following analysis of the matching efficiency, an elliptical position cut in the form

$$\sqrt{2} > \sqrt{\left(\frac{x_{hit} - x_{intersection}}{\Delta x_{cut}}\right)^2 + \left(\frac{y_{hit} - y_{intersection}}{\Delta y_{cut}}\right)^2} \quad (7.6)$$

is applied.

Here,  $x$  and  $y$  describe the detector-local position of the hit and the track intersection.  $\Delta x_{cut} = 3 \text{ cm}$  and  $\Delta y_{cut} = 5 \text{ cm}$  have been chosen to consider a track matched for this analysis. This corresponds to approximately twice the matching width in each direction.<sup>9</sup> The timing of the hit and the momentum of the track will not be taken into account to avoid auto-correlations in the particle identification.

Due to the limited pointing accuracy of the tracks, a significant part of the eTOF active area is affected by border effects. Tracks pointing near a counter may have indeed crossed the counter and be match-able to a hit on the counter. Similarly, tracks pointing to the edge of the counter might have actually missed it. To calculate the matching efficiency in a well normalized way, all track intersections within the nominal counter surface area are counted, independent of whether they are matched or not. Of the intersections within one matching width outside the counter, only those that can be matched are counted. These compensate those tracks that are wrongly assumed to cross the counter and thus counted too much. If

---

<sup>7</sup>the counter closest to the beam-line

<sup>8</sup>counter 1,2,3,10,11,12...

<sup>9</sup>For the production of eTOF data, a wider matching cut of  $x_{cut} = 5 \text{ cm}$  and  $y_{cut} = 7 \text{ cm}$  has been chosen. This more inclusive choice allows to adjust the cuts at post-production level to fit specific physics analysis requirements.

a track has intersections with multiple eTOF counters, it is also only counted once, when considering the matching efficiency of eTOF as a whole. When looking at the matching efficiency of individual counters on the other hand, each intersection of a track with a different eTOF counter is considered.

Furthermore, a set of cuts is applied to filter out low quality tracks:

- $p_{track} > 150 \text{ MeV}$
- At least 15 track points are available in the TPC.
- At least 52% of all possible TPC track points have been included in the track fit.
- The track is a primary track.

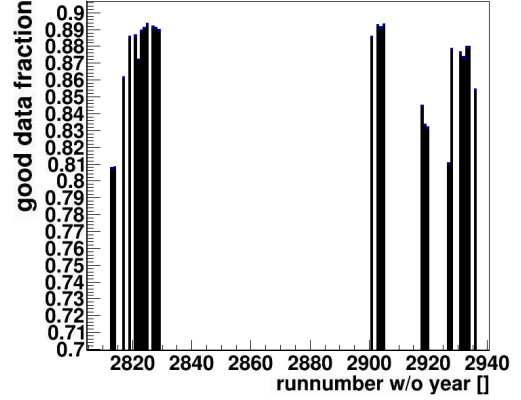


**Figure 7.27:** Fraction of `goodEventFlag()` set in each run of the data sample. One flag is calculated for each counter and each event (compare to Figure 6.17 and the explanations there.)

For now, only intersections on eTOF counters with `goodEventFlag()` set in a given event are taken into account. On average, the flag is set for 87.3 % of all counters in an event. This fraction varies between runs in the range of 80.9 % to 89.7 %. The distribution the fraction of `goodEventFlag()` set in each run can be seen in Figure 7.27.

The matching efficiency obtained this way for all USTC and THU counters collectively from the  $\sqrt{s_{NN}} = 7.7 \text{ GeV}$  FTX runs in 2020 is shown in Figure 7.28. A total of 12.3M events with eTOF hits are included in this sample. A strong momentum dependence can be observed. The efficiency of the MRPC depends only on the probability of a primary ionization in the upper region of the gap. This is more likely for low momentum particles in the Bragg-peak, but the eTOF counters have been designed to be efficient even for minimum ionizing particles. The steep drop of the matching efficiency towards low momenta is thus due to lower pointing accuracy (see Figure 7.25), higher energy loss and increased scattering. Fortunately, the low matching efficiency of eTOF in this momentum region is not impacting STAR's physics performance significantly, as particle identification is still possible with only the TPC's  $dE/dX$  measurement. For the further discussion on the matching efficiency, unless mentioned otherwise, the focus will thus be on the momentum region between  $p_{track} > 0.8 \text{ GeV}/c$  (an upper limit for the  $K/\pi$  separation capabilities of the  $dE/dX$  measurement) and  $p_{track} < 3.5 \text{ GeV}/c$  (the limit of the  $k/p$  separation capabilities of eTOF). These limits were decided early during the BES-II operation as the relevant efficiency window for eTOF and are kept in this analysis for comparability with earlier publications (for example: [86]).

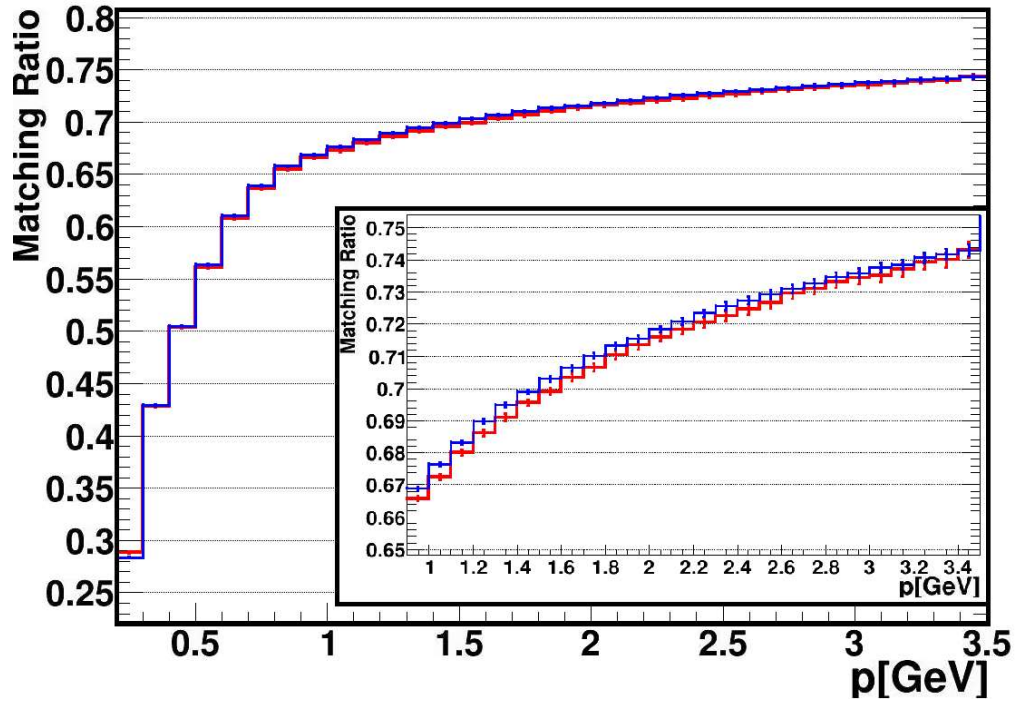


*Figure 7.28: Matching efficiency - Fraction of tracks with an intersection on an eTOF counter for which an close-by detector hit can be found, as function of track momentum. **Red:** All THU-type counters. **Blue:** All USTC-type counters. **Side box:** Zoom into the region of  $p > 1$  GeV/c. Error bars represent the  $5\sigma$  confidence interval (to improve visibility) for statistical uncertainties only.*

The integral efficiency over this region is 70.0 % and 69.7 % for USTC and THU counters respectively.

The dependence on the maximal matching distance cut is shown in Figure 7.29. This dependence can be used as a reference on the effect of reduced distance cuts in further analysis. While the matching efficiency does not level off in this range, more than half of all found matches (corresponding to a matching efficiency of 47.4 %) are within a narrow cut range of  $dx < 0.6 \text{ cm}$  and  $dy < 1.0 \text{ cm}$ . A cut of  $dx < 1.5 \text{ cm}$  and  $dy < 2.5 \text{ cm}$ , half the cut range used in this analysis, already yields a matching efficiency of 61.9 %. This matching efficiency of course has to be balanced against the purity of the matching.

A quick estimate of this trade-off can be done using Monte-Carlo simulations. This estimate uses the same MC sample as used in Chapter 7.2.2. Figure 7.30 shows the integral purity as function of the same elliptical radius as the matching efficiency. Purity is here defined as the fraction of matches for which the MC

truth id of the track agrees with the MC truth id of the matched hit. One can observe that for a large cut, as used in this analysis, a significant fraction of tracks,  $> 30 \%$ , are already mismatched. At cut of  $dx < 1.5 \text{ cm}$  and  $dy < 2.5 \text{ cm}$ , half the cut range used in this analysis, a purity of 84.0 % is reached. It should also be noted, that the mismatch fraction is not negligible even at the tightest cuts. On the other hand, this quick analysis underestimates the purity slightly due to two reasons: Firstly, cases in which a track is matched to a hit generated from a short-range secondary track, generated for example in the box of the MRPC, of the correct track are counted as mismatches. Secondly, all tracks matched to a hit which has been reconstructed from contributions from more than one

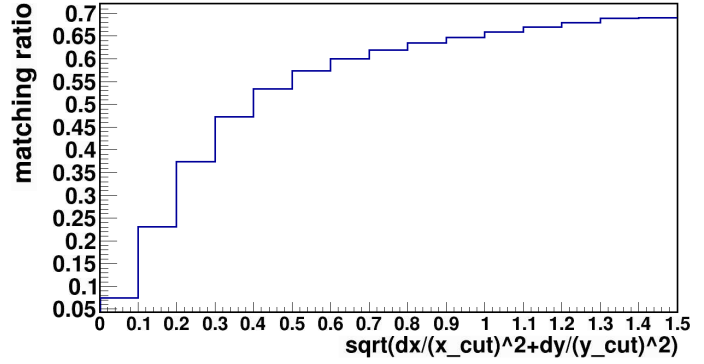


**Figure 7.29:** Integrated matching efficiency over the track momentum range of  $0.8 \text{ GeV}/c < p < 3.5 \text{ GeV}/c$  as function of the elliptical cut range (Compare with Eq.7.6) for all of eTOF.

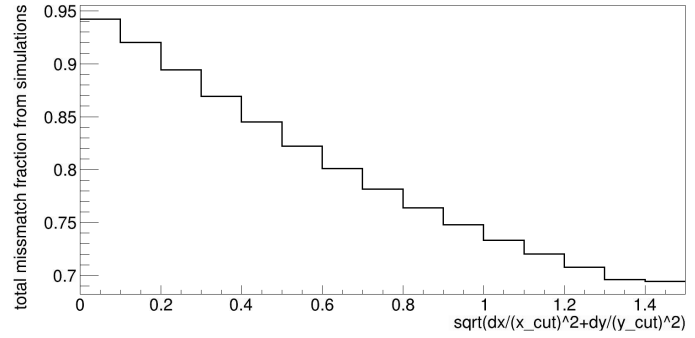


**Figure 7.30:** Integrated purity over the track momentum range of  $0.8 \text{ GeV}/c < p < 3.5 \text{ GeV}/c$  as function of the elliptical cut range (See Eq.7.6) for all of eTOF. Integrated purity means that each bin shows the purity of all matches within an elliptical distance smaller than the upper boundary of the bin.

track are counted as mismatches. A full analysis of these contributions requires a high-statistics simulation production including eTOF data and, based on that, a thorough validation of the eTOF simulation procedure.

The systematic uncertainty due to border effects can only be estimated by looking at two different approaches of counting matches and intersections on the edge. When counting all intersections on the nominal counter surface and neither intersections outside the counter surface nor their matches, the integral matching efficiency over the momentum range of  $0.8 \text{ GeV}/c < p < 3.5 \text{ GeV}/c$  is 69.3 % and 68.9 % for USTC and THU counters respectively. This approach underestimates the true matching efficiency as, due to limited pointing accuracy, not all counted intersections belong to tracks that actually crossed the counter. When counting only intersections which are close to the center of the MRPC and at least one matching distance away from the counter edge (3 cm in x-direction and 5 cm in y-direction) and their matches, the integral matching efficiency for the same momentum range is 71.2 % for both USTC and THU counters. This approach guarantees that only intersections belong to tracks that actually crossed the counter are counted. But it may overestimate the matching efficiency since potential detector inefficiencies due to the field drop-off at the counter edge are excluded. Comparing all three approaches, the uncertainty due to border effects can be estimated to be  $\pm 1.0 \%$ .

The first important dependence to study is the time dependence of the matching efficiency, given the observed FEE outages in the system (see Chapter 6.4.1). Figure 7.31 shows the matching efficiency of USTC and THU-type counters separately for each of the 26 runs in this data sample.

When looking at all events, without taking advantage of the `goodEventFlag()`, a significant variance in the matching efficiency can be observed between the runs. The RMS for these distributions is 2.06 % for USTC-type counters and 1.25 % for THU-type counters. The difference between the two MRPC types occurs because the two sectors (19 and 23) with most unstable FEEs both correspond to USTC-type counters. Using only events with `goodEventFlag()` set for each counter however, the matching efficiency is very stable. The RMS between runs is reduced 0.28 % and 0.40 % respectively. For comparison, the bTOF system, without any DAQ instabilities, has a run-by-run matching efficiency difference of 0.25 % RMS in the same dataset. The `goodEventFlag()` thus achieves its intended goal to provide a stable eTOF efficiency despite the instabilities of the FEE.

The residual variance between runs encompasses any residual calibration differences of both eTOF and TPC, as well as any performance-affecting differences in unmonitored variables like detector temperature or gas purity. It can therefore be seen as an estimate of the systematic uncertainty for predictions of the matching efficiency of eTOF in similar datasets.

The matching efficiency is also not homogeneous over all counters of one type. Figure 7.32 shows the matching efficiency for each counter of eTOF, both for all events and only for events with `goodEventFlag` set for each counter. It can be observed:



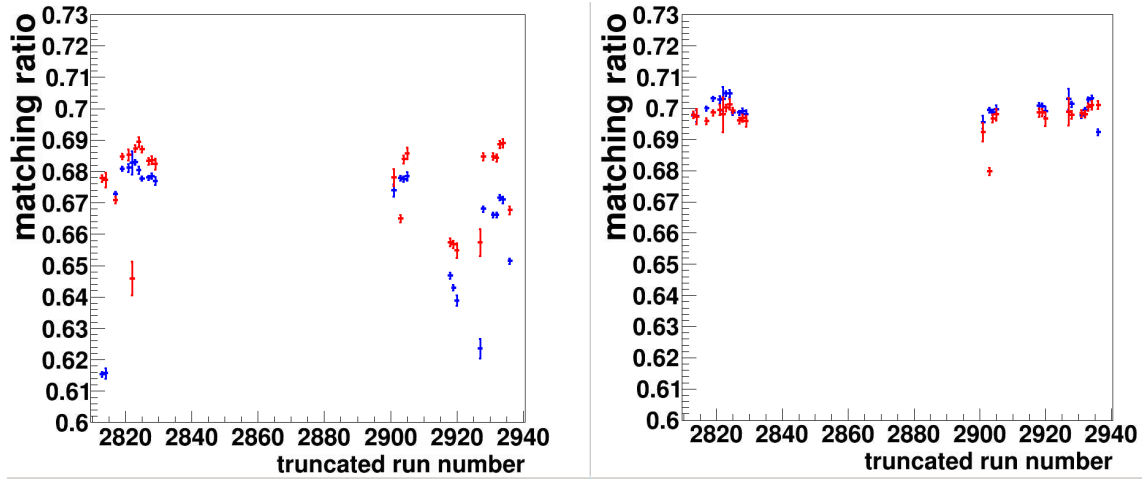


**Figure 7.31:** Integrated matching efficiency over the track momentum range of  $0.8 \text{ GeV}/c < p < 3.5 \text{ GeV}/c$  for each run in the data sample. The truncated run number (x-axis) is calculated as  $100 \cdot [\text{day in year}] + [\text{run number during day}]$ . For better visibility, Errors bars show the  $5\sigma$  statistical confidence interval as calculated by the ROOT::TEfficiency class. **Left:** All events in the sample. **Right:** only events with goodEventFlag set for each counter. **Red:** All THU-type counters. **Blue:** All USTC-type counters.

- The average over all counters is slightly lower than the global efficiency shown in Figure 7.28. eTOF's geometry allows multiple chances to detect tracks close to the overlap region. The global system efficiency is therefore higher than the average counter efficiency.
- The majority of all counters show a matching efficiency between 65 – 75 %.
- For the majority of counters, events with goodEventFlag set only show slightly improved matching efficiency by about 1 – 2 %. For many of the least efficient counters, a significant improvement of up to 15 % can be observed, bringing those counters back into the same range as all other counters.
- Only one outlier, counter 96 (Sector 23, module 3, counter 1), remains when using goodEventFlag(). This counter has already been observed to have significant problems with its FEE (compare with Figure 6.13 and 6.14). Even when goodEventFlag is set this counter under-performs significantly. This observation indicates counter damage in addition to the FEE instability. This damage was confirmed by the observed electrical breakdown of the counter following the data taking of this sample.
- No clear pattern similar to the one observed in the matching width (see Figure 7.26) can be seen in the efficiency. When averaging the counters of the same position in each sector, counter 1 in module 1 (the counter closest to the beam) and counter 2 in module 2 and 3 (counters partially shadowed behind



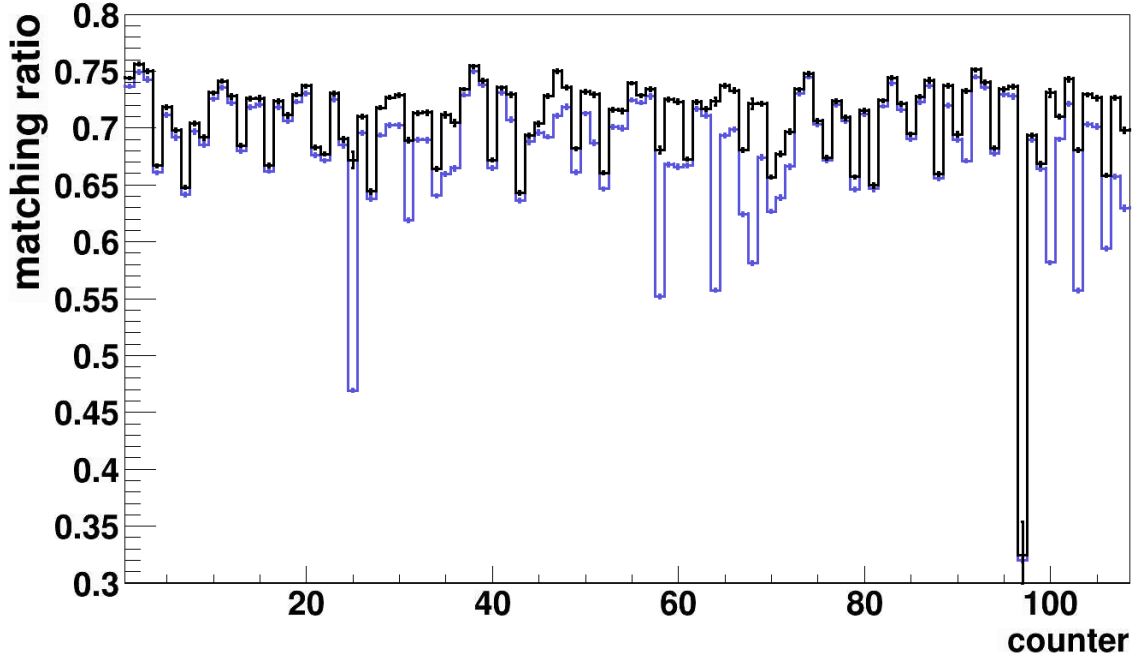


**Figure 7.32:** Integrated matching efficiency over the track momentum range of  $0.8 \text{ GeV}/c < p < 3.5 \text{ GeV}/c$  for each counter. The counter numbering ( $x$ -axis) is calculated as  $(\text{sector} - 13) \cdot 9 + (\text{module} - 1) \cdot (\text{detector} - 1)$ . For better visibility, Errors bars show the  $5\sigma$  statistical confidence interval as calculated by the ROOT::TEfficiency class. **Blue:** All events in the sample. **Black:** only events with goodEventFlag set for the respective counter.

the TPC sector boundaries) show lowered average matching efficiency by up to 7 % compared to the other counters. After correcting for the average matching efficiency of each counter's position inside the sector, the RMS of the matching efficiency between counters is still 4.0 %. This implies non-negligible differences in the intrinsic MRPC efficiencies.

The varying efficiency over the eTOF wheel can be better visualized in global coordinates. Figures 7.33 and 7.34 show the fraction of matches for primary tracks in different momentum ranges as function of the pseudo-rapidity and azimuthal angle of the track at the primary vertex. Unlike in the previous analysis of the matching efficiency, the number of matches is here normalized by the total number of tracks instead of only the tracks which intersect with eTOF counters. It thus includes also acceptance effect and will be denoted as matching "efficiency  $\times$  acceptance". In this normalization, it is also not possible to take the goodEvent-Flag() into account, as tracks are not checked for their intersection with individual counters. The bTOF region is included in this analysis to allow a direct comparison of eTOF and bTOF performance. The matching criteria for eTOF are as previously described in this analysis. For bTOF, the default matching criteria used in STAR data production have been applied.

The pseudo-rapidity is given relative to the fixed target vertex, but uses negative values to be consistent in direction with STAR collider conventions. The pseudo-rapidity of the beam is  $\eta = -\infty$  in this convention.  $\eta = 0$  thus corresponds to the west side edge of the TPC, where the target foil is located. Around  $\eta = -0.85$ , the central membrane of the TPC is located, causes the observable thin acceptance gap. bTOF covers the pseudo-rapidity region from  $0 > \eta > -1.4$ , while the region of  $\eta < -1.6$  is covered by the eTOF wheel. The raw distribution of tracks shows already an inhomogeneity due to the TPC reconstruction efficiency. When looking at higher momentum, straighter tracks (see Figure 7.34, left side) the sector structure of the TPC becomes clearly visible. A minor sinusoidal inhomogeneity in the azimuthal direction due to the displacement of the fixed target vertex from the center of the TPC can also be seen. On bTOF, Figure 7.34, center, shows the module and pad row structure of the east side. Several counters were inactive during this run period and can be seen as efficiency holes. On eTOF, the acceptance gap between sectors on the outer side of the wheel is visible (compare Figure 4.1) between  $-1.5 > \eta > -1.8$ . Towards lower pseudo-rapidities, an gap can be seen between the sectors due to the TPC sector boundaries. Around  $\phi = 1.1$  and  $\eta = -1.9$ , an efficiency hole in eTOF can be seen due to the damaged counter 23-3-1. One can also observe a low efficiency band over the full azimuthal range around  $\eta = -1.9$ . This can be traced to the shadow of the boundary between inner and outer TPC at a radius of  $1.25\text{ m}$  from the beam axis. In Figure 7.33 all these structures are washed out in azimuthal direction due to momentum-dependent the deflection of particles in the magnetic field.

Taking all these known issues into account, one can compare the matching efficiency in regions with low acceptance deficits: The center of each eTOF sector and

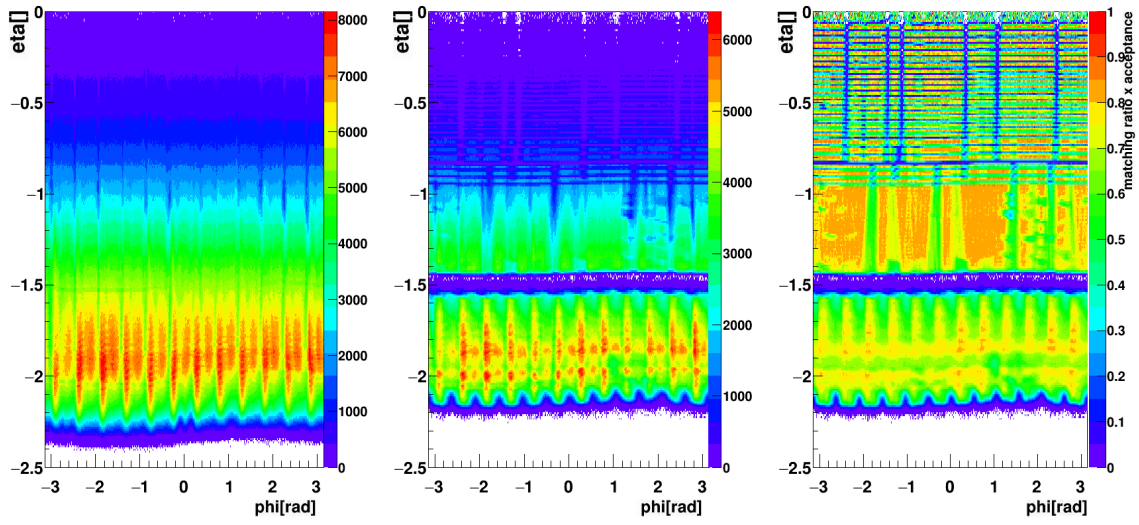


**Figure 7.33:** TOF matching efficiency  $\times$  TOF acceptance for primary tracks within a momentum range of  $0.8 \text{ GeV}/c < p < 3.5 \text{ GeV}/c$ , including both eTOF and bTOF as function of track pseudo-rapidity and azimuthal angle. **Left:** All TPC tracks. **Center:** TPC tracks with a bTOF or eTOF match. **Right:** Quotient of the center and left histogram, showing local matching efficiency  $\times$  acceptance.

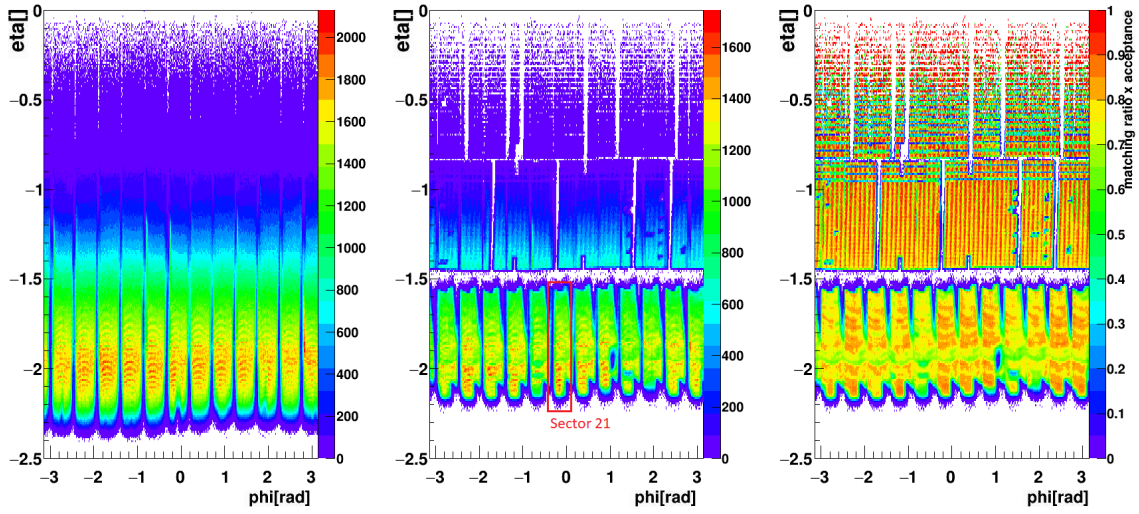


**Figure 7.34:** TOF matching efficiency  $\times$  TOF acceptance for positively charged, primary tracks within a momentum range of  $2.0 \text{ GeV}/c < p < 3.5 \text{ GeV}/c$ , including both eTOF and bTOF as function of track pseudo-rapidity and azimuthal angle. The higher momentum cut and exclusion of negative particles means all tracks are deflected similarly in the magnetic field. This allows a better resolution of local structures compared to Figure 7.33. **Left:** All TPC tracks. **Center:** TPC tracks with a bTOF or eTOF match. **Right:** Quotient of the center and left histogram, showing local matching efficiency  $\times$  acceptance.

the center of the bTOF east side modules. These regions cover a smaller fraction of eTOF compared to bTOF. eTOF is more impacted by acceptance limitations and material budget.

bTOF has a maximal matching efficiency of 80 – 82 % in the center of its east side modules (orange areas in 7.33). Meanwhile eTOF has a maximal matching efficiency in the center of its sectors (yellow / dark yellow areas in 7.33) between 70 – 80 %. As the detector efficiency of bTOF is assumed to exceed 95 % [50], this implies that eTOF has operated during the FXT runs close to the design detector efficiency of 90 %.

The largest remaining issue with eTOF track matching is the significant matching impurity, as shown in Figure 7.30. However, for physics analysis, the purity can be optimized by smart cut selection at post production level. As an example, a momentum dependent matching width cut of the form:

$$\begin{aligned} |\Delta x_{cut}| &< 2 \cdot MW_x(p) \\ |\Delta y_{cut}| &< 2 \cdot MW_y(p) \end{aligned} \quad (7.7)$$

is applied.  $MW_x(p)$  and  $MW_y(p)$  refer to the momentum-dependent matching width which can be read off from Figure 7.25. Figure 7.35 shows the matching efficiency and purity achieved with such a cut. The purity has been determined based on MC simulations and the matching efficiency has been calculated for the above used data sample from the  $\sqrt{s_{NN}} = 7.7 \text{ GeV}$  FXT run. The same number of track intersections have been used in the calculation as previously. Thus the matching efficiency in the high momentum region is obviously reduced as fewer matches pass the tighter cut.

In the intermediate momentum region between  $1 \text{ GeV}/c$  and  $2 \text{ GeV}/c$ , the matching efficiency declines, possibly indicating that this cut may progress too steeply in this region. At momenta above  $2.5 \text{ GeV}/c$ , the matching efficiency is rising again, as the cut is kept constant for higher momenta. Over the full eTOF PID relevant momentum region between  $0.8 \text{ GeV}/c$  and  $3.5 \text{ GeV}/c$  the integrated matching efficiency has been reduced from 69.9 % to 58.7 %. At the same time however, the integral purity in this momentum region is 90.5 %. This purity is significantly higher than what a flat reduction of the matching radius could achieve at a similar efficiency (compare figures 7.30 and 7.29).

A matching cut in this fashion thus allows eTOF data to achieve the high purity necessary to be used in precision analysis while preserving a good efficiency. The

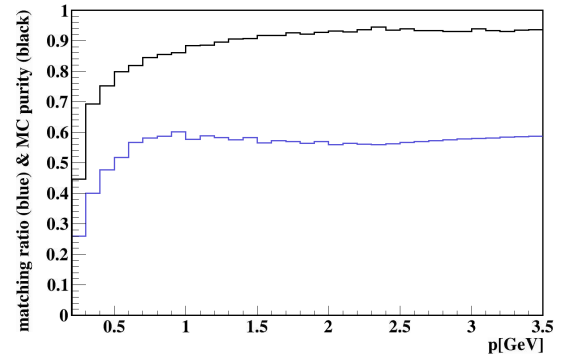


**Figure 7.35:** Matching efficiency (blue) and matching purity (black) estimate from Monte-Carlo using a momentum depended cut on the distance between hit and intersection.

purity could be further increased using cuts depending additional TPC dEdX information, especially in the momentum region  $p < 1.0 \text{ GeV}/c$ .

One final data point to look at is the performance of eTOF at the end of the BES-II run period. Figure 7.36 shows (analogue to Figure 7.28), the matching efficiency for USTC and THU counters at the end of the  $7.7 \text{ GeV}$  collider run in 2021. The used data sample contains, all data from the FastOffline production of the days 99 – 101<sup>10</sup>. This FastOffline production contains 8000 randomly sampled events from each run with preliminary TPC calibrations. The eTOF data have been calibrated offline. In total, the sample contains 410k events with eTOF hits (compared to 12.3M events in the previous analysis). Counter 23-3-1 was inoperable in 2021 and has thus been excluded from this analysis. Over the momentum region between  $0.8 \text{ GeV}/c$  and  $3.5 \text{ GeV}/c$  the integrated matching efficiency is 59.7 % to 64.3 %.

The largest effect leading to this reduction compared to the efficiencies shown at the beginning of the BES-II running (compare Figure 7.28) is the damage of the PADI boards suffered in 2020. The previously provided estimate for the efficiency loss due to the PADI damage (see Chapter 6.3.2) predicts the observed reduction of the matching efficiency within an error of 0.4 % for USTC counters and 1.3 % of THU counters. Additionally, this analysis uses non-final TPC calibrations and is based on runs in collider mode. In collider mode, tracks in the TPC are on average shorter as the primary vertex is not necessarily at the opposing end of the TPC. The track extrapolation quality towards eTOF is thus reduced slightly. Within these uncertainties, no evidence of MRPC degradation over the duration of BES-II is found. Given the relatively low particle flux in STAR compared to CBM, this observation agrees with the expectation for MRPC aging.

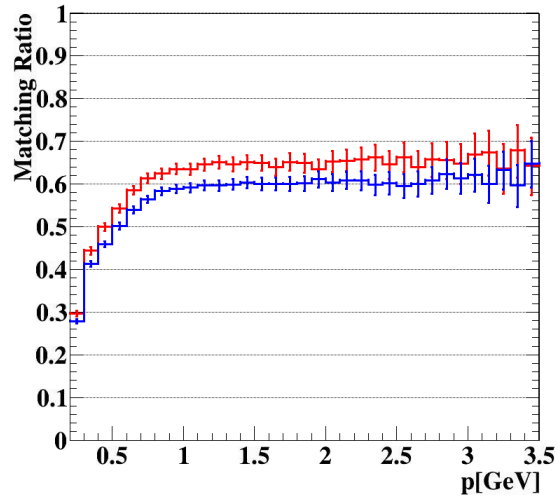


**Figure 7.36:** Matching efficiency from the FastOffline production of the  $7.7 \text{ GeV}$  collider run in 2021. **Red:** All THU-type counters. **Blue:** All USTC-type counters. Error bars show the  $5\sigma$  confidence interval (consistent with Figure 7.28) for statistical uncertainties only.

## 7.2.4 Conclusions - Efficiency

- The determination of the detector efficiency in eTOF is a challenging task. Both the overlap analysis and the comparison with bTOF suggest a detector efficiency around 90 %. However, a significant systematic uncertainty

<sup>10</sup>Final data production of 2021 data was not available at the time of this writing

remains, which could not be quantified.

- The average matching efficiency of eTOF was found to be close to 70 % at the beginning of BES-II, degrading to  $\approx 62\%$  at the end of BES-II due to pre-amplifier damages
- No evidence of MRPC aging was observed during BES-II.
- eTOF's matching efficiency varies significantly between runs due to FEE outages. This issue has been shown to be curable in analysis by focusing on counters and events with goodEventFlag set.
- A large dependence of the eTOF matching on the TPC track extrapolation was observed. This can be seen in the significant momentum dependence of the matching efficiency and the matching width.
- Significant impact of material budget in front of eTOF was observed, leading to increased matching widths and an inhomogeneous matching efficiency.
- The large matching width leads to a high combinatorial background in the eTOF track matching and consequently to a purity around 70 %. It was shown that this purity can be increased to above 90 % at a matching efficiency of 59.7 % using a momentum dependent cut on the distance between eTOF hit and matched track intersection.
- From this perspective, eTOF data are of sufficient quality to be used in physics analysis of BES-II.

## 7.3 Time Resolution

### 7.3.1 Aim of this Study

An MRPC is primarily a timing detector. As such, a good time resolution is its defining quality. For STAR, eTOF's main purpose is particle identification. Thus, the system time resolution of the full timing system is relevant. It includes the detector resolution of the MRPC and the start time resolution. The start time used for eTOF is derived from bTOF. It uses the timing and path length of dE/dX-identifiable tracks in the momentum range of  $0.2 \text{ GeV}/c < p < 1.0 \text{ GeV}/c$  to determine the time of the collision. Therefore, this term depends on the calibration of bTOF and the TPC. In this section, a quantification of the system time resolution, its uncertainties and dependencies will be given. Based on this result, the following chapter will then take a look at PID limits achievable with this time resolution. For CBM on the other hand, eTOF provides the first opportunity to study the variance in the detector resolution between counters, at least for USTC counters<sup>11</sup>. In

---

<sup>11</sup>25 THU-type MRPCs are installed in mCBM, providing another opportunity for statistical comparisons

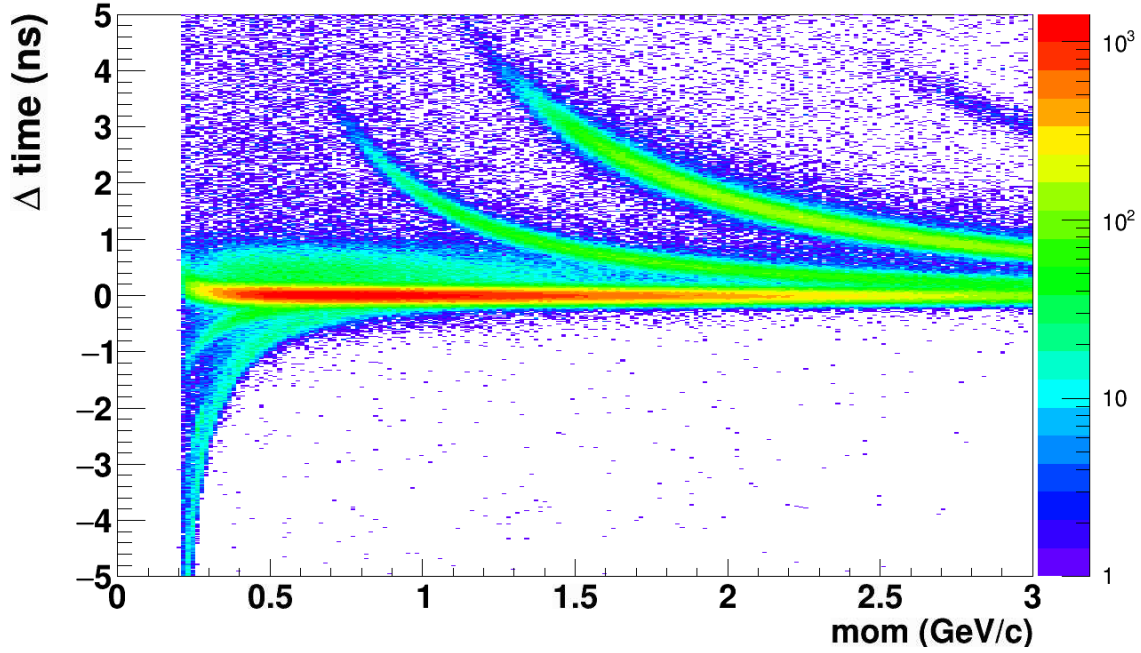


*Figure 7.37: Difference between measured particle time of flight and the expectation calculated from particle momentum and a pion mass hypothesis as function of particle momentum. Shown is an example USTC counter at medium distance from the beam-line. In addition to the pion band at  $\Delta t = 0$ , the electron and muon bands are seen at negative  $\Delta t$  and the kaon and proton band at positive  $\Delta t$  are visible. Above the pion band, background from track mismatches is visible at low momenta.*

STAR, there are two options to isolate the detector contribution to the system time resolution. The first option is the overlap analysis that was already introduced in Chapter 7.2.2. Despite its uncertainties in determining the detector efficiency, this analysis approach delivers good results for the time resolution. The disadvantage of this approach is that it only provides a combined resolution of DUT and REF detector and that only the 24 counters in the overlap region can be quantified. Nevertheless, it provides an important cross-check. In the second approach the system time resolution is determined for all counters using two different start times: The VPD start time and the start time provided by the bTOF system. Using both results as well as the event-by-event correlation of the two start times allows the unfolding of the different contributions. This approach will be shown for all 108 eTOF counters and compared to the requirements for CBM.

### 7.3.2 System Time Resolution

A time measurement only becomes meaningful when compared to an expectation. To determine the system time resolution in STAR, the measured time of flight is compared to an expectation calculated from the momentum of a track, its



projected path length, its momentum and a mass hypothesis. As pions are the most abundant particles at STAR energies and in the eTOF region, we use them for the mass hypothesis. The difference between measured ToF and expectation ( $tof - tof_\pi$ ) as function of momentum is shown in Figure 7.37 for an example counter. This plot contains all primary track matches with a cluster size of one (see Chapter 7.3.4), a distance between track intersection and MRPC hit of less than  $\Delta r < 3\text{ cm}$  and a specific energy loss within  $3\sigma$  of a pion. Only events with `goodEventFlag()` are taken into account. Unless mentioned otherwise, the same previously used sample of the 2020 FXT run at  $\sqrt{s_{NN}} = 7.7\text{ GeV}$  is analysed.

The  $tof - tof_\pi$  distribution as function of the track momentum splits into recognizable bands based on the true mass of the particle. The width of these bands is given by the time resolution of the system. At negative  $tof - tof_\pi$  and low momenta, the electron and muon bands can be seen. At momenta above  $\approx 0.3\text{ GeV}/c$  (muons) and  $\approx 0.5\text{ GeV}/c$  (electrons) these bands merge into the central pion band. At positive  $tof - tof_\pi$  and higher momenta, the kaon and proton band can be seen. The Kaon band merges into the pion band at momenta above  $\approx 2.0\text{ GeV}/c$ . Above the pion band at low momenta, a significant background from mismatched tracks can be seen. As pions are the most abundant particles, a mismatched track is most likely to be matched to a hit that has been produced by another pion, so this background is close to the pion band. An additional contribution to this background is multiple scattering of low energetic pions which increases their effective path length and thus delays their arrival at the MRPC. All these contributions widen the pion band thus worsen the time resolution extracted from the width. To minimize these contributions the system time resolution is extracted in the momentum range of  $1.0\text{ GeV}/c < p < 1.5\text{ GeV}/c$ . In this region, electrons and muons are already indistinguishable from pions and thus no longer deform the peak shape. Kaons on the other hand are still clearly separable. This leaves the combinatorial background as only distorting influence.

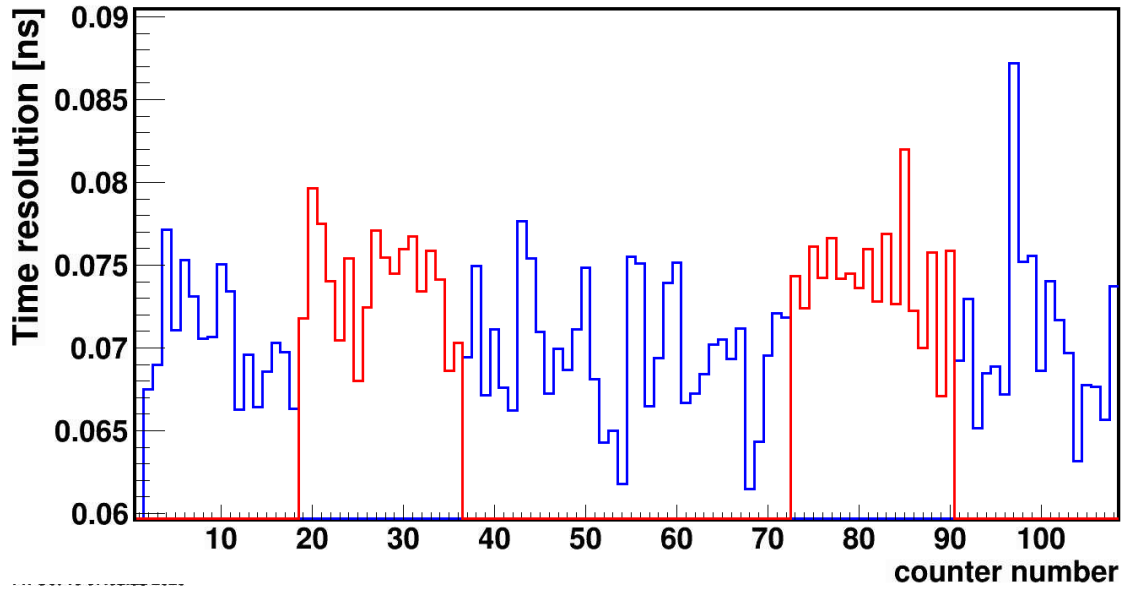
Within this momentum range, the projection of this distribution on the y-axis is fitted with a Gaussian function and a linear background function<sup>12</sup>.

Figure 7.38 shows the such determined system time resolution for each eTOF counter. With two exceptions, all counters show a time resolution below the eTOF design resolution of  $80\text{ ps}$ . One of the two exceptions is the damaged counter 23-3-1 (counter 97). The average time resolution is  $70.6\text{ ps}$  for USTC-type counter and  $74.8\text{ ps}$  THU-type counters. The RMS for the time resolution distributions of the two counter types is  $4.3\text{ ps}$  and  $3.8\text{ ps}$  for USTC-type and THU-type counters, respectively. The distribution of peak positions of the Gaussian fits between counters has an RMS of  $3.9\text{ ps}$ , which can be seen as residual calibration differences. To determine the methodical uncertainties of this analysis, a mixing technique is applied. The track matches from all eTOF counters are randomly distributed to

---

<sup>12</sup>In the form:  $f(x) = [0] \cdot e^{\left(\frac{x-[1]}{2 \cdot [2]}\right)^2} + [3] \cdot x + [4]$  with running variable  $x = tof - tof_\pi[\text{ns}]$  and free parameters  $[1] - [4]$ . The fit range is  $\pm 0.25\text{ ns}$  to exclude the kaon band. Parameter  $[2]$  of the fit, the Gaussian width, is taken as the measurement of the system time resolution.





**Figure 7.38:** System time resolution for all eTOF counters in the FXT runs at  $\sqrt{s_{NN}} = 7.7$  GeV from 2020. **Blue:** USTC-type counters. **Red:** THU-type counters.

one of 108 sub-events. Instead fitting the  $tof - tof_\pi$  vs. momentum distributions for each counter, the same analysis is applied on the  $tof - tof_\pi$  vs. momentum distributions for each of those sub-events. The mean resolution of the sub-events is  $73.3$  ps in good agreement with the counter mean resolution of  $72.0$  ps. The RMS of the distribution of sub-event time resolutions is  $0.2$  ps, which can be interpreted as the methodical error of this analysis. The low methodical uncertainty does not explain the observed variance in the counter resolutions. This variance is therefore primarily caused by actual performance differences between the counters.

Aside from intrinsic MRPC performance differences and calibration residuals, also differences in the track density and material budget in front of those detectors, which decrease the purity of this measurement, contribute to this variance. These contributions cannot be quantified in this analysis. However, one would expect a regular pattern between sectors (similar to the one visible in the matching width in Figure 7.26) if these contributions were dominant over the influence from detector differences. No such pattern can be observed in Figure 7.38.

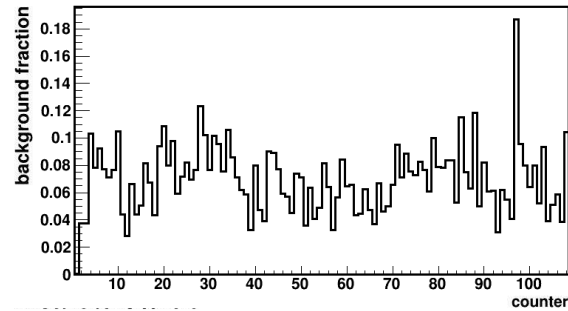


**Figure 7.39:** Background fraction in the fit region for each eTOF counter.

The system time resolution is relatively stable with respect to the track matching cuts as long as high purity is maintained. This can be checked by using the

momentum-dependent position cut on track matches introduced in Chapter 7.2.3 instead of the above used momentum-constant cut of  $\Delta r < 3 \text{ cm}$ . The system time resolution of the counter's shift by less than  $1 \text{ ps}$  on average between the two matching cut methods.

The purity of the pion band can be estimated by the contribution of the background terms in the fit. The impurity is estimated as the fraction of the integrated linear background term of the fit over the total integral of the fit. Figure 7.39 shows this quantity for each counter in eTOF. The average background fraction is 6.8 % with a range spanning from 3 % and 12 %. A higher background fraction is only seen in counter 23-3-1. This average is slightly lower than the purity estimates from simulations shown in Figure 7.35 for this momentum range. The difference is that this method is not sensitive to mismatches between particles closely related in velocity and path length like late produced secondaries.

### 7.3.3 Detector Resolution

To extract the detector contribution, the system time resolution now needs to be compared with different start time resolutions. Figure 7.40 shows the combined time resolution of all eTOF counters with bTOF start time and VPD start time as well as the correlation between bTOF start time and VPD start time. Using these three measurements we can, assuming simple quadratic addition of the contributions, calculate the contributions from eTOF, bTOF and VPD:

$$\begin{aligned}\sigma_{eTOF} &= 67.4 \text{ ps} \\ \sigma_{bTOF-start} &= 21.3 \text{ ps} \\ \sigma_{VPD-start} &= 51.4 \text{ ps}\end{aligned}$$

The unfolding shows that STAR bTOFs start-less T0 mode provides an excellent start time resolution. The VPD start time resolution is worse, as expected at these comparatively low energies, but a decent time resolution can still be reached. The contribution from eTOF counter resolution is the largest factor in the combined time resolution. For completeness, it should be mentioned that all contributions from the momentum uncertainties, track matching and path length uncertainties are attributed to the eTOF resolution in this approach. The contributions from path length and momentum uncertainty are estimated to be  $\approx 5 \text{ ps}$  and can thus be neglected <sup>13</sup>.

This result for the eTOF detector resolution can be cross-checked using the overlap analysis introduced in the previous Chapter 7.2.2. The observed efficiency issues with the overlap analysis have little relevance to the time resolution. To determine the time resolution, the selection of reference hits and the projection of the expected DUT hit position into the DUT plane is done analogue to the efficiency analysis. Around the expected DUT hit position, the closest DUT hit within the

---

<sup>13</sup>Assuming 0.1 % path length uncertainty and 1 % momentum uncertainty

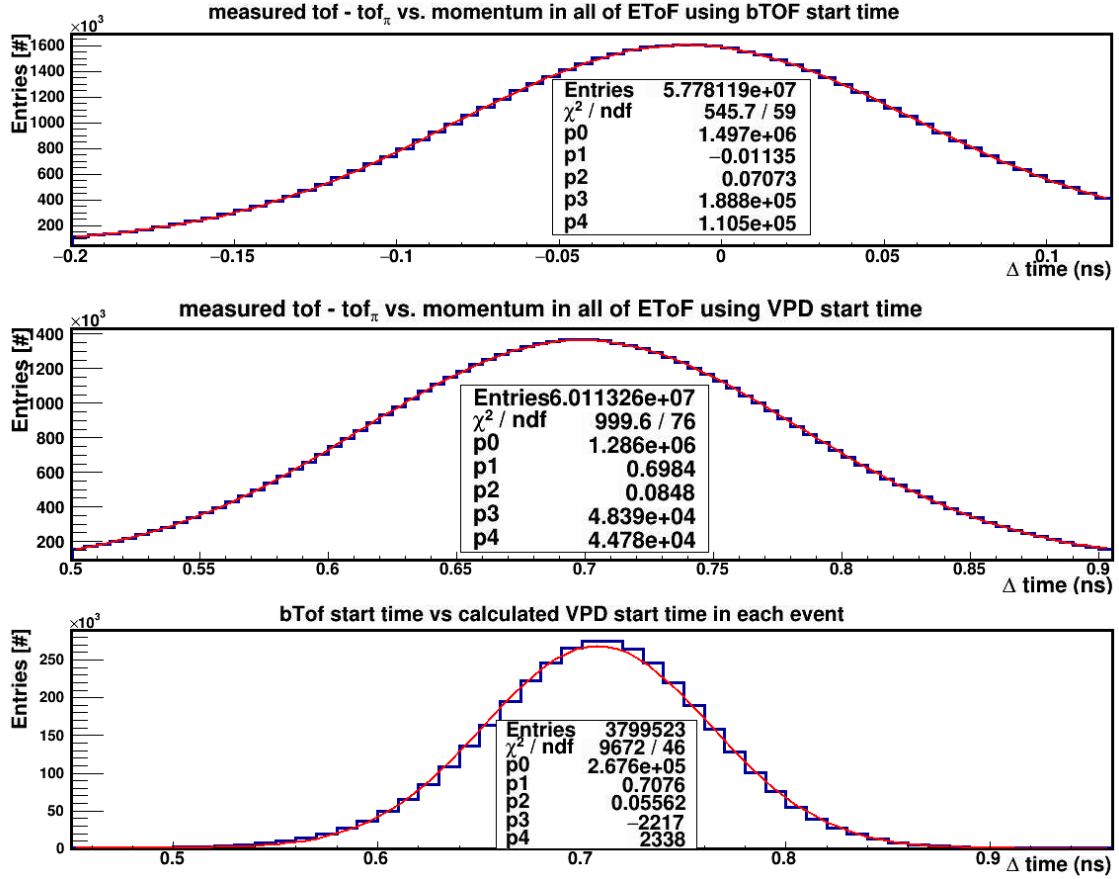


**Figure 7.40:** Unfolding the combined time resolution for eTOF in the FXT runs at  $\sqrt{s_{NN}} = 7.7 \text{ GeV}$  from 2020. **Top:**  $\text{tof} - \text{tof}_\pi$  of eTOF tracks using bTOF start time. **Middle:**  $\text{tof} - \text{tof}_\pi$  of eTOF tracks using VPD start time. **Bottom:** Event-by-event correlation of bTOF start time and VPD start time.

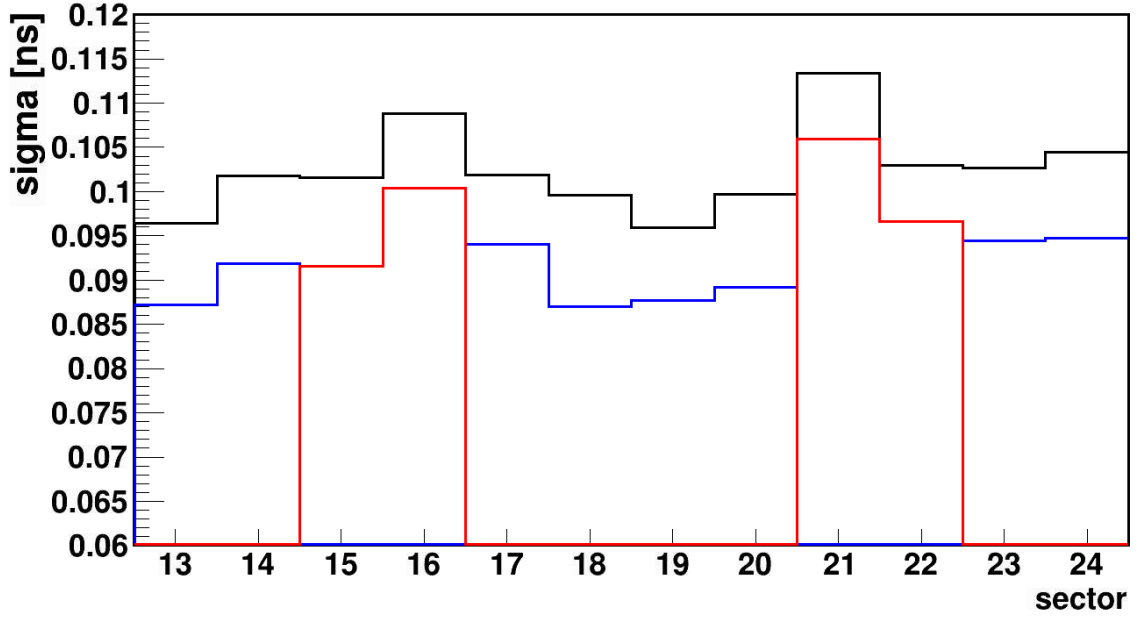


**Figure 7.41:** Time resolution from overlap analysis. **Black:** RMS of the corrected time difference distribution of DUT and REF hit for each DUT sector. **Blue:** Gaussian fit width for USTC DUT sectors. **Red:** Gaussian fit width for THU DUT sectors.

spatial cuts (see Chapter 7.2.2) is picked. The time difference between DUT hit and REF hit is then corrected by their three-dimensional distance divided by the measured velocity of the REF hit. Once a matching pair of DUT hit and REF hit is found, they are closely correlated. The resulting corrected time difference distribution can be fit with a pure Gaussian function without any additional background terms. The width of these fits are shown in Figure 7.41. The average fit width is  $93.4\text{ ps}$  over all sectors. The contributions of DUT and REF resolution cannot be disentangled from this width. However, if one assumes equal, quadratically added, contributions, the average eTOF counter in the overlap has a detector resolution of  $66.0\text{ ps}$ . This result is in good agreement with the previously presented detector resolution result obtained using the expected pion time of flight.

The determined above bTOF start time resolution can be subtracted quadratically from the individual counter system time resolution in Figure 7.38. Doing so leads to a mean counter resolution of  $68.5\text{ ps}$ , agreeing well with the combined result and the overlap. This indicates a good time alignment between the counters. For USTC counters, the average detector time resolution is  $67.4\text{ ps}$  and  $71.7\text{ ps}$  for THU counters. The RMS of the time resolution between all counters with start time subtracted is  $4.7\text{ ps}$ . The contributions from methodical uncertainties are small, as shown in the previous subsection and this distribution RMS characterizes the differences between counters. The important conclusion to draw from this, is that test results for the time resolution of prototypes (from mCBM or cosmic tests) can be generalized to a larger sample of MRPCs with an uncertainty of  $\approx 5\text{ ps}$ .

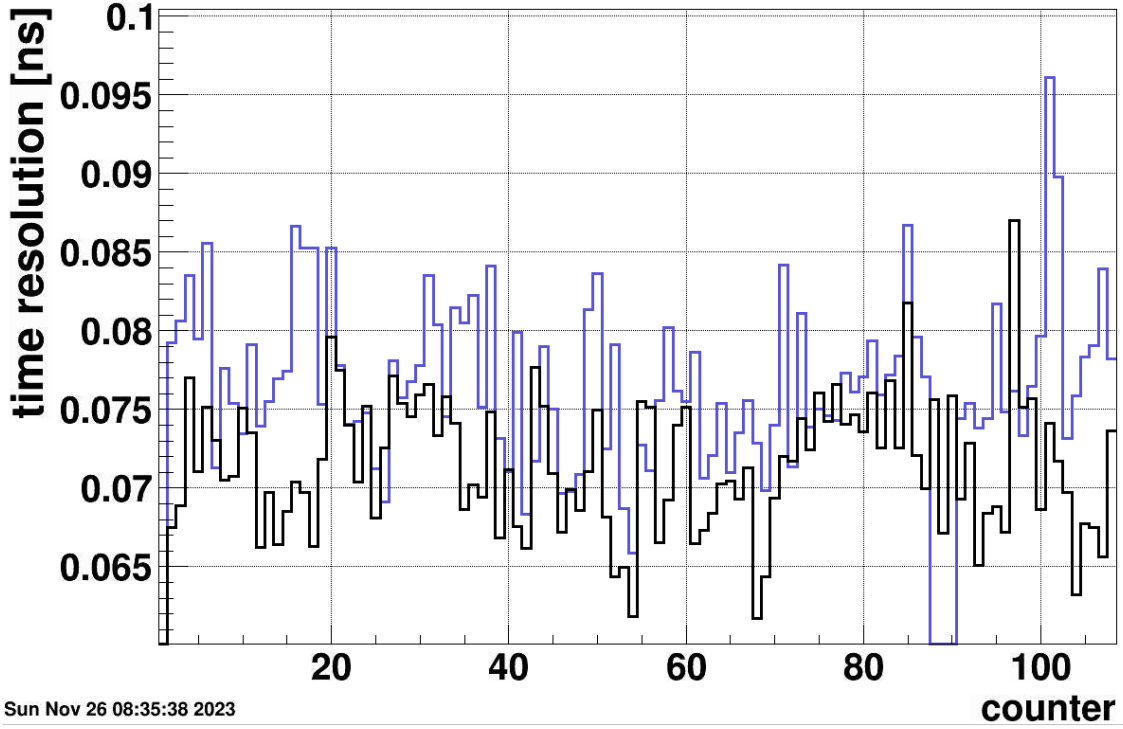


**Figure 7.42:** System time resolution (including bTOF start time) for each eTOF counter. **Blue:**  $\sqrt{s_{NN}} = 7.7 \text{ GeV}$  Collider data taken in 2021. **Black:**  $\sqrt{s_{NN}} = 7.7 \text{ GeV}$  FXT data taken in 2020.

The detector time resolution measured under reaction conditions in eTOF is on average higher  $\approx 10 \text{ ps}$  than previously measured in cosmic tests on samples of the same counters. At their respective field strength at eTOF of  $111.3 \frac{\text{kV}}{\text{cm}}$  for USTC counters and  $104 \frac{\text{kV}}{\text{cm}}$  for THU counters, time resolutions of  $56 \text{ ps}$  and  $62 \text{ ps}$  have been measured before on sample counters before shipping to STAR [87]. The best counters of each type in eTOF match the cosmic results with  $56 \text{ ps}$  and  $64 \text{ ps}$  time resolution for USTC-type and THU-type counters respectively.

### 7.3.4 Time Resolution Dependencies

#### Run Period Dependency

For better understanding of the spread in the counter time resolutions in eTOF, the time resolution in the 2020 FXT data is compared to collider data from the following year. For this, a data sample of 4.6M events from the 2021 collider run at  $\sqrt{s_{NN}} = 7.7 \text{ GeV}$  have been analyzed. This data sample has been calibrated by Y. Söhngen, using the algorithms introduced in this work. The walk calibration has been ported over from the 2020 FXT dataset at  $\sqrt{s_{NN}} = 7.7 \text{ GeV}$ , while strip alignment in time and position as well as the run-by-run corrections have been done independently. The collider data sample contains runs taken over a period of

80 days, while the FXT data have been taken within two days. Figure 7.42 overlays the system time resolution for each eTOF for the FXT dataset and the collider dataset. The collider dataset shows a slightly worse average time resolution,  $76.8\text{ ps}$  vs.  $72.0\text{ ps}$  in the FXT data. This discrepancy can be explained by a combination of effects:

- In collider mode, TPC tracks to eTOF are shorter with fewer fit points. Pointing accuracy and thus track matching performance is therefore reduced.
- The worse time resolution in the collider run can be traced down mostly to the run-by-run time offset corrections.
- The collider data have been taken over a much longer period and at significantly lower rate. Therefore, more runs with less statistics in the individual runs contribute to the data sample.

The precision of the run-by-run offset corrections (see Figure 5.16) is limited by run statistics, the description of the time distribution shape and the time binning. The correction is read off from the fitted peak position. For the fit to converge reliably, the distribution needs to be sufficiently smooth, requiring a sufficiently large bin width for a given available statistics per run. With the fit, the peak position can be determined with a resolution better than the bin width only if the (unbinned) peak shape is described sufficiently well by the fit function. There is no compelling reason for the peak to be Gaussian-shaped, especially in the presence of background, but a more complex description of the peak shape and the background requires more fit parameters and therefore more statistics to constrain these parameters. With more parameters in the fit, the association of the peak width parameter with the detector time resolution also becomes less clear.

Given these interconnected limitations, the run-by-run calibration does not reliably remove all timing offsets between runs with the available statistics in each run. The calibration residuals contribute to the observed spread in time resolution between the different detectors. However, since eTOF's time resolution is better than the design value of  $80\text{ ps}$  and due to time constraints in the STAR data production, further refining efforts on this algorithm have not been undertaken yet.

## Momentum Dependence

So far, the analysis of the system time resolution has been focused on the momentum interval of  $1.0\text{ GeV}/c < p < 1.5\text{ GeV}/c$ . The impact of this chosen momentum range needs to be quantified.

Figure 7.43 shows the dependence of the system time resolution on the track momentum. At lower momenta, the system time resolution is worse due to scattering, electron contamination and deteriorating track matching performance. Between  $1\text{ GeV}/c$  and  $2\text{ GeV}/c$ , the system time resolution is nearly constant,

decreasing by  $2\text{ ps}$  over this interval. The lower part of this interval was chosen in the previous analysis due to the higher available statistics and more reliably converging fits. Fits integrated over the full momentum range also result in a slightly larger time resolution due to a minor drift in the peak position.

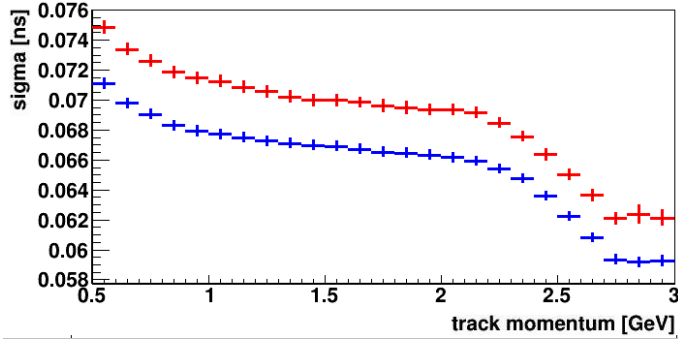


**Figure 7.43:** System time resolution (including  $b\text{TOF}$  start time) for all  $e\text{TOF}$  counter as function of momentum in  $\sqrt{s_{NN}} = 7.7\text{ GeV}$  FXT data. Error bars depict the variance between individual counters. **Blue:** USTC-type counters. **Black:** THU-type counters.

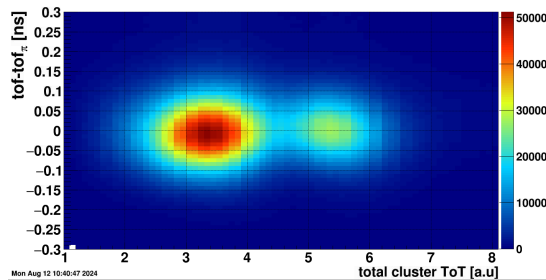
Due to this, the detector time resolution may be overestimated by  $1 - 2\text{ ps}$ . This is a minor effect, but may contribute to the difference between time resolution measurements here and cosmics measurements. The larger drop in time resolution fit width above  $2\text{ GeV}$  is an artifact of the fit. In this momentum region, the kaon peak is no longer clearly separated from the pion peak. This increases the influence of the background term and favors a lower width of the main pion peak. This width then can

no longer be associated with the system time resolution. The time resolution difference between THU-type counters and USTC-type counters stays constant over the full momentum range. This matches the expectations as the difference originates from the differences in MRPC design.

## Time over Threshold Dependence

Figure 7.44 shows the  $T_{of} - T_{of\pi}$  distribution as function of the total cluster time over threshold  $ToT_{cluster}$ , for cluster size 1 hits only. For those hits,  $ToT_{cluster}$  is simply the sum over the time over threshold of the digis from both ends of the strip. The large majority of hits fall into the region between  $2\text{ ns} < ToT_{cluster} < 4\text{ ns}$ . An additional  $\approx 15\%$  of the hits falls into the region of  $5\text{ ns} < ToT_{cluster} < 6.5\text{ ns}$ .

The regions of even higher or lower cluster ToT have little statistical impact. For comparison with other histograms (for example figures 5.12 or 7.3) presented in this thesis, a cluster ToT of  $2\text{ ns}$  corresponds to a single digi ToT of 5 GET4 ToT bins on bin on each side ( $200\text{ ps}$  per bin, per side).



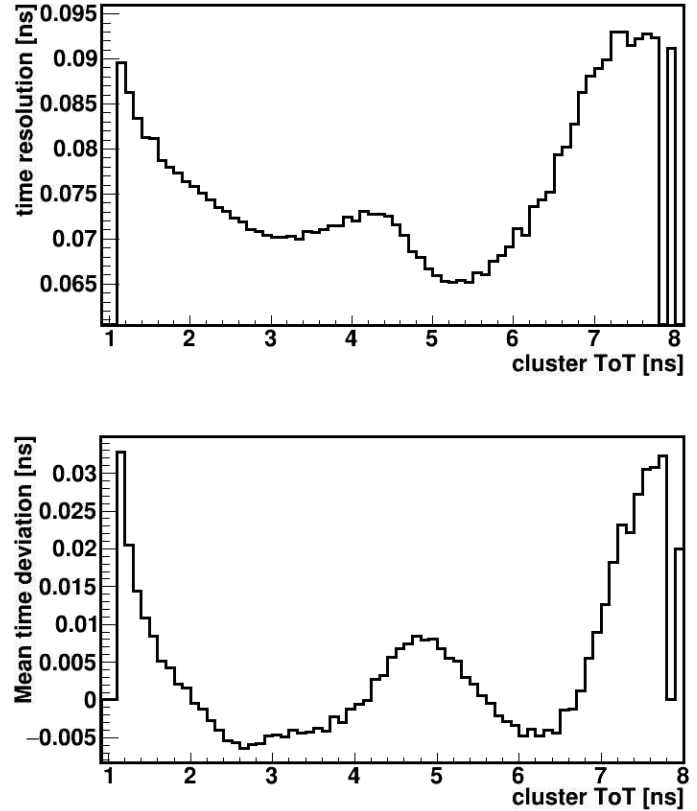
**Figure 7.44:**  $T_{of} - T_{of\pi}$  distribution as function of  $ToT_{cluster}$  for cluster size one hits.

Figure 7.45 shows the fitted system time resolution and peak position as function of  $ToT_{cluster}$ . It can be observed that for the two high statistics regions the peak positions are in the range  $-5\text{ ps}$  to  $+5\text{ ps}$ . This can be interpreted as the calibration residual of the walk calibration. The impact on the system time resolution from the peak shifts is therefore minor. The walk calibration is working as intended.

However, it can also be seen that the time resolution is not constant in the different cluster ToT regions. The clusters below  $2\text{ ns}$  in ToT correspond to small MRPC signals very close to the threshold.

For these signals, the time resolution of the front-end electronics worsens, impacting the system time resolution. The statistical impact of hits in this region is low. The general system time resolution is dominated by hits from the region of  $2\text{ ns} < ToT_{cluster} < 4\text{ ns}$ . In this region, the ToT on one sides is often impacted by the absorption of a reflected signal (see Chapter 7.1.4 and Figure 7.9). The ToT is thus ambiguous and the walk calibration cannot remove the time over threshold dependence of the hit time completely. The region between  $5\text{ ns} < ToT_{cluster} < 6.5\text{ ns}$  is mostly formed by hits where both digis absorb a reflected signal. As this is most likely to occur when the hit is close the center of a strip,

the ToT distortion is similar for both sides of the strip and the walk correction can determine the correct time shift for a digi of such a distorted ToT. The time resolution is significantly improved by about  $5\text{ ps}$  compared the lower ToT region. This observation answers the open question of the impact of the signal reflections observed at STAR on the time resolution from Chapter 7.1.4. The reflection behavior is also not consistent between different MRPCs (see Figure 7.1, right side), so these differences contribute also to the observed spread in the detector time resolution via the walk calibration. Furthermore, this time resolution dependence also quantifies the potential to improve the time resolution with a



**Figure 7.45:** *Top:* System time resolution (including bTOF start time) for all eTOF counter as function of cluster time over threshold in  $\sqrt{s_{NN}} = 7.7\text{ GeV}$  FXT data. *Bottom:* Corresponding deviation of pion peak as function of cluster ToT.



future improved walk calibration. Such an improved walk calibration needs to take the y-position along the read-out strip in addition to the ToT of a hit into account to isolate and correct the contribution from signal reflections. System time resolutions around  $67\text{ ps}$  could be achievable this way.

At even higher ToTs, the system time resolution worsens again, but the statistical impact of this region is again low.

## Cluster Size Dependence

So far, this analysis has focused on hits with cluster size one. This was done both to avoid issues from the clock jump correction (the clock jump flag is coded as cluster size  $\neq 100$ ) and issues from intra-cluster time alignment. In principle, a cluster size greater than one can be seen as multiple independent time measurements of the same avalanche in the MRPC and the cluster time resolution should improve by averaging over those measurements. In practice, this is only valid if the width of the distribution of time differences between two single-strip hits inside the same cluster, is sufficiently small. This intra-cluster time resolution is impacted by time walk differences and front-end electronics resolution.

Figure 7.46 shows the system time resolution and peak position shift for the cluster sizes one to four. Cluster size one shows the global time resolution of  $70.7\text{ ps}$  already seen in Figure 7.40, top panel. As the cluster size one hits dominate the statistics, this number is very close to the cluster size integrated time resolution of  $71.0\text{ ps}$ . The impact of cluster size one cut in the previous analysis is thus small. Cluster size two hits show a slight improvement in the time resolution of  $66.7\text{ ps}$ . For higher cluster size, the time resolution worsens, as the additional contributions from intra-cluster time resolution apparently outweigh the advantage of the multiple time measurements. Hits with a cluster size greater than two are increasingly

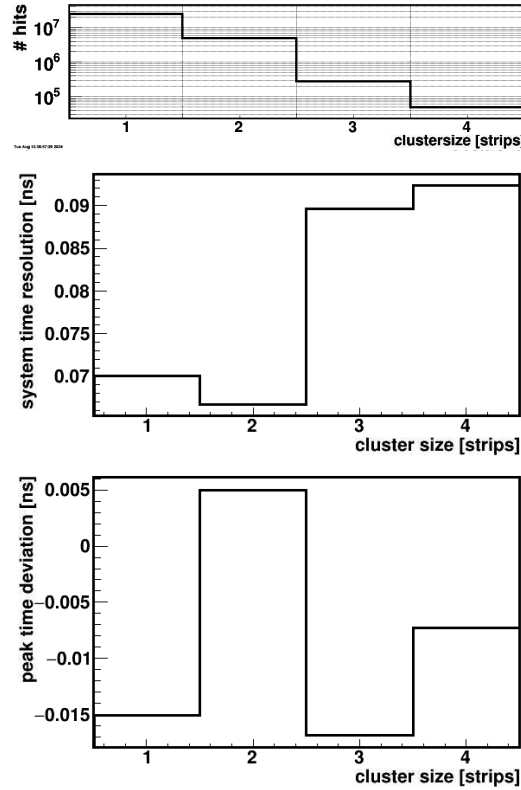


**Figure 7.46:** *Top:* Cluster size distribution for all eTOF counter in  $\sqrt{s_{NN}} = 7.7\text{ GeV}$  FXT data. *Middle:* System time resolution (including bTOF start time) as function of cluster size. *Bottom:* Deviation of pion peak as function of cluster size.

rare and thus have a small impact on the total time resolution. The lower panel of Figure 7.46 shows the shift in the peak of the timing distribution between different cluster sizes. Cluster size two hits show a significant time delay of about  $20\text{ ps}$  compared to cluster size one hits. This effect has been observed before in cosmics measurements by I. Deppner[82] and in simulations by C. Simon[88]. The explanation is that for cluster size two hits the avalanche occurs most likely in between the two strips. The center of the induced signal is in this case offset with respect to the read-out strip. The gradient of the induced signal is therefore not aligned with the direction of the strip. The observed signal on the strip is wider and flatter compared to signals centered on the strip. This signal is thus registered at the pre-amplifier later than its ToT would suggest and the hit is registered delayed. This effect could be corrected. Since calibrations in eTOF are applied at digi-level, before the cluster size is known, such a correction would require the introduction of a second calibration stage after the hit building. Due to the statistical dominance of cluster size one hits, the impact such a calibration on the total system time resolution is low. Therefore, no such additional calibration step was applied. This decision may be revisited in the case of future reproductions of eTOF data.

### Track Matching Dependence

Figure 7.47 shows the dependence of the system time resolution on the distance between the MRPC hit and the extrapolated intersection of the TPC track with the counter surface. As there is little influence of the track momentum measurement, this dependence essentially measures the dependence of the time resolution on the purity of the matching. The system time resolution stays stable up to a distance of  $2\text{ cm}$ . Comparing with Figures 7.29 and 7.30, this distance corresponds to a cut scale factor of  $\approx 0.5$  and accordingly a matching efficiency of  $60\%$  and an estimated (integral) purity of  $85\%$ . For higher distances, the time resolution degrades significantly. It should be mentioned that Figure 7.47 shows the time resolution in each fit bin, not the integral fit up to each bin. As the statistics in the further away bins is much lower, the integral time resolution is rather similar to the time resolution for the closest hits.

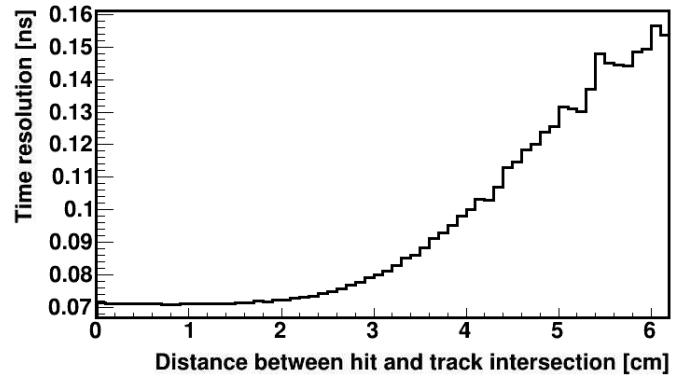


**Figure 7.47:** System time resolution (including bTOF start time) for all eTOF counters as function of the distance between hit and extrapolated track intersection on the MRPC surface in  $\sqrt{s_{NN}} = 7.7\text{ GeV}$  FXT data.

## Electronics Resolution

The time resolution of each counter is also impacted by the time resolution of its electronics. To be more precise, electronics resolution in this context refers to the resolution of the GET4 TDC. The resolution of the PADI pre-amplifier is for the purpose of eTOF inseparable from the MRPC resolution. GET4s theoretical time resolution is:

$$\sigma_{tRes,theo} = \frac{1}{\sqrt{12}} \cdot \frac{\tau_{clock}}{N_{delay\ elements}} = \frac{6.25\ ns}{\sqrt{12} \cdot 112} = 16.1\ ps \quad (7.8)$$

In practice, the time resolution is impacted by TDC non-linearities and, as always at least two GET4s contribute to the timing of an eTOF hit, imperfect clock synchronization. For eTOF, the two sides of a module are connected to one GBTX each, so the time resolution of a hit is also impacted by the clock synchronization between two GBTX (see Chapter 4.5). The time difference width between two GET4s on different GBTX was found to be  $\sigma_{tRes,Lab} \approx 35\ ps$  in measurements by J. Frühauf at the GSI electronics laboratory [77]. The electronics time resolution in eTOF can be measured from the time difference of the two pulsers inserted into one channel of the last GET4 on each side of the counter.

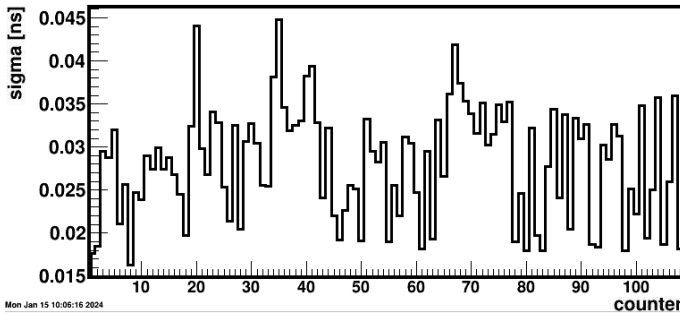


**Figure 7.48:** Width of a Gaussian fit to the pulser time difference between both sides of each eTOF counter, divided by  $\sqrt{2}$ , in  $\sqrt{s_{NN}} = 7.7\ GeV$  FXT data.

Figure 7.48 shows the width of a Gaussian fit to the time difference between the two pulsers on each eTOF counter, divided by  $\sqrt{2}$  to estimate a single GET4 contribution. This figure is based on data from all events of the previously used FXT data sample at  $\sqrt{s_{NN}} = 7.7\ GeV$ . Due to DAQ restarts, the time difference between two pulsers can shift between runs. The Gaussian fit has been applied to a range of  $\pm 150\ ps$

around the maximum of the time difference distribution. This cut ensures that the fit is not distorted by pulser time shifts.

In mean, the pulser resolution is  $28.1\ ps$ , corresponding to a fit width of  $39.5\ ps$ . This is slightly worse than the previous measurements in the lab. However, significant differences between the counters can be observed. In the best case, a pulser resolution close to  $16\ ps$ , the nominal GET4 resolution is observed. The worst cases show a resolution up to  $45\ ps$ . The RMS of the pulser resolution distribution is  $6.4\ ps$ . Given the average eTOF detector resolution of  $67.4\ ps$  and the RMS of  $4.7\ ps$  between detector resolutions, this RMS between the electronics resolutions could account for the majority of the differences between counters

( $2.67\text{ ps}$  or  $56.7\%$ ). However, there is no observable correlation between the pulser resolution measured on a counter and its time resolution (correlation coefficient:  $-0.03$ ).

There is also no observable correlation between the time resolutions of the pulsers inside the same module. One can therefore assume that the observed spread in the pulser resolution is representative for the spread between any two GET4s on different GBTX. The two pulser channels on each counter never contribute to the timing of a hit, as they are connected to different strips. The GET4s on opposing sides of each strip, which contribute together to the timing of a hit, will likely show a similar spread in resolution as seen in Figure 7.48, but not the same resolution as the measured pulser resolution of the counter. This explains why no correlation between pulser resolution and detector time resolution is observed. The measured pulser resolutions therefore contribute only qualitatively to the observed differences in counter resolutions. As there are 8 GET4 pairs contributing to the timing of hits on each counter, it is also likely that part of the variance observed in the pulser resolution is averaged out when looking at the time resolution of the full detector.

### 7.3.5 Conclusions: Time Resolution

eTOF has been shown to achieve an average system time resolution of  $70.7\text{ ps}$ , exceeding its design resolution of  $80\text{ ps}$ . USTC-type counters show a slightly better time resolution than THU-type counters. The good system time resolution is helped by an excellent start time resolution of  $< 25\text{ ps}$  provided by the bTOF system.

The detector time resolution varies significantly with an RMS of  $4.7\text{ ps}$  between different MRPCs. This can be taken as an uncertainty for generalizations of time resolution measurements on CBM-TOF prototypes. The performance of the different MRPCs changes between different datasets, indicating that much of the observed variance is not due to intrinsic MRPC differences but due to calibration residuals. The main contributors to those residuals are the run-by-run calibration and the walk calibration. The run-by-run calibration is limited by the amount of statistics on each counter in a run and the walk calibration is limited by the distortions on the measured ToT due to reflections. Another contributor to time resolution variations between counters are significant observed variations in the electronics resolution.

Combined, all these effects as well as smaller dependencies of the timing on momentum and track matching distance can explain the differences in observed average time resolution in eTOF and prior cosmic measurements. The best performing counters in eTOF provide a time resolution matching the cosmic results.

For STAR, the achieved time resolution is sufficient for the physics goals of BES-II.

For CBM, these results show that its target system time resolution can be

achieved on a large scale with current the MRPC prototypes and similar calibration algorithms, if a start time resolution of  $< 43\text{ ps}$  can be provided. Further developments of the electronics chain aim to remove the necessity for a run-by-run calibration and improve the electronics resolution slightly. With improved electronics stability, larger uniform calibration samples will be available, allowing for more multi-differential calibrations. A cluster size and y-position dependent walk calibration to remove ambiguities in the ToT measurement has shown potential for small further improvements of the detector resolution. This would loosen the requirements on the start time resolution further.

## 8 Physics Performance

### 8.1 The KFPARTICLE Reconstruction Package

KFPARTICLE [89] is a software package for the topological reconstruction of short-lived particles and their properties in a detector-geometry independent way. Initially developed for CBM, it was introduced to STAR as part of CBM's FAIR-Phase 0 efforts. It has since been tested and validated on BES-I and early BES-II data and shown improved signal-to-background ratios for various reconstructed particles [90].

KFPARTICLE is based on the Kalman filter, a mathematical method to obtain an optimal estimate for a state vector from a series of consecutive measurement and their known uncertainties. In the case of KFPARTICLE, the state vector of the mother particle  $(x, y, z, p_x, p_y, p_z, E)^T$  and its uncertainties are reconstructed by successively filtering over the state vectors of the individual daughter particles, propagated back to the position of the decay vertex. For identification of the daughter particles, KFPARTICLE works on a hypothesis model. Each track is assumed to be a particle of every particle species which is not excluded by the available PID information. At the time of this writing, each hypothesis is treated with the same weight. For each decay vertex and every valid combination of daughter particle identities, a candidate for the mother particle is reconstructed. Figure 8.1 shows the valid PID combinations for mother particle reconstruction in KFPARTICLE. For each mother particle candidate, a  $\chi^2$  is calculated from its state vector and its uncertainties as well as from topological matching criteria. This  $\chi^2$  can be used to discriminate between likely candidates and the combinatorial background induced by the PID identity hypothesis approach.

As input, KFPARTICLE is provided with the TPC tracks as well as a covariance matrix of detector uncertainty estimates and a vector of PID hypotheses for each track. A dedicated interface class, `StKFPIInterface`, handles conversion of `StTracks` into KFPARTICLE's internal structure, the calculation of PID hypotheses from `PidTraits` and  $dE/dX$  information as well as track selection and propagation of topological cuts to KFPARTICLE.

For this work, the interface class has been modified to use eTOF PID information in addition to bTOF PID information for PID hypotheses. Usage of eTOF specific information (`goodEventFlag()` and `deltaX()`, `deltaY()`) and a particle identification scheme based on eTOF information has been added. Additionally, a mechanism for track mixing between different events for background determination has been implemented.



## 8.2 $\Lambda^0$ Reconstruction

The lightest strange baryons,  $\Lambda^0$ -baryons are an important probe of strangeness in heavy ion collisions. As such, their reconstruction is of general interest for physics analyses of BES-II data (see 2.5.3).

$\Lambda^0$ -baryons are among the longest living particles which decay inside the STAR acceptance. Their decay vertex into a proton and a pion is well separated from the primary vertex. Its mean decay length is about 20 *cm*.  $\Lambda^0$ s occur in high abundance and the decay products are easy to identify. These features make  $\Lambda^0$  reconstruction a prime application case for the topological reconstruction approach of KFParticle. The mother particle reconstruction can be done well relying just on the TPCs specific energy loss measurement for particle identification.

In this section,  $\Lambda^0$  reconstruction is studied as a sanity check for eTOF data quality. Despite the good reconstruction quality without TOF information, any good TOF information should improve the reconstruction of  $\Lambda^0$  particles. This additional information will reduce the number of valid particle hypothesis per track and thus lower the number of proton-pion pairs forming  $\Lambda^0$  candidates. The quality of the particle reconstruction is quantified in this analysis by the significance of the  $\Lambda^0$  peak. The aim is to show the additional value eTOF data provide to physics analysis as well as to demonstrate some of the pitfalls when integrating this information into KFParticle.

The abundance and easy topological reconstruction of  $\Lambda^0$ -baryons can also be used to create a pure sample of proton tracks from the decay daughters. These tracks are compared to their eTOF matches as a data driven approach to assess eTOF's track matching performance and purity.

### 8.2.1 Analysis

For the first part of this analysis, the fast offline PicoDst sample of the  $\sqrt{s_{NN}} = 7.7$  *GeV* FXT run in 2019 was used. It contains 5.7 million events with a reconstructed primary vertex. Due to the preliminary start time calibration in this dataset, the eTOF system time resolution is 85 *ps*.

Tracks are considered proton and pion candidates if their  $dE/dX$  value is within three standard deviations of the nominal value for the respective particle species and momenta. Estimates for the uncertainties of the specific energy loss are provided by the TPC group.

For the time of flight PID, track candidates are required to have a measured inverse relativistic velocity  $1/\beta_{tof}$  withing  $3.5 \sigma_{1/\beta}$  of the expectation. The expectation is calculated from the momentum measurement and each mass hypothesis has been applied in this part of the analysis. The expected width  $\sigma_{1/\beta}$  is calculated as

$$\sigma_{1/\beta} = 2 \cdot \frac{\sigma_{TRes}}{ToF_{measured}} \cdot \frac{1}{\beta_{ToF}} + \frac{C[m_{hypothesis}]}{p^2} \quad (8.1)$$



where,  $p$  is the measured momentum,  $\sigma_{TRes}$  is the eTOF time resolution and  $C[m_{hypothesis}]$  is a constant which is fitted to the width of the mass spectrum for each particle species ( $p$ ,  $K$ ,  $\pi$ ) in the very low momentum region. If only the time uncertainty is taken into account, the width of the mass spectrum at  $p \rightarrow 0$  should be zero. In practice, that is not the case due to scattering and energy loss. This constant is phenomenologically accounting for this fact. Values of are  $C[p] = 0.05 \text{ GeV}^2$ ,  $C[K] = 0^1$  and  $C[\pi] = 0.01 \text{ GeV}^2$  are used here.

Estimates for the uncertainties in position and momentum of the tracks are provided by their associated covariance matrix. Those are used to calculate a  $\chi^2$  value for the distance of closest approach to a given vertex or track. For this analysis, particles are considered secondary particles if  $\chi^2 > 30$  with respect to the primary vertex. This loose requirement is applied to reduce background in the  $\Lambda^0$  spectrum from more short-lived decays.

Secondary proton and pion pairs are considered  $\Lambda^0$  candidates if  $\chi^2 < 10$  for the distance of closest approach between the two tracks. As the focus of this analysis is on the impact of eTOF, it is required that the pseudo-rapidity of the proton is within eTOF acceptance of  $-1.6 > \eta > -2.1^2$  is applied. Figure 8.2 shows the invariant mass spectrum for  $\Lambda^0$  candidates. This spectrum is fitted with a Gaussian function of the peak and a linear function for the background under the peak. The fit ranges from  $m_{\Lambda^0} - 3\Gamma < m_{\Lambda^0} < m_{\Lambda^0} + 3\Gamma$ , where  $\Gamma$  is the nominal decay width of the  $\Lambda^0$ -Baryon. It is assumed that the number of  $\Lambda^0$  candidates follows a Poissonian distribution and that the statistical uncertainty of the number of candidates in a momentum interval can be calculated as  $\sigma_{N_{candidates}} = \sqrt{N_{candidates}}$ . The significance ( $n\sigma$ , in units of the standard deviation) of the  $\Lambda^0$  peak can then be calculated as

$$n\sigma = \frac{S}{\sqrt{N_{candidates}}} = \frac{S}{\sqrt{S+B}} \quad (8.2)$$

where  $S$  and  $B$  are the respective integrals over the signal and background functions in a range of  $\pm 0.005 \text{ GeV}/c^2$  around the peak position.

Figures 8.3 to 8.5 show the momentum distribution of  $\Lambda^0$  candidates as well as significance and signal fractions for different approaches to use eTOF information. In the default way to include time of flight information in KFP a particle hypothesis for a TOF-matched track is considered valid only if both  $dE/dX$  and TOF measurement agree to this hypothesis. This method was implemented previously for bTOF data. Directly porting this approach to eTOF (green line in figure 8.3 to 8.5) leads to reduced significance compared to TPC-only reconstruction (red line) for all but the lowest momenta. Figure 8.5 shows that the signal fraction does

<sup>1</sup>The kaon band does not extent to very low track momenta in eTOF, therefore the constant is not necessary for kaons.

<sup>2</sup>In the default STAR coordinate system, the FXT beam travels into negative Z direction. Negative pseudo-rapidities indicate forward tracks from the collision

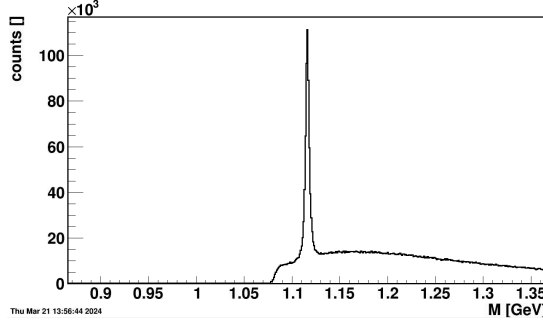


**Figure 8.2:** Invariant mass spectrum of  $\Lambda^0$  candidates in the eTOF pseudo-rapidity range from the 7.7 GeV FXT fast offline data sample. Proton identification with combined dE/dX and eTOF PID.

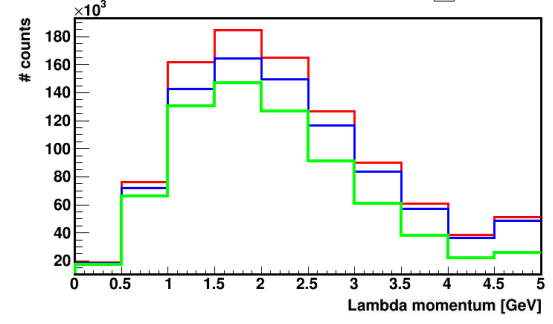


**Figure 8.3:** Momentum distribution of  $\Lambda^0$  candidates in the eTOF pseudo-rapidity range from the 7.7 GeV FXT fast offline data sample. **Red:** Particle identification with dE/dX only. **Green:** Particle identification with dE/dX and eTOF. Mass hypothesis of dE/dX and eTOF have to agree if a eTOF match exist. **Blue:** Particle identification with dE/dX and eTOF. dE/dX mass hypothesis is considered valid alone if eTOF has no valid mass hypothesis.

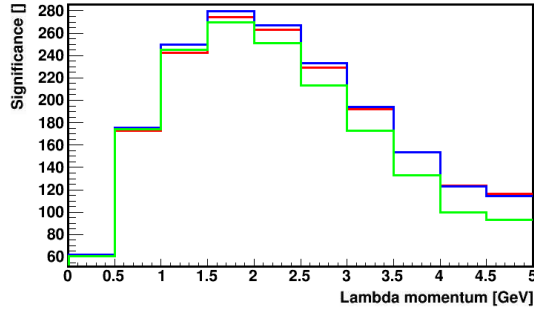


**Figure 8.4:** Significance  $\frac{S}{\sqrt{S+B}}$  of  $\Lambda^0$  candidates in the eTOF pseudo-rapidity range from the 7.7 GeV FXT fast offline data sample. **Red:** Particle identification with dE/dX only. **Green:** Particle identification with dE/dX and eTOF. Mass hypothesis of dE/dX and eTOF have to agree if a eTOF match exist. **Blue:** Particle identification with dE/dX and eTOF. dE/dX mass hypothesis is considered valid alone if eTOF has no valid mass hypothesis.

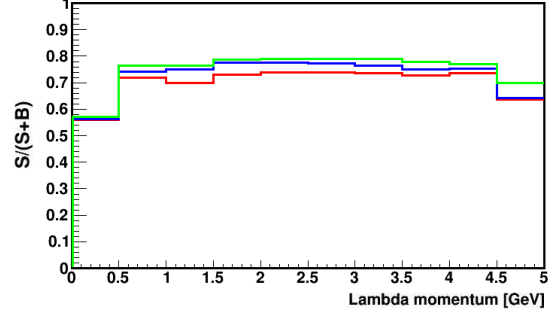


**Figure 8.5:** Signal fraction  $\frac{S}{S+B}$  of  $\Lambda^0$  candidates in the eTOF pseudo-rapidity range from the 7.7 GeV FXT fast offline data sample. **Red:** Particle identification with dE/dX only. **Green:** Particle identification with dE/dX and eTOF. Mass hypothesis of dE/dX and eTOF have to agree if a eTOF match exist. **Blue:** Particle identification with dE/dX and eTOF. dE/dX mass hypothesis is considered valid alone if eTOF has no valid mass hypothesis.

indeed increase slightly due to the additional particle discrimination power of eTOF. However, this gain is more than negated by the loss of statistics due to the

rejection of  $\Lambda^0$  candidates in the peak region. The difference is small, however, it means that in this implementation, eTOF data fails the sanity check that the additional information must improve reconstruction quality.

The reason for this loss in significance lies in the mismatches between TOF information and TPC tracks. This issue is obviously not present when using dE/dX identification only. In Chapter 7.2.3, it was already shown that a non-negligible fraction of tracks are not matched to their correct eTOF hits in simulations (compare figures 7.30 and 7.35). The background seen in the timing spectra in Chapter 7.3.2 highlight these issues in the experimental data. In this case, as the reconstruction without eTOF matches already works very well, even a moderate rate of mismatches will worsen the overall result. A similar effect can also be observed with bTOF matches, albeit at an insignificant magnitude.

The way to remedy this issue is to ensure that only good eTOF matches are used in the analysis and, most importantly, that tracks with improper eTOF matches are not discarded, but treated the same as tracks with dE/dX identification only. To ensure the later, tracks with no valid PID hypothesis from TOF are set to ignore the TOF information. For example, tracks with  $m_{TOF} \approx 600 \text{ MeV}$  fit to none of the particle species. Such tracks are obvious mismatches or erroneous time measurements (due to clock jumps) and need to be sorted out. This change in the TOF information interfacing to KFParticle then leads to a small increase both signal fraction and significance compared to the case with only TPC information (blue line in 8.4 and 8.5). While this change is not large, it means that eTOF data now pass the intended sanity check. Further refinement of the eTOF data quality can be done by cutting on the previously introduced matching quality criteria like the distance between track and intersection (deltaX, deltaY) or goodEventFlag() (see Chapter 7.2.3).

## 8.2.2 Proton PID Purity Estimate from Lambda Decays

The fact that the  $\Lambda^0$  is both comparatively abundant and can be reconstructed well with a topological approach, and with TPC information only, can be used to obtain a proton track sample with high purity. Since the PID for this sample is known a priori to the TOF measurement, it can be used to check the purity of TOF matching. This data driven approach will be compared to the previously shown purity estimate from Monte-Carlo simulations (see Figures 7.30 and 7.35).

The sample contains the proton tracks from decays of  $\Lambda^0$  candidates in the mass range of  $\pm 3 \text{ MeV}/c^2$  of the nominal  $\Lambda^0$  mass. The purity of this track sample is assumed to be equal to the  $\Lambda^0$  signal fraction  $\frac{S}{S+B}$ . Each track that has an eTOF match is considered as a TOF identified proton if the measured mass is within  $3.5 \sigma_{m_{proton}}$  around the proton mass.  $\sigma_{m_{proton}}$  is calculated according to equation 4.4, assuming a time resolution of  $75 \text{ ps}$ , a momentum resolution of  $2\%$  and a path length uncertainty of  $1 \text{ mm}$ . Since the shape of the proton mass distribution is

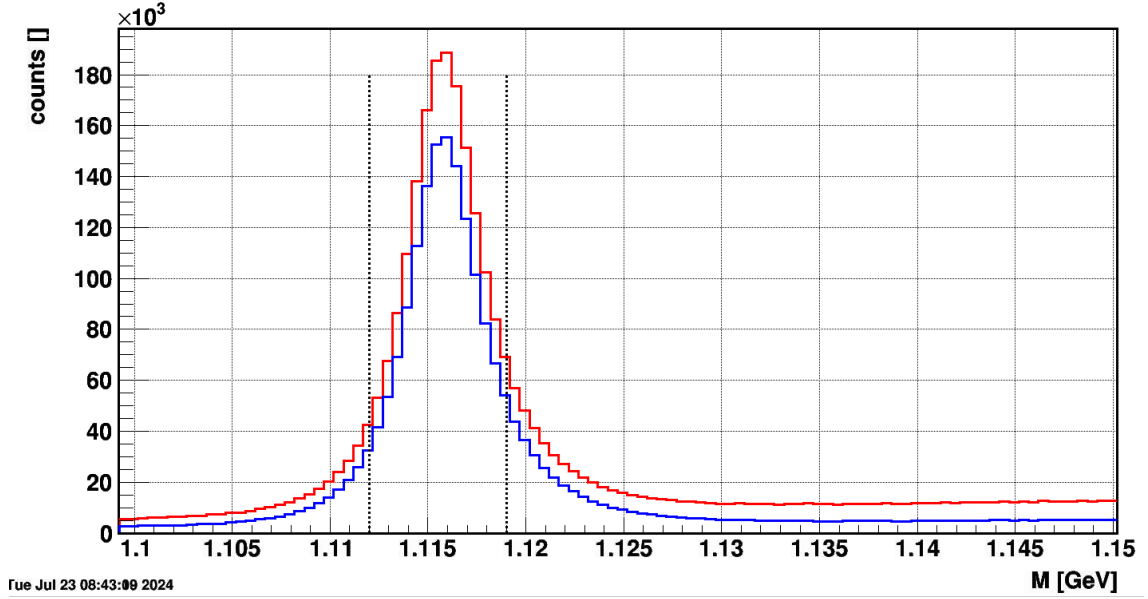


**Figure 8.6:** Mass distribution of  $\Lambda^0$  candidates reconstructed using only TPC information. The signal region is marked by dotted lines. **Red:** All candidates. **Blue:** Candidates with posterior eTOF identification of the proton daughter track.

close to Gaussian, this cut is expected to include approximately 99.98 %<sup>3</sup> of all mass measurements of correctly identified protons.

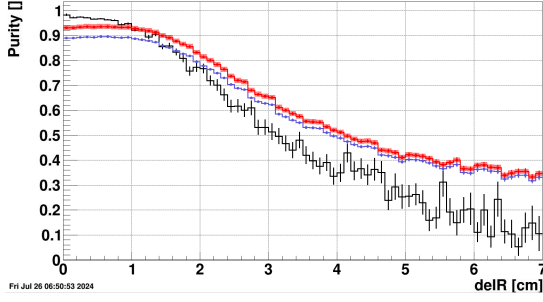
If a TOF mass measurement for a proton sample track is incompatible with the proton mass, it is therefore highly likely that one of two possibilities occurred: Either the TPC track was mismatched to the TOF hit or the track was not actually a proton. One can correct for the later possibility using Bayes theorem:

$$P(m_p|p) = \frac{P(p|m_p) \cdot P(m_p)}{P(p)}, \quad (8.3)$$

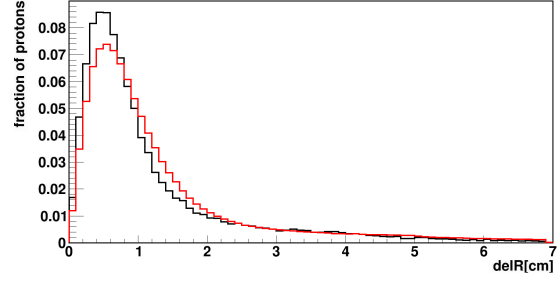
where  $P(m_p)$  is the probability to measure a proton mass for a track and  $P(p)$  is the probability that the track is actually a proton.  $P(p|m_p)$  corresponds to the purity of the proton track sample.  $P(m_p|p)$  can then be directly identified with the TOF matching purity.

Figure 8.6 shows the invariant mass distribution of reconstructed  $\Lambda^0$  candidates. The signal fraction  $S/(S+B)$  in the selected region is determined by a fit with a Gaussian component for the signal and a first order polynomial component for the background. For all  $\Lambda^0$  candidates,  $S/(S+B) = 86.8\%$  (corresponding to  $P(p)$ ). The subset of  $\Lambda^0$  candidates for which the proton daughter track can afterwards be matched to an eTOF hit with a proton mass,  $S/(S+B) = 90.8\%$  (corresponding to  $P(p|m_p)$ ). For the track matching to eTOF, an elliptic match distance cut with the half-axis of  $\delta x < 5\text{ cm}$  and  $\delta y < 7\text{ cm}$  is applied. In this sample, 82.8 % of all

<sup>3</sup>corresponding to the Gaussian confidence interval of 3.5 standard deviations



**Figure 8.7:** Proton purity as function of the distance between eTOF hit and track intersection. **Black:** MC proton tracks with  $p < 0.9 \text{ GeV}/c$ . **Blue:** Probability to measure a proton mass for tracks from  $\Lambda^0$  decays. **Red:** Matching purity for proton tracks after bayesian correction. Error bars denote statistical error. Shaded area shows the uncertainty of the bayesian correction.



**Figure 8.8:** Distance between proton track intersection and eTOF hit. The fraction of protons has been scaled with the purity for a given purity. **Red:** Data, proton tracks from  $\Lambda^0$  decays. **Black:** MC, all proton track with  $p < 0.9 \text{ GeV}/c$ .

tracks have a TOF mass compatible with a proton mass hypothesis (corresponding to  $P(m_p)$ ). Using equation 8.3, the eTOF matching purity is calculated to be  $P(m_p|p) = 86.6 \%$ . By varying the integration range of signal and background in the  $\Lambda^0$  invariant mass distribution, a systematic uncertainty of  $\pm 1.0 \%$  due to the impurity correction is obtained.

The eTOF matching purity extracted this way depends of course on the choice of track matching criteria. The overall proton purity was found to exceed 90 % for a requirement of up to  $\Delta r < 3.5 \text{ cm}$  for distance between hit and intersection. This requirement contains 92.6 % of all matched proton tracks from  $\Lambda^0$  decays. This result is compared to the matching purity from Monte-Carlo simulations. For comparability, a simulated track sample of protons with a momentum range of  $p > 0.9 \text{ GeV}/c$  is used to match the momentum range of the proton tracks from  $\Lambda^0$  decays. The MC matching purity matches with 87.0 % very well to the data approach. However, when looking into more details, the simulation and data approaches differ.

Figure 8.7 shows the purity estimates from simulations and from protons from  $\Lambda^0$  decays as function of the matching distance between track intersection and eTOF hit. The simulation approach predicts a slightly higher purity for close matches, but significantly lower purity for hits further away from the intersection. Figure 8.8 shows the distribution of the distance between hit and intersection for simulations and data. Also here, the simulations predicts a hit distribution closer to the track intersection. Combining the two observations, one can infer that for pure matches the distance between hit and intersection is significantly smaller in MC compared to data. The widths of the distance distributions are  $RMS_{data} = 1.00 \text{ cm}$  compared to  $RMS_{MC} = 0.82 \text{ cm}$ . The chosen matching radius

is large enough that the overall purity agrees with data despite this difference in the distance distribution width. The overall matching widths of eTOF tracks (see figures 7.23 and 7.24) have been adjusted in the simulations to fit data. This has been done by adjusting the simulated input position resolutions of eTOF. The required eTOF resolutions are significantly wider than what is expected from strip width (x-position resolution) and electronics resolution (y-position resolution). Both the wide resolution required to fit the overall matching widths in the MC and the above shown closer distributions of the pure proton matches indicate that the current simulation description may overestimate the pointing accuracy of STAR tracks onto the eTOF plane. A direct comparison in which also the MC proton tracks are taken from  $\Lambda^0$  decays is needed to further validate the method presented in this section once a large simulation production is available.

## 8.3 $\phi$ -Meson Reconstruction

Kaon identification presents one of the greatest challenges for a time of flight (ToF) system. Due to the relatively low mass of kaons, they reach relativistic speeds even at intermediate momentum levels. This makes the separation between kaons and pions difficult, using ToF measurements alone. Additionally, the low natural abundance of kaons makes kaon samples particularly prone to contamination from various background sources, such as mismatched tracks or high-energy-loss pions. This makes kaons an intriguing choice for evaluating the physics performance of the eTOF system. A data-driven approach to assess whether the kaon sample identified by eTOF is suitable for further physics analysis is to associate them with a specific particle decay. Among the few light, abundant particles that decay into kaons with a high branching fraction is the  $\phi$  meson.<sup>4</sup> The  $\phi$  meson decays into a  $K^+K^-$  pair near the primary vertex. Moreover, the  $\phi$  meson is an interesting candidate for further physics analysis in BES-II, since BES-I measurements indicate that its elliptic flow deviates from NCQ scaling within the BES-II energy range (see Chapter 2.5.2).

This section first presents a study of eTOF's kaon identification purity. It will then show the benefits of eTOF to STAR's  $\phi$ -meson reconstruction in terms of phase-space coverage and reconstruction yield.

The analysis was conducted on the P23d picoDST production of  $\sqrt{s_{NN}} = 7.7\text{ GeV}$  Au+Au FXT data from February 2021, utilizing the calibration introduced in previous chapters.

### 8.3.1 Kaon Identification and Purity

The first step in  $\phi$ -meson reconstruction is identifying kaon candidates. Figure 8.9 presents the inverse relativistic velocity spectrum for primary tracks with eTOF

---

<sup>4</sup>The other such particle, the  $K^*$  meson, is challenging to separate from background due to its large decay width.

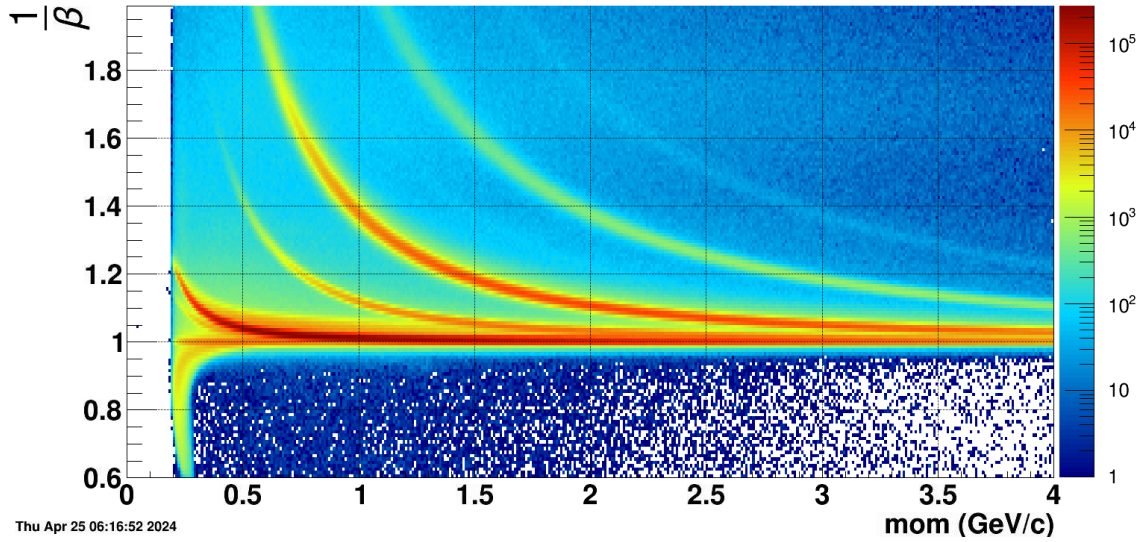


*Figure 8.9: Inverse relativistic velocity spectrum as function of particle momentum (per unit charge) for eTof matched tracks. A matching radius cut of  $\Delta r < 2$  cm is applied. Pion, kaon, proton and deuteron bands are clearly visible. Electrons and muons can be separated from pions at momenta below 0.5 GeV/c. Helium is faintly visible above the deuteron band hints of a triton band between deuterons and protons can be seen. At low momenta at contribution from mismatched tracks can be seen apparent super-luminal velocities.*

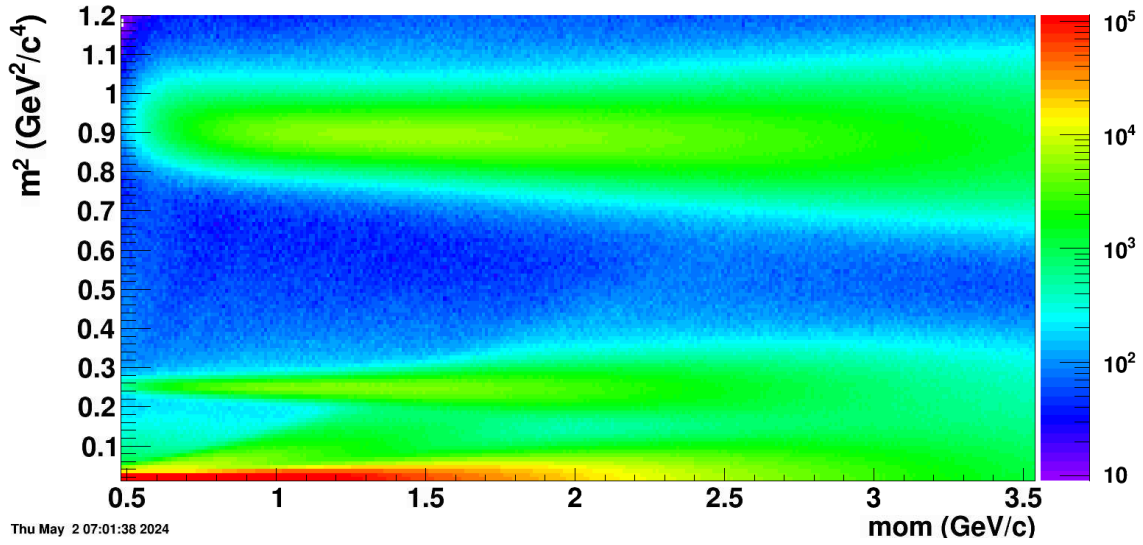


*Figure 8.10: Corresponding squared mass spectrum as function of track momentum. The colour axis has been adjusted to increase contrast in the kaon mass region.*



matches. A matching radius requirement of  $\Delta r < 2 \text{ cm}$  was applied to select for well-matched tracks. While the kaon band is visibly separated from the pion band up to approximately  $p \approx 2 \text{ GeV}/c$ , a notable background is also observed around the particle bands. Figure 8.10 shows the same data in the  $m^2$  versus momentum representation. In this representation, the width of the kaon distribution at a given momentum depends solely on the momentum resolution of the TPC, the ToF time resolution, and the path length uncertainty. This theoretical width,  $\sigma_{m^2}^{theo}$ , can be calculated from the known detector uncertainties in the mass measurement (see Equation 4.4) as:

$$\sigma_{m^2}^{theo} = 2 \cdot m_{kaon} \cdot \sigma_m \quad (8.4)$$

In STAR, the common approach for determining PID purity involves fitting the mass distribution of the target particle. Purity is then calculated as the integral of the signal fit function within the peak region, divided by the total number of entries in that region. In this analysis, the signal region is defined as  $\pm 3.5 \sigma_{theo}$  around the nominal kaon mass squared, aligning with the applied eTOF PID selection. The fitted mass distributions are obtained by projecting momentum slices of Figure 8.10 onto the mass axis, with each slice spanning  $0.1 \text{ GeV}/c$  in momentum. The analysis covers the kaon momentum range from  $0.5 \text{ GeV}/c$  to  $2.5 \text{ GeV}/c$ . To calculate a common  $\sigma_{m^2}^{theo}$  from Equation 4.4 for each slice, a series of assumptions is required due to variations in individual track properties

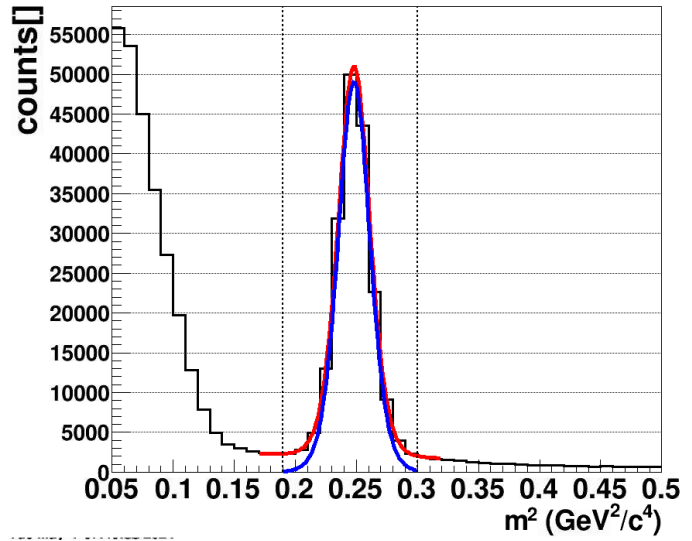


**Figure 8.11:** Example of a kaon purity fit. **Red:** Combined fit. **Blue:** Signal fit. **Black dotted lines:** Integration range for purity calculation.

- The particle momentum  $p$  is assumed to correspond to the center value of each momentum slice.
- The relative momentum error is estimated to be 2 %.
- The track path length  $L$  is assumed to be  $516 \text{ cm}$ , i.e. the average path length of all eTOF tracks.
- The track length error is assumed to be  $1 \text{ mm}$ . This assumption, or even an order of magnitude higher estimate, has little impact on the calculated  $\sigma_{m^2}^{theo}$ .



- The time of flight  $\Delta t_{tof}$  for each slice is calculated for a Kaon of nominal mass with the assumed momentum and path length.
- The eTof system time resolution is conservatively assumed to be 75 ps (Compare with Chapter 7.3.2).

Since the Gaussian shape of the distribution cannot be assumed, the more general Student's t-distribution is used as the signal fit function. The background shape is modeled in a phenomenological approach by a double exponential function.

The background model is too simplistic to fully describe the background shape for all momentum slices perfectly. However, more complex background models introduce additional parameters, which can result in highly unpredictable fits. Furthermore, no model currently exists to describe the various background sources (such as mismatched tracks, scattered particles in the detector, and poorly reconstructed tracks) from first principles. Therefore, the simple double-exponential background model is employed.

One of the exponential background terms is left unconstrained in the combined fit and accounts for the additional background component from pions. The second exponential function is fixed by a separate fit to the region from  $0.4 \text{ GeV}^2/c^4$  to  $0.5 \text{ GeV}^2/c^4$  and is intended to model the background between the kaon and pion peaks. This fitted exponential function is then included in the combined S+B fit with a phenomenological scaling factor of 0.8. The scaling factor is introduced to prevent an overestimation of the background in the region from  $0.18 \text{ GeV}^2/c^4$  to  $0.23 \text{ GeV}^2/c^4$ . Overestimating the background in this range would destabilize the signal fit in the peak region, resulting in a poorer description of the peak shape.

The quality of the combined fit then depends critically on the initialization of the fit parameters and the varying background shapes of the different slices. The fit range for the combined fit is therefore varied from  $4\sigma_{theo}$  to  $6\sigma_{theo}$  to quantify the systematic uncertainties due to this limitation. The background fits are also not used directly in the calculation of the purity. Instead, the signal integral over the signal range is compared to integrated entries of the mass square histogram in the same range. The  $\pm 3.5\sigma_{theo}$  integration range is extended to match the binning of the histogram. This ensures that signal and background are compared over the same range.

The average calculated purity and uncertainties from the fit range for each momentum slice is shown in Figure 8.12. In the intermediate momentum range between  $0.7 \text{ GeV}/c$  and  $1.6 \text{ GeV}/c$ , the calculated PID purity is relatively stable, ranging from 80 % to 90 %. These values can be compared to the matching purity from Monte-Carlo simulations shown in Figure 7.30 for similar spatial requirements<sup>5</sup>. Considering that the simulation estimate (Figure 7.30) only takes impurities from track mismatches into account and the limitations of the available

<sup>5</sup>The matching cut used in this analysis corresponds to  $\approx 0.4$  units on the elliptic cut scale in used in Figure 7.30

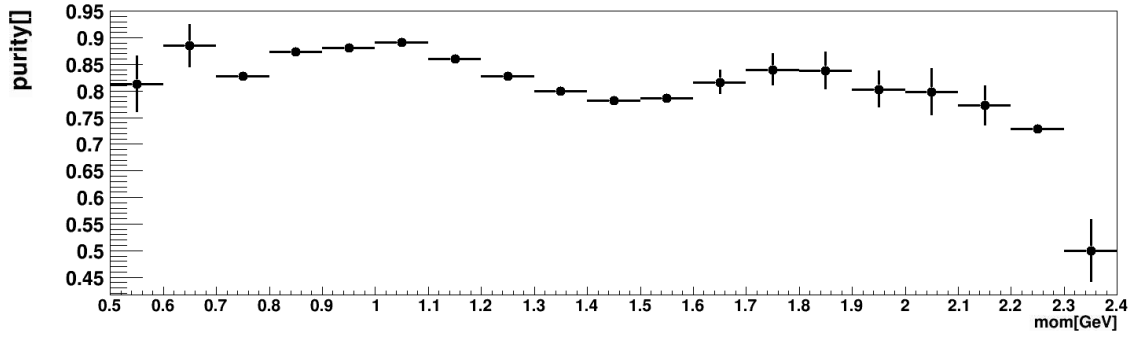


**Figure 8.12:** Kaon purity from a Student  $t$ -distribution fit to the  $e$ TOF mass square distribution as function of particle momentum in  $\sqrt{s_{NN}} = 7.7$  GeV FXT data. Results have been averaged over fits with different fit ranges. Error bars show the systematic uncertainty from the fit range. Statistical errors are smaller than the marker size.

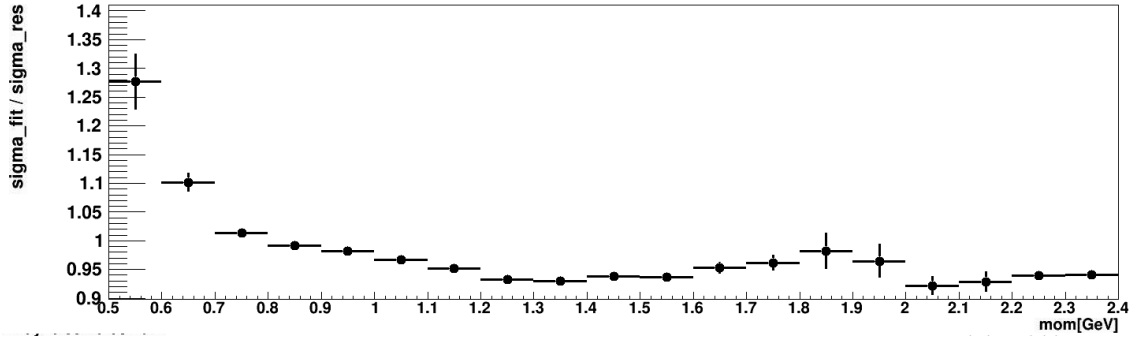


**Figure 8.13:** Ratio of fitted signal width of the Student  $t$ -distribution over  $\sigma_{m^2}^{theo}$ . Error bars show the systematic uncertainties from the background fit range.

simulation dataset, the values are in good agreement. The systematic uncertainties from the fitting procedure are small in this region, suggesting that the method produces stable results. The rise in the PID purity from  $0.7 \text{ GeV}/c$  to  $1.1 \text{ GeV}/c$  can be explained by increasing matching quality and is qualitatively mirrored in both matching efficiency and matching quality (compare Figures 7.25 and 7.35). The decline in the PID purity from  $1.1 \text{ GeV}/c$  to  $1.6 \text{ GeV}/c$  can be explained by a gradual increase in pion contamination. Figure 8.13 shows the signal width parameter of the Student t-distribution, normalized to  $\sigma_{m^2}^{theo}$ . Over the full momentum range from  $0.7 \text{ GeV}/c$  to  $1.1 \text{ GeV}/c$ , the fitted kaon peak width agrees within  $< 8\%$  with  $\sigma_{m^2}^{theo}$ , the expectation calculated from the detector resolution. The small systematic overestimation of the fitted width by the theoretical expectation is attributed to the conservative estimates for the eTOF system time resolution and TPC momentum resolution. This is an indication that the signal fit indeed describes kaons with a mass distribution which is dominated by the detector resolution.

At lower ( $p < 0.7 \text{ GeV}/c$ ) and higher ( $p > 1.6 \text{ GeV}/c$ ) momenta, the calculated averaged PID purity is similar, but the results vary significantly between the different fit ranges. This is due to an increased background component from mismatched low-momentum tracks which distorts the background shape and makes it difficult to isolate the signal contribution. At higher momenta, the proximity between the wider pion peak and the kaon peak leads to a similar effect.

In the low-momentum region, the fitted width parameter is also significantly larger than  $\sigma_{m^2}^{theo}$ , pointing to an increased background residual in the signal fit. In the high momentum range, the signal width remains close to the expectations. However, the shapes of the fits become increasingly non-Gaussian, signified by a lower  $\nu$  parameter of the Student t-distribution.

These observations may indicate that this method no longer delivers a reliable purity result outside the intermediate momentum range. Fortunately, this covers eTOF's main kaon PID range (compare figure 8.9).

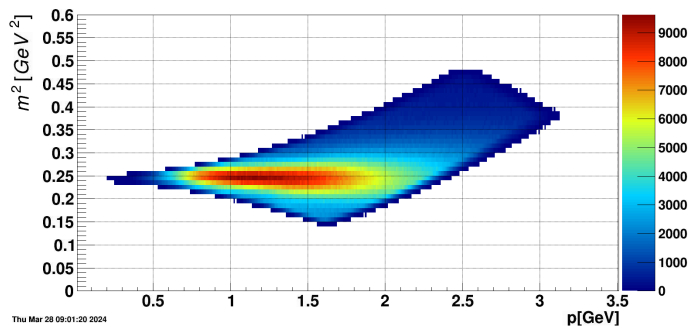


**Figure 8.14:** Mass square distribution of eTOF identified kaon candidates with pion/proton exclusion cut.

momenta, good purity values can be maintained by tightening the PID mass cuts. One possible approach is to do so is to require identified kaons to obey the conditions  $|m^2 - m_{pion}^2| > 3.5 \cdot \sigma_{theo,pion}$  and  $|m^2 - m_{proton}^2| > 3.5 \cdot \sigma_{theo,proton}$ . As such

The purity shown in this section in the intermediate mass region are sufficient for the majority of kaon-based analyses on BES-II data. It may not meet the high standards set in STAR's ongoing fluctuation measurements, but these analyses are done with less challenging probes like protons. Further refined particle selection criteria may be used to improve the PID purity. At higher

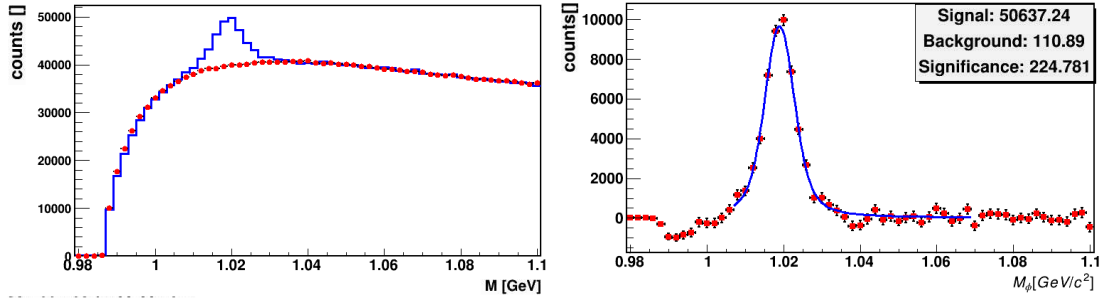


**Figure 8.15:** Invariant mass distribution of  $\phi$ -meson candidates in  $\sqrt{s_{NN}} = 7.7$  GeV data using combined bTOF only. **Blue:** Data candidates. **Red:** Mixed event background. Residual background is described by a linear function included in the fit. bTOF data only.

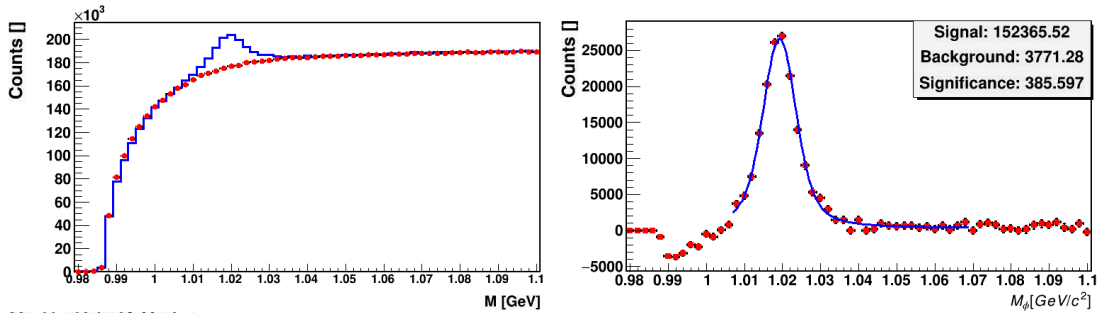


**Figure 8.17:** Invariant mass distribution of  $\phi$ -meson candidates in  $\sqrt{s_{NN}} = 7.7$  GeV data using combined bTOF and eTOF PID. **Blue:** Data candidates. **Red:** Mixed event background. Residual background is described by a linear function included in the fit. Combined eTOF and bTOF data

selections on the particle mass distort the mass spectrum, they have not been applied in the analysis shown in this section. These pion and proton exclusion cuts result in the mass distribution for eTOF identified kaon candidates shown in Figure 8.14. Additionally, requiring the TPC dE/dX identification to agree with the kaon hypothesis further reduces the background.

### 8.3.2 $\phi$ Reconstruction with Combined TOF

This sample of primary kaons is used to reconstruct  $\phi$ -meson candidates. Any kaon tracks with  $\chi^2_{primary} < 30$  are considered primary in this analysis. This loose selection criterion is primarily used as a safeguard against uncertainties in the vertex errors. As there are few particles decaying into kaons outside the fireball,

no significant increase in background is observed due to the loose selection. For eTOF, kaon tracks are identified as described above. For bTOF, this analysis relies on the  $n\sigma_{Kaon} < 3.5$  which is provided by the bTOF reconstruction chain. Kaon pairs from  $\phi$ -meson decays are kinematically indistinguishable from other pairs of primary kaons with similar invariant mass. Therefore, the invariant mass spectrum of  $\phi$ -meson candidates has a significant background. To describe this background and statistically separate signal from background, a mixed event method is used.

To generate mixed events, the positive tracks from each event in the data sample are combined with the negative tracks from up to 50 previously processed events of similar centrality. The number of charged tracks in the east side (closer to eTOF) of the TPC is used as a proxy for centrality. Two events are considered to be sufficiently similar in centrality if they fall into the same bracket with respect to the number of east-side tracks. The size of each bracket is 5 tracks.

As a reference, the invariant mass distribution and background estimate for  $\phi$ -meson candidates shown in Figure 8.15 are obtained using only TPC and bTOF. The background estimate from the mixed-event method is scaled to match the data integral in the invariant mass region from  $0.985 \text{ GeV}/c^2$  to  $0.995 \text{ GeV}/c^2$  and from  $1.030 \text{ GeV}/c^2$  to  $1.200 \text{ GeV}/c^2$ . Figure 8.16 shows the  $\phi$  signal after background subtraction. The signal peak is fitted with a Voigtian distribution.<sup>6</sup> The residual background is described by a linear function added to the fit. In Figure 8.16, the residual background contribution to the fit is negligible. It can be seen that the mixed event background slightly overestimates the data in the low-mass region between  $0.985 \text{ GeV}/c^2 < m < 1.005 \text{ GeV}/c^2$ . This is likely a feature of the mixed event method which also removes non- $\phi$ -decay related correlations between tracks in the same event from the data. The impact of this overestimation of low mass background on the signal yield is small.

With this method, STAR, using only TPC and bTOF, is able to reconstruct 50.6k  $\phi$  signal candidates in this data sample. The significance of the signal is 224.8.

The corresponding distributions after including eTOF in the analysis can be seen in figures 8.17 and 8.18. Despite the relatively small slice of angular acceptance added by eTOF, the raw signal yield increases by 301 % to 152.4k signal candidates. The corresponding significance is 385.6. This increase in available statistics shows the massive improvement eTOF provides for physics analysis in this energy range. It will enable further multi-differential  $\phi$ -meson analyses and significantly contribute to the understanding of uncertainties.

The impact of the acceptance increase can be understood when considering that bTOF acceptance in this energy range ( $\sqrt{s_{NN}} = 7.7 \text{ GeV}$  FXT) is far from mid-rapidity. eTOF extends the combined kaon acceptance close to mid-rapidity at  $y = -2.1$  in the STAR laboratory system<sup>7</sup>. The majority of these candidates are

<sup>6</sup>The Voigtian distribution is a convolution of a Gaussian distribution, which describes the detector mass resolution and a Breit-Wigner distribution which describes the natural line width of the decay. The numerical implementation of the Voigtian function provided by the RooFit package is used.

<sup>7</sup>For consistency with collider and raw data, the default STAR coordinate system is used in which

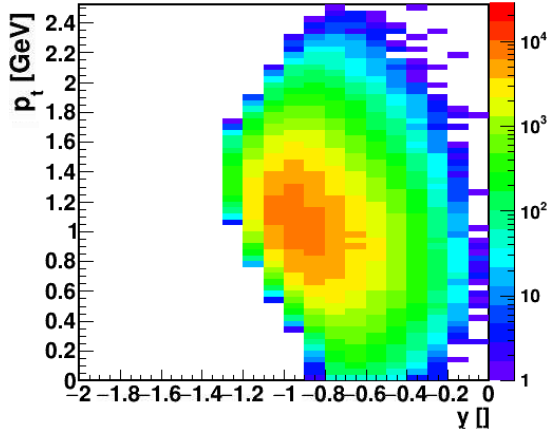


Figure 8.19

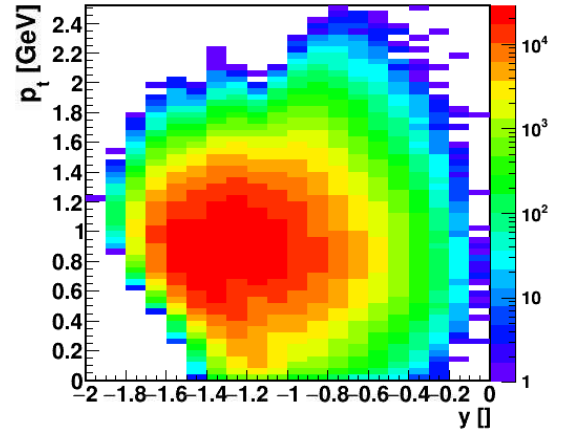


Figure 8.20

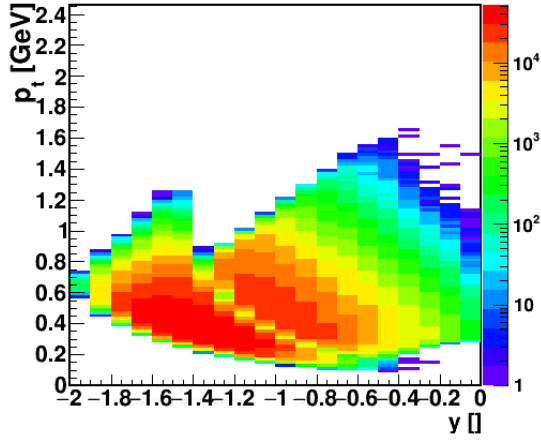
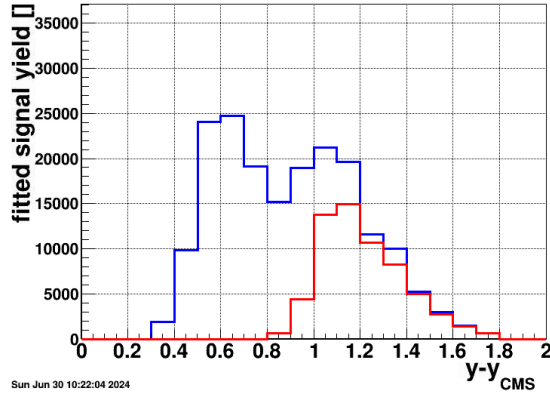
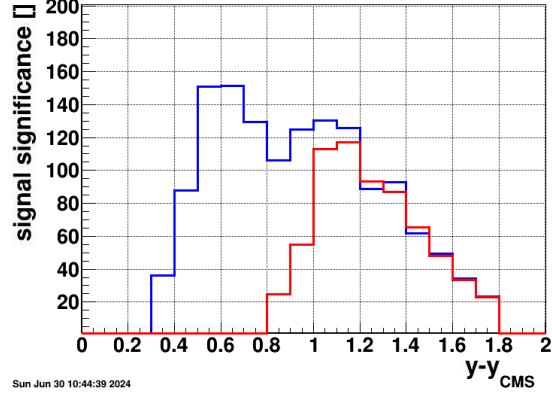


Figure 8.21

Phase-space distribution of  $\phi$ -candidates with  $0.999 \text{ GeV}/c^2 < m_{inv} < 1.039 \text{ GeV}/c^2$ . Rapidity is shown in the laboratory reference system. **Fig.8.19:** Reconstruction using bTOF only. **Fig.8.20:** Reconstruction using bTOF and eTOF combined. **Fig.8.21:** Phase-space distribution of daughter kaons for combined TOF reconstruction.



**Figure 8.22:** Fitted signal yield of  $\phi$ -mesons after subtraction of mixed event background as function of rapidity in the CMS system. **Red:** PID with bTOF only. **Blue:** PID with bTOF and eTOF combined.



**Figure 8.23:** Signal significance of  $\phi$ -mesons after subtraction of mixed event background as function of rapidity in the CMS system. **Red:** PID with bTOF only. **Blue:** PID with bTOF and eTOF combined.

reconstructed from one kaon in the bTOF acceptance and one kaon in the eTOF acceptance.

Figures 8.19 and 8.20 illustrate the increase in phase space coverage when combining eTOF and bTOF PID. Shown are all primary kaon pairs with an invariant mass within  $20 \text{ MeV}$  (5 times the decay width of the  $\phi$  meson) of the nominal  $\phi$  mass. Figure 8.21 shows the phase-space distribution of the corresponding decay kaons. Here, the contributions of eTOF and bTOF are clearly distinguishable. This kaon acceptance agrees with the acceptance predictions (see Figure 4.4) for eTOF with a time resolution of  $80 \text{ ps}$ . On the other hand, bTOF loses acceptance in the high- $p_t$  region due to the default bTOF PID logic applied here.

The main physics interest in  $\phi$ -mesons lies in their flow behavior, where they probe the influence of strangeness on the behavior of baryonic matter at high densities (see for example Chapter 2.7). At mid-rapidity, influences from longitudinal motion of particles cancel out due to the symmetry of the system. Measurements at mid-rapidity are therefore often easier to interpret and compare to models. This makes mid-rapidity a region of special physics interest. Figure 8.22 and 8.23 show the background-corrected signal yield and signal significance as a function of rapidity in the center-of-mass system. Without eTOF, no significant  $\phi$ -meson peak can be detected within 0.8 units of rapidity around mid-rapidity. Adding eTOF extends the coverage down to a rapidity of 0.3 with a remaining peak significance of 38 (for a bin width of 0.1 units in rapidity). This significance is still sufficient for flow analysis [92]. At this highest FXT energy of  $\sqrt{s_{NN}} = 7.7 \text{ GeV}$  even with eTOF, mid-rapidity is not covered. However, this energy is also covered in BES-II in collider mode where mid-rapidity coverage is available. The extended coverage from eTOF in FXT mode does provide direct rapidity overlap with the STAR

---

eTOF and the forward direction of the FXT collisions map to negative rapidities.

acceptance in collider mode and allows direct comparison of collider and FXT results. eTOF also demonstrates direct mid-rapidity coverage for all FXT energies below  $\sqrt{s_{NN}} = 6.2 \text{ GeV}$ , corresponding to a mid-rapidity at  $y_{lab} = -1.87$ .



## 9 Conclusions

During this thesis work, eTOF data from the STAR BES-II run have been taken, calibrated and analyzed. A software package for the reconstruction and calibration of these data has been developed. The calibration and analysis efforts have been focused on the 2020 FXT program, especially the  $\sqrt{s_{NN}} = 7.7 \text{ GeV}$ . Three main points have been the center of the analysis: The investigation of DAQ features, the characterization of MRPCs with respect to their dark rate, efficiency and time resolution and demonstration of eTOF's physics impact. This research has led to improved understanding in various areas for CBM and STAR:

### 9.1 Learnings for CBM

The STAR eTOF project represents the first large-scale test of CBM-TOF MRPC prototypes, a free-streaming DAQ prototype and their integration into a large DAQ system.

The first important findings of the project were necessary improvements in the electronics. Extensive developments have been done by J. Frühauf to protect the input stage of PADI against damage from power spikes. These protections aim to prevent similar damage as the PADIs suffered during BES-II at CBM. Tests by I. Deppner and N. Herrmann have failed to recreate the PADI damage events at GSI under mCBM conditions. Another area where eTOF spurred further development is the stability of the TDC timing measurements. During this work, several data issues due to re-synchronization features of the GET4 FEEs have been documented: Outages of GET4s in events, clock-jumps and time-shifts between runs (see Chapters 6.4.1 and 5.4.7). While significant efforts to correct the eTOF data in STAR on the software side have yielded good results, residual timing and acceptance issues remain. Developments by E. Rubio and J. Frühauf for the CBM common read-out interface (CRI), the successor to the gDBP used in eTOF improve significantly on synchronization issues. A bug in the GET4-ASIC which led to the majority of epoch mismatches has been cured in the firmware. A consistent initialization of the clock phase prevents time shifts after DAQ restarts.

With regard to the MRPC time resolution, this work demonstrates that CBM-TOFs current prototypes are reaching the target system time resolution of  $80 \text{ ps}$  in a large system if CBM can achieve a start time resolution of  $< 45 \text{ ps}$  (see Chapter 7.3.3). Avenues to further improve the MRPC time resolution and relax the requirements on the start time system have also been shown in this thesis. Calibration residuals due to timing shifts in the DAQ could be removed with larger timing-stable datasets (see Chapter 7.3.4). A walk calibration which takes the position

of hits along the strips into account may reduce the influence of absorbed signal reflections (see Chapter 7.1.4). Pre-measured signal velocities in a controlled test setup may reduce the uncertainties in the determination of the signal velocity (see Chapter 7.1.3). A timing correction for the delay of cluster size 2 hits would slightly improve the overall time resolution (see Chapter 7.3.4). Furthermore, significant differences in the time resolution between individual MRPCs have been observed. The RMS of the distribution of MRPC time resolutions is  $4.3\text{ ps}$  and  $3.8\text{ ps}$  for USTC-type counters and THU-type counters respectively. The time resolutions for individual counters were found to be not well correlated when comparing different run periods, so the majority of the differences can be attributed to the above mentioned calibration residuals. USTC-type counters were found to perform slightly better than THU-type counters with an average system time resolution of  $70.6\text{ ps}$  versus  $74.8\text{ ps}$ . This result qualitatively matches the expectations from the different gas gap size.

The detector efficiency of the MRPC prototypes has been challenging to measure directly in the STAR setup. Two different estimates, from the overlap between eTOF counters (see Chapter 7.2.2) and from a comparison with the bTOF system (see Chapter 7.2.3) point to a detector efficiency around 90 %, close to the CBM requirements. CBM will use a gas mixture with a higher dielectric strength which will allow to improve the efficiency slightly. A newer version of PADI will also detect MRPC signals close to the discrimination threshold more reliably due to an in-built signal stretcher.

The dark rate of the MRPCs was observed to increase over operation periods of multiple months in this work. It did not reach levels at which data analysis is impacted by significant background. Most dark rate hits occur in the vicinity of the fishing lines. Between run periods, dark rate levels decline again. No evidence of permanent detector degradation due to aging has been observed over two years of operation in the BES-II program.

It has also been observed that a significant fraction of digi-signals are stretched by what appears to be absorbed reflected signals. This observation was unexpected since the MRPC prototypes have been impedance matched between the read-out strips and the pre-amplifier input. This asks for further studies of the MRPCs signal transmission path and impedance behavior.

## 9.2 BES-II Data for STAR

For STAR, the main objective for the eTOF project has been to deliver PID data at forward rapidity. This work aims to deliver calibrated eTOF data and show their readiness for physics analysis.

A calibration scheme has been developed and applied for the first production of 2020 FXT runs. eTOF achieves an average system time resolution of  $70.7\text{ ps}$ , exceeding the design system time resolution of  $80\text{ ps}$  (see Chapter 7.3.2) in these data.

The achieved track matching efficiency is close to 70 % in the 2020 FXT runs. In regions with full acceptance and no significant additional material budget in front of eTOF, a local matching efficiency of  $\approx 80\%$  is achieved. This result is comparable to the bTOF matching efficiency. In the 2021 data, the matching efficiency declined to 59.7 % and 64.3 % for USTC-type counters and THU-type counters due to damaged PADI pre-amplifiers (see Chapter 7.2.3). The stability of eTOF's matching efficiency over different events has been a major concern due to GET4 re-synchronizations. The GoodEventFlag introduced in this work has been shown to provide a matching efficiency which is stable to  $< 2\%$  variation between runs. Using the GoodEventFlag comes at the price of an event-by-event variation in the eTOF acceptance. One strategy to circumvent this drawback is to exclude the regions with the lowest fractions of GoodEventFlags from the analysis and afterwards focus only on events in which all GoodEventFlags are set in the remaining area. This strategy is currently employed in the ongoing proton fluctuation analysis of the FXT data.

Another question to eTOF's data quality has been the purity the particle identification. As the time resolution of the system is sufficient, this is mainly a question of correct track matching. This work introduces cut strategies to maintain high purity with good efficiency (see Figure 7.35). The purity of eTOF data has been estimated in two data-driven approaches. Using a high-purity sample of proton tracks from  $\Lambda^0$ -decays eTOF's purity for protons with  $p > 0.9 \text{ GeV}/c$  has been estimated. The overall proton purity was found to exceed 90 %, the minimum required purity for a proton fluctuation analysis (see Chapter 2.6), for a cut on distance between hit and intersection up to 3.5 cm. Such a cut retains 92.6 % of all matched proton tracks from  $\Lambda^0$  decays. In this case, the purity is limited by the track matching between eTOF and TPC instead of the time resolution of eTOF.

Another purity estimate has been presented for kaons. Kaon PID is more sensitive to the eTOF time resolution due to the small mass gap to pions. Here, the  $m_{kaon}^2$  distribution has been fitted by a Student's t-function for the Kaon peak and a background function. The purity has been estimated as the fraction of the peak function integral over the total number of entries in the signal mass region. eTOF has shown to be able to deliver a kaon purity of  $> 80\%$  over a momentum range of  $0.7 \text{ GeV}/c < p_{kaon} < 1.6 \text{ GeV}/c$  (see Figure 8.12). The width of the peak fit was found to agree with theoretical predictions from the eTOF time resolution and TPC momentum resolution with  $< 7\%$  in this range. Qualitatively, the purity estimate for kaons agrees with the methodologically different proton purity estimate when accounting for the lower combinatorial background in the proton mass region. The kaon PID range can be extended to lower momenta by including TPC information. At higher momenta, up to  $p < 3.0 \text{ GeV}/c$ , an asymmetric mass cut can allow for high kaon purity with reduced PID efficiency (see Figure 8.14).

To show the successful integration of eTOF into the STAR physics analysis, a comparison of  $\phi$ -meson reconstruction between STAR with and without eTOF has been presented (see Chapter 8.3.2.). The inclusion of eTOF has been shown to increase the yield of reconstructed  $\phi$ -mesons by 301 % in the  $\sqrt{s_{NN}} = 7.7 \text{ GeV}$  FXT

dataset. The majority of those extra  $\phi$ -mesons are reconstructed from one kaon detected by eTOF and one kaon detected by bTOF. This demonstrates the good integration of the two sub-systems. Furthermore, eTOF is shown to extend STAR's forward rapidity coverage for  $\phi$ -mesons from  $y - y_{cms} > 0.8$  to  $y - y_{cms} > 0.3$  (see Figure 8.23) in this energy range. It can be inferred that eTOF provides direct mid-rapidity coverage at most lower FXT energies. This acceptance extension has major benefits for flow analyses, the main point of physics interest for the  $\phi$ -meson. eTOF's inclusion is also necessary to obtain an overlap in the rapidity coverage between  $\sqrt{s_{NN}} = 7.7 \text{ GeV}$  FXT and  $\sqrt{s_{NN}} = 7.7 \text{ GeV}$  collider data. This allows direct comparison of physics results between the two detector configurations and is therefore an important step to validate the analysis of the FXT program in general. Extending STAR's forward acceptance in the FXT program was a major physics motivation for the eTOF project. This analysis demonstrates that eTOF was successful in that regard.

## 10 Danksagungen

Besonderer Dank geht an:

Prof. Dr. Norbert Herrmann für die langjährige Betreuung und Unterstützung dieser Arbeit.

Prof. Dr. Ulrich Uwer für die Übernahme des Zweitgutachens und der Zweit-Betreuung.

Prof. Dr. Peter Fischer und Prof. Dr. Jan Martin Pawlowski für die Mitwirkung an dieser Disputation.

Dr. Ingo Deppner und Dr. Christian Simon für die langjährige Beratung und all die interessanten Gespräche.

Dr. Pengfei Lyu, Florian Seck und Yannik Söhngen für die gute Zusammenarbeit an diesem Projekt.

Meinem Bruder, Peter Weidenkaff, für viele Ratschläge und Korrekturen.

Meiner Mutter, Gudrun Weidenkaff, für all die Unterstützung die es mir ermöglicht hat diese Arbeit abzuschließen.

Meinem Vater, Martin Weidenkaff, dafür dass du immer an mich geglaubt hast. Ruhe in Frieden.

My Girlfriend, Qiunan Zhang, for all your love, support and patience with me.

## 11 References

1. Wikipedia. "Phase diagram" 2022. [https://en.wikipedia.org/wiki/Phase\\_diagram](https://en.wikipedia.org/wiki/Phase_diagram).
2. Goldstone, J. *et al.* "Broken Symmetries". *Phys. Rev.* **127**, 965–970. <https://link.aps.org/doi/10.1103/PhysRev.127.965> (3 1962).
3. Weinberg, S. "The Making of the Standard Model". *Eur. Phys. J. C* **34**, 5–13 (2004).
4. Wikipedia. "Standard Model" 2024. [https://en.wikipedia.org/wiki/Standard\\_Model](https://en.wikipedia.org/wiki/Standard_Model).
5. Huston, J. *et al.* "Quantum Chromodynamics". <https://pdg.lbl.gov/2022/reviews/rpp2022-rev-qcd.pdf> (2022).
6. Deur, A. *et al.* "The QCD Running Coupling". *Nucl. Phys.* **90**, 1 (2016).
7. Möller, P. & Sierk, A. "80 Years of the liquid drop—50 years of the macroscopic-microscopic model". *International Journal of Mass Spectrometry* **349-350**, 19–25. <https://www.sciencedirect.com/science/article/pii/S1387380613001346> (2013).
8. CERN. "New State of Matter created at CERN" 2000. <https://home.web.cern.ch/news/press-release/cern/new-state-matter-created-cern>.
9. BNL. "RHIC Scientists Serve Up 'Perfect' Liquid" 2005. <https://www.bnl.gov/newsroom/news.php?a=110303>.
10. Bzdak, A. *et al.* "Mapping the phases of quantum chromodynamics with beam energy scan". *Physics Reports* **853**, 1–87. <https://www.sciencedirect.com/science/article/pii/S0370157320300156> (2020).
11. Aoki, Y. *et al.* "The Order of the quantum chromodynamics transition predicted by the standard model of particle physics". *Nature* **443**, 675–678 (2006).
12. Niida, T. & Miake, Y. "Signatures of QGP at RHIC and the LHC". *AAPPS Bull.* **31**, 12 (2021).
13. Bazavov, A. *et al.* "Chiral crossover in QCD at zero and non-zero chemical potentials". *Phys. Lett. B* **795**, 15–21 (2019).
14. De Forcrand, P. "Simulating QCD at finite density". *PoS LAT2009*, 010 (2009).
15. Fu, W.-j. *et al.* "QCD phase structure at finite temperature and density". *Phys. Rev. D* **101**, 054032 (2020).

16. Huth, S. *et al.* “Constraining Neutron-Star Matter with Microscopic and Macroscopic Collisions”. *Nature* **606**, 276–280 (2022).
17. Lattimer, J. M. & Prakash, M. in *From Nuclei to Stars: Festschrift in Honor of Gerald E Brown* 275–304 (2011).
18. Gerstung, D. *et al.* “Hyperon–nucleon three-body forces and strangeness in neutron stars”. *Eur. Phys. J. A* **56**, 175 (2020).
19. Nayak, T. K. “Heavy Ions: Results from the Large Hadron Collider”. *Pramana* **79**, 719–735 (2012).
20. Deppner, I. “Development of a fully differential Multi-gap Resistive Plate Chamber for the CBM Experiment” PhD thesis (Ruperto-Carola-University of Heidelberg, 2013).
21. Bzdak, A. *et al.* “Mapping the Phases of Quantum Chromodynamics with Beam Energy Scan”. *Phys. Rept.* **853**, 1–87 (2020).
22. Adam, J. *et al.* “Nonmonotonic Energy Dependence of Net-Proton Number Fluctuations”. *Phys. Rev. Lett.* **126**, 092301 (2021).
23. Stephanov, M. A. “On the sign of kurtosis near the QCD critical point”. *Phys. Rev. Lett.* **107**, 052301 (2011).
24. Fries, R. J. *et al.* “Coalescence Models For Hadron Formation From Quark Gluon Plasma”. *Ann. Rev. Nucl. Part. Sci.* **58**, 177–205 (2008).
25. Adamczyk, L. *et al.* “Elliptic flow of identified hadrons in Au+Au collisions at  $\sqrt{s_{NN}} = 7.7\text{--}62.4$  GeV”. *Phys. Rev. C* **88**, 014902 (2013).
26. Adam, J. *et al.* “Strange hadron production in Au+Au collisions at  $\sqrt{s_{NN}} = 7.7, 11.5, 19.6, 27, \text{ and } 39$  GeV”. *Phys. Rev. C* **102**, 034909 (2020).
27. Becattini, F. & Lisa, M. A. “Polarization and Vorticity in the Quark–Gluon Plasma”. *Ann. Rev. Nucl. Part. Sci.* **70**, 395–423 (2020).
28. FAIR. “Accelerators” 2022. <https://fair-center.eu/overview/accelerator>.
29. APPA. 2022. <https://fair-center.de/user/experiments/appa>.
30. PANDA. 2022. <https://panda.gsi.de/>.
31. NUSTAR. 2022. <http://www.fair-nustar.de/>.
32. Friese, V. “The high-rate data challenge: computing for the CBM experiment”. *J. Phys. Conf. Ser.* **898**, 112003 (2017).
33. Friman, B. *et al.* “The CBM Physics Book” (Julius Springer Verlag, 2011).
34. Akishina, V. & Kisel, I. *Online event reconstruction in the CBM experiment at FAIR in EPJ Web of Conferences* **173** (2018).
35. CBM-TOF Collaboration. “Technical Design Report for the CBM Time-of-Flight System (TOF)” (ed Herrmann, N.) 182 S. <https://repository.gsi.de/record/109024> (GSI, Darmstadt, 2014).

36. Petris, M. "SPS-CERN in-beam test performance of Bucharest-MGMSRPC prototypes" Internal communication, 28. CBM collaboration meeting, Tübingen. 2016.
37. Lyu, P. "Summary of Tsinghua MRPCs' Performance in SPS Beamtest (Nov 2015)" Internal communication, 28. CBM collaboration meeting, Tübingen. 2016.
38. The CBM Collaboration. *mCBM@SIS18* tech. rep. CBM (Darmstadt, 2017), 58 S. <https://repository.gsi.de/record/220072>.
39. Zhang, Q. *et al.* "mTOF performance during the first main commissioning beam time at mCBM". *JINST* **15**, C12007 (2020).
40. Petris, M. *In-beam test of the MSMGRPC prototypes for the CBM-TOF inner zone in the mCBM experimental setup* tech. rep. 2022 (Darmstadt, 2022), 239 p. <https://repository.gsi.de/record/246663>.
41. US Department of Energy. "STAR Detector on the move" 2018. <https://phys.org/news/2018-10-star-detector.html>.
42. Beddo, M. E. *et al.* "STAR: Conceptual design report for the Solenoidal Tracker at RHIC". BNL-PUB-5347 (1992).
43. Adler, C. *et al.* "Identified Particle Elliptic Flow in Au+Au Collisions at  $\sqrt{s_{NN}} = 130\text{ GeV}$ ". *Phys. Rev. Lett.* **87**, 182301 (18 2001).
44. Adams, J. *et al.* "Narrowing of the Balance Function with Centrality in Au + Au Collisions at  $\sqrt{s_{NN}} = 130\text{ GeV}$ ". *Phys. Rev. Lett.* **90**, 172301. <https://link.aps.org/doi/10.1103/PhysRevLett.90.172301> (17 2003).
45. Adams, J. *et al.* "Evidence from  $d + \text{Au}$  Measurements for Final-State Suppression of High- $p_T$  Hadrons in Au + Au Collisions at RHIC". *Phys. Rev. Lett.* **91**, 072304. <https://link.aps.org/doi/10.1103/PhysRevLett.91.072304> (7 2003).
46. Adams, J. *et al.* "Strange antiparticle-to-particle ratios at mid-rapidity in  $s_{NN}=130\text{ GeV}$  Au+Au collisions". *Physics Letters B* **567**, 167–174. <https://www.sciencedirect.com/science/article/pii/S0370269303009390> (2003).
47. The Star Collaboration. *Studying the Phase Diagram of QCD Matter at RHIC* Whitepaper (The Star Collaboration, 2014). [https://drupal.star.bnl.gov/STAR/files/BES\\_WPII\\_ver6.9\\_Cover.pdf](https://drupal.star.bnl.gov/STAR/files/BES_WPII_ver6.9_Cover.pdf).
48. Anderson, M. *et al.* "The STAR time projection chamber: a unique tool for studying high multiplicity events at RHIC". *Nuclear Instruments and Methods in Physics Research Section A: Accelerators, Spectrometers, Detectors and Associated Equipment* **499**, 659–678. <https://www.sciencedirect.com/science/article/pii/S0168900202019642> (2003).
49. The Star Collaboration. *A Proposal for STAR Inner TPC Sector Upgrade (iTPC)* Star Note (The Star Collaboration, 2015). [https://drupal.star.bnl.gov/STAR/system/files/STAR\\_iTPC\\_proposal\\_06\\_09\\_2015.pdf](https://drupal.star.bnl.gov/STAR/system/files/STAR_iTPC_proposal_06_09_2015.pdf).



50. Wu, J. *et al.* "A barrel TOF for STAR at RHIC". *Journal of Physics G: Nuclear and Particle Physics* **34**, S729–S732. <https://doi.org/10.1088/0954-3899/34/8/s83> (2007).
51. The STAR Collaboration. *BEMC Technical design report* Technical design report (STAR). <https://drupal.star.bnl.gov/STAR/system/files/BEMC+TDR.pdf>.
52. Adams, J. *et al.* "The STAR event plane detector". *Nuclear Instruments and Methods in Physics Research Section A: Accelerators, Spectrometers, Detectors and Associated Equipment* **968**, 163970. <https://www.sciencedirect.com/science/article/pii/S0168900220304344> (2020).
53. Brandenburg, J. D. "Figure : STAR FXT ORTHO" 2022. <https://jdbburg.com/posts/figure-star-fxt-ortho/>.
54. Tlusty, D. *The RHIC Beam Energy Scan Phase II: Physics and Upgrades in 13th Conference on the Intersections of Particle and Nuclear Physics* (2018). arXiv: 1810.04767 [nucl-ex].
55. Yang, C. "The STAR beam energy scan phase II physics and upgrades". *Nucl. Phys. A* **967**, 800–803 (2017).
56. Liu, C. *et al.* "Summary of the 3-year Beam Energy Scan II operation at RHIC". *JACoW IPAC2022*, 1908–1911 (2022).
57. Cebra, D. "Beam Energy Scan II (BES-II) and FXT:Status and Plans" Talk at CBM-STAR Joint Workshop 2017. 2017.
58. Hu, D. *et al.* "MRPC3b mass production for CBM-TOF and eTOF at STAR". *JINST* **14**, C06013 (2019).
59. "Physics Program for the STAR/CBM eTOF Upgrade". arXiv: 1609.05102 [nucl-ex] (2016).
60. D.E.Groom, S. "Passage of Particles Through Matter" 2021. <https://pdg.lbl.gov/2021/reviews/rpp2020-rev-passage-particles-matter.pdf>.
61. Weidenkaff, P. "Characterizations of Multi-Gap Resistive Plate Chamber Prototypes in a Freestreaming Read-Out Environment" Master-Thesis. 2016.
62. Sauli, F. in *Lectures given in the Academic Training* (CERN, 1977).
63. Lippmann, C. "Detector Physics of Resistive Plate Chambers" PhD thesis (Johann Wolfgang Goethe-Universität, Frankfurt am Main, 2003).
64. Riegler, W. *et al.* "Detector physics and simulation of resistive plate chambers". *Nuclear Instruments and Methods in Physics Research Section A: Accelerators, Spectrometers, Detectors and Associated Equipment* **500**. NIMA Vol 500, 144–162. <https://www.sciencedirect.com/science/article/pii/S0168900203003371> (2003).

65. Wang, Y. *et al.* in *Proceedings of the 8th International Conference on Quarks and Nuclear Physics (QNP2018)* (). <https://journals.jps.jp/doi/abs/10.7566/JPSCP.26.024006>.
66. Lyu, P. "MRPC3a Review Readiness Report" Internal communication, 29. CBM collaboration meeting, Darmstadt. 2017. [https://indico.gsi.de/event/4759/contributions/22222/attachments/16306/20580/MRPC3a\\_ReviewReadinessReport.pdf](https://indico.gsi.de/event/4759/contributions/22222/attachments/16306/20580/MRPC3a_ReviewReadinessReport.pdf).
67. Deppner, I. & Herrmann, N. "The CBM Time-of-Flight system". *Journal of Instrumentation* **14**, C09020. <https://dx.doi.org/10.1088/1748-0221/14/09/C09020> (2019).
68. Sun, Y. "MRPC3b Review Readiness Report" Internal communication, 29. CBM collaboration meeting, Darmstadt. 2017. [https://indico.gsi.de/event/4759/contributions/22221/attachments/16304/20576/MRPC3b\\_ReviewReadinessReport-1.1.pdf](https://indico.gsi.de/event/4759/contributions/22221/attachments/16304/20576/MRPC3b_ReviewReadinessReport-1.1.pdf).
69. Ciobanu, M. *et al.* "New Models of PADI, an Ultrafast Preamplifier–Discriminator ASIC for Time-of-Flight Measurements". *IEEE Trans. Nucl. Sci.* **68**, 1325–1333 (2021).
70. Ciobanu, M. *et al.* "PADI, an Ultrafast Preamplifier - Discriminator ASIC for Time-of-Flight Measurements". *IEEE TRANSACTIONS ON NUCLEAR SCIENCE* (2014).
71. Deppe, H. & Flemming, H. "The GSI Event driven TDC with 4 Channels GET4" tech. rep. (GSI, Darmstadt, 2019).
72. Moreira, P. *et al.* "GBTX MANUAL" 2018. <https://readthedocs.web.cern.ch/ate/files/113213790/113213791/1/1556910129000/gbtXManual.pdf>.
73. OHWR. "AMC FMC Carrier Kintex (AFCK)" 2017. <http://www.ohwr.org/projects/afck/wiki>.
74. Xilinx. "Kintex 7 FPGA family" 2017. <https://www.xilinx.com/products/silicon-devices/fpga/kintex-7.html>.
75. Loizeau, P. A. *Streaming DAQ used for the eTOF in STAR* "Internal communication, Streaming Readout VI Virtual Workshop". 2020.
76. D. Hutter J. de Cuveland, V. L. "CBM FLES input interface developments". *GSI SCIENTIFIC REPORT* (2014).
77. Frühauf, J. *CBM ToF @ STAR* "Internal communication, EE-Meeting". 2017.
78. Deppner, I. *The FAIR Phase 0 program of the CBM Time-of-Flight project* "15th Workshop on Resistive Plate Chambers and Related Detectors". 2020.
79. Wikipedia. "Constant fraction discriminator" 2023. [https://en.wikipedia.org/wiki/Constant\\_fraction\\_discriminator](https://en.wikipedia.org/wiki/Constant_fraction_discriminator).

80. STAR shift crew. *STAR electronic shift log 2019* 2019. <https://online.star.bnl.gov/apps/shiftLog2019/>.
81. Frühauf, J. "Padi damage" Internal communication, CBM-Tof Weekly Meeting. 2021.
82. Deppner, I. "CBM-TOF internal communications: Recent observations from mCBM." 2022.
83. Lyu, P. "Development and Application Study of the High-rate Multi-gap Resistive Plate Chamber for CBM Experiment" PhD thesis (Tsinghua University, Beijing, 2019).
84. Hu, D. *The study on MRPC application in Heavy-ion experiment and the quality control of mass production for STAR/CBM-eTOF upgrade* PhD thesis (University of Science and Technology of China, Hefei, 2019).
85. Söhngen, Y. "CBM-TOF internal communications" 2022.
86. Senger, P. & Friese, V. *CBM Progress Report 2021* tech. rep. 2022 (Darmstadt, 2022), 239 p. <https://repository.gsi.de/record/246663>.
87. Sauter, D. *MRPC Prototype 3a & 3b performance studies at the cosmic radiation test setup of the CBM-TOF group in Heidelberg* Master-Thesis. 2018. [https://indico.gsi.de/event/8240/contributions/36256/attachments/26291/32899/Masterthesis-Dennis\\_Sauter.pdf](https://indico.gsi.de/event/8240/contributions/36256/attachments/26291/32899/Masterthesis-Dennis_Sauter.pdf).
88. Simon, C. "private communications" 2021.
89. Gorbunov, S. & Kisel, I. *Reconstruction of decayed particles based on the Kalman filter* 2007. <https://www.star.bnl.gov/~bouchet/KFParticle/DOC-2007-May-14-1.pdf>.
90. Ju, X.-Y. *et al.* "Applying the Kalman filter particle method to strange and open charm hadron reconstruction in the STAR experiment". *Nucl. Sci. Tech.* **34**, 158 (2023).
91. Kisel, I. "Real-Time Event Reconstruction and Analysis in CBM and STAR Experiments". *J. Phys. Conf. Ser.* **1602**, 012006 (2020).
92. Han, J. "private communications" 2024.

## 12 List of Publications

1. Weidenkaff, P. *et al.* *Simulation and Software Verification of CBM-ToF beamtime analysis* in *CBM Progress Report 2017* (2018).
2. Weidenkaff, P. *et al.* *Hit building and calibration of CBM-ToF detectors in the StRoot framework for Phase-0 activities* in *CBM Progress Report 2018* (2019).
3. Weidenkaff, P. *et al.* *Status of the eTOF at STAR program after the 2019-2020 beam campaign* in *CBM Progress Report 2019* (2020).
4. Weidenkaff, P. *et al.* *Systematic evaluation of eTOF performance in the STAR RUN20* in *CBM Progress Report 2020* (2021).

# Curriculum Vitae

## Personal Data

Name: Philipp Christian Weidenkaff  
Date of Birth: 01.03.1991  
Place of Birth: Heidelberg  
Citizenship: German  
Marital Status: single

## School Education

0.9.1997 - 06.2001      Grundschule Schönbrunn  
09.2001 - 06.2009      Hohenstaufen-Gymnasium Eberbach  
Graduation: Abitur

## Civil Service

10.2009 – 07.2010      Seniorenzentrum Rosengarten, Obrigheim

## Academic Studies

Since 10.2010      Physics Studies, University of Heidelberg  
03.2010      B.Sc. Physics, Topic:  
Aufbau und Test eines RPC-Referenc-Systems für CBM-Detektor-Tests  
05.2015 – 08.2015      Internship at Tsinghua University, Beijing  
03.2010      M.Sc. Physics, Topic:  
Characterization of Multi-Gap Resistive Plate Chamber Prototypes  
in a Freestreaming Read-Out Environment

## Graduate Studies

Since 09.2017      Graduate Studies, University of Heidelberg  
Topic:  
The eTOF Project at STAR:  
Characterization, Calibration and Data Validation  
of a large-scale multi-gap resistive plate chamber system

Erklärung:

Ich versichere, dass ich diese Arbeit selbstständig verfasst habe und keine anderen als die angegebenen Quellen und Hilfsmittel benutzt habe.

Heidelberg, den

.....